RALT–175

A Measurement of the Mean B-Hadron Lifetime Using the Central Drift Chambers of the OPAL Experiment at LEP

Gary John Barker
Department of Physics
Queen Mary and Westfield College
University of London

A thesis submitted in accordance with the regulations for the Degree of Doctor of Philosophy in the University of London

To My Parents.

Abstract

Using the precision tracking information of the OPAL Vertex Drift Chamber and surrounding Jet Chamber, a powerful technique for identifying the decays of B hadrons has been developed based on the reconstruction of secondary vertices inside the jets of multihadronic events.

By fitting the decay positions of B hadrons with a precision of $\sim$400 μm along the direction of flight it was possible to tag $b\bar{b}$ events, with an efficiency (purity) of 20% (80%), by selecting jets with a significant decay length. B hadrons at LEP travel on average a distance of 2 mm before they decay.

By performing a one parameter fit to the decay length distribution from multihadronic events collected in 1990 by the OPAL detector, we obtain a value for the mean B-hadron lifetime of

$$\langle \tau_{\mathrm{B}} \rangle = 1.359 \pm 0.055(\mathrm{stat.}) \pm 0.111(\mathrm{syst.})\ \mathrm{ps}\,.$$

Our result is consistent with the current world average and also represents a significant improvement in precision over previous determinations of $\langle \tau_{\mathrm{B}} \rangle$ based on a measure of the B decay length. Combined with an earlier measurement of the branching ratio $Br(\mathrm{B} \to \ell\nu X)$ by OPAL, the CKM matrix element $|V_{\mathrm{cb}}|$ is determined to be

$$|V_{\mathrm{cb}}| = 0.042 \pm 0.002(\mathrm{expt.}) \pm 0.003(\mathrm{theory})\,.$$

Preface

Using data collected in 1990 by the OPAL detector at the LEP e^+e^- storage ring, this thesis presents a measurement of the average B-hadron lifetime, $\langle\tau_B\rangle$.

Chapter 1 introduces the Standard Model of particle physics which encompasses the present theories of the electroweak and strong interactions between elementary particles. Emphasis is placed on the theoretical description of bottom-quark production and the subsequent emergence of B hadrons containing these quarks from the original e^+e^- annihilation. The lifetime of these hadrons before their decay into lighter flavours, is seen to be of fundamental importance to the understanding of how different generations of quarks within the Standard Model mix with one another.

After presenting in Chapter 2 a brief introduction to LEP and the components of the OPAL detector, in Chapter 3 we describe in some detail the tracking of charged particles in OPAL. Of most relevance to the subsequent physics analysis is the Vertex Chamber of OPAL, which provides precision spatial coordinates close to the e^+e^- interaction region. All aspects of the construction, operation and performance of the Vertex Chamber are reviewed.

The extraction from the data of a value for $\langle\tau_B\rangle$ relies heavily on Monte Carlo techniques for generating events and simulating detector response. These areas are described in Chapter 4 with particular emphasis placed on those aspects of the event generation affecting the production of bottom flavoured quarks and hadrons, and on those aspects of the detector simulation concerning the Vertex Chamber.

In the remaining two chapters we follow the development of a variable sensitive to the B-hadron lifetime and the subsequent use of this variable to extract a measurement of $\langle\tau_B\rangle$. Chapter 5 reviews the relative merits of variables designed to recognise various physical properties of $e^+e^- \rightarrow Z^0 \rightarrow b\bar{b}$ events with the aim of being able to separate this class of event from the background. We conclude that a measure of the B-hadron decay length in the detector is the best suited to identifying events containing b quarks, and this variable is then further developed for use in a lifetime determination. The measurement of $\langle\tau_B\rangle$ and an evaluation of the associated statistical and systematic uncertainties is then presented in Chapter 6.

Acknowlegements

This thesis would not have been possible without the efforts of many people. It is a pleasure to thank my supervisor, Steve Lloyd, and Roger Jones for their consistently expert advice, guidance and careful reading of previous drafts. Special thanks go also to Tony Carter for first giving me the chance to work at CERN and for always taking a keen interest in my research.

The many people at QMW who deserve my thanks for their help and friendship during my time there include: Paul Kyberd and Murrough Landon for solving my computing problems, the Family Pritchard (Terry for teaching me electronics and some interesting things too, plus Christine and Little Steve for worrying me into writing-up), Derek Newman-Coburn for having no hair and a constant stream of (bad) jokes, Graham Beck, the late Mirek Lasota, Daddy Assif, Adil Hasan, Small Fat Areeb, Simone Robins, Paul Singh, Andy Yeaman, Andy Cooper, Paul Harrison and Terry Wyatt-who taught me more particle physics than he probably realises.

The success of the OPAL vertex drift chamber-project was the result of hard work by many competent people. I am especially indebted to the Carleton University/NRC group for the construction and expert running of the chamber, to the RAL Electronics Division (especially Mick Jeffs) and to all in the Cambridge University group including The Great John Hill, Mirrors, Julie, Silly Teapot Billy, Roach-Man and David Ward-who had to endure more stupid questions from me than is fair. Thanks also must go to Bob Kowaleski for setting up the Lifetime Working Group which gave me somewhere to talk, Nigel Watson who would never say 'no' to me (oo-err), Glenn Patrick who allowed me to use RALVM so inefficiently, and to Mette and Sue in the OPAL office and Mary and Sue (again) in the SERC office for smoothing over those everyday problems. Outside of work big thanks go to those that make Geneva a place you can drink in, namely Dave Robbo and his big German car, Scottish Person, The Scottish Girls, Lucas and Sybille, Mike Mcdermot, Pete (like), Anna for being very Swedish, Matty Couch, Johnny Walker, Planet Thackeray and especially Sabine for laughing at my jokes.

A quick mention too for all my new colleagues and friends at Oxford who have helped make my transition there painless. Here's to Martin Bates for his huge physics insight, Rude Girl Beeston, Cliffy Hodgson, Guy 'Big Girls Blouse' Wilkinson, Paula

Collins (who is OK for a woman), Rashid Zuberi, Fluffy Stevie, John Holt, Nathalie Lieske and a special thanks must go to Paul Dauncey who is not lardy but just 'big-boned' and who has been VERY patient with me while finishing.

I acknowledge the Science and Engineering Research Council for financial support.

Contents

List of Figures

List of Tables

Chapter 1

Theoretical Background

1.1 The Standard Model Of Particle Physics

Modern particle physics recognises the existence of two intrinsically different types of elementary point-like particle; *fermions* and *bosons*. The fermions are particles of half-integer spin that obey Fermi-Dirac statistics and comprise quantum states asymmetric under (identical) particle interchange. Bosons are integer spin particles forming symmetric states obeying Bose-Einstein statistics. All matter is then made up of two types of fermion known as quarks (up (u), down (d), charm (c), strange (s), bottom (b) and top (t)) and leptons (electron (e), muon (μ), tau (τ) and their associated neutrinos (ν_ℓ)).

Success in the development of theories to describe the fermions and their interactions, has been made possible by exploiting a class of relativistic quantum field theory known as local non-Abelian gauge theories. These are theories based strongly on symmetry principles. In field theory, the Lagrangian density ($\mathcal{L}$) is always unaltered by an arbitrary change of global [1] phase in the fermion fields. The transformations of interest however, occur when we also demand invariance under a phase shift that can be different at each point of space time i. e. *local* gauge transformations of the general form

$$S(x) = \exp(ig \sum_{a=1}^{N} \alpha_a T_a(x)) \quad x \equiv (ct, \mathrm{x}), \tag{1.1}$$

for α_a a set of real parameters and $T_a(x)$ a set of Hermitian operators [2]. It is also convenient within this definition to introduce a common factor g, that subsequently is interpreted as a coupling strength for the interaction. The consequence of requiring the invariance of $\mathcal{L}$ to local transformations of the kind $S(x)$, is the necessary introduction of bosonic vector fields (gauge bosons), one for each generator of the

[1] Meaning the same at all points in space-time.

[2] In the language of group theory, the operators T_a are the generators of a Lie group of dimension N, whose general element is defined by the unitary transformation $S(x)$. Groups whose generators commute (do not commute) amongst themselves are termed Abelian (non-Abelian).

group and the appearance of fermion-boson interaction terms in the free-field Lagrangian. Thus it is in this way that the Yukawa picture of fermion interactions generated by the exchange of boson fields, is accounted for in gauge theories.

The gauge theory of the electromagnetic interactions, termed **Q**uantum **E**lectro **D**ynamics (QED), is based on the Abelian gauge group U(1). Fermions interact via the exchange of a single gauge boson (the photon, (γ)), illustrated in Figure 1.1 (a) for the process $e^+e^- \rightarrow \mu^+\mu^-$. In QED the coupling strength of the fermions to the

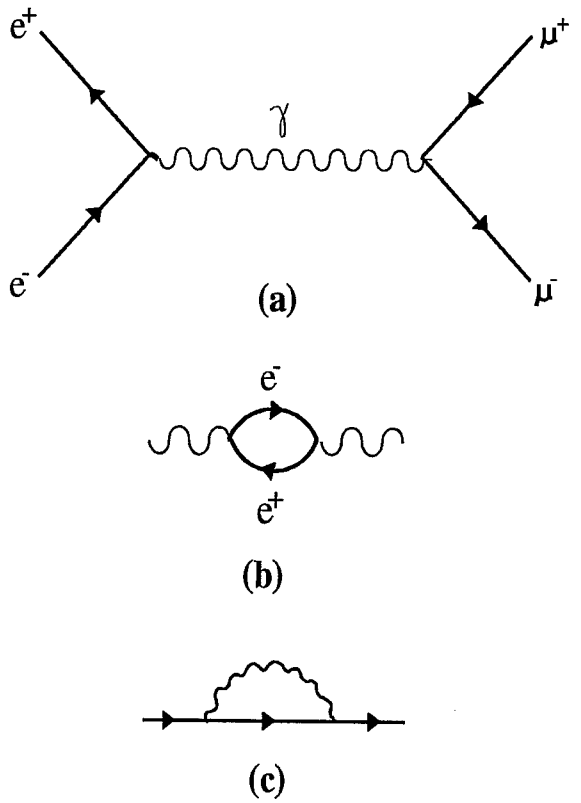

Figure 1.1: (a) The lowest order (or Born level) QED-Feynman diagram for the process $e^+e^- \rightarrow \mu^+\mu^-$. Two examples of divergent diagrams in QED: (b) the creation and re-annihilation of an e^+e^- pair, and (c) the emission and reabsorption of a photon by a charged fermion.

photon is proportional to the fermion electric charge which, as a consequence of the U(1) symmetry, is a conserved quantity in all QED processes.

QED calculations to higher orders in perturbation theory than that represented by the Born level diagram involves the inclusion of closed-loop processes such as those shown in Figures 1.1(b) and (c). These diagrams however correspond to divergent integrals which make infinite contributions to any amplitude calculations attempted beyond leading order. In QED it is found that these infinite terms may be absorbed by a redefinition of the charges and masses to be equal to their physically measured values. The application of this technique, known as *renormalisation*, then renders all amplitude and hence cross-section calculations to be finite. The requirement that a candidate theory of particle interactions be renormalisable is

clearly a prerequisite if physical predictions beyond leading order in the perturbation expansion are to be possible. It was shown by 't Hooft in 1971 [1] that, in fact, all gauge theories are renormalisable.

The formulation of a gauge theory of the weak interaction consistent with experimental measurements requires invariance with respect to the non-Abelian group SU(2) × U(1). To accommodate the parity-violating nature of the weak interaction, fermion states of right-handed helicity enter the theory as $SU(2)_W$ singlets [3] with the left-handed states transforming as doublets of $SU(2)_W$ (see Table 1.1). To maintain the invariance of the theory requires the introduction of three gauge

Generation			Quantum Numbers			
I	II	III	Q^{em}	Y	I^W	I_3^W
$\begin{pmatrix} \nu_e \\ e \end{pmatrix}_L$	$\begin{pmatrix} \nu_\mu \\ \mu \end{pmatrix}_L$	$\begin{pmatrix} \nu_\tau \\ \tau \end{pmatrix}_L$	$\begin{matrix} 0 \\ -1 \end{matrix}$	-1	+1/2	$\begin{matrix} +1/2 \\ -1/2 \end{matrix}$
$\begin{pmatrix} u \\ \mathrm{d}' \end{pmatrix}_L$	$\begin{pmatrix} c \\ \mathrm{s}' \end{pmatrix}_L$	$\begin{pmatrix} t \\ \mathrm{b}' \end{pmatrix}_L$	$\begin{matrix} +2/3 \\ -1/3 \end{matrix}$	+1/3	+1/2	$\begin{matrix} +1/2 \\ -1/2 \end{matrix}$

Table 1.1: The fermion content and associated quantum numbers of the electroweak theory. Here, Q^{em} is the electromagnetic charge, Y is the weak hypercharge and I^W and I_3^W are the weak isospin and third component of weak isospin respectively. The lower members of the quark doublets carry a prime to denote weak eigenstates and are discussed further in Section 1.4.1. (The top quark remains unobserved by experiment and there is only indirect evidence for the existence of ν_τ. A recent review [2] quotes the value, $m_t = 144^{+30}_{-33}\,\mathrm{GeV}/c^2$, based on current values for Standard Model parameters and the best experimental limit presently stands at $m_t > 89\,\mathrm{GeV}/c^2$ (@95 % CL) [3]).

bosons ($W_i, i = 1,2,3$) coupling to weak isospin (I^W) and associated with the three generators of the SU(2) group. The physical mediators of the weak charged current interaction (the $W^\pm$ bosons) are then identified as being the following linear combinations,

$$W^\pm = \frac{1}{\sqrt{2}}(W_1 \mp iW_2). \tag{1.2}$$

The $W^\pm$ bosons mediate weak charged current interactions of the type shown in Figure 1.2(a). In addition, there is a boson singlet field, B, associated with the

[3] Use of the 'W' subscript stands for 'weak' and distinguishes this use of the group SU(2) from any other.

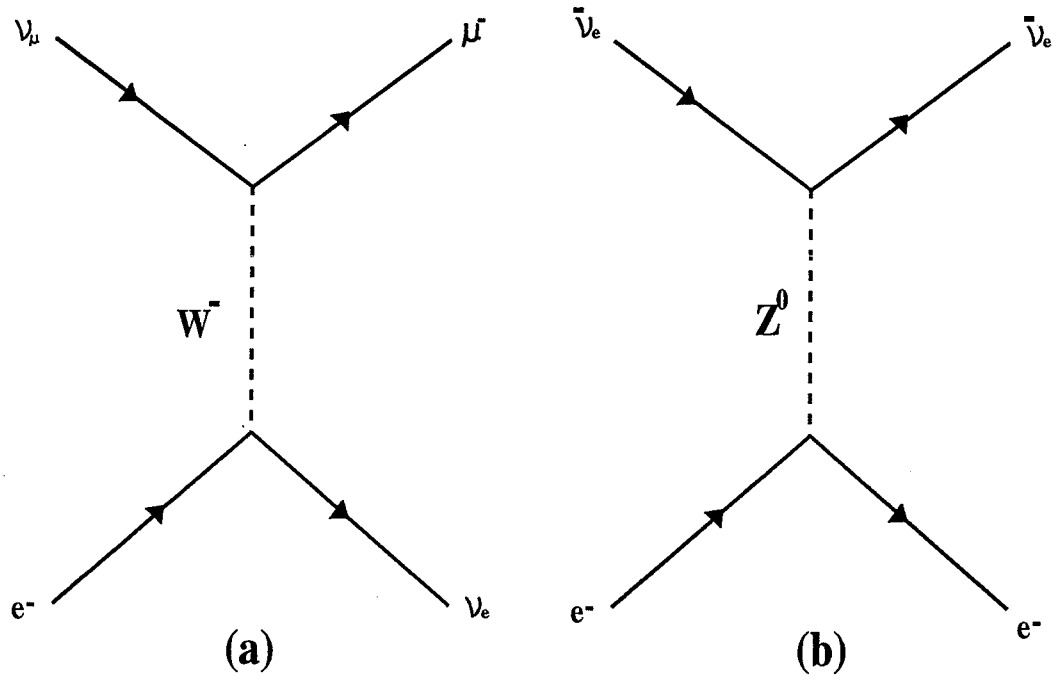

Figure 1.2: Examples of weak (a) charged current and (b) neutral current processes.

$U(1)_W$ group and which couples to the weak hypercharge (Y). Through a mixing of the $SU(2)_W$ boson field W_3 with the B it is possible to recover exactly the photon field (A^μ) of QED, with the orthogonal combination predicting the existence of a new neutral boson field (Z^0):

$$A^\mu = B^\mu \cos\theta_W + W_3^\mu \sin\theta_W. \quad (1.3)$$

$$Z^\mu = -B^\mu \sin\theta_W + W_3^\mu \cos\theta_W \quad (1.4)$$

The mixing is specified by a single angle, θ_W, known as the weak mixing or Weinberg angle. This $SU(2)_W \times U(1)_W$ gauge invariant interaction, first introduced by Glashow in 1961 [4], is commonly termed the *electroweak* interaction reflecting the fact that in a certain sense it unifies the weak and electromagnetic interactions. The presence of Z^0 bosons in the theory predicted that there should be weak neutral current interactions of the type shown in Figure 1.2(b). These were duly observed in the early 1970's, so providing one of the earliest direct confirmations of the electroweak formulation.

The electroweak theory as outlined above describes massless fermions and bosons. Simply introducing mass terms into the Lagrangian density is not possible without forfeiting the $SU(2)_W \times U(1)_W$ local symmetry with the consequence that the theory is no longer renormalisable. One solution to this problem, introduced independently by Weinberg and Salam [5], is the application of the Higgs mechanism to generate

masses for fermions and gauge bosons in a way that retains the gauge invariance of the Lagrangian density. In the minimal solution, a weak isospin doublet of complex scalar fields is introduced. Three field components provide the longitudinal polarisation states, and hence allow masses for the $W^{\pm}$ and Z^0, leaving one physical scalar field associated with the neutral Higgs boson H^0. The H^0 mass is not predicted by the theory [4].

The masses attained by the $W^{\pm}$ and Z^0 bosons can be expressed in terms of three experimentally well known parameters; the fine structure constant $\alpha = e^2/4\pi\epsilon_0$, the Fermi coupling constant G_F and θ_W,

$$m_W = \left(\frac{\alpha\pi}{\sqrt{2}G_F}\right)^{\frac{1}{2}} \frac{1}{\sin\theta_W} \tag{1.5}$$

$$m_Z = \left(\frac{\alpha\pi}{\sqrt{2}G_F}\right)^{\frac{1}{2}} \frac{2}{\sin 2\theta_W}. \tag{1.6}$$

Crucial confirmation of the electroweak theory came in 1982 with the discovery of the $W^{\pm}$ bosons by the UA1 and UA2 Collaborations [7], to be followed in 1983 by the detection of the Z^0 [8].

Quantum Chromo Dynamics (QCD) is the name given to the gauge theory of the strong interaction and is based on the non-Abelian gauge group SU(3). The idea that quarks contain an additional 'colour' degree of freedom was initially introduced to resolve the spin statistics problem of baryon states such as the Ω^-, to which the quark model assigned three identical fermions in a symmetric spin state. It was postulated that the quarks each exist in one of three possible colour states and further that they only combine to form overall colour singlets i. e. the baryons and mesons. An important verification of the colour charge hypothesis comes from measurements of the Drell ratio

$$R = \frac{\sigma(e^+e^- \rightarrow q\bar{q})}{\sigma(e^+e^- \rightarrow \mu^+\mu^-)} \tag{1.7}$$

where; $\sigma(e^+e^- \rightarrow \mu^+\mu^-)$ and $\sigma(e^+e^- \rightarrow q\bar{q})$ are the QED e^+e^- annihilation cross sections to μ and quark pairs respectively. Ignoring any strong interaction effects between final state quarks and considering energy regions away from the immediate vicinity of resonances, R is expected to equal $3\sum_i (Q_i^{em})^2$, where Q_i^{em} is the electric charge (in units of the electronic charge e) of quark flavour i and the sum goes over all flavours for which the collision energy is above threshold. The dependence on Q derives from the QED coupling strength being proportional to the charge and the factor of 3 accounts for the extra colour degree of freedom that the quarks carry but the muons do not. Figure 1.3 presents measurements of R from various

[4]The experimental limit for the mass of a Standard Higgs boson currently stands at, $m_{H^0} > 57\,\mathrm{GeV}/c^2$[6].

e^+e^- annihilation experiments over a range of centre-of-mass energies and provides good evidence for the existence of quark colour charge.

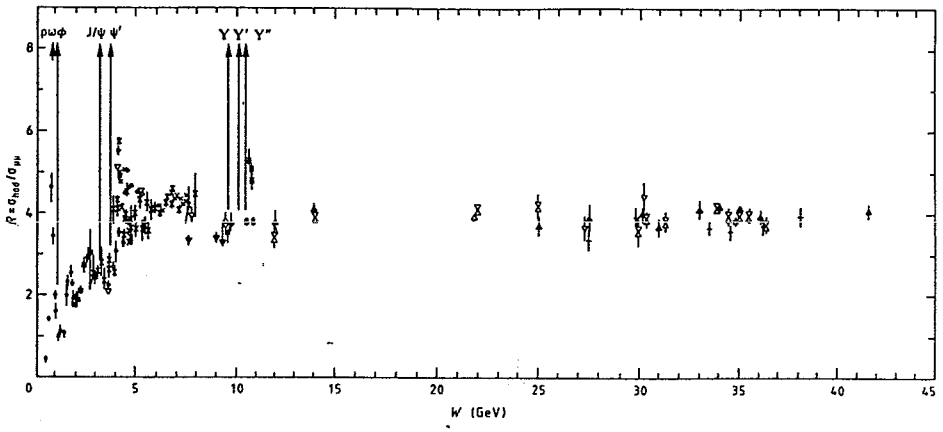

Figure 1.3: Measurements of the Drell ratio, $R = \frac{\sigma(e^+e^- \to q\bar{q})}{\sigma(e^+e^- \to \mu^+\mu^-)}$, over a range of centre-of-mass energies.

In the framework of QCD quarks transform as colour triplet representations of $SU(3)_C$ via the exchange of eight, massless, gauge bosons termed gluons [5]. The gluons carry a colour and an anti-colour quantum number which allows coupling not only to the colour charge of the quarks, but also between other gluons in processes of the kind shown in Figure 1.4. Gauge boson self interactions are a general feature of gauge theories based on non-Abelian groups and should be contrasted with the photon of the $U(1)_{QED}$ theory that carries no electric charge and for which there is no equivalent diagram to figure 1.4.

The non-Abelian nature of the $SU(3)_C$ interactions leads to fundamental differences in the nature of QCD compared to QED. In analogy to QED where the strength of the electromagnetic coupling can be expressed in terms of $\alpha = e^2/4\pi\epsilon_0$, strong interactions are governed by a coupling parameter α_s which in lowest order takes the form,

$$\alpha_s(Q^2) = \frac{12\pi}{(33 - 2n_f)\ln(Q^2/\Lambda^2)} \tag{1.8}$$

where; Q is the momentum transfer scale of the interaction, n_f is the number of quark flavours and Λ is the QCD mass scale ($\sim 200\,\text{MeV}$) representing the scale at which the coupling becomes 'strong'. The dependence (or 'running' nature) of α_s with Q^2 is seen also in the behaviour of the QED coupling but at a much weaker level and in the opposite direction. This basic difference has its origin in the presence of gluon self interactions. The effect of bare charge 'screening' in QED acts to increase effective electric charges as the momentum transfer increases. The

[5] The subscript 'C' stands for 'colour' and distinguishes this application of the SU(3) group from any other.

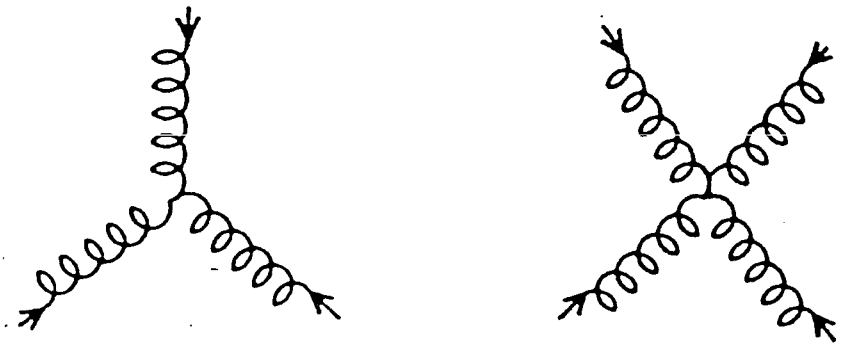

Figure 1.4: Gluon self-interaction processes.

effect of gluon (and quark) loop vacuum fluctuations however in QCD act to spread out the effective quark colour charge as Q^2 increases resulting in an anti-screening of colour charge.

We could equivalently view the running properties of α_s with regard to a distance rather than a momentum-transfer scale. At large quark separations (low Q^2) therefore, α_s is large with the consequence that quarks are effectively *confined* within colour singlet hadrons. No experiment has ever unambiguously observed an isolated quark (or even a composite quark state of net non-zero colour). At small separations (or equivalently large Q^2), α_s can fall to levels where the quarks can be considered as essentially non-interacting states - this is the regime of so-called *asymptotic freedom.* The fact that α_s tends to be relatively large (~ 0.12 at 91 GeV) means that in general perturbative calculations in QCD are significantly less precise than those possible in the electroweak sector. Further, at energy scales typical of hadronic processes the strong coupling becomes large enough ($\alpha_s \sim 1$) that perturbation theory can no longer be applied and the theory becomes incalculable. This constraint necessitates the implementation of phenomenological models to describe low Q^2 processes such as quark fragmentation (described in Section 1.3).

The $SU(3)_C \times SU(2)_W \times U(1)_W$ gauge invariant theory outlined above forms what has become known as the *Standard Model* of particle physics. The predictive success of the theory when compared to experiment will be discussed further in the next section. It is however prudent to mention at this point that the Standard

Model is in many respects unsatisfactory. Indeed it is generally accepted that the $SU(3)_C \times SU(2)_W \times U(1)_W$ theory is likely to be just the low energy remnant of some 'unified' theory whose inherent symmetry has been broken. At the heart of the problem is the dependence of the current theory on experimental input. There are a number of parameters including coupling constants, mixing angles and particle masses, that have to be supplied whose values the theory treats as being arbitrary. In addition, there are facets of the Standard Model which are included by design but are understood at no deeper level than empirical fact. Under this heading are such questions as; why are there apparently three particle generations ? (see Table 1.1), why is there the distinction between left and right-handed fermion states ?, and why are the relevant gauge symmetries based on the gauge groups U(1), SU(2) and SU(3) specifically ? Answers to these questions may come from a *Grand Unified Theory* [9] that truly unifies the electromagnetic, weak and strong interactions based on a single gauge group which contains the $SU(3)_C \times SU(2)_W \times U(1)_W$ symmetry as a sub-group.

1.2 The Process $e^+e^- \rightarrow b\bar{b}$ at the Z^0 Resonance

The first evidence for the existence of a fifth quark, came with the discovery in 1977 by the CFS Collaboration [10] of a narrow resonance (Υ) and first excited state (Υ') in the invariant mass spectrum of μ-pairs from the process: p + Nucleus $\rightarrow \mu^+\mu^- +$ X. Interpreting the Υ as the (1s) bound state $|b\bar{b}\rangle$, accounted for the relatively long lifetime of the state since the major decay mode available is the OZI-suppressed [11] strong decay to three gluons. Confirmation of this result and the discovery of additional excited states of the Υ followed from studies of e^+e^- annihilations which are well suited to the clean production of b-quark resonances. Figure 1.5 shows the presence of the Υ resonance and the first three excited states as measured by the CLEO Collaboration at the e^+e^- storage ring CESR, at Cornell, USA. In 1980 the fourth resonance, $\Upsilon(4S)$, was found [13] at 10.58 MeV centre-of-mass energy. It is a much broader resonance than the previous three states, indicating that the threshold has been crossed for production of pairs of the lightest B mesons; B_u and B_d. Since the discovery, threshold e^+e^- machines (notably CESR at Cornell and DORIS-II at DESY) running at the $\Upsilon(4S)$ (and higher excited states of the Υ), have provided a great wealth of data concerning B meson decay properties.

Bottom quarks are produced from e^+e^- annihilation via one of the two processes[6] illustrated in Figure 1.6. The production of fermion pairs, $f\bar{f}$, via photon or Z^0exchange

[6]Production via Higgs exchange is negligible for the known fermions.

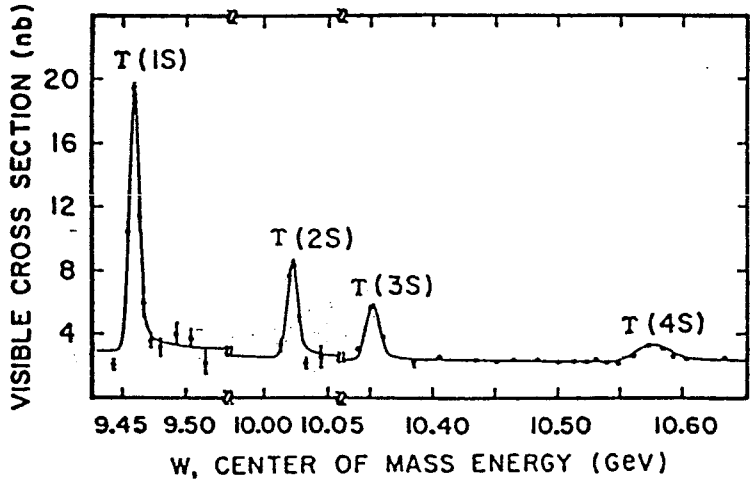

Figure 1.5: The cross section for Υ production as measured by the CLEO Collaboration. From [12].

is described within the framework of the electroweak theory by the neutral current

$$e\sum_i Q_i^{em}\bar{f}_i\gamma^\mu f_i A_\mu + \frac{g}{2\cos\theta_W}\sum_i \bar{f}_i\gamma^\mu(v_i - a_i\gamma^5)f_i Z_\mu, \tag{1.9}$$

where; $g = e/\sin(\theta_W)$ and the sum goes over all types of fermion field. The first term in Equation 1.9 relates to the process of Figure 1.6(a) and describes electromagnetic interactions (QED). The photon coupling is seen to be eQ_i^{em} (as noted in Section 1.1). The second term is the weak neutral current interaction corresponding to Figure 1.6(b). In contrast to the $W^\pm$ couplings of the charged weak current, the Z^0 couples to both left and right-handed fermions (albeit not equally due to their different weak isospin and hypercharge assignments-see Table 1.1). The fermion couplings to the Z^0 can be conveniently expressed in terms of a vector and axial-vector part as,

$$\begin{aligned} v_i &\equiv I_3^W(i) - 2Q_i^{em}\sin^2\theta_W \\ a_i &\equiv I_3^W(i). \end{aligned} \tag{1.10}$$

Defining an angle θ to be that between the outgoing fermion and the incoming e^- direction from the production diagrams of Figure 1.6, the differential cross-section takes the form

$$\frac{d\sigma_{f\bar{f}}}{d\cos\theta}\alpha(1+\cos^2\theta + \frac{8}{3}A_{FB}\cos\theta). \tag{1.11}$$

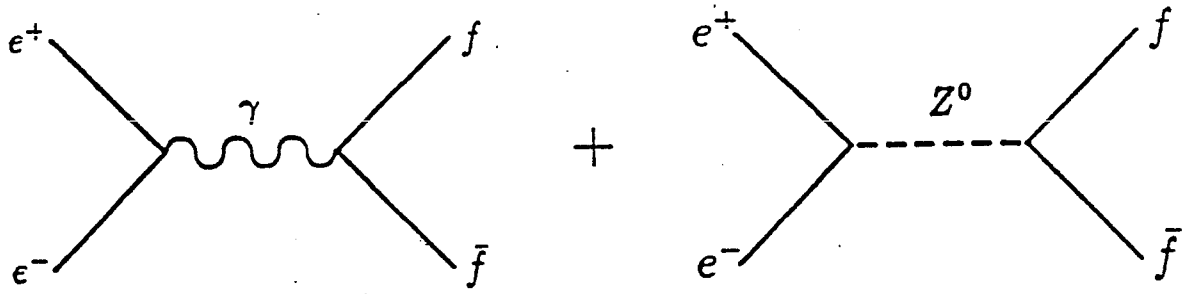

Figure 1.6: Fermion production (to lowest order) in e^+e^- annihilation via a (a) photon and (b) Z^0 propagator.

The term linear in $\cos\theta$ introduces a forward-backward asymmetry to the angular dependence which derives from interference between the vector and axial couplings of the Z^0, both with the initial e^+e^- pair and with the final state fermions. This asymmetry is quantified by the parameter A_{FB}, which for the case of b quark production takes the form,

$$A_{FB}^{b} = \frac{3}{4}\frac{2v_e a_e}{(v_e^2+a_e^2)}\frac{2v_b a_b}{(v_b^2+a_b^2)}. \tag{1.12}$$

The phenomenon of $b\bar{b}$ mixing, where a neutral $B^0(\bar{B}^0)$ meson can transform into its charge conjugate before decay, introduces a correction to A_{FB}^{b}. The $B\bar{B}$ mixing parameter, χ, is the probability of a B^0 meson turning into a $\bar{B}^0$ meson before decay and has been measured by the LEP experiments to have a mean value [2],

$$\chi = 0.144 \pm 0.020.$$

The measured forward-backward asymmetry can then be related back to the intrinsic quantity via

$$A_{FB}^{b} = \frac{A_{FB}^{b}(\text{measured})}{1-2\chi}. \tag{1.13}$$

Correcting the average LEP measured value for the asymmetry by the value for χ given above gives [2],

$$A_{FB}^{b} = 0.126 \pm 0.022.$$

For centre-of-mass energies in the the vicinity of the Z^0 mass, the cross section for $e^+e^- \to f\bar{f}$ is completely dominated by the presence of the Z^0 resonance. The situation is well illustrated by Figure 1.7. Here, cross-section measurements from various e^+e^- annihilation experiments operating well below the Z^0 pole show the expected $1/s$ dependence characteristic of the photon exchange process of Figure 1.6(a). The measurements from the LEP collider operating at the Z^0 pole show clearly the large enhancement that results from crossing the threshold for producing real Z^0 bosons from the process pictured in Figure 1.6(b).

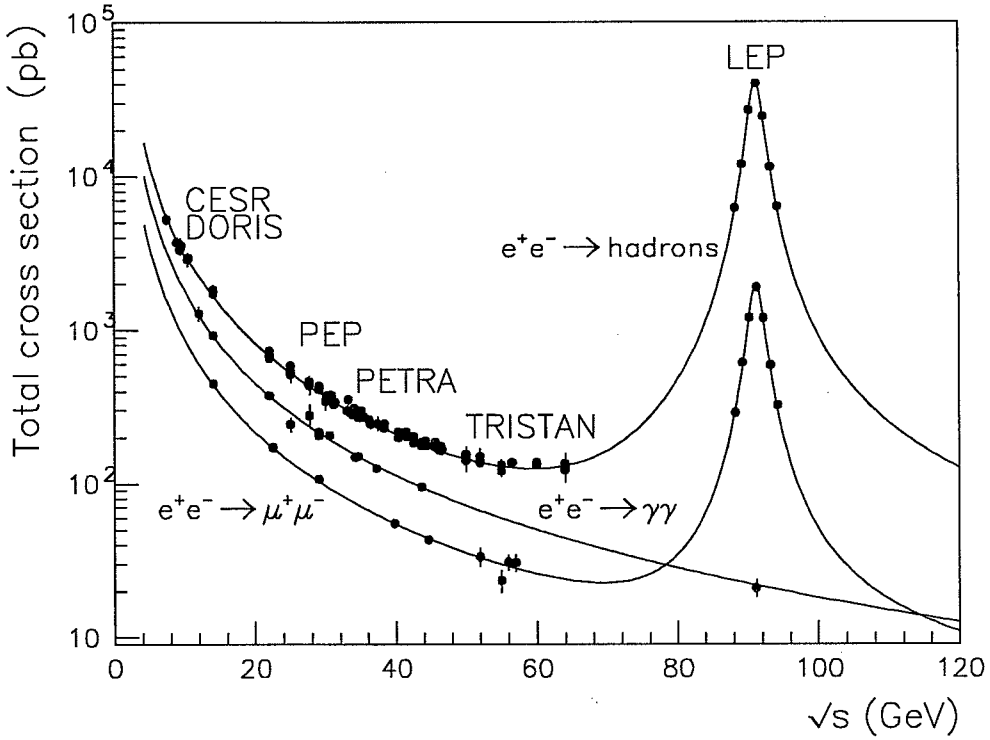

Figure 1.7: Measurements of the cross section $\sigma(e^+e^- \to f\bar{f})$ as a function of centre-of-mass energy $\sqrt{s}$.

The Standard Model lowest order expression for the cross section at the Z^0 pole is,

$$\sigma(e^+e^- \to f\bar{f}) = \frac{12\pi(s/m_Z^2)\Gamma_{e^+e^-}\Gamma_{f\bar{f}}}{(s-m_Z^2)^2 + s^2\Gamma_Z^2/m_Z^2} \tag{1.14}$$

where $\Gamma_{e^+e^-}$ and $\Gamma_{f\bar{f}}$ are the *partial widths* for the processes $Z^0 \to e^+e^-$ and $Z^0 \to f\bar{f}$ respectively. The *total* decay width of the Z^0, (Γ_Z), is then defined as the sum

$$\Gamma_Z = \sum_{\ell} \Gamma_{\ell\bar{\ell}} + \sum_{q} \Gamma_{q\bar{q}} + \Gamma_{inv}. \tag{1.15}$$

Here, Γ_{inv} represents the 'invisible' partial width of the Z^0 decaying via the channel $Z^0 \to \nu_i\bar{\nu}_i$, $i = 1, \ldots, N_\nu$, where N_ν is the number of neutrino species above the production threshold.

The cross section of Equation 1.14 is inadequate for the comparison of LEP data with the Standard Model. Significant contributions from diagrams of higher order than those pictured in Figure 1.6 are required. These corrections are generically termed *radiative corrections* and take account of such processes as photon and gluon radiation from fermions, modifications to the propagator of the type illustrated in Figure 1.1 and vertex corrections. The most significant source of radiative correction is due to initial state photon Bremsstrahlung which accounts for a $\simeq 30\%$ [2] reduction in the peak cross section. Table 1.2 presents the current experimental knowledge of various Z^0 lineshape parameters and compares the results to their Standard Model predictions. The agreement is found to be remarkably good to measurements which in many cases are now known to an accuracy of better than 1%.

Quantity	Measured Value	Standard Model
m_Z (GeV/c^2)	$91.187 \pm 0.007^\star$	Input
Γ_Z (GeV)	$2.492 \pm 0.007^\star$	2.488 ± 0.006
$\Gamma_{\ell\bar{\ell}}$ (MeV)	$83.0 \pm 0.6^\bullet$	83.7 ± 0.02
$\Gamma_{q\bar{q}}$(MeV)	$1736.0 \pm 11.0^\bullet$	83.7 ± 0.02
Γ_{inv}(MeV)	$502.0 \pm 9.0^\bullet$	501.0 ± 1.0
m_W (GeV/c^2)	$80.22 \pm 0.26^\bullet$	80.21 ± 0.16

Table 1.2: Measurements of some selected Standard Model parameters at the Z^0 pole. Values flagged '$\star$' are taken from [14] whereas those marked '$\bullet$' are from [15]. The theory predictions from [15], are based on $m_Z = 91.17 \pm 0.02\,\mathrm{GeV}/c^2$, $50\,\mathrm{GeV}/c^2 < m_{H^0} < 1\,\mathrm{TeV}/c^2$ and $m_t = 150^{+23}_{-26}\,\mathrm{GeV}/c^2$(for $m_H = 250\,\mathrm{GeV}/c^2$).

The partial decay width for the channel $Z^0 \rightarrow b\bar{b}$ in lowest order and ignoring the b-quark mass is given by,

$$\Gamma_{b\bar{b}} = \frac{G_F m_Z^3}{8\sqrt{2\pi}}(v_b^2 + a_b^2). \tag{1.16}$$

Measurements of $\Gamma_{b\bar{b}}$ are of particular interest because of the near independence of the width on the top quark mass (see, for example, [16]). This independence derives from a fortuitous partial cancellation of the top-quark vacuum polarisation amplitude by final state vertex corrections involving the top quark that are specific to the process $Z^0 \rightarrow b\bar{b}$ (see Figure 1.8). This effect translates into a difference between $\Gamma_{b\bar{b}}$ and $\Gamma_{d\bar{d}}$ at the level of 2% [17] for a top quark mass of $150\,\mathrm{GeV}/c^2$- a test of which is beyond the present level of experimental accuracy. Review [18] cites an average value for LEP of $\Gamma_{b\bar{b}} = 361 \pm 19\,\mathrm{MeV}$ to be compared with a Standard Model prediction of $\Gamma_{b\bar{b}} = 378^{+1}_{-4}\,\mathrm{MeV}$.

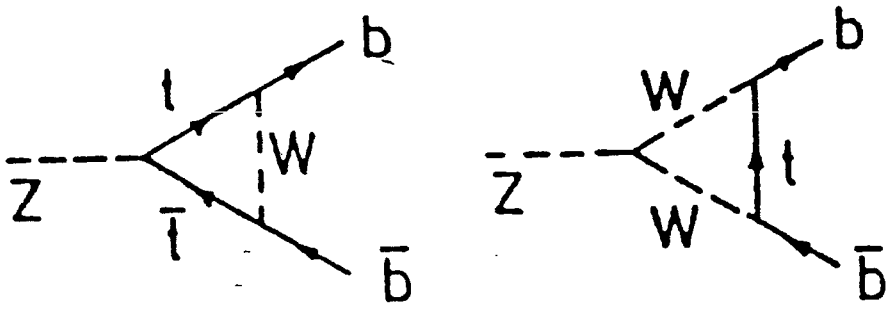

Figure 1.8: Electroweak vertex corrections that are specific to the $Z^0 \rightarrow b\bar{b}$ vertex.

1.3 Bottom Quark Hadronisation

That the electroweak theory is eminently satisfactory in accurately describing the production of b quarks from Z^0 decay is clear from the previous section. The experimental observation of $Z^0 \rightarrow b\bar{b}$ events however reveals extra layers of complexity. Quarks manifest themselves only as bound states of colourless hadrons that emerge from the original e^+e^- annihilation surrounded by other hadrons that together form what is known as a *jet*. The transition process of quark→hadron we term *hadronisation* and is illustrated in Figure 1.9, which shows the detection of a candidate $Z^0 \rightarrow b\bar{b}$ event.

Multi-hadronic events, such as Figure 1.9, often contain more than the two jets associated with the $q\bar{q}$ pair, which are attributed to hard gluon Bremsstrahlung from either (or both) of the quarks. Perturbative QCD calculations at present exist only up to $\mathcal{O}(\alpha_s^2)$, which can describe at most four partons and are insufficient to describe the data at the Z^0. In Chapter 4 we describe, in the context of Monte Carlo simulation, how the implementation of a *parton shower* model can be used to retain good agreement with the data.

Describing the development of a hadronic jet within QCD involves tracing many quark and gluon branchings into more and more partons with smaller and smaller virtual masses. Eventually, the limit introduced in Section 1.1 is reached where the characteristic momentum transfer is small enough (i.e. $Q^2 \sim \Lambda$) to ensure that

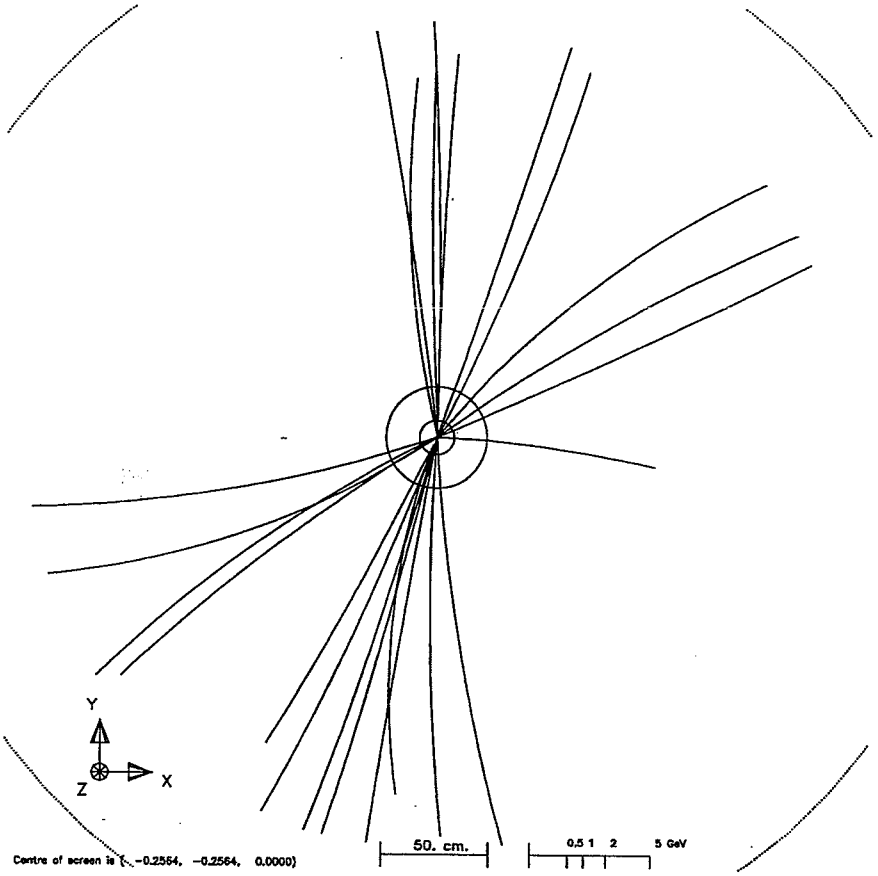

Figure 1.9: A candidate $Z^0 \rightarrow b\bar{b}$ decay in the OPAL detector (see Chapter 2). The specific quark flavour of the Z^0 decay is inferred from the presence of a high momentum muon track (see Chapter 5 for more details). For obvious reasons, Z^0 decays to quark pairs are often known as *multi-hadronic* events.

α_s becomes too large to permit perturbative calculations. At this point phenomenological models must be invoked to describe the final binding of quarks into hadrons in a process known as *fragmentation.* We return to the subject of fragmentation in Chapter 4 with regard to the Monte Carlo modelling of multi-hadronic events.

Hence, the process of hadronisation can be viewed as the combination of an initial perturbative QCD phase where the general underlying jet structure of the event is determined, followed by low Q^2 non-perturbative processes from which partons emerge bound up inside jets of associated hadrons. The hadronisation of the b quark is expected to be hard simply because the inertia carried by the heavy quark is retained in the hadron. Evidence for this comes from measurements of the quantity $\left\langle x_E^B \right\rangle$ defined as the mean fraction of the electron beam energy taken by a B hadron. A mean value based on the measurements of the LEP experiments is [17],

$$\left\langle x_E^B \right\rangle = 0.705 \pm 0.011. \tag{1.17}$$

1.4 B-Hadron Decays

1.4.1 Weak Quark Mixing

Within the electroweak theory, quark states can transform into their $SU(2)_W$ doublet partner through the emission of a $W^{\pm}$ boson which, in the absence of any mixing between the quark generations, renders the b-quark stable. Decay into the more massive top quark doublet partner is energetically impossible and all lighter quark flavours belong to $SU(2)_W$ doublets from different generations (see Table 1.1). The wealth of experimental evidence for charged current transitions between generations, is thus theoretically accounted for by considering the weak quark eigenstates (d′, s′, b′) as mixtures of the mass eigenstates (d, s, b)[7]. This can be expressed in terms of a unitary mixing matrix due to Cabibbo, Kobayashi and Maskawa (CKM) [19],

$$\begin{pmatrix} d' \\ s' \\ b' \end{pmatrix} = \begin{pmatrix} V_{ud} & V_{us} & V_{ub} \\ V_{cd} & V_{cs} & V_{cb} \\ V_{td} & V_{ts} & V_{tb} \end{pmatrix} \begin{pmatrix} d \\ s \\ b \end{pmatrix} \tag{1.18}$$

The accurate measurement of the CKM matrix elements has great importance in constraining the uncertainty of predictions from the electroweak theory.

The current value of the CKM matrix from experiment (at 90% confidence level) [15] is shown below, where the unitarity property of the matrix has been used to determine those elements involving the top quark:

$$\begin{pmatrix} 0.9747 - 0.9759 & 0.218 - 0.224 & 0.002 - 0.007 \\ 0.218 - 0.224 & 0.9735 - 0.9751 & 0.032 - 0.054 \\ 0.003 - 0.018 & 0.030 - 0.054 & 0.9985 - 0.9995 \end{pmatrix} \tag{1.19}$$

It can be seen that in general, the diagonal terms of the CKM matrix are close to unity whereas the off-diagonal terms are small but nonzero. The implication for decays of the b-quark is therefore that transitions b → c and b → u can occur with amplitudes proportional to $|V_{cb}|$ and $|V_{ub}|$ respectively, albeit at a rate slower than that predicted for the process t → b. Equation 1.19 illustrates the important fact that the degree of mixing between the second and third generation is somewhat less than that existing between the first and second (compare for example $|V_{cb}|$ with $|V_{us}|$). This has the consequence that the lifetime of the b-quark (and of any hadron containing a b-quark) is longer than would perhaps be expected, and hence came as somewhat of a surprise when the first B-hadron lifetime measurements were made (see Section 6.1). In addition, Equation 1.19 illustrates that $|V_{cb}|$ is approximately an order of magnitude larger than $|V_{ub}|$ reflecting that b → c decays dominate.

[7]Note that the (d,s,b) states are chosen to mix rather than (u,c,t) by convention only.

1.4.2 The Spectator Quark Model

In the *Spectator Model* of B-hadron decay the b-quark decays essentially as a free particle under the assumption that the light antiquark in B^0, B^-, B_s^0 and the diquark in Λ_b, have a negligible effect on the decay process i. e. they are merely 'spectators'. This mechanism is illustrated in Figure 1.10 where the final state c or u quark forms a colour singlet with the spectator quark, while the virtual W decays either into a second colour singlet $q_i q_j$ or a lepton pair $\ell\bar{\nu}_\ell$. For the decay of a free b quark to

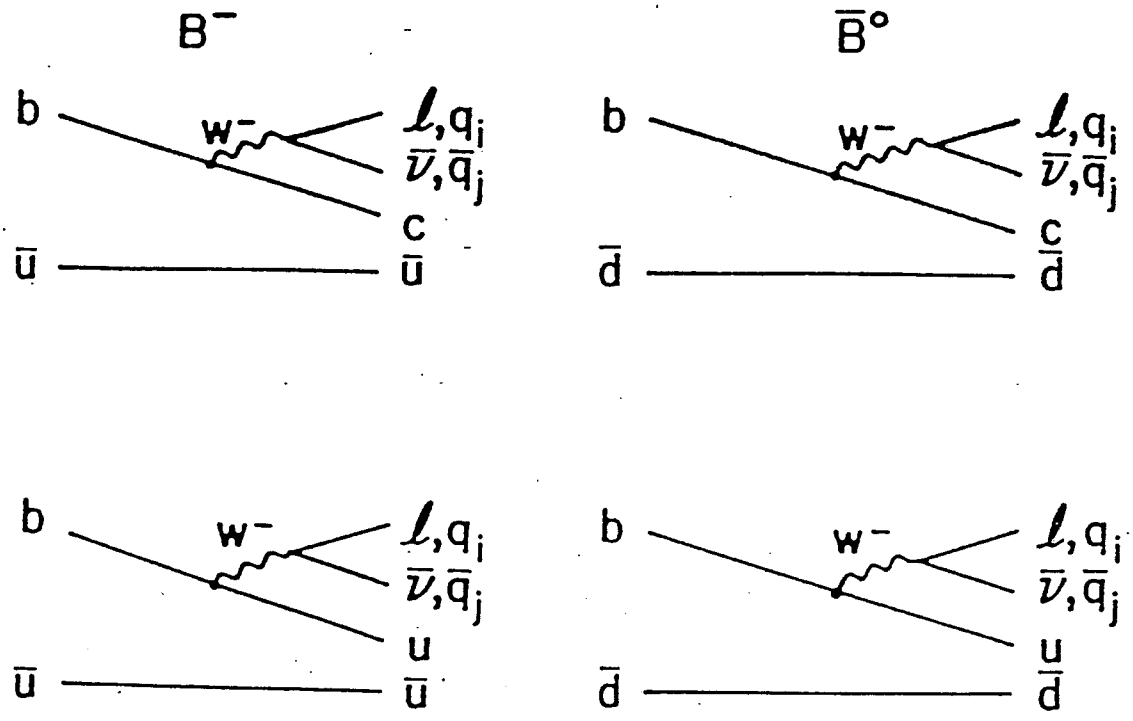

Figure 1.10: Spectator model diagrams for B-hadron decay.

a lighter quark flavour q and an additional fermion pair $f_i\bar{f}_j$, the predicted decay width has the form of a modified muon width $\Gamma(\mu \to e\nu\bar{\nu})$ as:

$$\begin{aligned}\Gamma(b \to q f_i \bar{f}_j) &= \left[N_C\,|V_{qb}|^2 \left(\frac{m_b}{m_\mu}\right)^5\right].\Gamma(\mu \to e\nu\bar{\nu}) \\ &= N_C\,|V_{qb}|^2 \cdot \left[\frac{G_F^2 m_b^5}{192\pi^3}\right] \qquad (1.20)\end{aligned}$$

where all fermions are assumed massless and the colour factor $N_C = 1$ when $f_i\bar{f}_j$ is a lepton pair and $N_C = 3$ for a quark pair (in which case Equation 1.20 should also be scaled by a factor $|V_{ij}|^2$). The width depends on the CKM matrix element

$|V_{qb}|$ which is unity for muon decay since there is no lepton mixing analogous to that described in Section 1.4.1 for quarks. Naively, if we consider only the extra colour factor associated with the hadronic decay channels, Equation 1.20 predicts:

$$\Gamma(W^* \rightarrow \bar{u}d : \bar{c}s : \bar{\nu}_e e : \bar{\nu}_\mu \mu : \bar{\nu}_\tau \tau) = 3 : 3 : 1 : 1 : 1$$

where Γ is in units of $|V_{cb}|^2 G_F^2 m_b^5/192\pi^3$. The predicted semi-leptonic branching fraction is thus, $Br_{sl} = \frac{1}{9} = 11\%$, for each lepton flavour.

This rather naive picture of B-hadron decay can be extended by applying three corrections to the spectator width of Equation 1.20 i. e.

$$\Gamma(\bar{b} \rightarrow q f_i \bar{f}_j) \rightarrow \Gamma(b \rightarrow q f_i \bar{f}_j)\Phi_{ps}\Phi_{sg}\Phi_{hg}. \tag{1.21}$$

We briefly consider each of these corrections in turn;

(1) Phase Space Suppression (Φ_{ps}): A factor $\Phi_{ps} = \Phi_{ps}(\frac{m_q}{m_b}, \frac{m_{f_i}}{m_b}, \frac{m_{\bar{f}_j}}{m_b})$ is introduced to each partial decay width to account for non-negligible fermion masses compared to the b-quark mass. Taking account of m_q only, this factor evaluates to [22]:

$$\Phi_{ps}(\epsilon_q, 0, 0) = 1 - 8\epsilon^2 + 8\epsilon^6 - \epsilon^8 - 24\epsilon^4 \ln \epsilon \tag{1.22}$$

where $\epsilon_q \equiv m_q/m_b$. Effective quark masses have been measured by CLEO and ARGUS, in the context of the ACM model [20], by fitting the spectrum of prompt leptons from B meson decays at the $\Upsilon(4S)$. The results are [21]:

$$\begin{aligned} m_b &= 4.95 \pm 0.04\,\mathrm{GeV/c^2}\ \text{(CLEO)} \\ m_b &= 4.95 \pm 0.07\,\mathrm{GeV/c^2}\ \text{(ARGUS)} \\ m_b - m_c &= 3.30 \pm 0.02\,\mathrm{GeV/c^2}\ \text{(ARGUS)}. \end{aligned} \tag{1.23}$$

For the case of b $\rightarrow$ u transitions, and taking $m_u = 0.20\,\mathrm{GeV}/c^2$, the phase space correction is small and $\Phi_{ps}(\epsilon_u, 0, 0) = 0.99$. For the case of b $\rightarrow$ c transitions however and using the above ARGUS and CLEO mass results ($m_b = 4.95\,\mathrm{GeV}/c^2$, $m_c = 1.65\,\mathrm{GeV}/c^2$) we find that $\Phi_{ps}(\epsilon_c, 0, 0) = 0.45$. The suppression of $\bar{c}s$ and $\bar{\nu}_\tau\tau$ states is even higher. After applying the phase space correction, the total decay width for the case of b $\rightarrow$ c transitions is a factor three smaller than that from the naive model, and Br_{sl} (for electrons and muons) increases to 16%.

(2) Soft Gluon Radiation (Φ_{sg}): This correction accounts for the two $\mathcal{O}(\alpha_s)$ processes shown in Figure 1.11. The correction factor can be expressed as [22]:

$$\Phi_{sg}(\epsilon_q) = 1 - \left(\frac{2\alpha_s}{3\pi}\right).g(\epsilon_q), \tag{1.24}$$

which has a similar form to the correction applied in muon decay to account for QED radiation (substituting α_s for α). For the case of b $\rightarrow$ c transitions this results

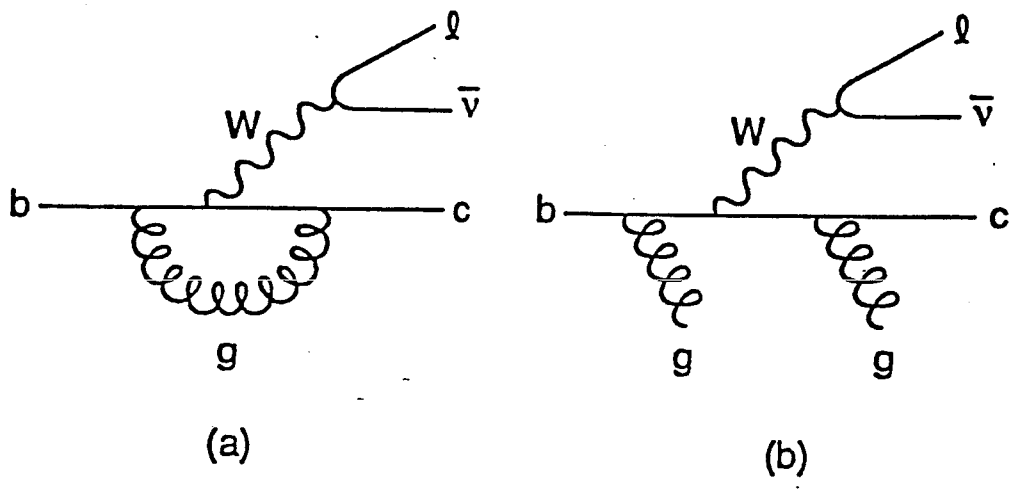

Figure 1.11: Soft gluon radiative corrections to the B-hadron decay rate for the b → u transition: (a) One-loop gluon correction to the W vertex, and (b) the Bremsstrahlung of soft gluons.

in a soft gluon correction to the decay width of -10% for semi-leptonic decays (see Section 1.4.3) and -4% for non-leptonic decays. The correction causes the predicted value of Br_{sl} to fall slightly to 15%.

(3) Hard Gluon Exchange (Φ_{hg}): As stated earlier, the spectator quark usually forms a colour singlet with either the resulting c or u from the b decay. This situation is illustrated in Figure 1.12(a) for the case of b → c. This third correction to the spectator model takes account of the colour-suppressed process shown in Figure 1.12(b), where a hard gluon exchange between the quark lines can rearrange the colour indices such that the $\bar{u}d$ pair from the decay of the W no longer forms a colour singlet. The new colour singlets are the $c\bar{u}$ and $\bar{q}d$. A correction can be calculated in QCD [23] that acts to modify the usual colour factor of 3 and results in the hadronic decay modes being enhanced by approximately 13%. Since the semi-leptonic modes are unaffected by gluon exchange of this type, the semi-leptonic branching fraction is further reduced. Including all corrections up to this point we obtain a prediction from the corrected spectator model of $Br_{sl} = 14\%$.

Table 1.3 presents measurements of Br_{sl} made at the Υ(4S) and at the Z^0 resonance. The measurements from the LEP experiments are seen to be consistent with $Br_{sl}(\Upsilon(4s))$ (except maybe for the L3 number) despite there being a different mix of B-hadron species in the two cases (hadronisation at LEP produces B_s^0 and B-baryons in addition to the B_u and B_d mesons produced in Υ(4S) decay). These results are however difficult to reconcile with the prediction of the corrected spectator model, which is in discrepancy with the data by (at worst) $\sim 20\%$.

The reasons for the failure of the spectator model at this level, are largely asso-

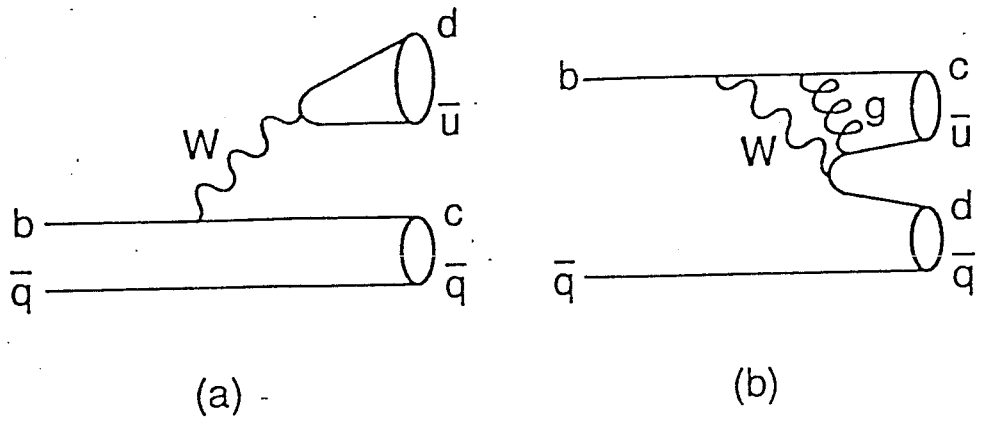

Figure 1.12: Hard gluon corrections to the B-hadron decay rate: (a) Hadronic decay producing the usual colour singlets. (b) In the colour suppressed diagram, a hard gluon is exchanged between quark lines and rearranges the colour indices to produce an alternate set of colour singlets.

Experiment	Br_{sl}
Υ(4S)	$10.3 \pm 0.2\%$
ALEPH	$10.3 \pm 0.4 \pm 0.4\%$
DELPHI	$10.4 \pm 0.6 \pm 0.5\%$
L3	$11.9 \pm 0.3 \pm 0.6\%$
OPAL	$10.4 \pm 0.3 \pm 0.6\%$

Table 1.3: Measurements of the B meson semi-leptonic branching ratio. The value from the Υ(4S) represents an average [24] over data from the ARGUS, CLEO, CUSB and Crystal Ball Collaborations. The results from the LEP experiments are collected together (for example) in [12].

ciated with calculating the hadronic decay width. QCD interactions at the bottom mass scale are only marginally perturbative which leads to uncertainties associated with the calculation of hard and soft gluon effects as described above. Most importantly however, the fundamental assumption of the spectator model, namely that the spectator quark plays no role in the decay process, can be a rather poor approximation when considering non-leptonic decay channels. Figure 1.13 shows the non-spectator diagrams that also contribute to B-hadron decay.

The departure from the spectator model is seen at a much larger level in the D hadron system. This is illustrated by the measurement of rather different D^0 and D^+ semi-leptonic decay branching ratios [15]:

$$\begin{aligned} Br(D^0 \rightarrow e^+ + X) &= 7.7 \pm 1.2\% \\ Br(D^+ \rightarrow e^+ + X) &= 17.2 \pm 1.9\% \end{aligned} \tag{1.25}$$

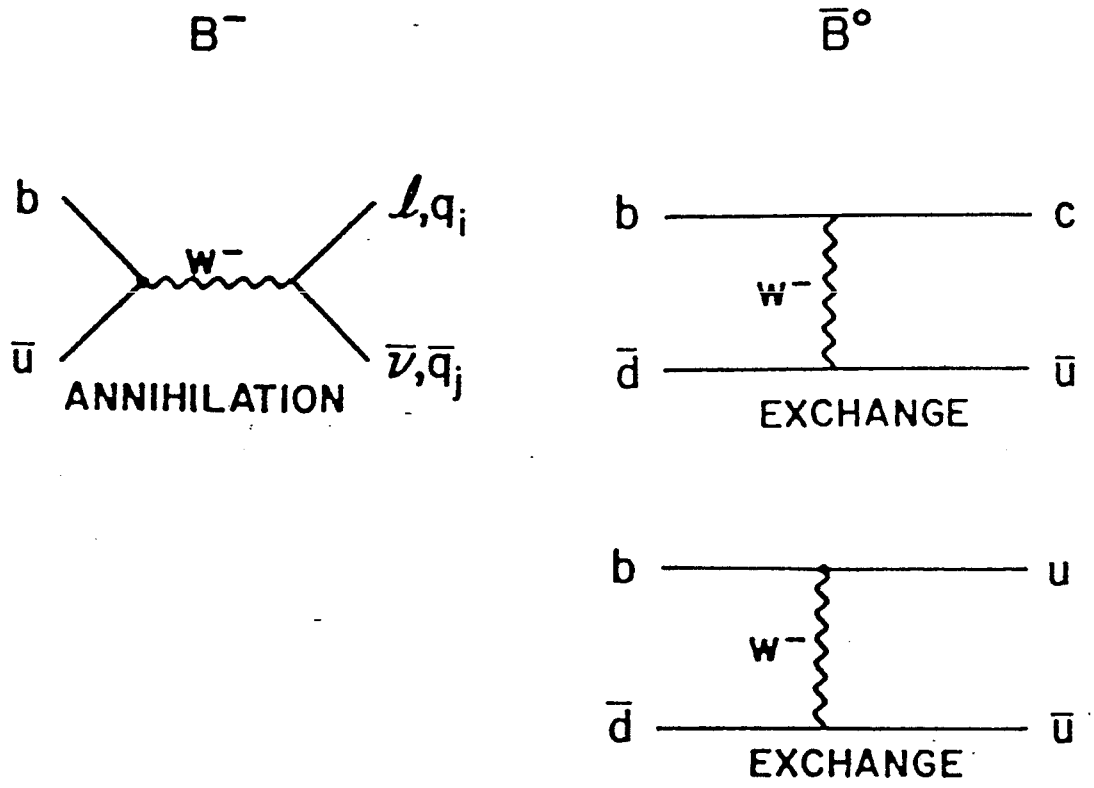

Figure 1.13: The non-spectator model diagrams for b-decay.

$$\frac{Br(\mathrm{D}^+ \rightarrow \mathrm{e}^+ + \mathrm{X})}{Br(\mathrm{D}^0 \rightarrow \mathrm{e}^+ + \mathrm{X})} = 2.23 \pm 0.43\%.$$

Further evidence comes from considering the respective decay lifetimes of the D^0 and D^+. The spectator model would suggest that all hadrons containing the heavy quark will have the same lifetimes which is in marked contrast to the measured values [15]:

$$\begin{aligned} \tau_{\mathrm{D}^0} &= 0.420 \pm 0.008\,\mathrm{ps} \\ \tau_{\mathrm{D}^+} &= 1.066 \pm 0.023\,\mathrm{ps} \\ \frac{\tau_{\mathrm{D}^+}}{\tau_{\mathrm{D}^0}} &= 2.54 \pm 0.07 \end{aligned} \qquad (1.26)$$

The fact that the ratio of the branching fractions (Equation 1.25) and of the lifetimes (Equation 1.26) are consistent with one another, tends to indicate that the semi-leptonic widths are in agreement and that it is the hadronic widths for D^+ and D^0 that are different. We conclude that the spectator model of heavy flavour decay has difficulty in describing hadronic channels but is in fact a rather good model of semi-leptonic decay channels.

1.4.3 The B-hadron Lifetime

The B-hadron lifetime is simply related to the total decay width via

$$\tau_B = \frac{1}{\Gamma_{TOT}}, \ (\hbar = c = 1), \tag{1.27}$$

where Γ_{TOT} can be considered as the sum of two parts; one for semi-leptonic decays and one for hadronic decays,

$$\Gamma_{TOT} = \Gamma_{sl} + \Gamma_{had}. \tag{1.28}$$

Further, by introducing the branching ratio for semi-leptonic decays (Br_{sl}) we can express τ_B as,

$$\tau_B = \frac{Br_{sl}}{\Gamma_{sl}}. \tag{1.29}$$

Formulating τ_B in terms of semi-leptonic decay quantities has some obvious advantages; The conclusion of Section 1.4.2 was that the semi-leptonic decay of B-hadrons is well described by the spectator model and, further, Br_{sl} is experimentally a well measured quantity.

From Equations 1.20 and 1.21 we can write down the form of the B inclusive semi-leptonic width in the corrected spectator model:

$$\Gamma_{sl}(b \to q) = \frac{G_F^2 m_{\mathrm{b}}^5}{192\pi^3}\left[\Phi_{ps}(\epsilon_{\mathrm{u}},0,0)\Phi_{sg}(\epsilon_{\mathrm{u}})\left|V_{\mathrm{ub}}\right|^2 + \Phi_{ps}(\epsilon_{\mathrm{c}},0,0)\Phi_{sg}(\epsilon_{\mathrm{c}})\left|V_{\mathrm{cb}}\right|^2\right]. \tag{1.30}$$

The factors Φ_{sg} (defined in Equation 1.24) are evaluated by using the following numerical approximation for the terms $g(\epsilon_{\mathrm{q}})$ [25]:

$$g(\epsilon_{\mathrm{q}}) = \left(\pi^2 - \frac{31}{4}\right)(1-\epsilon_{\mathrm{q}})^2 + \frac{3}{2}. \tag{1.31}$$

Based on the quark mass determinations of Equation 1.23 (with $m_{\mathrm{u}} = 0.2\,\mathrm{GeV}/c^2$ and using $\alpha_s = 0.23$ [8]) Φ_{sg} evaluates to 0.83 (0.88) for the case of b $\to$ u (b $\to$ c). Combining this result together with the earlier determination of the phase space factors $\Phi_{ps}(\epsilon_{\mathrm{q}},0,0)$ from Section 1.4.2, allows us to express the B lifetime of Equation 1.29 in the following form:

$$\tau_{\mathrm{B}} = \frac{Br_{sl}}{40.67\left(2.08\left|V_{\mathrm{ub}}\right|^2 + \left|V_{\mathrm{cb}}\right|^2\right)}\ \mathrm{ps}. \tag{1.32}$$

Equation 1.32 illustrates clearly how a measurement of τ_{B} provides a handle on the CKM matrix elements, V_{ub} and V_{cb}. In fact since $|V_{\mathrm{cb}}|^2 >> |V_{\mathrm{ub}}|^2$ (see 1.19), it follows that a measurement of τ_{B} is essentially a measurement of $|V_{\mathrm{cb}}|$.

[8] The value $\alpha_s = \alpha_s(m_{\mathrm{b}}) = 0.23^{+0.03}_{-0.02}$ [26] is obtained by extrapolating the OPAL measurement valid at the scale of m_{Z} [27], back to the scale of the b-quark mass.

Finally, we note that the lifetime hierarchy among the hadrons of the D-system, illustrated in Section 1.4.2 for the case of the D^0 and D^+ mesons, is expected to also be present within the different species of the B-system. For D hadrons, the lifetime differences derive from non-spectator processes such as those illustrated in Figure 1.13. These channels are less significant in the B-system where the spectator model is a much closer description of the hadron decay process. The expectation is for the following hierarchy of lifetimes,

$$\tau(\Lambda_b) < \tau(B^0) < \tau(B_s{}^0) < \tau(B^{\pm}),$$

but where the spread in the lifetimes is at the level of 10% of the lifetimes themselves.

Chapter 2

The OPAL Experiment at LEP

2.1 LEP

The Large Electron-Positron collider (LEP) at CERN, is a conventional synchrotron in which electrons and positrons are accelerated and stored in counter rotating bunches. Situated between the Jura mountains and Geneva airport, the main ring (see Figure 2.1) consists of four straight sections and four arcs giving a total 'circumference' of 26.7 km and making LEP currently the world's largest synchrotron. The machine parameters are listed in Table 2.1. The ring is buried at an average depth of approximately 100 m underground with the plane of the ring tilted at 1.5° to the horizontal for geological reasons emanating from the construction phase.

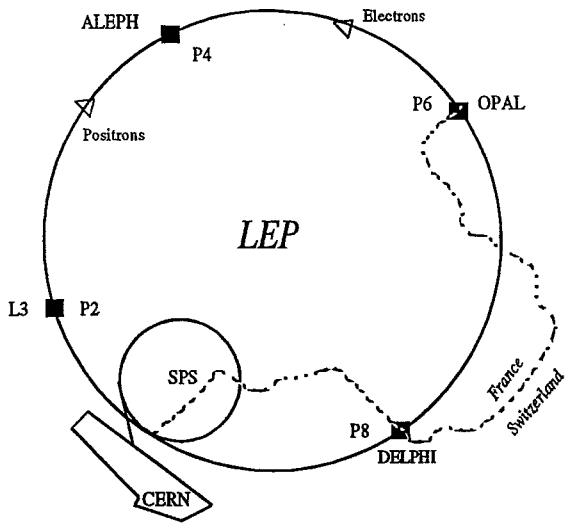

Figure 2.1: The LEP storage ring showing the main experimental locations

The bending field required to maintain the electrons and positrons in orbit is supplied by 3368 dipole magnets and in addition there are 808 quadrupole and 510 sextapole magnets used to focus and correct the beam. The two straight sections containing the P2 and P6 experimental areas, are instrumented with a total of 128 copper RF cavities providing a total of 16MW of RF power. Hence beams are

accelerated to energies at and around 45GeV and are maintained at this energy compensating for synchrotron radiation losses. The electrons and positrons counter rotate in four pairs of bunches and intersect at eight points. They are brought to a focus and made to collide at four of these positions where the LEP experiments (ALEPH, DELPHI, L3 and OPAL) are situated to record the collisions.

The injection system for LEP, pictured in Figure 2.2, utilizes where possible existing CERN accelerator facilities. The starting point is the production and initial

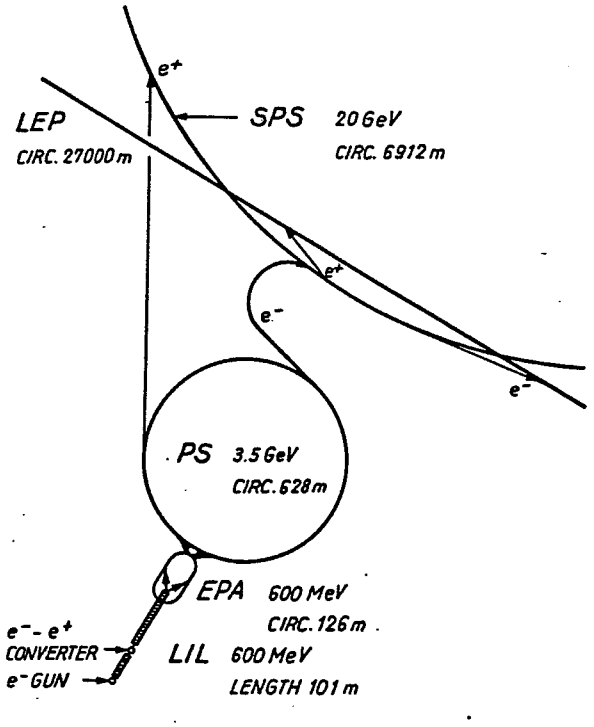

Figure 2.2: The LEP injection system.

acceleration of electrons and positrons by the combination of two linear accelerators together called LIL. The first linac is a high current 200 MeV machine that produces the electron beam for subsequent injection into the second linac in addition to a further electron beam that becomes the source of the positron beam (via electron-positron conversion in a tungsten target). This second linac accelerates the electron and positron beams to an energy of 600 MeV before injecting them into the Electron-Positron Accumulator (EPA) where they are collected, stored and the bunches are made. From here further acceleration up to 3.5 GeV in the Proton Synchrotron (PS) and in the SPS completes the initial acceleration phase of the beams up to their LEP-injection energy of 20 GeV. This process of e^+e^- production and accumulation in the LEP ring is repeated in successive 15 s periods, termed *supercycles*, until the required beam currents are achieved. Acceleration to full energy can then take place and collisions induced at the experimental regions.

Circumference	26.66 km
Active length of RF structure	272 m
Injection energy	20 GeV
Maximum beam energy	55 GeV
Dipole field	0.0645 T
RF frequency	352 MHz
r.m.s. bunch length	15.7 mm
r.m.s. beam radii:	
σ_x	255 μm
σ_y	15.3 μm
Revolution time	90 μs
Bunch spacing	22 μs
Current per beam	3 mA
Number of particles per bunch	4.2×10^{11}
Nominal luminosity	1.6×10^{31} $(\mathrm{cm}^{-2}\mathrm{s}^{-1})$
Beam lifetime (h)	6 h
Synchrotron radiation loss per turn	0.262 GeV

Table 2.1: LEP(Phase 1) Design Machine Parameters. From [28].

2.2 The OPAL Detector

OPAL, the **O**mni-**P**urpose **A**pparatus for **L**EP, is a multipurpose detector designed to efficiently reconstruct and identify all types of e^+e^- event. A general purpose design was specifically chosen based mainly on technology that had proven itself with existing detectors, particularly the JADE detector at PETRA.

The main features of the detector are:

- The reconstruction of charged particle tracks inside a magnetic field enabling a measurement of momentum, particle identification (by $\mathrm{d}E/\mathrm{d}x$) and the reconstruction of primary and secondary vertex positions.
- The identification of electrons and photons together with a measure of their energy via electromagnetic shower detection.
- The measurement of hadronic energy by total absorption.
- The detection of Bhabha scattering events at low angles with respect tothe beam line, providing a measurement of the absolute luminosity.

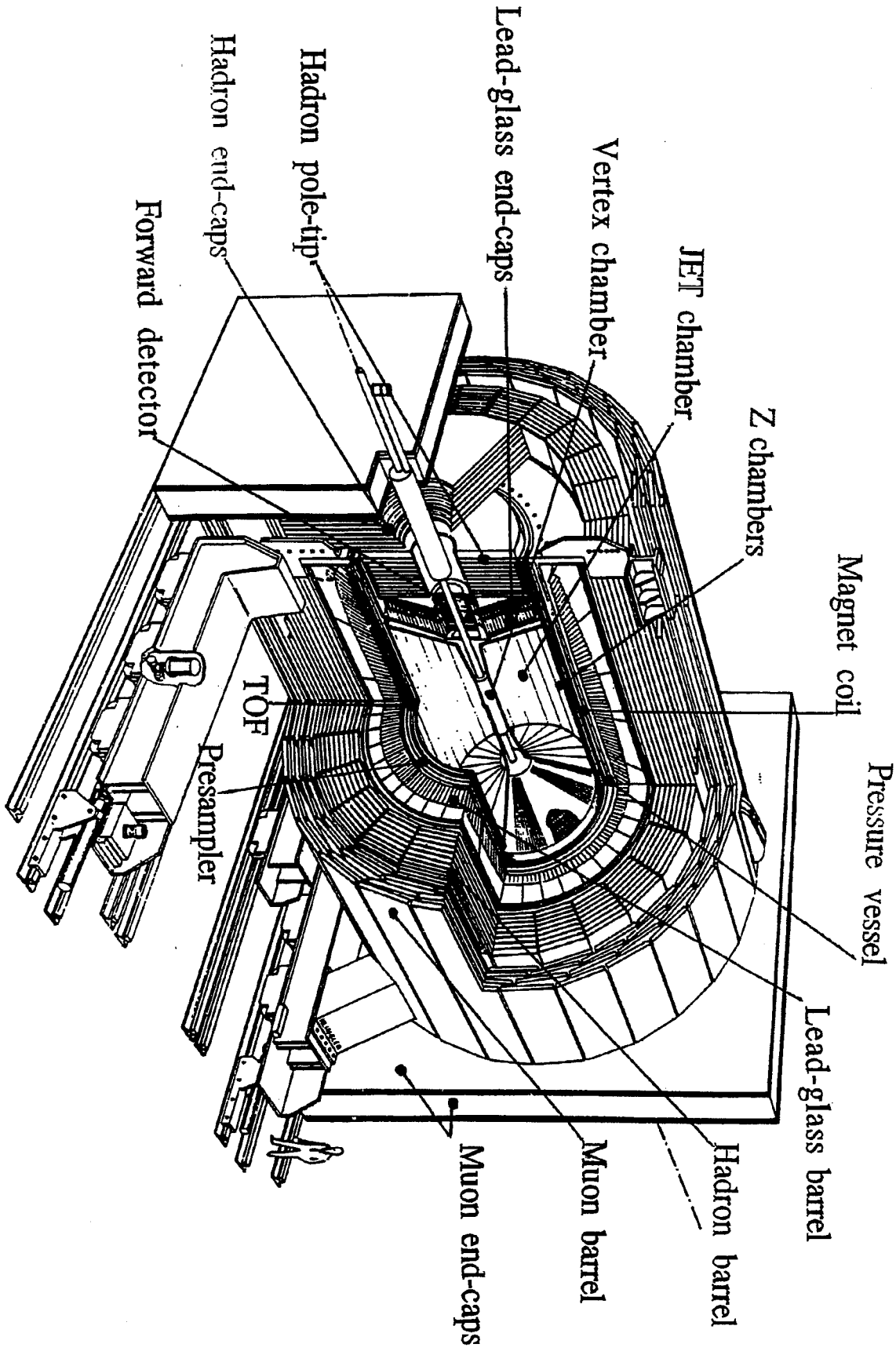

Figure 2.3: The OPAL detector.

The layout of the detector is shown in Figure 2.3. Particle tracking is performed in the Central Detector. This is a system of three drift chamber devices: the Vertex Detector, Jet Chamber and surrounding z-Chambers all situated inside a pressure vessel holding the system at a common pressure of 4 bar. The pressure vessel also provides mechanical support for a solenoid mounted around it that supplies a uniform axial magnetic field for the Central Detector of 0.435 T. Outside of the solenoid in successive layers is a Time-Of-Flight counter array, an Electromagnetic Calorimeter with presampler , a Hadron Calorimeter (instrumenting the solenoid iron return yolk) and Muon Chambers. The Forward Detector measures the luminosity. What follows is a brief account of each of the detector components [29].

2.2.1 Beampipe

The beampipe in the region of the OPAL detector forms the inner wall of the pressure vessel for the Central Detector. The final design was necessarily a compromise between:

- Physical strength.
- Keeping the number of radiation lengths to a minimum to reduce gamma conversions and multiple scattering.
- Starting the charged particle tracking as close to the interaction point as possible for the detection of the decay vertices from short lived particles.
- Avoiding the worst effects from the expected flux of synchrotron radiation close to the interaction point.

The beampipe consists of an inner aluminium tube covered in layers of carbon fibre epoxy. The pipe was constructed in three sections, the central section having a 1.3 mm carbon fibre covering representing 0.66% of a radiation length (X_0). The inner radius of the pipe was chosen to be 78 mm.

2.2.2 Vertex Detector

The Central Vertex Detector is a high precision cylindrical drift chamber of 'jet chamber' design. It is 1 m in length with a diameter of 470 mm and consists of two layers of 36 sectors each. The inner layer contains the axial sectors, each containing a plane of 12 sense wires strung parallel to the beam direction. The wires range radially from 103 to 162 mm at a spacing of 5.3 mm. The outer layer contains the stereo sectors each containing a plane of 6 sense wires inclined at a stereo angle of $\sim 4°$. The stereo wires lie between the radii 188 and 213 mm at a spacing of 5 mm.

A precise measurement of the drift time onto axial sector sense wires allows the $r-\phi$[1] position to be calculated. Measuring the time difference between signals at either end of the sense wires allows a fast but relatively coarse z coordinate that is used by the OPAL track trigger and in pattern recognition. A more precise z measurement is then made by combining axial and stereo drift time information offline.

A more detailed account of the vertex detector and its performance is given in Chapter 3.

2.2.3 Jet Chamber

The Central Jet Chamber is a cylindrical drift chamber of length 4 m with an outer (inner) diameter of 3.7 (0.50) m respectively. The chamber consists of 24 identical sectors each containing a sense wire plane of 159 wires strung parallel to the beam direction.

The coordinates of wire hits in the $r-\phi$ plane are determined from a measurement of drift time. The z coordinate is measured using a charge division technique and summing the charges received at each end of a wire allows the energy loss, $\mathrm{d}E/\mathrm{d}x$ to be calculated. At least 8 hits on a track are obtained over a solid angle of 98% of 4π.

A more detailed account of the Jet Chamber and it's performance is given in Chapter 3.

2.2.4 z-Chambers

The Central z-Chambers provide a precise measurement of the z coordinate of tracks as they leave the Jet Chamber. They consist of a layer of 24 drift chambers 4 m long, 50 cm wide and 59 mm thick covering 94% of the azimuthal angle and the polar angle range 44° to 136°. Each chamber is divided in z into 8 cells of 50 cm $\times$ 50 cm, with every cell containing 6 sense wires spaced at 4 mm and with a stagger of ± 250 μm in order to resolve the left-right ambiguity. The chambers use the same gas as the Jet Chamber with a uniform field of 800 V/cm over the full drift distance of 25 cm in z. A FADC system is employed to determine the drift distance and a charge division technique is used to give a coarse ϕ measurement.

The intrinsic z resolution performance of the chambers ranges from $\sim$100 μm for the smallest drift distances to $\sim$200 μm for the largest. The mean absolute resolution achieved, which is ultimately limited by the accuracy of the OPAL survey information, is of the order 300 μmand the mean $r-\phi$ resolution is $\sim$1.5 cm.

[1] See Appendix A for a definition of the OPAL coordinate system.

2.2.5 Magnet

The OPAL magnet consists of a warm solenoid and an iron return yolk. The field distribution has to satisfy two main requirements:

- High uniformity throughout the Central Detector volume.
- A field not exceeding a few tens of Gauss in the annular region between the solenoid and the iron yolk to facilitate the operation of photomultiplier tubes in surrounding sub-detectors.

In order to satisfy the latter requirement it was found necessary to wind the solenoid as one complete unit. The field in the central detector region is measured to be 0.435 T and to be uniform to within $\pm 0.5\%$. The solenoid and pressure vessel together represent $\sim 1.7\ X_0$ of material.

2.2.6 Time-Of-Flight Counters

The **T**ime-**O**f-**F**light (TOF) system provides fast triggering information, an effective rejection of cosmic rays and, in principle, charged particle identification in the range 0.6-2.5 GeV.

The TOF system consists of 160 scintillation counters forming a barrel layer 6.84 m long and mean radius 2.36 m surrounding the OPAL coil and covering the region $|\cos(\theta)| < 0.82$. Light is collected from both ends of each counter via plexiglass light guides glued directly onto phototubes that are shielded from stray magnetic fields. The output signal from each phototube is then split into two parts. The first, for the timing measurement, goes to a constant fraction discriminator, TDC and mean timer. The second goes to an ADC for a pulse height measurement that can be used to correct the pulse heights of the electromagnetic and hadronic calorimeters. The TOF trigger signals derive from the mean timers with the requirement that the time of flight was within 50 ns and that discriminators at both ends fire within 50 ns of each other.

The TOF system achieves a timing resolution for multi-hadronic events in the central region of the counters of 350 ps with a z resolution ~ 10 cm.

2.2.7 The Electromagnetic Calorimeter

The function of the Electromagnetic Calorimeter is to detect and identify electrons and photons. It consists of a lead glass total absorption calorimeter split into a barrel and two end cap arrays. This arrangement, together with two forward lead scintillator calorimeters of the Forward Detector (see later), makes the OPAL acceptance for electron and photon detection almost 99% of the solid angle.

The presence of $\sim 2X_0$ of material in front of the calorimeter (due largely to the solenoid and pressure vessel) results in most electromagnetic showers initiating before reaching the lead glass. Presampling devices are therefore installed in front of the lead glass in the barrel and endcap regions to measure the position and energy of showers to improve overall spatial and energy resolution and give additional γ/π^0 and electron/hadron discrimination.

Barrel Electromagnetic Presampler

The Barrel Electromagnetic Presampler consists of 16 chambers forming a cylinder of radius 239 cm and length 662 cm. Each chamber consists of two layers of drift tubes operated in the limited streamer mode with the anode wires running parallel to the beam direction. Each layer of tubes contains 1 cm wide cathode strips on both sides at $\pm 45°$ to the wire direction. Spatial positions can then be determined by reading out the strips in conjunction with a measurement of the charge collected at each end of the wires to give a z coordinate by charge division. The hit multiplicity is approximately proportional to the energy deposited in the material in front of the presampler allowing the calorimeter shower energy to be corrected with a corresponding improvement in resolution.

From test beam results the presampler can achieve a spatial resolution for electromagnetic showers in the plane perpendicular to the shower direction of 6 to 4 mm for incident energies in the range 6 to 50 GeV. The resolution in z for an isolated charged particle is $\sim$10 cm.

Barrel Lead Glass Calorimeter

The **E**lectromagnetic **B**arrel lead glass calorimeter (EB) consists of a cylindrical array of 9440 lead glass blocks at a radius of 246 cm and covering $|\cos(\theta)| < 0.82$. Lead glass provides an excellent intrinsic energy resolution ($\sigma_E/E \sim 5\%/\sqrt{E}$, for E in GeV), spatial resolution ($\sim$1 cm) and linearity response over a wide dynamic range. To achieve good energy resolution at high energies, shower leakage from the back of the calorimeter must be minimised. This is achieved by using a very dense glass (24.6 X_0) with each block being 37 cm in depth and $\sim 10 \times 10\,\mathrm{cm}^2$. In order to maximise detection efficiency the longitudinal axis of each block is angled to point at the interaction region. The focus of this pointing geometry is slightly offset from the e^+e^- collision point in order to reduce particle losses in the gaps between blocks.

Čerenkov light from the passage of relativistic charged particles through the lead glass is detected by 3 inch diameter phototubes at the base of each block. Each phototube is shielded from the stray field of the magnet so that operation up to 100 G is possible with a gain deviation of less than 1%. Light signals are digitised

by charge integrating 15-bit ADCs with a fine scale covering the range up to 120 pC and a coarse scaling operating up to 900 pC. The non-linearity of the ADC was measured to be better than ± 1 count over the full range of the coarse channel.

Before installation, the gains of each lead glass counter were calibrated to 0.1% and the non-linearity of the counters was found to be less than 1% in the energy range 6 to 70 GeV for electrons in the CERN-SPS beamline. In order to ensure the quality of the gain calibration for each phototube over long time periods a gain monitoring system based on a Xenon light source is employed.

Endcap Electromagnetic Presampler

The Endcap Presampler is a multiwire proportional counter located in the region between the pressure bell and the endcap lead glass detector. The device consists of 32 chambers arranged in 16 sectors covering all ϕ and the polar angle range $0.83 < |\cos(\theta)| < 0.95$.

Performance results from test beam electrons and pions show that the spatial resolution attained is in agreement with the expected $1/\sqrt{12}$ of the strip or wire effective pitch, which is 2 mm for the anode strips and 3.2 mm for the cathode planes.

Endcap Electromagnetic Calorimeter

The **E**ndcap **E**lectromagnetic calorimeter (EE) consists of two dome-shaped arrays of 1132 lead glass blocks located in the region between the pressure bell and the Pole Tip hadron calorimeter. It has an acceptance coverage of the full azimuthal angle and $0.81 < |\cos(\theta)| < 0.98$.

A major difference from the barrel calorimeter is that the glass blocks follow a non-pointing geometry. Due to tight spatial constraints, the blocks are mounted coaxial with the beam line. The lead glass blocks provide typically 22 X_0 of material and come in three lengths (380, 420 and 520 mm) to form the domed structure following the external contours of the pressure bell. The blocks are housed in brass cans that provide both electrical isolation and mechanical strength.

Another major difference to EB is that the endcaps feel the full OPAL magnetic field. Conventional photomultipliers cannot work under these conditions and so special **V**acuum **P**hoto **T**riodes (VPT) were developed in conjunction with industry. These are special field tolerant one stage devices (intrinsic gain of 12.3 at $B = 0.4$ T), with a window radius of 3.75 cm that is attached to the back of a block by epoxy resin. Large additional amplification is needed before the VPT signals are input to similar charge integrating ADCs as used by the EB. The amplifier is the main source of signal noise which has an overall typical equivalent energy of 14 MeV per

channel.

Each endcap assembly was calibrated a number of times in a CERN-SPS electron beam. The response was found to be stable to within 0.2% in the mean over a 7 month period. The performance of all blocks can be monitored long term by use of laser and LED reference light sources associated with each block that mimic the response to 10 and 20 GeV electrons respectively.

From test beam results the energy response has been found to be linear to within 1% over the range 3-50 GeV and from OPAL data the optimum energy resolution is known to be $\sigma_E \sim 5\%/\sqrt{E}$ (for E in GeV).

2.2.8 Hadron Calorimeter

The hadron calorimeter is built in three sections: the barrel, the endcaps and the pole-tips. By positioning detectors between the layers of the magnet return yoke a sampling calorimeter is formed covering a solid angle of 97% of 4π and offering at least 4 interaction lengths of iron absorber to particles emerging from the electromagnetic calorimeter. Essentially all hadrons are absorbed at this stage leaving only muons to pass on into the surrounding muon chambers.

To correctly measure the hadronic energy, the hadron calorimeter information must be used in combination with that from the preceeding electromagnetic calorimeter. This is necessary due to the likelihood of hadronic interactions occurring in the 2.2 X_0 of material that exists in front of the iron yolk.

Hadron Endcap and Barrel Calorimeter

The barrel region contains 9 layers of chambers sandwiched between 8 layers of 100 mm thick iron. The barrel ends are then closed off by toroidal endcaps consisting of 8 layers of chambers sandwiched between 7 slabs of iron.

The chambers themselves are limited streamer tube devices strung with anode wires 10 mm apart in a gas mixture of isobutane (75%) and argon (25%) that is continually flushed through the system. The signals from the wires themselves are used only for monitoring purposes. The chamber signals result from induced charge collected on pads and strips located on the outer and inner surfaces of the chambers respectively.

The layers of pads are grouped together to form towers that divide up the detector volume into 48 bins in ϕ and 21 bins in θ. The analogue signals from the 8 or so pads in each chamber are then summed to produce an estimate of the energy in hadronic showers which is subsequently digitised by a 12-bit ADC. From pion test beam results, the tower response was found to be linear with energy and gave a resolution of $\sigma_E = 120\%/\sqrt{E}$ at an energy of 10 GeV.

The strips are made from aluminium of width 4 mm, that run the full length of the chamber centred above the anode wire positions. They hence run parallel to the beam line in the barrel region and in a plane perpendicular to this in the endcaps. Strip hits thus provide muon tracking information with positional accuracy limited by the 10 mm wire spacing. Typically, the hadronic shower initialized by a normally incident 10 GeV pion produces 25 strip hits and generates a charge of 600 pC.

Hadron Pole-Tip Calorimeter

Complementing the barrel and endcap regions, the Pole-Tip extends the coverage of hadron calorimetry from $|\cos(\theta)| = 0.91$ down to 0.99. The sampling frequency in this region is increased to 10 in an effort to improve the OPAL energy resolution in the forward direction.

The detectors themselves are 7 mm thick multiwire proportional chambers containing a gas mixture of CO_2 (55%) and n-pentane (45%), strung with anode wires at a spacing of 2 mm. Again, the chambers have pads on one side (of typical area 500 cm^2) and strips on the other. Corresponding pads from the 10 layers then form towers analogous to the treatment in the rest of the calorimeter.

With no material in front of the detector, hadron test beam results have shown the energy response to be linear and for energies below about 15 GeV the resolution was $\sigma_E = 100\%/\sqrt{E}$ (E in GeV).

2.2.9 Muon Detector

The Muon Detector aims to identify muons in an unambiguous way from a potential hadron background. To make the background manageable, before reaching the Muon Detector, particles have traversed the equivalent of 1.3 m of iron so reducing the probability for a pion not to have already interacted in the detector material to be less than 0.001.

Barrel Muon Detector

The barrel region consists of 110 drift chambers that cover the acceptance $|\cos(\theta)| < 0.68$ for four layers and $|\cos(\theta)| < 0.72$ for one or more layers. The chambers range in length between 10.4 m and 6 m in order to fit between the magnet support legs and all have the same cross sectional area of 120 cm × 9 cm. From survey information, the final chamber positions are known to 1 mm.

Each chamber is split into two adjoining cells each containing an anode signal wire running the full length of the cell, parallel to the beamline. Each contains a gas mixture of ethane (10%) and argon (90%) giving a maximum electron drift time of 8 μs for the largest drift distance of some 30 cm. The inner surfaces of the

cells have 7.5 mm cathode strips etched in them to define the drift field, and in the regions directly opposite the anode wires are diamond shaped cathode pads. In all, six signals are read out from each cell (one from each end of the anode wire and four from the cathode pads) and are digitised via an 8-bit FADC.

Spatial position in the ϕ plane is derived using the drift time onto the anode and can be reconstructed to an accuracy of better than 1.5 mm. A rough estimate of the z coordinate is also achieved by using the difference in time and pulse height of the signals arriving at both ends of the anode wire. A much better measure of the z coordinate is given by using induced signals on two sets of cathode pads whose diamond shape repeats every 17.1 cm and 171 cm respectively. This results in a z coordinate accurate to 2 mm, modulo 17.1 cm or accurate to 3 cm modulo 171 cm.

Endcap Muon Detector

Each Endcap Muon Detector consists of two layers of four quadrant chambers (6 m $\times$ 6 m) and two layers of two patch chambers (3 m $\times$ 2.5 m), for an angular coverage of $0.67 < |\cos(\theta)| < 0.99$. Each chamber is an arrangement of two layers of limited streamer tubes in the plane perpendicular to the beam line, where one layer has its wires horizontal and the other vertical.

The basic streamer tube used has a cross section of 9 mm $\times$ 9 mm with the inner walls coated with a carbon-suspension cathode. Each plane of tubes is open on one side and closed on the other to rows of aluminium strips 8 mm wide. The strips on the open side, run perpendicular to the tube anode wires and typically have charge induced over five or so strips. By finding a weighted average using the recorded pulse heights, the streamer is located to better than 1 mm. The strips on the closed side run parallel to the tube wires and so can only give that coordinate to the nearest wire or $9/\sqrt{12}$ mm.

Within each chamber therefore, with two layers of tubes each with two layers of strips, the x and y coordinates of a track can be measured once accurately and once relatively coarsely. As with the barrel region, the actual position of the strips is known to about 1 mm via survey information.

2.2.10 The Forward Detector

The **F**orward **D**etector (FD) consists of an array of devices, listed below, whose primary objective is to detect low angle Bhabha scattering events. This almost purely QED process is very well understood and hence provides a way of determining the LEP luminosity [30], for the normalisation of measured reaction rates from Z^0 decays.

To achieve this, the FD enjoys a relatively clean acceptance for particles 47-

120 mrad from the interaction point, with the only obstructions being the beam pipe and 2 mm of aluminium from the Central Detector pressure vessel.

- Calorimeter: The forward calorimeter consists of 35 sampling layers of lead-scintillator sandwich divided into a presampler of $4\,X_0$ and the main calorimeter of $20\,X_0$. Well contained Bhabha events suggest an energy resolution of $\sigma_E = 17\%/\sqrt{E}$ (E in GeV).

- Tube Chambers: There are three layers of proportional tube chambers positioned between the presampler and main sections of the calorimeter. The positioning is known to ± 0.5 mm and they can give the position of a shower centroid to ± 3 mm.

- Gamma Catcher: The gamma catcher is a ring of lead scintillator sandwich sections of 7 X_0 thickness. They plug the hole in acceptance between the inner edge of EE and the start of the forward calorimeter.

- Far Forward Monitor: The far forward monitor counters are small lead-scintillator calorimeter modules, $20\,X_0$ thick, mounted either side of the beampipe 7.85 m from the intersection region. They catch electrons scattered in the range 5-10 mrad that are deflected outwards by the action of the LEP quadrupoles.

2.3 The OPAL Data Acquisition Chain

2.3.1 Overview of Dataflow

The OPAL data aquisition chain, as defined here, starts with the selection of a bunch crossing based on a trigger decision and ends with the storage on magnetic tape of an event summary, consisting of all the essential measured quantities on which a physics analysis of the data could be based.

The on-resonance Z^0 production rate at the LEP design luminosity of $1.6 \times 10^{31}\mathrm{cm}^{-2}\mathrm{s}^{-1}$ is 0.7 Hz. It is thus undesirable and indeed impossible to fully read out the detector data for every beam crossing i. e. every 22μs. Instead a decision on whether to accept the event must be made by the trigger logic based on information from various sub-detectors. With a maximum response time of about $8\,\mu$s from the drift chambers and electronics reset times of up to $7\,\mu$s, there is a window for a decision to be made of only a few microseconds before the next beam crossing. If the decision is positive all triggers are inhibited until all sub-detectors indicate that their data has been read-out and they are ready to accept a new trigger. Typically this deadtime is 20-25 ms.

After triggering, sub-detector event records are buffered in Local System Crates (LSC) before being routed to the so-called Event Builder. Here, the event records of each sub-detector taking part in the run are collected and merged into a common data structure. This system also acts as an event buffer for the Filter which consists of a parallel microprocessor matrix which performs a first, fast analysis of the complete event. From here events are transferred via an optical link to the main online computer, a VAX 8700, used to write the raw data to IBM 3480 cartridges. The final link in the dataflow chain is then the processing of these cartridges by the OPAL reconstruction program, (see Subsection 2.3.5), running on one of an array of Apollo DN10000 machines.

The full data collection scheme outlined above is shown schematically in Figure 2.4.

2.3.2 Trigger

It is the purpose of the trigger to select those bunch crossings that gave rise to a genuine e^+e^- interaction, from the background. In particular the detector must be capable of triggering efficiently on the major physics processes of interest namely, multi-hadronic and leptonic decays of the Z^0 together with low angle Bhabha events for determining the luminosity.

Sources of background to these processes come mainly from the interactions of beam particles with residual gas inside, or with the walls of, the beam-pipe and from synchrotron radiation. To a lesser extent, cosmic rays and detector noise also contribute background to the trigger rate. Background events are thus characterised by not originating from the expected interaction point and by having low track multiplicities and measured energy.

High triggering efficiency is achieved by ensuring that most physics processes are triggered by several sources of trigger signal. This redundancy then allows the calculation of trigger efficiencies by the comparison of one independent trigger with another.

The components of the OPAL trigger most relevant to triggering on multi-hadronic events are described below.

- Track Trigger: Tracking information from both the vertex chamber and the jet chamber is used to look for tracks that originate from the event vertex in both the $r-\phi$ and z planes [31]. The track trigger uses the fact that charged tracks in the z plane are essentially straight lines and if they truly originate from the event vertex the track hits will have, to good approximation, the same value of z/r, where z is the coordinate along the beam axis and r is the radial coordinate. In contrast, the measured points on a track not originating

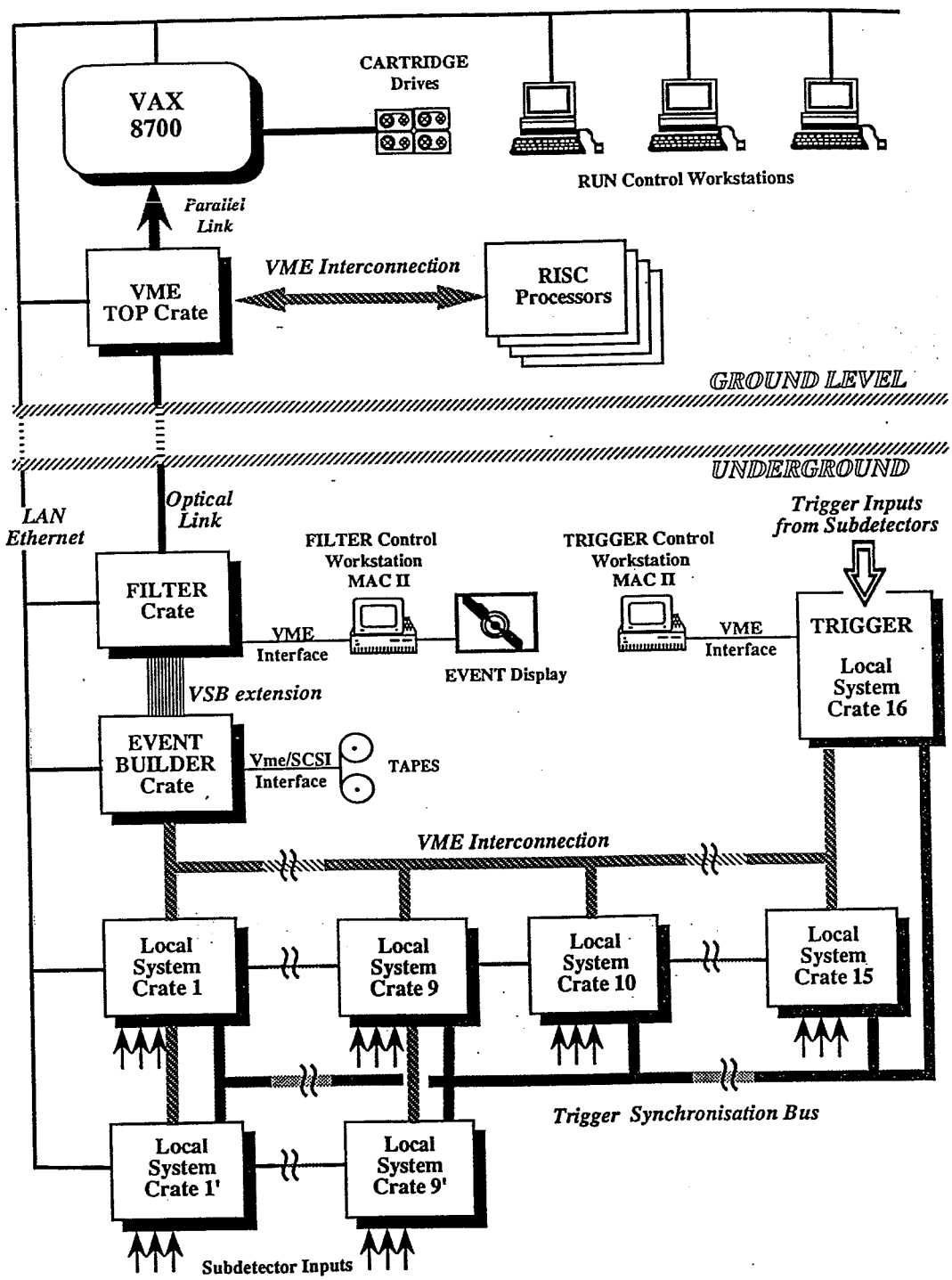

Figure 2.4: The OPAL data acquisition system. From [29].

from the event vertex ($z = 0$) will have z/r values that vary with radius.

- Time-of-Flight Trigger: The TOF scintillation counters supply coincidence trigger signals from the phototubes at each end of a counter. The coincidence is required to fall within a ± 50 ns window of the nominal beam crossing time.

- Electromagnetic Calorimeter Trigger: The electromagnetic calorimeter triggers are simply total energy triggers based on the analogue sums of groups of about 48 lead glass blocks throughout the barrel and endcap calorimeters.

The trigger signals provided from the various sub-detectors described above, fall into two categories: the first are the 'direct' signals such as total energies or track multiplicities whereas the second type form inputs to the '$\theta - \phi$ matrix'. The 4π solid angle covered by OPAL is sub-divided into 144 overlapping bins - 6 bins in θ and 24 bins in ϕ. By providing sub-detector trigger signals matched to this binning, trigger conditions based on coincidences related in space can be formed [32].

For 1990 data, those conditions most relevant for triggering on multi-hadronic events are listed in Table 2.2. By using the triggering redundancy the triggering efficiency is found to be essentially 100% for multi-hadronic events defined by the analysis cuts in [30].

2.3.3 Online Processing

The initial link in the data aquisition chain for each sub-detector is the data collection and local buffering of an event record from the 'front-end' digitising electronics. Any processing of the data at this stage is highly dependent on the sub-detector in question.

Raw data from the Jet Chamber, for example, is subject to data reduction by zero suppression and an online pulse shape analysis to extract the drift time and a z coordinate through charge division (see Chapter 3 for more details). This information is then used to perform a quick and hence simple track reconstruction [33] the results of which are subsequently used by the Filter process. For the case of the electromagnetic calorimetry, data reduction in the form of signal pedestal subtraction and zero-suppression are performed at this stage.

The data collection and the sub-detector mode of running is all controlled from the LSC of the sub-detector in question. Based on an OPAL common VME[2] skeleton [34], the LSC assembles the sub-event and formats the data based on the ZEBRA

[2]The digitising electronics of the various OPAL sub-detectors were housed in a variety of bus systems (FASTBUS, CAMAC etc) that were optimal to their individual needs. VMEbus was then chosen by OPAL to be its standard, interfaced to the many other buses, from the LSC stage onwards in the DAQ chain.

Trigger Condition	Rate (Hz)
More than 3 tracks	0.2
More than 2 tracks in the barrel region	0.2
Track trigger collinear $\theta - \phi$ bins	0.15
Track trigger/EM calorimeter $\theta - \phi$ coincidence	0.03
Track trigger/TOF $\theta - \phi$ coincidence	0.3
Total energy in barrel region $\geq$ 7 GeV	0.1
One or more EM $\theta - \phi$ bins in EM barrel with $\geq$ 2.6 GeV	0.2
Total energy in left or right EM endcaps $\geq$ 6 GeV	0.1
$\geq$ 4 GeV in both EM endcaps	0.04
$\geq$ 1 $\theta - \phi$ bins in either EM endcap with $\geq$ 3.0 GeV	0.15
Collinear $\theta - \phi$ bins in the EM calorimeter	0.15
$\geq$ 4 GeV in EM endcap AND in the EM barrel	0.03
$\geq$ 4 GeV in EM barrel AND a barrel track or TOF hit	0.2
$\geq$ 4 GeV in EM barrel AND $\geq$ 1 barrel track	0.05
$\geq$ 4 GeV in either EM endcap AND a track on the opposite side	0.08
EM endcap $\theta - \phi$ bin AND $\geq$ 1 barrel track	0.10
EM endcap $\theta - \phi$ bin AND $\geq$ 1 track a track on the opposite side	0.15
TOF/EM calorimeter $\theta - \phi$ coincidence	0.25
$\geq$7 overlapping TOF $\theta - \phi$ bins	0.2

Table 2.2: The most important trigger conditions for multi-hadronic events. The rates quoted are averages over a typical LEP fill.

[35] standard, in preparation for the software Filter. From the LSC through to the offline analysis of the event, the underlying structure of the event is the FZ ZEBRA memory format.

2.3.4 Event Builder and Filter

The Event Builder synchronizes the readout of LSC's containing the assembled sub-events and formats them into a complete event which is then buffered and made accessible to the Filter processes.

The Filter takes input from the TOF, Muon Detector, the calibrated calorimeter signals and the tracks found in the Jet Chamber LSC processes as described above, and performs an analysis of the event.

The objective is to identify the gross physics properties of the event and hence to classify it via software flags set in a special event header word that is written into the data structure. An example of a filter-set event classification of relevance to this thesis is that of a **G**old **P**lated **M**ulti-hadron **E**vent (GPMH). Below are the cuts imposed by the filter processor on an event for it to be classified as a GPMH:

- Σ_E in electromagnetic clusters (EE + EB) $>$ 8 GeV
- Number of electromagnetic clusters (EE + EB) $\geq$ 6
- Σ_E of electromagnetic clusters in the hemisphere opposite the highest energy cluster $>$ 2 GeV
- Event passes halo muon rejection cut
- Number of TOF(tight) hits $\geq$ 3 with the condition that Σ_E for EB clusters be $\geq$ 2 GeV and the number of EB clusters be $\geq$ 2

A complete list of filter event classifications can be found in [36]. The definitions of electromagnetic clusters and TOF hits require description here since the processing of data in the filter is of a rather simplistic nature compared to the full offline treatment in ROPE.

Electromagnetic Clustering: The filter lead glass clustering works by firstly searching for all all blocks above an 'initiator' threshold. This level is set to 100 MeV for EB and 200 MeV in EE. These blocks are then used as possible clustering centres and eight nearest-neighbour blocks are checked to see if they have energy above a lower noise threshold. This level is set to 50 MeV for EB and 100 MeV in EE. If these nearest blocks fall above the noise level they are simply added to the initiator cluster which means clusters can be up to nine blocks big. If all neighbouring blocks fall below threshold the initiator is assumed to be noise and ignored.

TOF Reconstruction: All TOF bars with TDC values for both ends are considered. Assuming that only one relativistic particle has struck the bar, the z coordinate is estimated and from this a time-of-flight deduced. If this calculated time then agrees with the measured time-of-flight to better than 27 ns, the TOF bar is termed 'in time'. To be classed as a 'tight' TOF hit requires the timing to agree at the 10 or so nanosecond level.

2.3.5 ROPE

The final link in the data chain is the reconstruction program for OPAL, ROPE. ROPE stands for **R**econstruction of **OPAL** **E**vents and it accepts as input raw data digits produced by the detector itself or by the OPAL simulation package GOPAL (described in Chapter 4). As output the ROPE code produces an extensive event summary of calculated quantities such as reconstructed track momenta or energy clusters in the calorimetry, which form the **D**ata **S**ummary **T**apes or DST [37]. An important additional output of ROPE is a copy of the essential raw data structure in a much compressed form. This so-called **D**ense **D**ata (DD) output then allows the complete event to be re-processed by ROPE if some variation on the original processing is deemed necessary.

The standard ROPE output consists of both the DD and DST information in a common data stream (known as the DDST output). In practice this means that the DDST output from ROPE can be used for detector monitoring, calibration, debugging and physics analysis in a very convenient way.

The large scale structure of ROPE is that of a central steering routine that calls various 'processes', one for each sub-detector and others which combine the information from different sub-detectors. These come under the five broad classifications listed below:

1. Central Detector Tracking: Track reconstruction in the Vertex, Jet and z-chambers and the subsequent merging of track segments. Details of this procedure are found in Chapter 3. Use of the subsequent tracking information for finding primary and secondary vertices and extrapolation of the tracks into the outer detectors.
2. Electromagnetic Calorimetry: Processing of the time of flight, presampler and lead glass raw data and the merging of this information to build electromagnetic clusters.
3. Hadronic Calorimetry: Processing of the barrel, end-cap and poletip hadron calorimeter and subsequent merging to build hadronic clusters.
4. Muon Detector: Muon tracking in the barrel and endcap of the muon

chambers and merging of the track segments with information from the inner detectors.

5. Forward Detector: Track reconstruction and calorimetry in the forward region.

In order to successfully reconstruct an event ROPE requires the additional input of quantities, some of which are essentially fixed over long time scales and others which need to vary over time scales as short as one data-taking run. To achieve this ROPE is interfaced to the OPCAL database [38]. OPCAL holds the calibration constants of each sub-detector, together with some more general detector quantities (such as the magnetic field strength) essential for data processing. The database allows regular updating of calibration records as either running conditions change or understanding of the detector improves. By labelling constants with periods of validity it is ensured that the correct constants structure is invoked for the reconstruction of all data. Since it is important to retain all knowledge concerning how events have been reconstructed, ROPE outputs along with the events the constants structure used together with information concerning which specific processing options and analysis cuts were used.

Finally, a feature of ROPE worth mention here, is the graphic processor GROPE [39]. This package runs within the ROPE framework and provides an event viewing and scanning facility of raw data, partially processed data or the fully reconstructed DST output. Use of GROPE thus provides a valuable tool for both assessing the performance of the detector in a convenient way and in gaining insight as to the physical properties of events for analysis purposes (e. g. see Figure 5.20).

Chapter 3

The Tracking of Charged Particles in OPAL

Particle tracking in OPAL is performed by a combination of three drift chamber sub-detectors, introduced in Chapter 2, collectively known as the Central Detector (CD) [1]. The relationship of the components to each other is displayed schematically in Figure 3.1.

The Central Jet Chamber (CJ) provides tracking throughout most of the CD volume and is surrounded by the Central z-Chambers (CZ) for an improved determination of the z-coordinate. Sitting inside the CJ and directly surrounding the beam pipe, is the Central Vertex drift chamber (CV) that provides precision spatial tracking points close to the interaction region. All components of the CD are enclosed by a pressure vessel formed from the solenoid, the beam pipe and two aluminum end bells operating at a pressure of 4 bar absolute and inside the full OPAL solenoidal field of 0.4 T.

The physics analysis presented in Chapters 5 and 6 makes exclusive use of OPAL tracking in the $r - \phi$ plane. Thus a thorough understanding of all contributions to the tracking process is essential. To this end the present chapter describes in some detail the content, operation and performance of the CV and CJ, and finishes with an account of how their information is combined to form a Central Detector Track (CT). (see Section 3.3).

3.1 The Central Vertex Detector

The design of the CV evolved over a period of about five years as the result of a research program undertaken by the Carleton University/N.R.C group in Ottawa, Canada together with Cambridge University, Queen Mary and Westfield College and the Rutherford and Appleton Laboratory in the U.K. The essential criteria that the chamber had to meet were the following:

[1] We shall refer only to the configuration of the OPAL tracking devices in 1990. A two-layered silicon microvertex detector has since been installed.

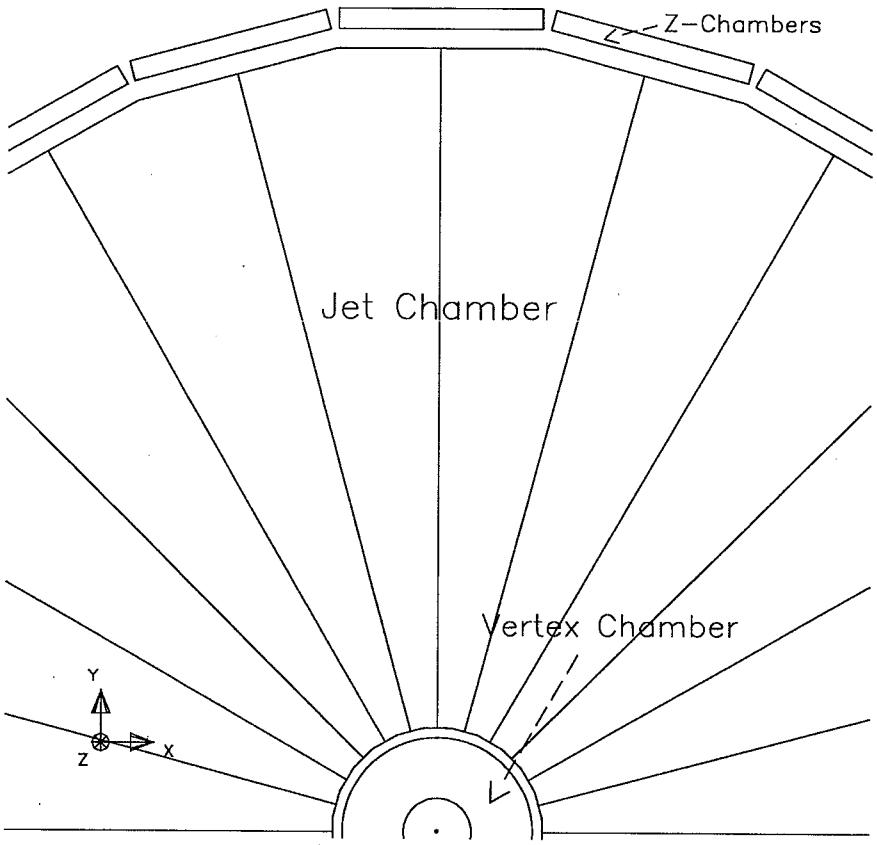

Figure 3.1: A section through the Central Detector.

- A high spatial resolution and good two-track separation capability to allow track reconstruction inside the dense track environment of a hadronic jet.
- A electrostatic field configuration that is both well defined and stable, ensuring a constant drift velocity throughout long periods of operation.
- The ability to operate the chamber using different choices of gas.
- A design whose implementation is relatively simple and likely to be ready for the start of LEP physics in August 1989.

3.1.1 The Mechanical Design

The physical dimensions of the chamber were governed by the space available inside OPAL. Radially the chamber had to fit between the beam pipe and the inner wall of the CJ. The length of 100 cm was fixed by the presence of CJ laser calibration equipment, axial wire electrostatic stability and the position of the Forward

Detector[2].

Following the successful implementation by JADE [40] at PETRA, a classic jet design was chosen (see figure 3.2) to benefit from the proven high $r-\phi$ precison and two-track resolution attainable. By segmenting the drift region in the $r-\phi$ plane into 36 drift cells, the maximum drift distance was kept below 2 cm so minimising the effects of diffusion in the drift chamber gas. A precision z coordinate is obtained from stereo cells occupying an offset annulus about the inner layer of axial cells.

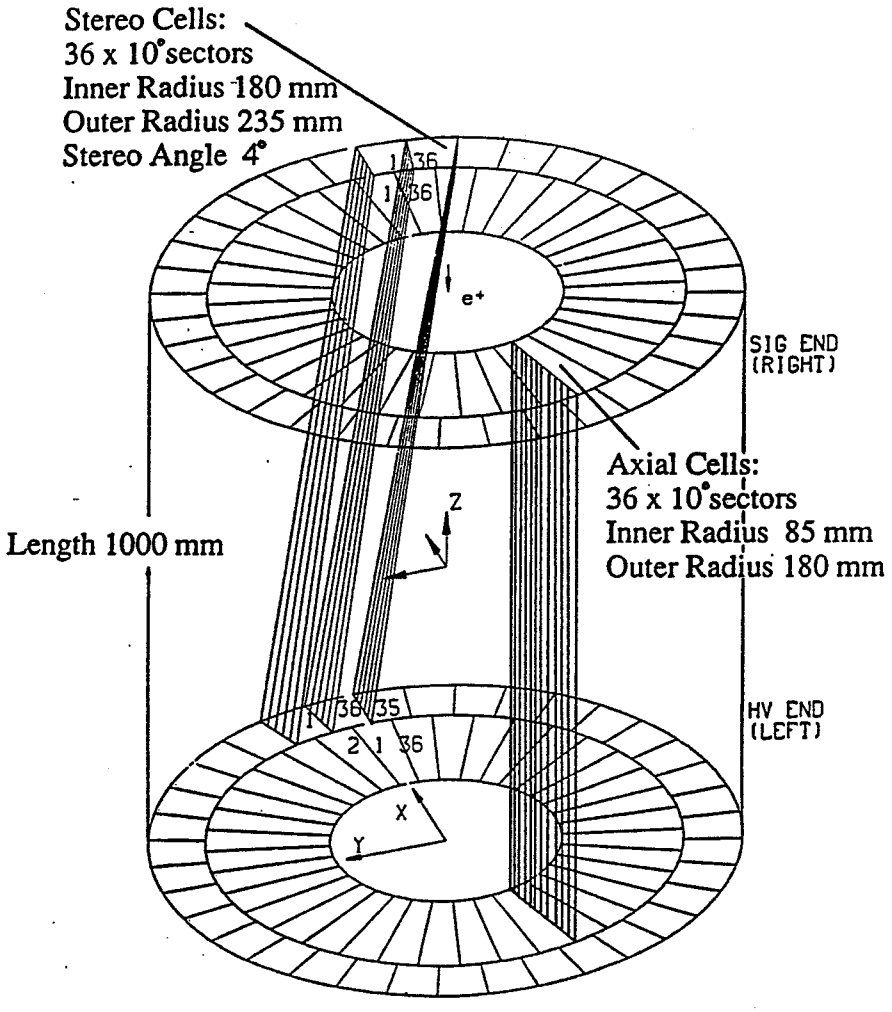

Figure 3.2: A schematic of the detector showing the location of the inner layer of axial sectors with respect to the surrounding layer of stereo sectors.

With reference to Figure 3.3 the chamber wires are strung between two 32 mm thick G10 [3] endplates, which are held 100 cm apart against the final wire load of

[2]For the Forward Detector to have a clean acceptance there must be no material within 120 milliradian of the beam pipe.

[3]G10 is a fibre-glass composite (60/40) of SiO_2 and epoxy.

2300 kg, by a 1.5 mm thick carbon fibre tube. This tube defines the outer wall of the chamber at 23.5 cm while at the inner radius of 8.8 cm, there is an aluminized mylar tube which allows the vertex chamber to utilise an independent gas supply and recirculation system within the common CD pressure vessel. A sensitive pressure feedback system ensures that the pressure gradient between the CV and CJ, stays within a safe range. The CV gas volume is extended at both ends by gas-tight inner and outer aluminium cylinders terminated by an aluminium end bulkhead. Inside this extended volume and mounted onto the G10 endplates are the preamplifiers for the anode wires and high voltage distribution components. The bulkhead houses the feedthroughs for high voltage and signal cables.

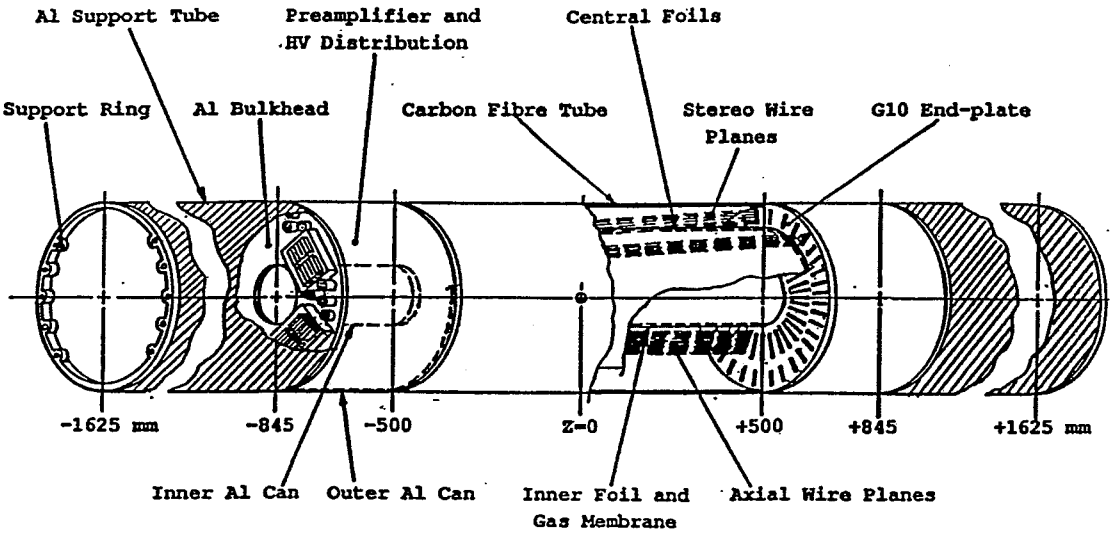

Figure 3.3: A z-axis projection of the complete CV assembly.

Attached directly to the bulkheads at either end is an aluminium extender tube (2 mm thick and 47 cm diameter) giving the support necessary to hold the chamber in position while at the same time providing cable routing for gas, signal and high voltage. These tubes connect onto the inner edge of the CJ end cones (see Figure 2.3) and as a result make the CV mechanically independent of the OPAL beam pipe. The total length of the complete CV assembly as outlined above is 325 cm.

Figure 3.4 shows in detail the layout of the CV drift cells. Cell boundaries coincide with cathode planes that consist of 125 μm diameter copper-beryllium wires at a spacing of 1 mm. The centre of each cell has an anode plane consisting of alternating 200 μm diameter gold-plated copper beryllium potential wires and 20 μm di-

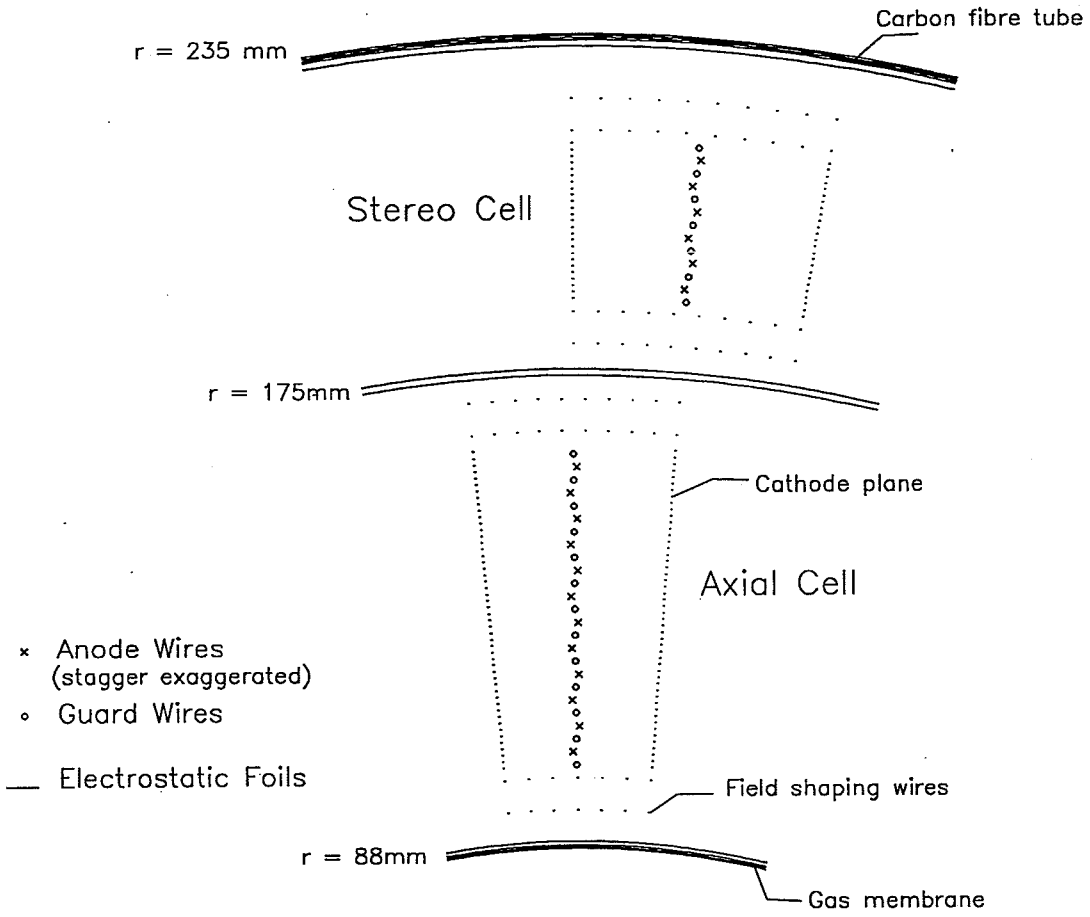

Figure 3.4: Wire locations throughout an axial and stereo sector.

ameter gold-plated tungsten-rhenium anode wires. In addition, the anode wires are alternately staggered by $\pm$ 40 μm with respect to the guard plane in order to unambiguously resolve which side of the cell the ionising particle traversed.

In order to optimise the potential resolution of any drift chamber it is essential to ensure accurate construction. The wire positions of the CV anode and cathode planes are defined by plexiglass combs found on the G10 endplates. The cumulative uncertainty in the position of anode wires is estimated to be less than 10 μm i. e. less than a wire radius.

3.1.2 Chamber Electrostatics and the High Voltage System

Within a drift cell, the electrostatic operating conditions are defined by the anode wire surface field (which determines the gas gain) and the drift field. These fields are determined by the negative voltages applied to the potential and cathode wires

with the anode wires being held at ground potential. Typically the chamber is operated with the surface and drift fields set to 360 kV/cm and 2.5 kV/cm respectively. Figure 3.5 shows the shape of the drift field in the absence of an external magnetic field. The field lines are perpendicular to the anode plane and the field is uniform over the majority of the drift cell i. e. to within a few millimetres of the anode wires. The tapered cell geometry and the desire for a uniform drift field makes it neces-

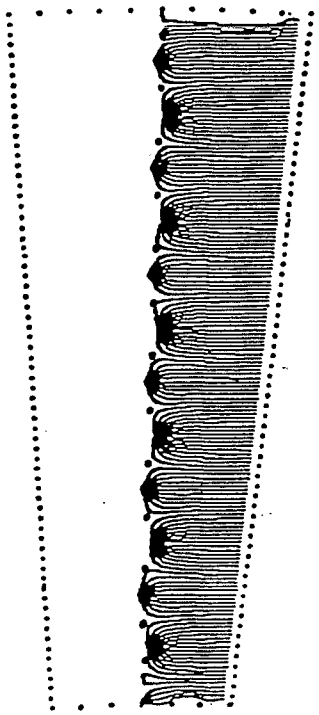

Figure 3.5: The drift field configuration shown for one half of an axial cell. The lines are perpendicular to the anode plane up to a radius of a few mm and terminate radially at each anode wire.

sary for the potential on the cathode wires to increase linearly with radius. The potential wires within a cell are held at the same voltage to ensure a uniform gain for all anode wires. Figure 3.4 shows that the inner and outer radial cell boundaries are terminated with two concentric rings of field shaping wires whose potentials are set by resistor networks tied to the cathode plane voltage supplies. In addition, the axial and stereo sectors are electrostatically isolated from each other by a mylar sheet faced on each side with a foil. The chamber also includes four cylindrical foil surfaces located at the inner and outer radii of the axial and stereo cell layers. These foils act to terminate the field patterns and are operated at a fixed potential.

The high voltage distribution system for the chamber is modular, with each HV cell corresponding to two anode wire planes in axial and stereo. Hence, eighteen such cells are needed to control the entire chamber.

3.1.3 The Electronics Readout System

For each anode-wire signal (or hit) in the chamber, three raw data values are recorded:

- a measurement of the ionisation drift time (TDC),
- the time difference between signals arriving at each end of the anode wire (ZDC),
- the hit pulse height (ADC).

The spatial coordinates of hits are then reconstructed from the raw data using calibration constants and is the subject of Section 3.1.4.

Figure 3.6 shows the full electronics readout chain for a single anode wire. The

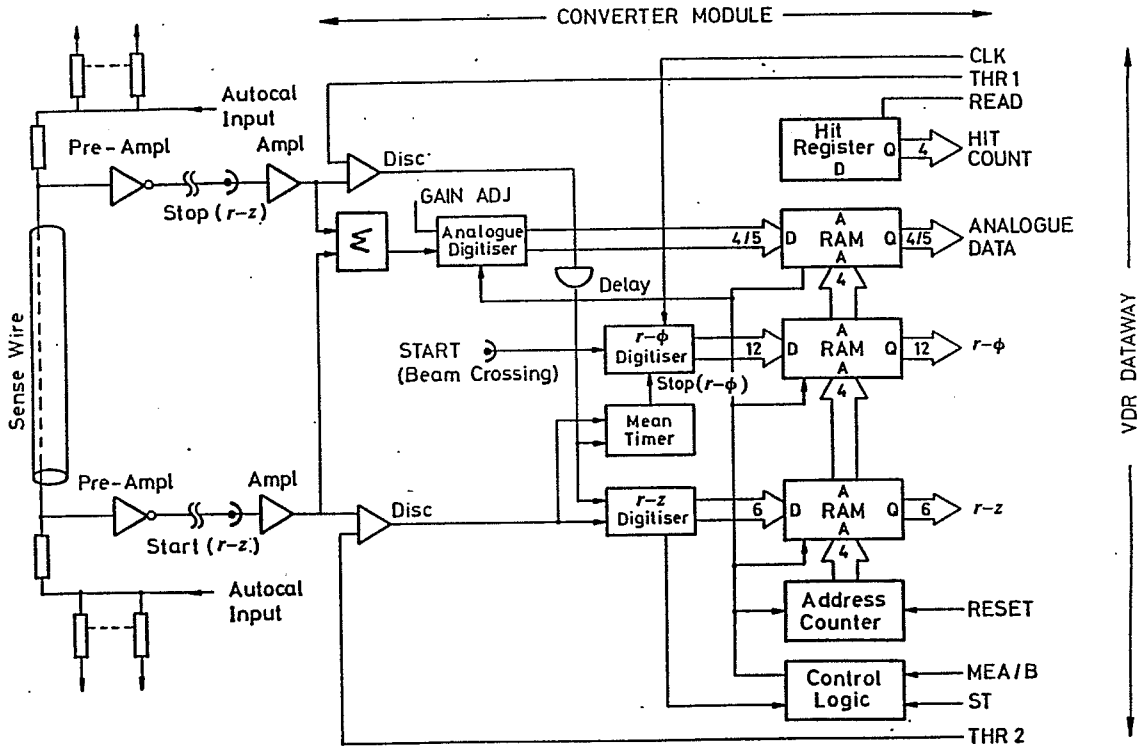

Figure 3.6: The electronics readout chain for a single anode wire. The readout electronics were both designed and constructed by the electronics group of the Rutherford Appleton Laboratory.

pre-amplification of chamber signals is performed by endplate mounted preamplifiers of gain 2.5 and a matched impedance of 360 Ω. Experience gained in operating

prototype vertex chambers led to crosstalk effects between anode wires being compensated for via resistive feedback in the preamplifiers; 8 % of the signal is fed to adjacent wires and 3 % to the next adjacent channels.[4]

If chamber pulses are close together in time, the superposition of the two pulses may keep the amplitude above the discrimination level so reducing the hit efficiency attainable. To minimise these effects, the fall time of pulses is reduced by differentiating in the preamplifier with pole-zero cancellation to ensure there is no undershoot of the differentiated pulse.

The signal from each preamplifier is then passed through ~38 m of coaxial cable, linking the CV bulkhead to the front-end digitizing electronics. This consists essentially of *Converter Modules* inside which all timing measurements and digitization are performed. Converter Modules are housed in triple height Eurocard crates, each crate fully servicing two vertex cells of axial and stereo sectors, making a total of eighteen crates to cover the whole chamber.

Signals from both ends of an anode wire are further amplified by a factor 40 in the Converter Modules before being fed into a constant fraction discriminator. A discriminator threshold of approximately half the full amplitude is used to exploit the region of the rising edge where the chamber signals are seen to change most rapidly. The outputs are then combined in a *mean-timer* so eliminating any dependence on the hit position along the wire. For pairs of inputs less than 10 ns apart, the mean-timer produces an output with not more than 100 ps jitter.

TDC is a measurement of the interval between an e^+e^- beam crossing signal (BX) and a signal derived from the output of the mean-timer. This is achieved by recording the pulses of a quartz referenced clock (operated at 93 MHz), by an 8-bit counter. The mean timer output then initiates the linear discharge of a capacitor that is halted by the arrival of the next clock pulse. The remaining voltage across the capacitor is then measured by a 4-bit **F**lash **A**nalog to **D**igital Converter (FADC) for an intrinsic timing precision (C_l) of 0.67 ns.

In addition to being passed to a mean-timer, the signals emerging from the two discriminators are passed to a unit that performs the *ZDC* measurement. The signal from one end of the chamber (termed the STOP end) is delayed by 5 ns [5] ensuring that it always arrives later than the pulse from the other end (the START end). The START signal then initiates the charging of a capacitor which is halted by the arrival of the STOP signal, whereupon the remaining voltage across the capacitor is measured using a 6-bit FADC.

[4]Crosstalk effects can also occur if chamber wires are not correctly terminated. Again, experience gained running the detector prototype means that anode, guard and cathode wires in the chamber are all correctly terminated. A report on the vertex detector full scale prototype can be found in [41].

[5]This is slightly longer than the pulse transit time down the wire length of 1 m.

This procedure maintains the desired precision and stability by employing an auto-calibration technique that fires calibration signals every 22 μs (between LEP bunch crossings) alternately to the two ends of the chamber. These signals thus simulate the maximum and minimum time differences that can occur. The FADC reference levels are then automatically adjusted until the output reads full scale and zero for the two cases respectively. Each front-end crate has a dedicated *Autocal Module* to perform this task.

The design of the readout chain allows the complete digitization process outlined above, to be repeated every 40–45 ns. In the dense track environment of hadronic jets, the ability to record hits arriving closely spaced in time is important and the CV data aquisition allows up to seven hits per wire to be stored per event.

Figure 3.7 shows a distribution of *TDC* for hits assigned to CV axial tracks within a single sector. Ideally the front edge of this distribution would be a step

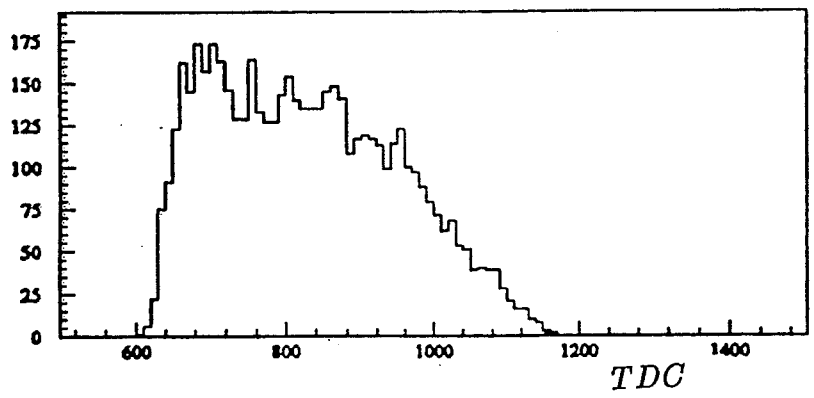

Figure 3.7: Distribution of raw TDC values for a single CV axial sector.

function with the turn on point corresponding to the minimum possible drift time. In practice the turn-on shape has a slight downward gradient due to the intrinsic resolution of the timing measurement and wire-to-wire variations within the sector. The 'plateau' region of the distribution contains a small gradient to larger times as a result of the ~40 ns reset time of the readout electronics, inside which no hits can be recorded, so biasing the hit detection to low drift times. The long falling back edge of the distribution is due to the tapered CV cell geometry, with the outer sector wires responsible for the longest drift times.

3.1.4 Coordinate Reconstruction

Determining the $r-\phi$ Coordinate

The raw drift time measured as described above is clearly an overestimate of the drift time (t_D) defined as; the time taken for charge liberated by the passage of an ionising particle to drift onto an anode wire. This can be expressed as,

$$t_D = TDC.C_l - (t_0 + t_{BXMON}). \tag{3.1}$$

The drift-time offset t_0 can in principle take a different value for each of the 648 readout channels. This is conveniently handled by considering t_0 as the sum

$$t_0 = t_0^{sec} + t_0^{wir}. \tag{3.2}$$

Here, t_0^{sec} accounts for the time it takes signals to travel down the anode wire, through the preamplifier electronics and then via the 38 m of cable to the digitizing electronics, and is common to all wires in a sector. Any variations due to differences in electronic delays and cabling of individual channels are then collected in t_0^{wir}. The t_0 offset to the raw drift time is a calibration constant that must be determined from the data.

The additional correction, t_{BXMON}, is applied to account for any measured variations in the BX signal. In OPAL the BX signal derives from synchronizing a pickup pulse (from the passage of an e^+ bunch), with an RF timing signal from the LEP machine. Occasionally the BX signal can become synchronized to the wrong RF 'bucket', in which case an error of approximately ± 3 ns is introduced to the drift time. Variations of this size and larger, are also occasionally seen between the CV BX-signal and that used by (for example) CJ. These relative shifts were attributable to local differences in the BX transmission bus to the various sub-detectors. Since timing offsets at the few-nanosecond level could significantly degrade the chamber resolution a local monitor (accurate to 50 ps), of the CV-BX timing relationship to the beam pickup signal, was installed. The output (t_{BXMON}) is written into the CV raw data structure to be used in drift time correction [6] whenever the BX signal is deemed to have shifted significantly.

Given a drift-time measurement with some fixed precision, the ultimate resolution attainable for the reconstruction of spatial coordinates is set by both the choice of drift gas and the degree to which the drift properties of electrons through the gas are understood.

Gas studies [42], were initiated at QMW to investigate the properties of various gases in the CV environment. The tests concluded that potentially the best resolution results from use of a so-called 'slow' gas based on CO_2. These gases, although

[6] Due to practical considerations t_{BXMON} contains a constant offset that must first be subtracted before it is used as in Equation 3.1.

generally unsaturated (see figure 3.8) and hence difficult to calibrate, are particularly attractive due to their relatively slow drift velocity and small longitudinal diffusion. During initial tests of the chamber however, HV breakdown problems meant that the required operating point using a slow gas mixture could only be attained safely for a pressure of 2 bar. This essentially ruled out the use of slow gas given the CD operating pressure is 4 bar.

The next preferred gas resulting from these studies was a mixture of argon (88.2 %), methane (9.8 %) and isobutane (2.0 %) termed 'OPAL gas' (since it is also the choice of gas used in the CJ and CZ). The addition of alkanes to argon acts to lower the mean energy of electrons so increasing the drift velocity but significantly decreasing diffusion effects. As can be seen from figure 3.8 the unsaturated behaviour of the velocity is much less of a problem in OPAL gas than for the CO_2-based mixtures.

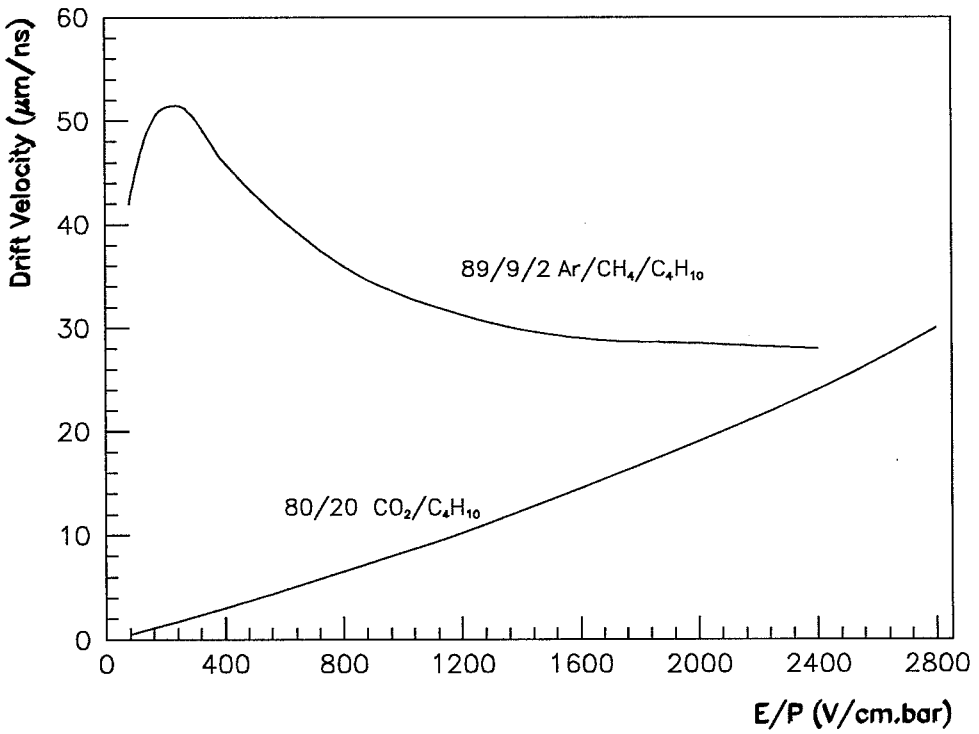

Figure 3.8: The variation of drift velocity with operating conditions in OPAL gas compared to a slow gas.

In order to determine the function that converts the drift time measurement to a drift distance in OPAL gas, a set of predicted drift distances and corresponding drift times were calculated using the method which accurately reproduced laser data in the QMW studies. This 'predicted' data set was found to be well reproduced by a parameterisation of the form,

$$D(t_D) = a(1 - e^{-b(t_D)^{1.3}}) + v_D t_D \qquad (3.3)$$

where parameters a, b are v_D are calibration constants to be determined. The form of function $D(t_D)$ is shown in Figure 3.9 for typical parameter values. For large

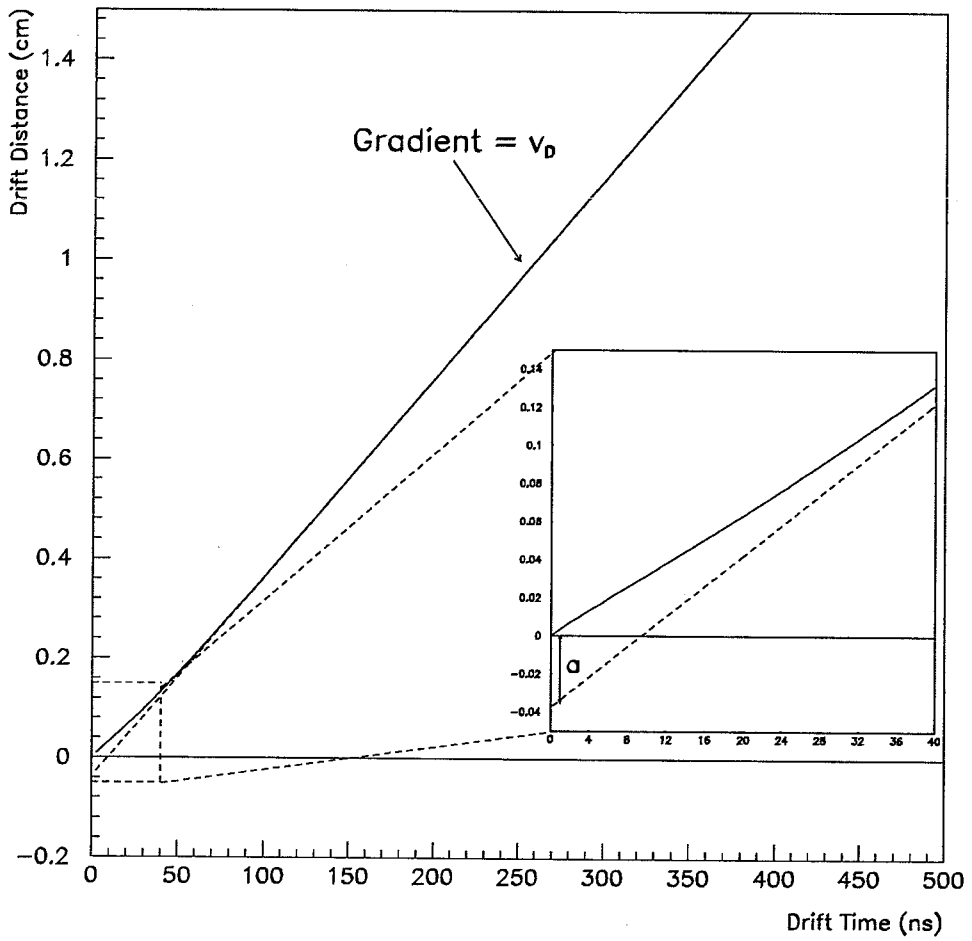

Figure 3.9: The form of $D(t_D)$ using parameter values relevant for the use of OPAL gas: $a = 370\,\mu$m, $b = 0.0135\,\text{ns}^{-1.3}$ and $v_D = 40\,\mu$m/ns.

values of t_D equation 3.3 reduces to the linear form, $D(t_D) = a + v_D t_D$ (with constant drift velocity v_D), reflecting the constant drift field that exists far from the sense wires. The non-linear term in expression 3.3 becomes important for distances $\lesssim 3\,$mm, with the b-parameter controlling how fast the drift velocity tends to the constant value. This represents a decrease in the drift velocity from the constant value reflecting the rapid rise of the electric field close to the surface of anode wires. The staggering of the anode wires leads to the classification of wire hits as being 'near' or 'far'. This depends on whether the effect of the stagger makes the drift distance smaller or larger than if there were no stagger. This distinction is necessary since the drift field conditions will be slightly different for the two cases and requires the introduction of two sets of a and b-values $(a_{near}, a_{far}, b_{near}, b_{far})$.

The final conversion of the drift distance as specified above into a spatial coor-

dinate in the $r-\phi$ plane requires knowledge of the direction of drift onto the wire in addition to the actual wire position itself.

It is the Lorentz angle (α_L) which specifies the angle at which ionisation drifts onto the wire due to the crossed electric and magnetic field configuration existing in the drift cell. A value of $\alpha_L = 5.6°$ ($\alpha_L = 7.2°$) in axial (stereo) layers was assumed based essentially on the results of the original gas studies [7]. Wire positions must also be corrected for electrostatic bowing effects which are parameterised in the form

$$B_w(1-(z/L)^2), \tag{3.4}$$

for B_w a constant and L the half length of the wire. The bows were set to their nominal values of $B_w = 25\,\mu$m in axial sectors and $B_w = 15\,\mu$m in stereo sectors.

3.1.5 Determining the z Coordinate

It is assumed that the z coordinate (z_w) for a hit on a wire uncorrected for the bowing effect, can be related to the raw time difference (ZDC) measurement by just a polynomial parameterization of the form

$$z_w = z_0 + z_1.ZDC + z_2.ZDC^2 + \ldots + z_n.ZDC^n, \tag{3.5}$$

where $z_0, z_1, \ldots, z_n$ are calibration constants to be determined.

Once calibrated a z coordinate from this method, termed the 'fast z' is available for use in the OPAL Track Trigger [31] and for pattern recognition. A superior measurement is however available by utilising the geometry of the stereo wires, which introduces a correlation between the $r-\phi$ coordinates of hits on these wires and the corresponding z coordinate. The resulting 'stereo' z coordinates are seen in Section 3.3.2 to be essential in achieving optimal z-resolution at the CT-track level and are the basis for the calibration of the fast-z measurement (briefly described in Section 3.1.7).

3.1.6 Pattern Recognition

The result of hit reconstruction in CV, for the case of three well separated tracks in a multi-hadronic event, is shown in Figure 3.10. All tracks leave hits in axial and stereo sectors and both ambiguities of each hit are displayed.

It is the job of the pattern recognition algorithm to determine which set of reconstructed space points are likely to be associated with a common track. The algorithm employed starts by forming hit 'triplets' on a sector-by-sector basis beginning at the outer wires where confusion is expected to be least. A triplet is a

[7] These values were also consistent with the CJ determination of α_L (see Table 3.2.4) once allowance is made for the change in field conditions.

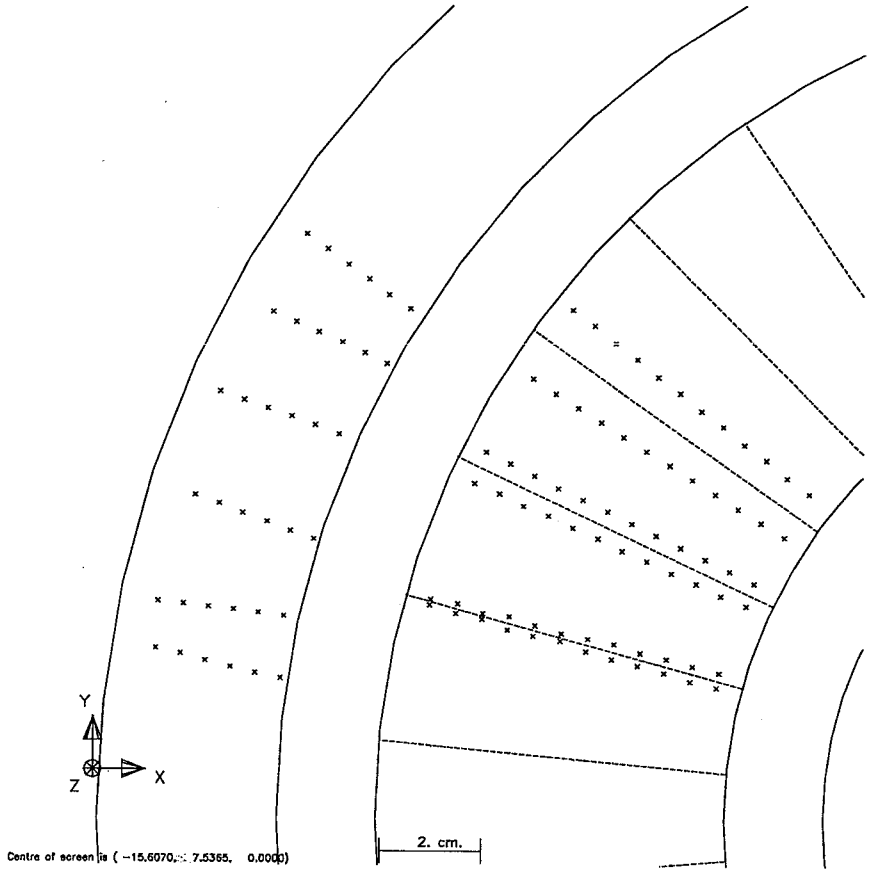

Figure 3.10: An example of reconstructed $r - \phi$ hit positions in the CV. The pattern of hits shown relates probably to the passage of three tracks through different sectors in the CV. The anode plane positions in axial sectors are indicated. Stereo hit positions are calculated assuming $z = 0$ for display purposes.

series of three contiguous hits that are consistent with forming a straight line. This line is then extrapolated inwards and new hits added to the proto-track definition if they fall within a 'road' [8] width either side of the line. For each point added the straight line is recalculated using the new hit and the two preceding hits. In this way a straight or curved track trajectory can be followed.

In order to decide which side of the anode plane the measured hits are valid for, the above procedure takes place on both sides of the sector. Since the road width is large compared to the anode wire stagger of 100 μm, often a track is found on both sides of the anode plane originating from the same chamber hits. This left-right ambiguity can be resolved internally to CV by fitting a circle through both sets of hits and retaining that track with the smallest χ^2. In fact, in order to optimise the merging of CV and CJ information, it is preferred to retain both ambiguities of CV

[8] A road width of 400 μm is used which optimises the efficiency for assigning 'correct' hits to tracks.

track segments and decide which to keep at the CT processor level (see Section 3.3).

Once the hits on a track have been defined, track fits are carried out separately in the $r-\phi$ and $s-z$ planes for each track candidate. Axial track segments are the result of fitting hits from axial sectors to a circle in the $r-\phi$ plane and to a straight line in the $s-z$ projection[9], of the OPAL MRS coordinate system (see Appendix A). In the stereo sectors both fits are to straight lines. The result of track fitting is to define the track trajectory in terms of the five parameters κ, ϕ_0, d_0, $\tan\lambda$ and z_0 (see Appendix B for a definition) and their associated covariance matrix. After the initial track fit, all points in $r-\phi$ ($s-z$) more than 5 (3) standard deviations from the fit position, are rejected and the fit repeated. To be accepted, a track must contain in the $r-\phi$ projection, a minimum of six axial or four stereo hits and in addition possess a $\chi^2/d.o.f.$ that is better than 10.0. If the track fails similar criteria in the $s-z$ plane, the track is accepted albeit with the $s-z$ track parameters flagged as being unusable.

For the case of axial tracks only, an attempt is made to add extra track hits from both within the same sector and neighbouring sectors. Within the same sector, tracks are interpolated to wires that contain no associated hits. The closest such hit to the track will then be added to the list of associated hits if it falls within 400 μm. In addition, tracks with no hits present on the end wires are extrapolated into neighbouring sectors where the nearest unassociated hit on each wire is added if falling within 600 μm of the track. If one or more extra hits are added in this way the original track is scrapped and a refit performed including all the new hits.

3.1.7 The Calibration Procedure

The approach to determining CV calibration parameters for the 1990 data set was motivated by the desire to ensure tracking at the full CT level was optimised. A calibration procedure developed that was based largely on tuning the parameters to optimize the spatial resolution as gauged by the d_0 properties of the CT track. It is important to note that throughout this discussion on CV calibration the track d_0 considered is geometrically corrected for an estimate of the interaction point and retains the signing convention of Appendix B. Tracks from Z^0 leptonic decays (e and μ-pair events) were used almost exclusively. These high momentum tracks are particularly suitable for calibration purposes since they are affected very little by multiple scattering and their simple event topology is well defined. In addition, with only two back-to-back tracks in the event any systematic effects related to multiple hits on wires (see Section 3.1.8) are avoided.

[9] s is the arc length of the track in the $r-\phi$ plane from the point of closest approach to the origin of the coordinate system.

What follows is a brief description of how those parameters that one may reasonably expect to be time-varying are adjusted to account for changing operating conditions of the detector. The parameters are updated typically once per running period, coinciding roughly with the frequency of which the CV gas supply is changed. In addition a normal running period would collect the few thousand lepton-pair events needed to determine parameters to a reasonable precision. Representative values and uncertainties for these quantities are then presented in Table 3.1.

Drift Velocity v_d

The drift velocity for the chamber is determined by studying the distribution of d_0 with respect to ϕ_{CV} [10], which effectively folds all sectors into a single sector. Use of the wrong drift velocity is then evident by the presence of a slope in this plot, the gradient of which is proportional to the magnitude of the required correction to v_d and the sign of the slope corresponds to the sign of the correction.

a_{near} and a_{far}

The 'a' parameters of Equation 3.3 are determined by the optimisation of a $\sum d_0$ or 'miss distance' [11] distribution made for each side of the CV anode plane. Both in practice and qualitatively [43], it is seen that $\sum d_0$ on one side (ϕ_-) of the anode plane is almost entirely dependent on a_{near} whereas, the opposite side (ϕ_+) is dependent on a_{far}. Hence the 'a' parameters can be adjusted so as to force $\langle \sum d_0 \rangle$ to zero simultaneously for both ϕ_- and ϕ_+.

Sector t_0's

Potentially the most accurate way of determining the t_0 offsets (and indeed also the drift velocity) is through the use of good quality anode and cathode-plane crossing tracks. In practice, running in the LEP environment, the occurrence of such tracks in the CV is found to be too low to be of practical use in the calibration procedure. Further, tracks that are found crossing boundaries in CV are typically of low momentum and sometimes not well reconstructed. These considerations are less valid to tracking in the CJ where boundary crossing tracks are used for calibration purposes (see Section 3.2.4).

[10] ϕ_{CV} is defined as being the azimuthal angle between the CV anode plane and the tangent to the track vector at the radius of the seventh axial wire.

[11] Defined as the distance between the crossing points of the extrapolated lepton tracks with the beam axis and should ideally be zero. It corresponds to the arithmetic sum of the d_0 track parameters of the track pair with d_0 defined as in Appendix B.

The method therefore used to determine sector time offsets (t_0^{sec}), follows closely the technique used to secure a_{near} and a_{far} but on a sector-by-sector basis. In this case it is demanded that $\langle d_0 \rangle$ (which ideally would be zero) for ϕ_-, be equal to that for ϕ_+. Explicitly this implies making the following correction to the sector t_0,

$$\Delta t_0^{sec} = \frac{\langle d_0 \rangle_{\phi_-} - \langle d_0 \rangle_{\phi_+}}{2v_d}. \tag{3.6}$$

The method is complicated somewhat by the assumption that v_d is uniform across the full CV drift cell although any effects can be minimised by ignoring tracks passing close to the anode plane.

Wire t_0's

The individual wire t_0's are determined by a similar operation to that used for t_0 but based on the *corrected* residuals [12] of hits to CV track fits in the $r - \phi$ plane. A residual is defined to come with a positive (negative) sign if the hit falls outside (inside) of the track circle.

By imposing that the mean residual $\langle R \rangle$ both sides of a single wire be the same, a correction to the wire t_0 is given by,

$$\Delta t_0^{wire} = \frac{\langle R \rangle_{\phi_+} - \langle R \rangle_{\phi_-}}{2v_d}. \tag{3.7}$$

Calibration Quantity	Typical Value	Typical Error
Drift velocity	40 μm/ns	0.1 %
a_{near}, a_{far}	370 μm	5 μm
Sector t_0	410 ns	0.1–0.2 ns
Wire t_0	$<$ 1 ns	–

Table 3.1: Typical values and associated uncertainties for selected CV calibration constants. Assigning uncertainties to these quantities is complicated by the t_0 and a parameters being correlated in the sense that they have a similar effect on tracking. In addition, the calibration procedure accommodates any CJ systematic effects that may push the constants away from their values suggested by an internal CV calibration technique. The values given are based on holding all but one of the parameters constant and observing at what level changes are detectable by the calibration process. No error on t_0^{wir} is quoted since for any individual wire only very large changes would affect the overall tracking.

[12] Corrections are applied to account for the fact that the endpoints of a least squares fit naturally carry more weight and hence will in general have smaller residuals.

Fast-z Calibration

By making use of stereo z coordinates on CV merged axial and stereo track segments, a plot of z against raw ZDC can be made and parameterised as suggested in Equation 3.5. In this way, the calibration can be made internal to CV but in practice the calibration is based on z measurements from CT track fits. For tracks matched to CV stereo segments, the z measurement may still be dominated by the stereo hits although accurate z information from CZ hits are also included.

In this way the calibration has the advantage of ensuring that CV z-measurements are consistent with those from the rest of the CD which is an important criterion in the Track Trigger, for example, where CV and CJ hits are required to lie at the same polar angle.

3.1.8 Systematic Effects

Chamber Rotations (α_{MRS})

In the 1990 data set for CJ tracks only, the distribution of d_0 over all azimuthal angles reveals a mean of $\simeq 30\,\mu$m. This is evidence for a systematic error in the angle of tracks from the CJ and, in the spirit of calibrating CV within the CT environment, this effect was accounted for at the CV level.

Since a non-zero mean in d_0 can be introduced by rotating CV about the z axis with respect to CJ (i. e. with respect to the MRS), the effect can be taken out by an adjustment to the α_{MRS} parameter (see Appendix A). Based on the mean of $\sum d_0$ for back-to-back lepton pair events, the magnitude of the adjustment was empirically determined to be

$$\Delta\alpha = \left\langle \sum d_0 \right\rangle / 25.5, \tag{3.8}$$

where both distances are in centimetres and the angle is in radians.

Anode Plane ϕ Corrections

From the t_0^{sec} adjustments of Section 3.1.7 the data has the property, $\left(\langle d_0 \rangle_{\phi_-}\right)_i = \left(\langle d_0 \rangle_{\phi_+}\right)_i$, for $i = 1 \rightarrow 36$ sectors. In general however it is found that $(\langle d_0 \rangle)_i \neq 0$. In the same way as adjusting α_{MRS} accounted for this problem at the level of the whole chamber, at the sector level a non-zero mean can in principle be accounted for by a form of local rotation. This was achieved by making slight alterations to the assumed ϕ locations of CV anode planes.

CV Second Hit Correction

Figure 3.11 shows d_0 distributions formed separately for each side of the CV anode plane from multi-hadronic events. All tracks reconstructed contribute to these plots

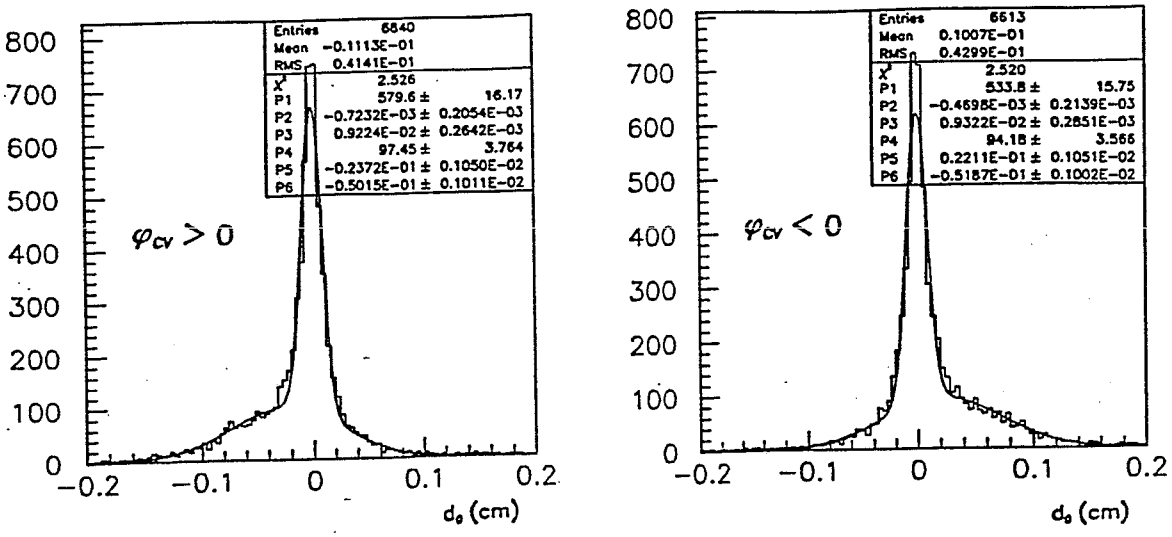

Figure 3.11: d_0 distributions uncorrected for second-hit effects, shown separately for each side of the anode plane. Tracks contain at least 6 CV axial hits and have momenta greater than 1 GeV/c.

i. e. those composed from first hits and from second (and higher) hits on wires. The plots clearly show a systematic offset in d_0 of opposite sign depending from which side of the anode plane tracks are chosen.

The cause of this effect was traced to the ~20% of CV tracks that contain hits that are second or higher hits on wires, and can be explained by the interference of wire signals with those subsequently collected on the same wire. The slow decay of the first pulse, adding to the amplitude of the second pulse, can cause it to cross threshold sooner than would normally be the case. The result is that tracks formed from these hits are artificially shifted towards the anode plane which in turn pushes the mean d_0 away from zero in a sense that flips sign according to which side of the anode we consider.

A correction for this effect to the drift distance of hits was developed [44] based on the pulse height of first and second hits and their separation in drift time. Although based on axial tracks formed from second hits on wires, the same form of correction is also applied to tracks composed of 3rd, 4th etc. hits on wires and to hits in stereo sectors. The effect of the correction can be seen from Figure 3.12.

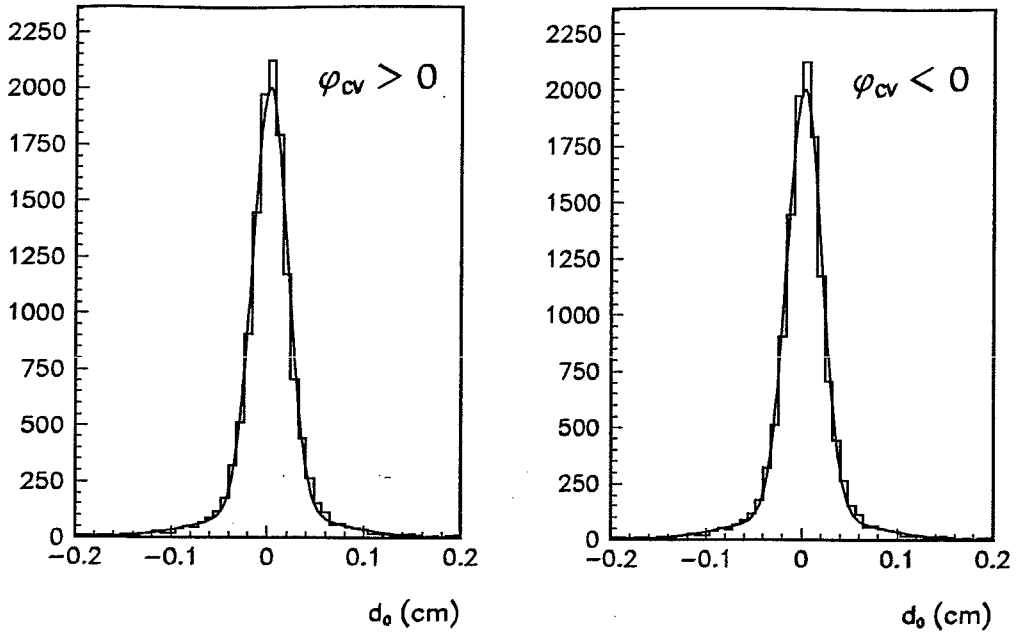

Figure 3.12: d_0 distributions corrected for second-hit effects, shown separately for each side of the anode plane. Tracks contain at least 6 CV axial hits and have momenta greater than 1 GeV/c.

Anode Region Drift Velocity

Figure 3.13 shows the population across a CV drift cell of CT tracks, in GPMH events, that contain at least ten CV axial hits. The presence of the 'hole' seen around the origin in ϕ_{CV} was found to originate at the CV track level. Using CV tracks only, a study of the anode region, revealed that the depletion of tracks corresponded to an overestimate of the drift velocity in the non-linear region of the drift distance-time relationship. This had the effect of biasing the reconstructed position of tracks away from the anode to larger drift distances.

Adjusting the velocity in this region was seen to fill in the hole but practical considerations meant that the 1990 data set used for the present analyses has not been corrected for this effect. To avoid the introduction of extra systematic uncertainty in the tracking, all CT tracks falling within $|\phi_{CV}| \leq 0.01$ radians of the CV anode region (indicated on Figure 3.13) are rejected from the subsequent analysis. This results in a loss of, on average, 3.7 CT-tracks per event.

3.1.9 Performance

Inefficiency due to dead readout channels in the axial sectors is typically kept to the 1% level. During initial testing of the chamber in 1989, four axial and two stereo wires were broken and were removed from their parent sectors without replacement. Subsequent electrostatic problems have also forced two complete stereo sectors to

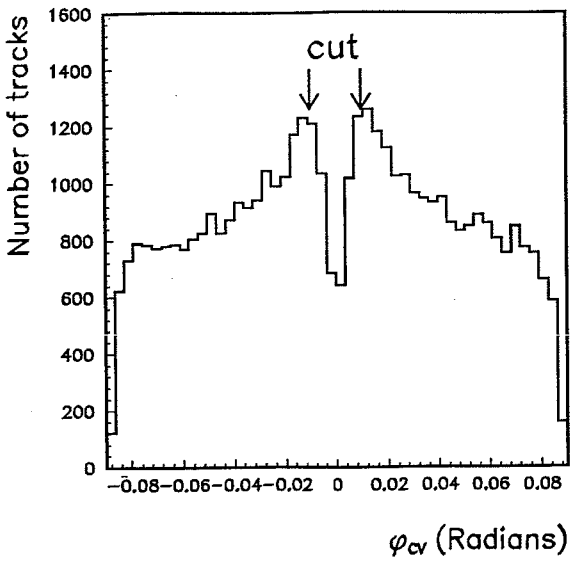

Figure 3.13: The distribution of tracks across a CV drift cell illustrating the hole that appears close to the anode plane. Tracks are from multi-hadronic events and contain at least ten CV-axial hits. The arrows indicate the position of the cut imposed to remove this region from the data.

be disconnected from the high voltage supply. Ignoring missing channels, the single hit efficiency averaged over all wires in axial sectors is found to be 97.4% from a study of hits on tracks in $Z^0 \to \mu^+\mu^-$ events. The equivalent hit efficiency for the dense track environment of multi-hadronic events was found to degrade by 7% due to the inefficiency associated with collecting multiple hits on wires. Tests show that hits on the same wire are essentially always resolved by the readout system for a hit separation in time of 45 ns.

The best estimate of the spatial resolution, including calibration uncertainties, is given by the standard deviations of the corrected track residuals (described in Section 3.1.7). Figure 3.14 shows distributions of $\sigma_{r\phi}$ and σ_z as functions of drift distance in multi-hadronic events based on axial tracks contained in a single sector and that do not cross anode or cathode planes. The resolutions exhibit the expected rapid rise at small drift distances due to sampling fluctuations and the slow rise at large drift distances due to the effects of diffusion. Averaged over all drift distances these resolutions correspond to 56 μm in the $r - \phi$ and 4.85 cm in the $s - z$ plane (based on the fast z measurement).

Figure 3.15 shows a distribution of the drift-distance difference between axial tracks in multi-hadronic events. The distribution shows that the two-track resolution achieved is approximately 2 mm, consistent with the known second hit resolution of 1.8 mm (based on $v_d = 40\,\mu$m and a timing resolution of 45 ns). An investigation of the spatial resolution based on tracks composed of second hits on wires shows an

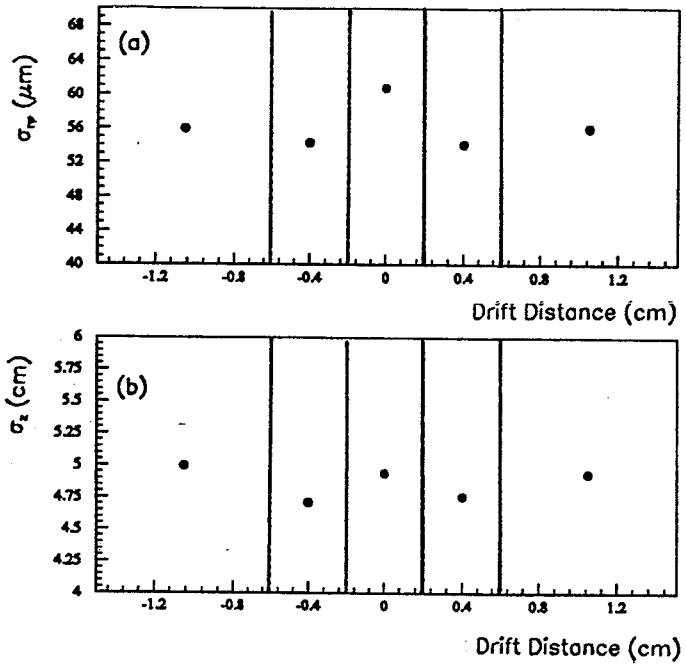

Figure 3.14: The variation of spatial resolution in the (a) $r-\phi$ and (b) $s-z$ planes as a function of drift distance. The lines indicate the binning boundaries in drift distance used.

associated degradation over the single hit values of approximately 8% in both the $r-\phi$ and $s-z$ planes.

3.2 Jet Chamber

3.2.1 The Mechanical Design

The OPAL Central Jet Chamber was introduced in Chapter 2. The principles of design draw heavily on the experience gained in constructing the jet chamber for the JADE experiment at PETRA [40].

Figure 3.16 shows the layout of chamber sectors within one quadrant of the detector. Each sector consists of a central plane of anode wires spaced by 1 cm (between radii of 25.5 cm and 183.5 cm), with two cathode wire planes which mark the boundary between adjacent sectors. The maximum drift distance ranges from 3 cm at the inner wires to 25 cm for the outermost wires.

The wires are stretched between two end plates held apart by a shell of 24 hollow aluminium panels. In order to minimise the material traversed by tracks, the chamber has no inner support tube. To withstand the tensional force of around 14 tons exerted by the wires, the endplates are conical in shape (with an angle of 15°) resulting in sector wires varying in length from 3.2 m at the inner radius to 4.0 m at

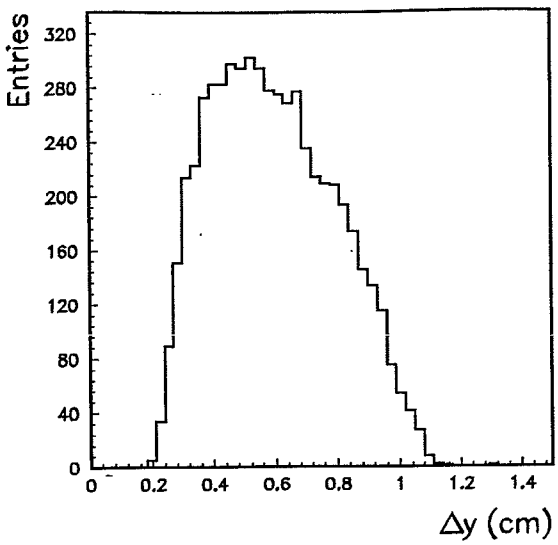

Figure 3.15: The mean drift-distance separation (Δy) of CV axial tracks contained in the same drift cell.

the outer radius. The design allows 73% of the full solid angle to be covered with the maximum of 159 space points on a track.

Figure 3.17 details a cross section through a single CJ sector. The anode wires made from gold-plated tungsten-rhenium are 25 μm in diameter and staggered by $\pm 100\,\mu$m as illustrated in Figure 3.17, in order to resolve the left-right ambiguity. Potential wires made from 125 μm diameter copper-beryllium alloy, are alternately spaced between the anode wires and tensioned such that the gravitational sag ($\sim$200 μm at $z = 0$) is equal within $\pm 5\,\mu$m for anode and potential wires.

The electrostatic properties within a sector are set by holding the anode wires at ground potential and applying graded voltages to the cathode wires made from 125 μm diameter copper-beryllium, and spaced at 1.3 mm intervals. To ensure equipotential lines parallel to the anode plane, the cathode wires are set at potentials ranging from -5 kV at the inner radius to -27 kV at the outer radius. The gas gain is determined by the voltage applied to the potential wires, set nominally to -2.5 kV. The correct electrostatic boundary conditions are provided by field shaping electrodes around the outer radius of each sector and on the endplates as shown in Figure 3.17.

In common with the CV, CJ is operated using OPAL gas which was shown in in Section 3.1.4 to be capable of providing high spatial resolution. The operating pressure of 4 bar optimizes particle separation from $\mathrm{d}E/\mathrm{d}x$, and also represents a compromise between the high pressure needed to minimise diffusion effects and the low pressure needed to minimise multiple scattering and so ensure a good momentum resolution. The electrostatic configuration described provides a drift field of

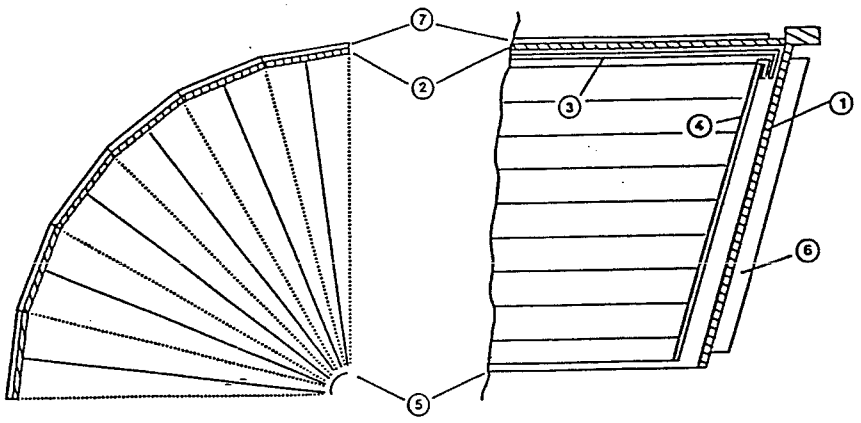

Figure 3.16: A quadrant of the Jet Chamber in cross sectional projection and in the plane perpendicular to the beam axis. The cathode and anode planes are shown together with, (1) the conical endplate, (2) the shell of aluminium panels, (3) the barrel, (4) and endcap field-shaping electrodes, (5) the inner field shaping foil, (6) the anode wire suspension and (7) the z-chambers. From [45].

890 V/cm resulting in a gas gain of 10^4.

Due to the beneficial effects concerning chamber ageing, the gas contains water at the level of 500 ppm. The strong dependence of the drift velocity however on water content means that this concentration has to be tightly controlled. Figure 3.18 illustrates this point. The stability of water content is kept to $\pm 10\%$ so ensuring a stability of the drift velocity to $\pm 0.1\%$.

3.2.2 The Electronics Readout System

The readout chain for a single CJ anode wire is presented in Figure 3.19. The output of a low noise preamplifier is input to a resistor network that provides crosstalk compensation [45] for the first and second neighbouring wires. The signals from both ends of all 3816 anode wires are transmitted via individually shielded twisted pair cables, to be recorded with 100 MHz FADCs (DL300) housed in 80 front-end crates.

The use of a FADC-based system is necessitated by the large drift distances across a CJ sector. For drift distances greater than a few centimeters, the effects of electron diffusion begin to limit the spatial resolution attainable from a 'leading-edge' measurement of the drift time as utilised by the CV. By accurately sampling the shape of a chamber pulse in time, the FADC readout is used to derive the mean of the arrival time of the electrons at an anode, which is largely insensitive

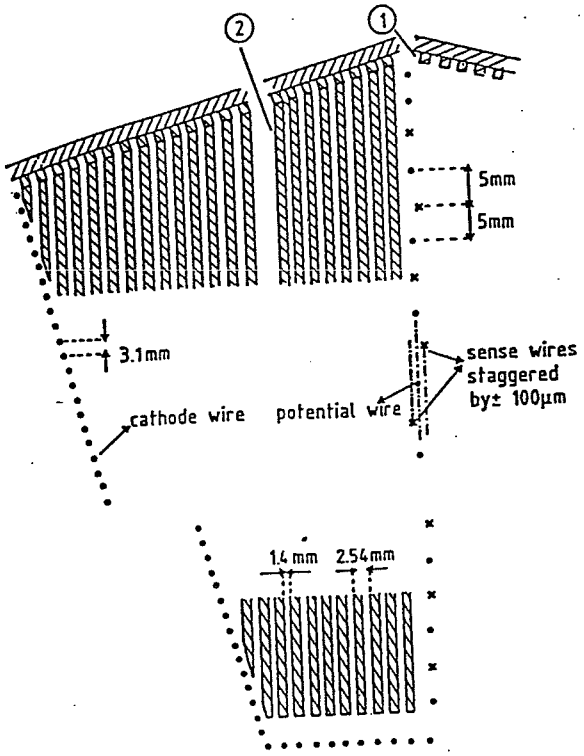

Figure 3.17: A cross section through one half sector indicating the locations of the anode and cathode planes as well as the field shaping electrodes in (1) the barrel and (2) the endcap. From [45].

to diffusion effects. The FADCs have an intrinsic dynamic range of 6 bits which is effectively extended to 8 bits for an improved amplitude resolution, by generating a non-linear response curve [47]. Hardware zero suppression performed at this stage reduces the amount of data before transfer to an array of 20 microprocessors of the 68030 type, housed in two VME crates.

The total readout time for a multi-hadronic event is less than 10 ms and the mean time available between triggers is large enough to enable a significant degree of online processing to occur. The first stage of this involves the determination of uncalibrated drift times and charges from both ends of the wires. Chamber hits are defined by a fast *difference of samples* algorithm [48] which derives essentially a mean drift time (t_D) for the chamber signal based on the differentiated pulse shape. The drift times are corrected for both individual channel and global t_0 offsets at this stage, but no fine corrections are made. The pulse charge is obtained by integrating each pulse shape over 200 ns with respect to the start of the signal. The subsequent values from each end of the wire give the z coordinate by a charge division technique described below in Section 3.2.3.

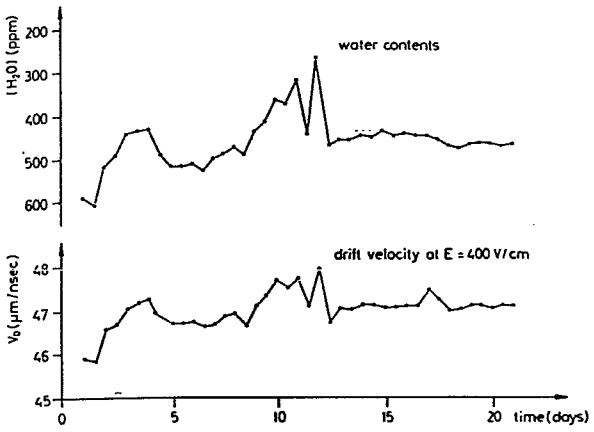

Figure 3.18: The variation of the measured drift velocity and the chamber gas water content over a running period of 20 days. The water content was not stabilized during the first 12 days of operation resulting in large fluctuations of the drift velocity. From [46].

The measurements of t_D and z described constitute essentially the CJ raw data output. The online microprocessor system does in addition however use this partly calibrated data as input to a fast on-line pattern recognition algorithm [33]. The resulting tracks then form an essential input to the OPAL event filter processor as described in Section 2.3.1.

3.2.3 Coordinate Reconstruction

In the $r-\phi$ plane, spatial positions x and y of a wire hit are given by,

$$\begin{aligned} x &= x_w - v_D.\sin\alpha_L.t_D \\ y &= v_D.\cos\alpha_L.t_D, \end{aligned} \tag{3.9}$$

with respect to a local sector reference frame with the x-axis pointing along the anode wire plane. Here, the x coordinate of the wire is given by x_w, v_D is the drift velocity, α_L is the Lorentz angle and t_D is the drift time.

Using resistive charge division, the z coordinate is calculated using the following relationship, for signal charges Q_L and Q_R going into the preamplifiers at the ends of each anode wire:

$$z = \frac{l_{eff}}{2}\frac{(gQ_L - Q_R)}{(gQ_L + Q_R)} \tag{3.10}$$

Here, l_{eff} is an effective wire length depending on the impedence of the wire and preamplifier and g is the relative gain of one end of the wire with respect to the other.

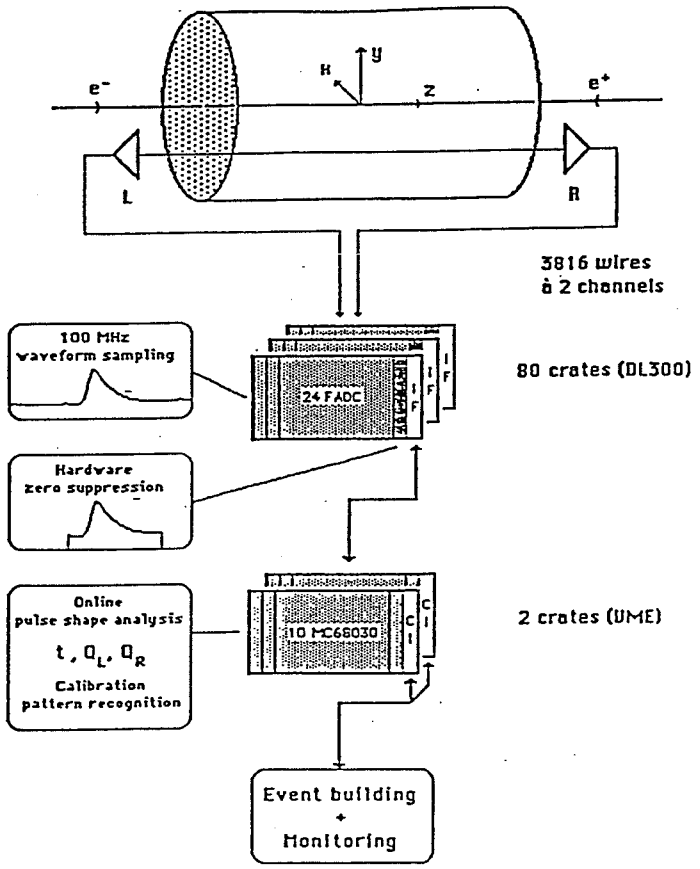

Figure 3.19: The electronic readout chain from the detector to the online microprocessor system. The data flow and reduction at each step is also shown. From [46].

Pattern Recognition

The assigning of hits to potential track segments follows a similar scheme to that used for pattern recognition in the CV. Starting from the outer wires of each sector triplet initiators are defined, to which extra hits are iteratively assigned if they fall within the designated road width (typically 5σ) of the extrapolated track. In the $r-\phi$ plane track segments within CJ sectors are fit to circles using the Conformal Mapping method [49]. After transforming all hits assigned to segments into the MRS reference frame, an attempt is made to merge those tracks in adjacent sectors consistent with originating from a common source. A minimum of ten space points are required in the definition of a CJ track segment.

3.2.4 Calibration Constants

Laser Calibration

To aid with calibration and monitoring tasks an ultraviolet Nd:YAG laser system [50] is employed. Two parallel beams separated by 10 mm in the $r-\phi$ plane can be injected through the centre of all 48 half-sectors. In the orthogonal plane the two beams originate from $z = \pm 1.20$ m.

The laser beam is assumed to follow an exactly straight path. Any measured deviations from a straight line therefore are due to individual channel timing offsets (t_0^{wir}), geometrical wire positions, or inhomogeneties of the drift field. Precise knowledge of the laser beam position in z allows the determination of the effective wire length l_{eff} and relative gain g for each wire.

During normal physics runs laser events are read out at a rate of 0.04 Hz and complete laser scans performed during LEP shutdown periods. Table 3.2 lists typical values and errors on calibration constants derived from the laser system.

Boundary Crossing Tracks

As was the case when considering tracking in the CV, discontinuities in tracks crossing sector boundaries are indicative of a miscalibration.

Tracks crossing anode planes are sensitive to the t_0 drift time offset i. e. the time between the BX signal and the FADC start trigger. By requiring continuity of tracks across the anode plane, offsets for each sector are determined. In addition, a linear dependence in the individual wire time offsets with radius (not detectable by the laser system) is measured by this class of track. Anode crossing tracks are also used to estimate the point at which the drift field is no longer constant. As was the case for a CV drift cell, this becomes significant close to anode wire positions (inside the so-called 'aberration radius') and is treated as a systematic correction to the drift velocity (see below).

Cathode crossing tracks are used to determine the drift velocity (v_D) and the Lorentz angle (α_L).

Table 3.2 lists typical values and uncertainties of constants derived from the use of boundary crossing tracks. To gain sufficient precision, a few thousand hadronic events containing such tracks are required.

3.2.5 Systematic Effects

Regions of the drift cell close to the electrostatic boundaries are particularly prone to non-uniform field conditions. Corrections to drift distances are necessary for the innermost 4 wires in each sector and the outermost 16, which can be up to

Calibration Quantity	Calibration Method	Typical Value	Typical Error
Effective wire length l_{eff}	Laser	460–560 cm	0.5%
Relative gain g	Laser	0.998	0.4%
Wire time offsets t_0^{wir}	Laser	−12 to 12 ns	0.8 ns
Effective wire staggering	Laser	115 μm	10 μm
Drift velocity	Boundary crossers	52.9 μm/ns	$< 0.05\%$
Lorentz angle	Boundary crossers	20.0°	$< 0.5\%$
Sector time offset t_0^{sec}	Boundary crossers	300 ns	< 0.6 ns
Linear dependence of time offsets	Boundary crossers	0–0.1 ns/cm	0.007 ns/cm
Aberration radius	Boundary crossers	4.435 mm	0.05 mm

Table 3.2: CJ calibration quantities and their typical values and errors. The effective wire staggering is the sum of the mechanical and electrostatic staggering at the z position of the laser beams. From [51].

800 μm in the worst cases. Corrections derived from anode crossing tracks are also applied within the aberration radius to each anode plane, to account for the onset of the region where the drift distance-time relationship becomes non-linear.

Finer corrections applied include compensation for a torsion effect found between the two endplates of the chamber of 50 μrad. Also the small variation in v_D and α_L with radius through a sector [13] was parameterised and applied as a correction.

Since the start of data taking in 1989, correcting for systematic effects has led to an improvement in the momentum resolution by a factor 2.5.

3.2.6 Performance

The efficiency of the chamber for hit and track finding is found to be excellent. The number of dead readout channels unavailable to the pattern recognition is typically only 0.3% due to failures somewhere along the electronics readout chain. It has not been necessary to replace any of the 3816 anode wires due to breakage. Ignoring these missing channels, the single-hit efficiency is found to be 99.2% from a study of hits on tracks in $Z^0 \to \mu^+\mu^-$ events. In dense track environments, multiple hits on the same wire are found to be cleanly resolved in 80% of cases where the hits are separated in drift distance by 2.5 mm or more. From Monte Carlo the ability to find tracks given these hit efficiencies can be gauged. For tracks inside hadronic jets with a momentum above 0.1 GeV/c and in the the barrel region, the track finding efficiency is determined to be 97.9%.

The intrinsic resolution in the $r - \phi$ plane ($\sigma_{r\phi}$) based on triplets of adjacent

[13] v_D and α_L found by the calibration procedure represent averages over all radii.

hits in $Z^0 \rightarrow \mu^+\mu^-$ events is found to be 135 μm averaged over all drift distances. Figure 3.20 shows the measured variation in $\sigma_{r\phi}$ as a function of drift distance. The observed variation is familiar to that seen earlier when considering the CV (see

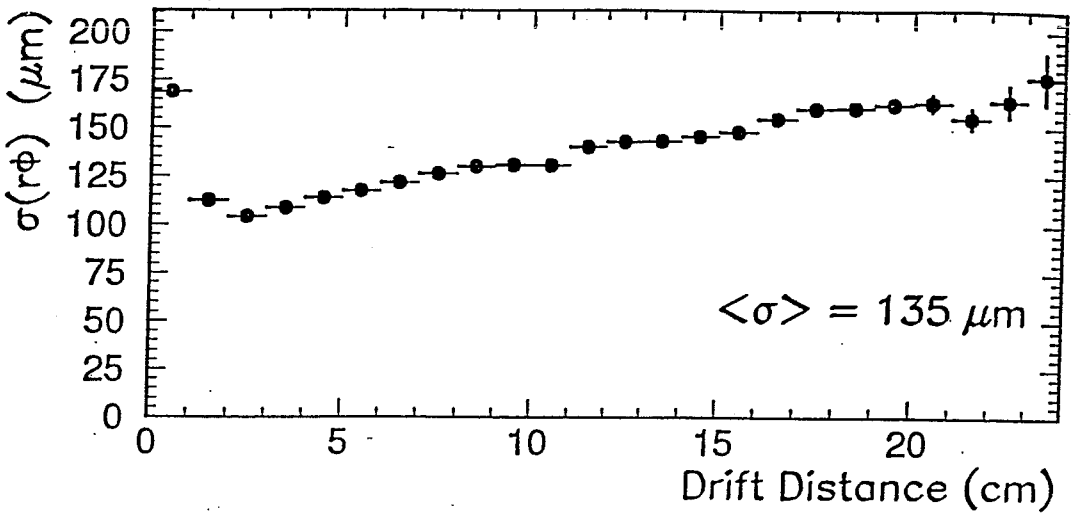

Figure 3.20: The triplet hit resolution $\sigma_{r\phi}$ as a function of drift distance. From [51].

Figure 3.14) and has the same explanation. This single hit resolution is degraded by a factor of 1.5 due to the effects of overlapping pulses, when considering hits separated by less than 3 mm.

Based on the $\sum d_0$ between muon tracks in $Z^0 \rightarrow \mu^+\mu^-$ events, the impact parameter resolution from CJ tracks only is measured to be $\sigma_{d_0} = 160/\sqrt{2} = 113\,\mu$m. The resolution close to the event vertex from OPAL tracking however, is dominated by the presence of CV hits and is discussed in the following Section 3.3. The momentum resolution in $Z^0 \rightarrow \mu^+\mu^-$ events is measured to be $\sigma_p/p^2 = 1.5\times10^{-3}\,(\mathrm{GeV/c})^{-1}$ corresponding to 6.8% at $p = 45\,\mathrm{GeV}/c$.

In the $s-z$ plane, an intrinsic coordinate resolution of $\sigma_z = 4.5$ cm and $\sigma_z = 6.0$ cm is measured for tracks in $Z^0 \rightarrow \mu^+\mu^-$ and multi-hadronic events respectively. These resolutions translate into 1-2% of a wire length which is typical for the charge division method.

3.3 Central Detector Tracks

The merging of information from CV, CJ and CZ to form composite CT tracks of the CD is achieved in two steps. The first is pattern recognition where track segments from the sub detectors are compared and associated to define a CT track. The second is track fitting to obtain the track parameters and their associated covariance matrix.

Pattern Recognition

By default the order in which associations are made is to first match CJ with CV axial segments, then with CZ segments and finally with CV stereo segments. A CJ track segment is a necessary and sufficient requirement for a CT track.

For the first step, each CJ track and both ambiguities of each CV axial segment are extrapolated to a cylinder of length 300 cm and radius 13.25 cm (i. e. mid-way radially through the CV axial layer). Candidate matches are decided on the basis of likelihood comparisons formed from the cylinder intersection coordinates and their uncertainties. A similar procedure is followed for the merging of CZ and CV stereo segments to the CJ track. After each stage of matching is complete, the CJ track $r-\phi$ parameters are updated by imposing the intersection point of the CV segment with the cylinder as a constraint. These updates do not affect the final fit but help to improve the pattern recognition efficiency.

3.3.1 Track Fitting

After track merging is complete, the list of hits from the associated segments are fit as a single track separately in the $r-\phi$ and $s-z$ planes.

Before fitting in $r-\phi$ commences a pass is made through the residuals of CJ hits to the final CJ track fit, and any points greater than 3σ from the track are ignored by subsequent fits, by setting their weight to zero. A track fit is then made to all of the points, using a method due to Billoir [52] that constantly updates the track parameters as each hit is added, with the effects of multiple scattering taken into account at each step. In the absence of multiple scattering, this procedure reduces to a circle fit. It is necessary however, to adjust the covariance matrix 'by hand' to take proper account of multiple scattering occurring between the CV and CJ (e. g. in the CV stereo foils and the carbon-fiber tube), for which the Billoir implementation is inappropriate. In addition the covariance matrix is adjusted for the effects of systematic measurement errors e. g. due to imperfect calibrations. Systematic adjustments can be made: (1) at the CJ track-segment level i. e. before any CV points have been added or (2) after the fit to all points. Changes of the

first kind have effects both on the resulting CT-track parameters and the covariance matrix whereas those of the second kind affect terms only in the covariance matrix. The systematic corrections applied are collected together in Table 3.3. If after the first iteration, hits still exist that are $> 3\sigma$ from the track trajectory, they are dropped as before and the fit repeated. Because of the strong correlation between $r-\phi$ and z that exists for CV stereo hits, they are ignored in the $r-\phi$ track fit by setting their weights artificially low.

Covariance Element	Level of Adjustment	Size (cm)
$\sigma^2_{\kappa\kappa}$	CJ	$(1.0 \times 10^{-6})^2$
$\sigma^2_{\phi_0\phi_0}$	CJ	$(1.0 \times 10^{-4})^2$
$\sigma^2_{d_0 d_0}$	CJ	$(1.5 \times 10^{-2})^2$
$\sigma^2_{\tan\lambda\,\tan\lambda}$	CJ	$(0.15 \times 10^{-1})^2$
$\sigma^2_{z_0 z_0}$	CJ	$(3.0)^2$
$\sigma^2_{d_0 d_0}$	CT	$(3.5 \times 10^{-3})^2$

Table 3.3: Systematic corrections to the covariance matrix made by the CT processor. The level of the adjustment refers to whether the change was made at the CJ track level (before the track fit included information from CV or CZ) or after the fit to all hits associated with the CT track.

The fit in the $s-z$ plane follows that in $r-\phi$. Any hit already dropped from the fit in $r-\phi$ is also ignored in $s-z$, and then the same procedure for the discarding of hits is applied to the z coordinates. A linear fit is performed in $s-z$ to determine the z_0 and $\tan\lambda$ of the track, where s is calculated from the $r-\phi$ position of each hit. If there are CV stereo points on the track, the z coordinates are updated using the stereo drift time measurements and the CT fitted trajectory in $r-\phi$.

Figure 3.21 illustrates the reconstruction of an isolated track from a multi-hadronic event. All hits including noise and unresolved left-right ambiguities are displayed in CV, CJ and CZ.

3.3.2 Performance

For tracks in multi-hadronic events, a study was made to measure the CV-CJ track-segment matching efficiency of the CT pattern recognition process. The efficiency calculation was based only on CV axial tracks that might reasonably be expected to pick up a CJ match. The criterion for this was the requirement that the extrapolated CV track crossed an imaginary cylinder of radius 100 cm and half-length 200 cm. The fraction of these tracks that were then subsequently merged into a CT track definition was found to be 90.7 ± 0.3 %. On average, 65.4 ± 0.2% of CT tracks are found to contain a match to CV axial track segments and of these 93.3% are to the preferred left-right ambiguity as determined by the CV anode wire stagger. If we

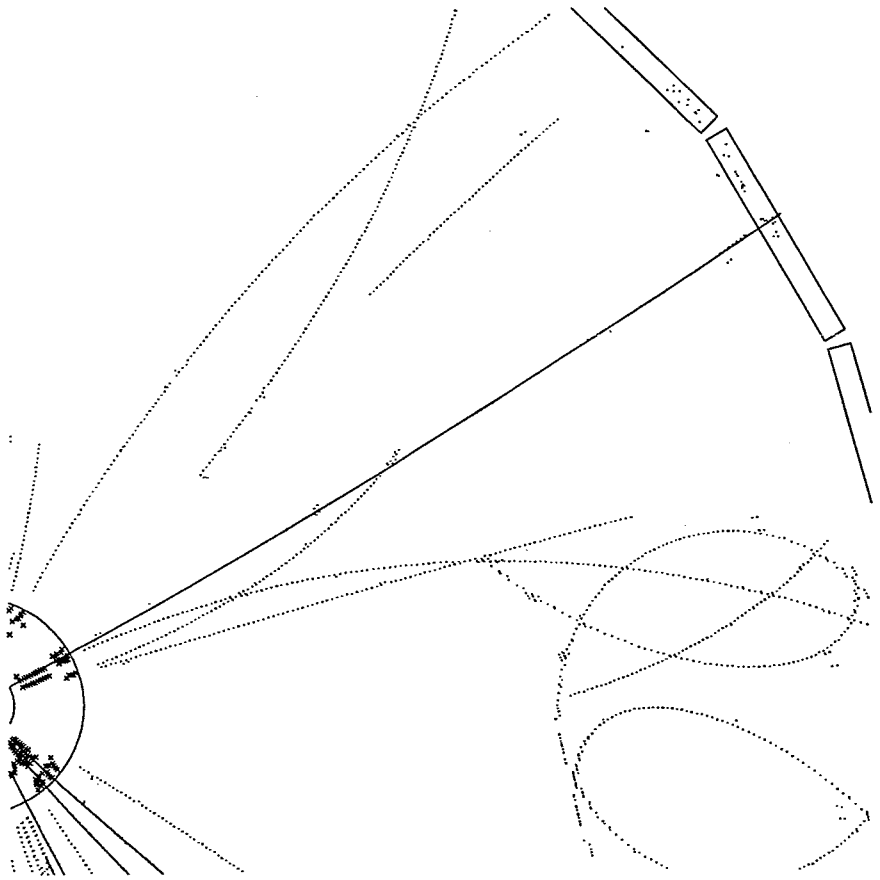

Figure 3.21: An example of a CT-track fit. The reconstructed track had a trajectory which followed closely a CJ cathode plane and, in fact, traversed the plane before reaching the CZ. Hits associated with the ambiguity of the track and with low momentum tracks are also visible (only CT tracks with a momentum $> 0.6\,\mathrm{GeV}/c$ are displayed).

require that the CT track be matched to **any** CV information (i.e. from axial or stereo) then the fraction with CV information increases to $77.4 \pm 0.1\%$. Further, the CV hit adding process that runs after track matching has been attempted, is seen to account for 10.9% of all eventual matches of CV axial information onto CT tracks.

An indication of the spatial resolution attainable in the $r - \phi$ plane from the d_0 of tracks in multi-hadronic events is given in Figure 3.22(a). The distribution gives clear evidence of the improvement in resolution attainable when CT tracks contain CV space points. The broader distribution corresponds to tracks that had no associated CV axial hits. A realistic measure of the **intrinsic** impact parameter resolution achieved by CT tracking is given by studying the 'miss distance' in $r - \phi$ of tracks extrapolated to the beam axis in μ-pair events. These high momentum tracks are essentially free from the effects of multiple scattering and the method is independent of any beamspot determination. A Gaussian fit to such a distribution,

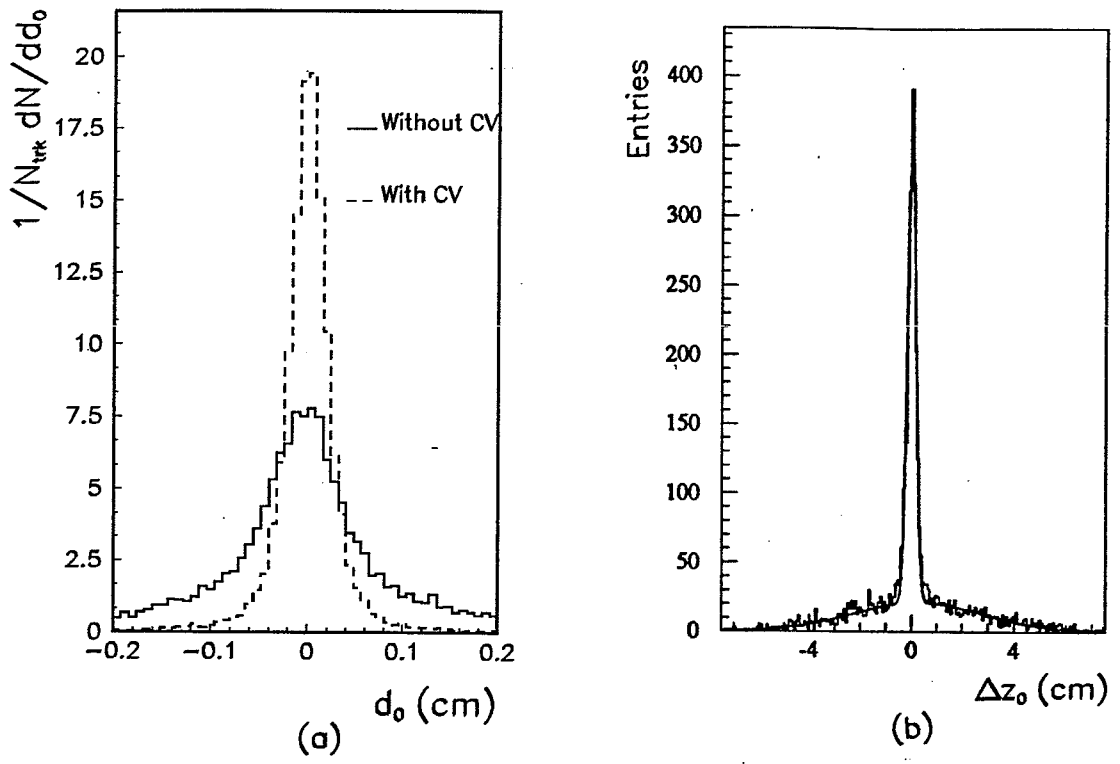

Figure 3.22: (a) The d_0 distribution (corrected for an estimate of the beamspot position) for tracks that contain no CV axial hits compared to the case where at least ten axial hits are associated with the track. The tracks come from multi-hadronic events and have a momentum greater than 1 GeV/c. (b) A Δz_0 distribution for μ-pair events.

requiring the tracks to contain CV information, produced a standard deviation of 60 μm corresponding to a resolution of 42 μm.

The resolution attained in the $s-z$ plane can analogously be evaluated from the distribution of z_0 difference (Δz_0) presented in Figure 3.22(b). The central narrow peak is due to tracks containing hits from CV stereo sectors and CZ, with the much broader background corresponding to tracks whose z information comes only from the CJ measurement. We find that the resultant resolutions in z are 1.2 mm for tracks containing both CZ and CV stereo information, 26 mm for tracks without CV stereo information and degrades to about 45 mm in z for a track containing only CJ hits.

Chapter 4

Multi-hadronic Event Simulation

4.1 Introduction

The products of a high energy e^+e^- annihilation are often the result of a long chain of complex intermediate processes. In practice this means that the record of the event, as given by a detector, offers only indirect information on any one of the physics processes that may have occurred between the initial and final state. A powerful tool for unfolding the contributions that these various processes make to an event record, is the direct comparison of the data with an accurate event simulation implemented via a Monte Carlo computer program.

This technique is used extensively in Chapter 5 to help evaluate the merits of various schemes able to identify b-quark decays of the Z^0. The comparison of data with a Monte Carlo simulation is also the method by which, in Chapter 6, a measurement of the mean B-hadron lifetime is made. It is therefore essential that the simulation contains all of the major known physics processes and detector effects that give rise to the observed properties of the data.

This chapter describes the content of a Monte Carlo data sample produced for the physics analysis of $Z^0 \rightarrow b\bar{b}$ events specifically. Particular attention was paid to achieving an accurate description of the production and decay of bottom-flavoured quarks and hadrons. In addition, a detailed study was made into modelling the response of the Vertex Detector in the data. This is particularly important since CV information on tracks proves to be essential in order to study the decay of B hadrons which occur well within the radius of the OPAL beampipe.

We consider the task of simulating e^+e^- annihilation in the OPAL detector as dividing naturally into two distinct areas: The first is the event generation itself where the topology and content of the event are chosen, where possible, according to analytical Standard Model results. The second then deals with simulating the passage of the particles generated through the detector so mimicing the effect of detector acceptance, efficiency and imperfections on the data. We conclude the chapter with a look at the relative success of this procedure via a comparison with data.

4.2 Event Generation

Event generation is performed within the framework of the JETSET [53] Monte Carlo (version 7.2), which originates from studies made in the early 1980's by the Lund Theory Group [54] into understanding jet fragmentation. With reference to Figure 4.1 we consider the event generation in four main stages: (1) primary quark production, (2) perturbative QCD (the parton shower), (3) non-perturbative QCD (fragmentation) and (4) the decay of unstable particles. Following loosely these four

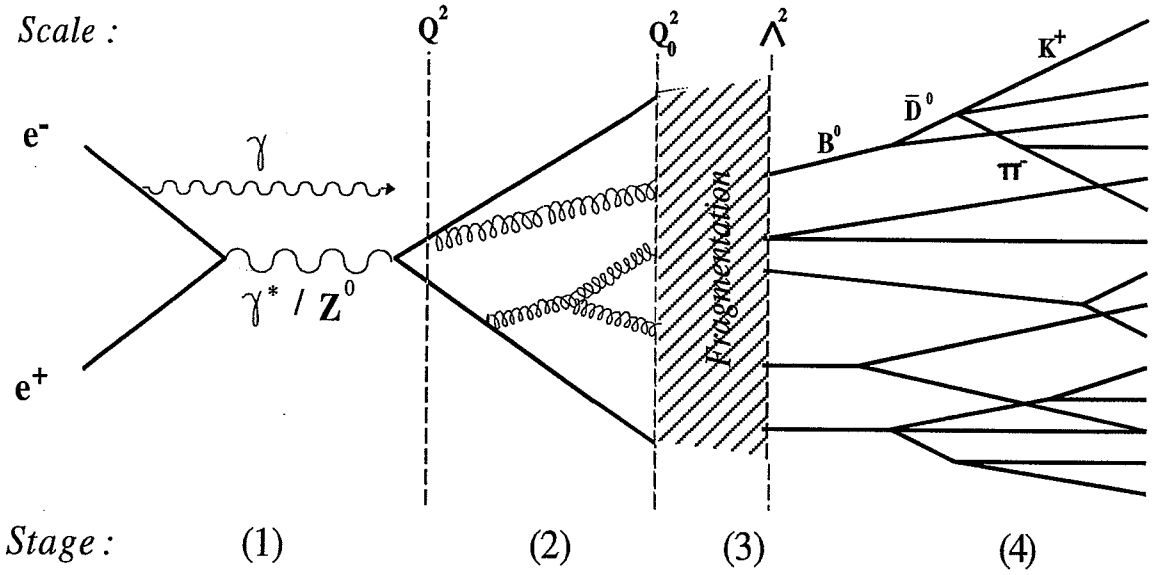

Figure 4.1: The stages of multi-hadronic event generation.

stages we now review aspects of the event generation pertinent to the production of b quarks and hadrons.

4.2.1 Primary Quark Production

In JETSET the relative probability for producing a quark pair $q_f\bar{q}_f$ (of flavour f =u, d, s, c, or b), is calculated based on the lowest order electroweak cross section for the process, $e^+e^- \rightarrow \gamma/Z^0 \rightarrow q_f\bar{q}_f$. QCD final state loop corrections to second order are included as are QED radiative corrections based on the first order results of [55].

Initial state radiation, of at most one photon, is possible between the soft and hard photon cut-off limits of 1% and 99% of the beam energy. The non-default JETSET option of allowing photon emission from the quarks and antiquarks of the parton shower phase (see below) is also chosen. The QED vacuum polarization diagram is included but there are no weak loop effects.

In Table 4.1 we list the assumed Standard Model parameter values that are input to JETSET.

JETSET Name	Value	Parameter Definition
PARU(101)	0.0072974	α_{em}
PARU(102)	0.2307	$\sin^2\theta_W$
PARJ(123)	91.154 GeV	m_{Z}
PARJ(124)	2.482 GeV	Γ_{Z}
PARJ(122)	0.5 GeV	$\Lambda_{\bar{M}S}$
PMAS(C6,1)	100.0 GeV	m_{t}
PMAS(C25,1)	100.0 GeV	m_{H}

Table 4.1: The Standard Model input parameter values to JETSET 7.2

4.2.2 Perturbative QCD-The Parton Shower

It is the radiation and subsequent fragmentation of gluons from the final state quark pair that gives rise to the multi-jet topologies common in high energy e^+e^- annihilations. As mentioned in Section 1.3 current matrix element calculations are complete only to second order and hence can describe at most four partons in the final state. That this is insufficient for an accurate description of the LEP data can be gauged by Figure 5.10, which shows the clear existence of five-jet events in the data.

For a more realistic description of the data we choose a phenomenological approach known as the JETSET *parton shower*. Here, a quark-gluon shower develops (analogous to an electromagnetic shower) caused by the continual application of the three basic branchings, $q \rightarrow qg$, $g \rightarrow q\bar{q}$ and $g \rightarrow gg$, as illustrated in Figure 4.2. This model yields an arbitrary number of partons in the final state.

The formalism for the parton shower model is that of the **L**eading **L**ogarithm **A**pproximation (LLA) of QCD, where the probability that a parton branching $p_a \rightarrow p_b p_c$ can occur is specified by the Altarelli-Parisi equations [56]. The development of the shower is terminated by imposing a minimum mass-squared value (Q_0) to which partons may evolve. This cutoff point then marks the scale at which perturbative theory breaks down and non-perturbative fragmentation models must be invoked

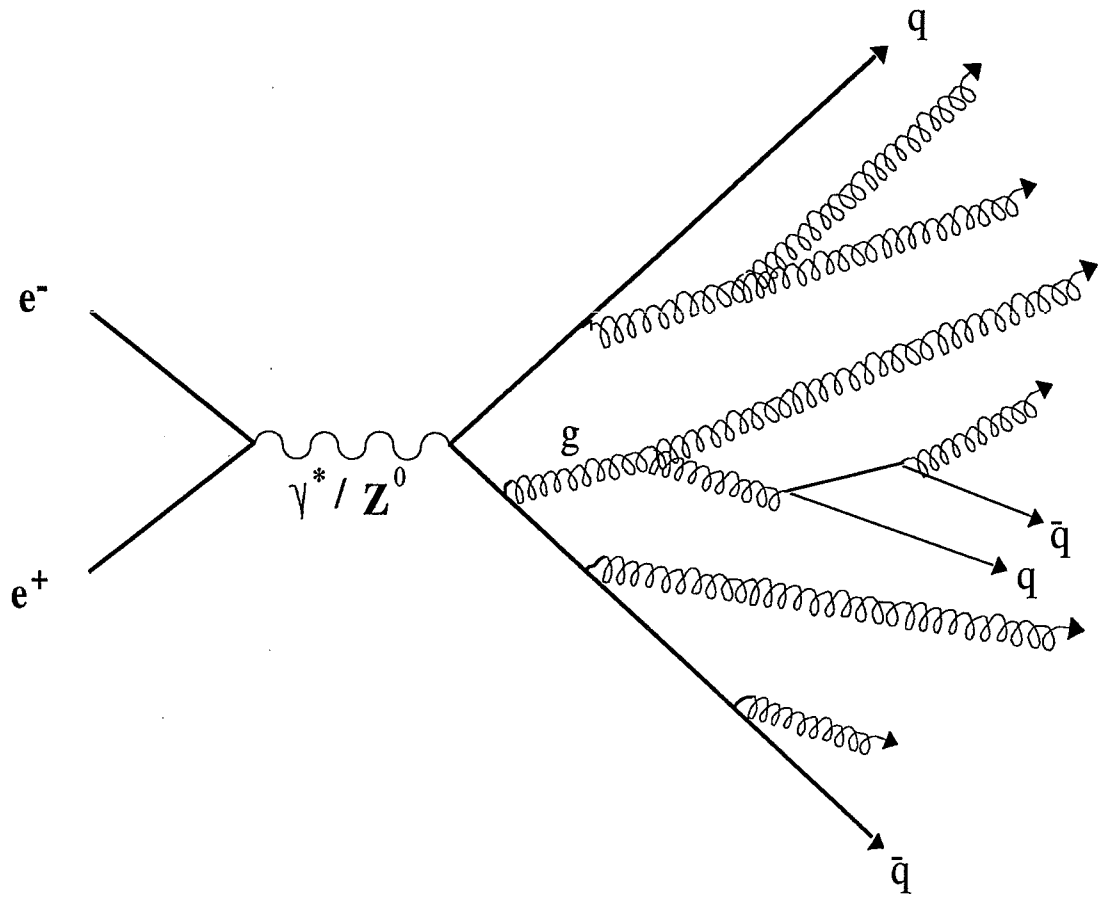

Figure 4.2: Schematic picture parton branchings in a parton shower.

(see Figure 4.1). The parameter Q_0 together with the QCD scale parameter value relevant within this approximation (Λ_{LLA}[1]), allow the parton shower phase of event generation to be effectively 'tuned' to best describe the data. Optimum values for these parameters were determined via a comparison of JETSET to OPAL data using a selection of event shape variables (some of which are defined in Chapter 5). Details of this procedure can be found in [57] and the resulting parameter values are listed in Table 4.2.

Finally, the JETSET parton shower incorporates an angular ordering to account for soft gluon coherence effects. OPAL, for example, has shown [58] that the inclusive momentum distribution of charged particles in multi-hadronic events is only correctly described by models that include this phenomenon. The JETSET implementation involves ordering the opening angle between the daughters of a branching parton in a decreasing fashion.

[1]The magnitude of Λ_{LLA} essentially determines the extent to which partons will branch.

Parameter	JETSET Name	Default Value	Optimized Value
Λ_{LLA}	PARJ(81)	0.40 GeV	$0.29^{+0.02}_{-0.01}$ GeV
Q_0	PARJ(82)	1.0 GeV	$1.0^{+0.8}_{-0.3}$ GeV
σ_q	PARJ(21)	0.35 GeV	$0.37^{+0.03}_{-0.05}$ GeV
a	PARJ(41)	0.50	$0.18^{+0.12}_{-0.05}$
b	PARJ(42)	0.90 GeV^{-2}	0.34 GeV^{-2}
ϵ_c	PARJ(54)	-	$0.037^{+0.033}_{-0.021}$
ϵ_b	PARJ(55)	-	$0.0035^{+0.0045}_{-0.0025}$

Table 4.2: JETSET parameter values tuned to OPAL data.

4.2.3 Fragmentation

To describe hadronisation subsequent to the termination of the parton shower phase, at characteristic momentum transfer scales of $Q^2 \sim 1\,\mathrm{GeV}^2/c^2$ (see Figure 4.1), models of fragmentation must be invoked to describe the emergence of hadrons.

The JETSET approach is founded on the Lund model. Here the confinement potential of QCD is modelled by the introduction of a uniform one-dimensional flux tube, or string, that links partons of a colour singlet state. For simplicity if we focus just on the development of a quark-antiquark pair ($\mathrm{q_0\bar{q}_0}$) moving apart back-to-back, then as they do so the potential energy stored in the string increases and the string may break by the production of a new $\mathrm{q_1\bar{q}_1}$ pair. The system now contains two string segments, $\mathrm{q_0\bar{q}_1}$ and $\mathrm{q_1\bar{q}_0}$, which can form two colour singlet mesons or continue to break into smaller pieces by $\mathrm{q\bar{q}}$ production if the invariant mass of the string pieces is large enough.

The $\mathrm{q\bar{q}}$ pair produced at each string break are assigned equal and opposite momentum (p_t) transverse to the string direction of a magnitude that is controlled by a Gaussian distribution with mean zero and standard deviation σ_q. Mesons produced by the above model would then have transverse momenta given by the linear sum in p_t of their $\mathrm{q\bar{q}}$ constituents. To completely specify the energy of the meson requires also the selection of the longitudinal momentum component (p_l) along the original string direction. To see how this component is assigned, we consider the initial quark $\mathrm{q_0}$ with an energy of E_0 and total momentum of p_0 ($p_0 = (p_l)_{\mathrm{q_0}}$, $(p_t)_{\mathrm{q_0}} = 0$). By defining the variable[2],

$$W_{+0} = E_0 + p_0 \tag{4.1}$$

the longitudinal kinematics of the primary or 'first-rank' meson $\mathrm{q_0\bar{q}_1}$ are then given

[2]Use of the light cone variable, $W_{+/-}$, instead of for example E or p_l separately, ensures that the fragmentation process is Lorentz invariant.

by,

$$W_{+1} = (E + p_l)_{q_0\bar{q}_1} = z_1 W_{+0} \tag{4.2}$$

where the fraction z_1 is chosen randomly from a probability distribution $f(z)$, termed the *fragmentation function.* This procedure then leaves a fraction, $(1-z)\,W_{+1}$, to be taken by the q_1 parton which may itself form part of a second rank meson $q_1\bar{q}_2$ (see figure 4.3) whose share of the available longitudinal momentum, z_2, would again be chosen at random from exactly the same fragmentation function. Since this

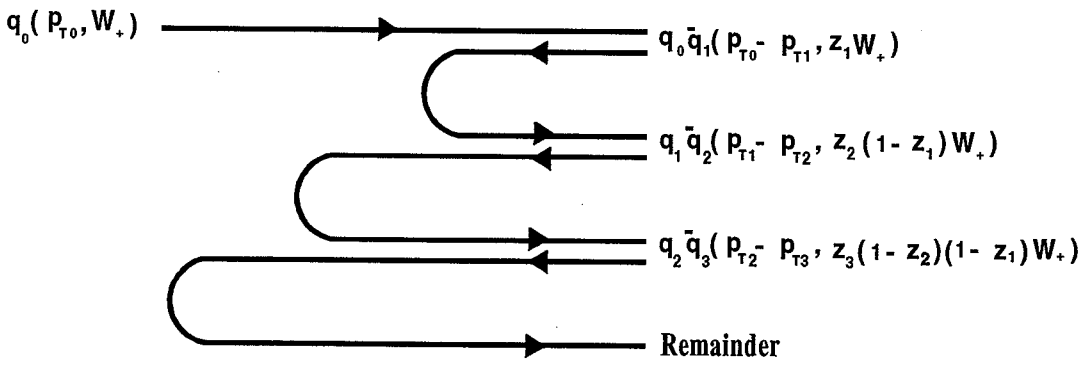

Figure 4.3: The iterative sharing of energy and momentum in the Lund-string fragmentation model.

fragmentation scheme must be independent of which end of the string the process begins at, the string breaking process is chosen at random to happen at either end with equal probability. The procedure described here continues until the situation arises where, just after a string break, the mass of the remaining string segment falls below a certain cutoff value. At this point it is decided that at the next string break two final hadrons will be produced rather than the usual hadron plus remainder of the fragmenting system.

JETSET fragmentation pulls quark pairs (i.e. $q_1\bar{q}_1, q_2\bar{q}_2, \ldots$) from the vacuum in the ratio $u\bar{u} : d\bar{d} : s\bar{s} = 1 : 1 : 0.3$. Thus there is no production of c or b quarks from the fragmentation process.

Within the Lund model, two types of fragmentation function were used depending on the flavour of the generated quark pair. For light quarks (u,d,s) a function

first proposed by the Lund group [54] was made:

$$f(z) \propto \frac{(1-z)^a}{z} \exp\left(\frac{-b\,m_t^2}{z}\right) \tag{4.3}$$

This function has essentially two free, but highly correlated, parameters 'a' and 'b' and varies with the transverse mass (m_t) of the hadron produced [3]. The correlation means that in practice only one of the parameters need be adjusted (in our case 'a') when determining the optimum value that best describes the data. The value chosen for the parameter σ_q, associated with the assignment of transverse momentum, was made also by tuning JETSET to OPAL data and is described in [57]. The values selected for these parameters are presented together in Table 4.2.

Theoretical predictions and now a wealth of experimental evidence supports the fact that fragmentation functions used for heavy (c and b) quarks should peak at larger z values than is the case for light quarks i. e. they show a 'harder' fragmentation. That this should be the case is naively explained if one considers attaching a light quark $\bar{q}_1$ to a heavy quark q_0. The large mass difference means that the lighter quark will decelerate the heavier by only a relatively small amount during the fragmentation process and so the meson combination $q_0\bar{q}_1$ will carry almost the full energy of q_0. For heavy quarks the fragmentation function chosen was that proposed by Peterson et al. [59]:

$$f(z) \propto \frac{1}{z[1-(1/z)-\epsilon_q/(1-z)]^2} \tag{4.4}$$

This choice has the advantage of having only one free parameter, ϵ_q, for each heavy flavour q.

Values for ϵ_q were chosen so as to be consistent with recent OPAL results. From a study of $D^{*\pm}$ production [60] OPAL has measured the quantity,

$$\langle x_E \rangle_{c\to D^*} = 0.52 \pm 0.03(\text{stat.}) \pm 0.01(\text{syst.})$$

where $\langle x_E \rangle_{c\to D^*} \equiv E_{D^*}/E_{beam}$. Assuming that (within the measurement errors), this result holds for the fragmentation of a charm quark into any charm hadron we can convert this result into a value for ϵ_c with the aid of Monte Carlo (see Figure 4.4). We obtain a value $\epsilon_c = 0.037^{+0.033}_{-0.021}$ where the error corresponds to conservative limits given the measured uncertainty on $\langle x_E \rangle_{c\to D^*}$.

OPAL has also made a detailed study of bottom quark fragmentation by utilising the momentum spectra ($p(\mu)$ and $p_t(\mu)$) of muons from semi-leptonic B meson decay [61]. This analysis uses JETSET as described with the fragmentation function of equation 4.4 for heavy flavours to produce distributions of $p(\mu)$ and $p_t(\mu)$ as

[3] $m_t^2 = m_0^2 + p_t^2$, where m_0 is the rest mass.

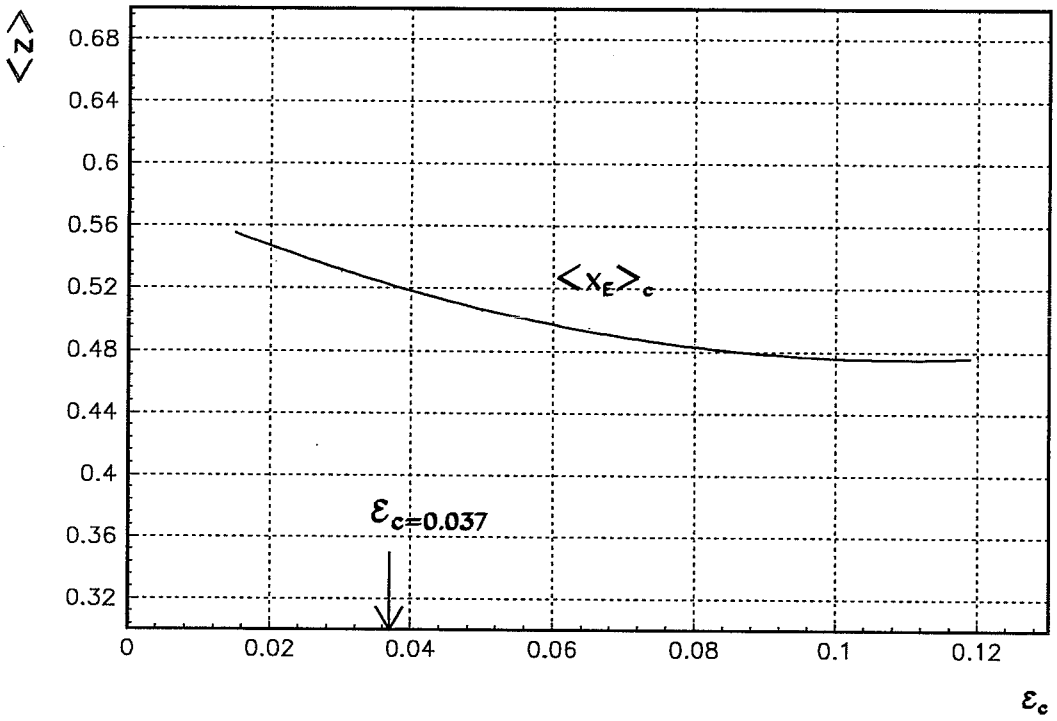

Figure 4.4: The variation of $\langle x_E \rangle$ for the first rank hadron produced in c quark fragmentation as a function of the Peterson-function parameter (ϵ_c). The value for ϵ_c chosen for use in the Monte Carlo is indicated. Adapted from [62].

a function of some suitably defined fragmentation variable. Then by fitting the $p(\mu)$ against $p_t(\mu)$ spectrum to the equivalent distribution in data, a value for ϵ_b that best describes the data is obtained.

Figure 4.5 shows how $\langle z \rangle$ and $\langle x_E \rangle$ (calculated for the first rank hadron in each case), vary as functions of the fragmentation parameter ϵ_b. Having derived $\langle z \rangle$, from a fit to the $p(\mu)$ against $p_t(\mu)$ spectrum, the Monte Carlo can be used to express the result in terms of variable x_E:

$$\langle x_E \rangle_b = 0.726 \pm 0.007(\text{stat.}) \pm 0.022(\text{syst.})$$

Using Figure 4.5 this result translates into a value for the Peterson parameter of $\epsilon_b = 0.0035^{+0.0045}_{-0.0025}$. This value was subsequently used to describe the fragmentation of b quarks with the fragmentation variable defined according to Equation 4.2. Figure 4.6 shows the shape of the Peterson function for the heavy flavour parameter values chosen.

In the Lund model gluons are treated as energetic kinks in the string that stretches between the quark and antiquark as illustrated in figure 4.7. For events where hard acollinear gluon Bremsstrahlung has taken place, the gluon will itself initiate a jet of hadrons by the string breaking on either side of the kink with the associated production of $q\bar{q}$ pairs. This then leaves effectively colour singlet systems

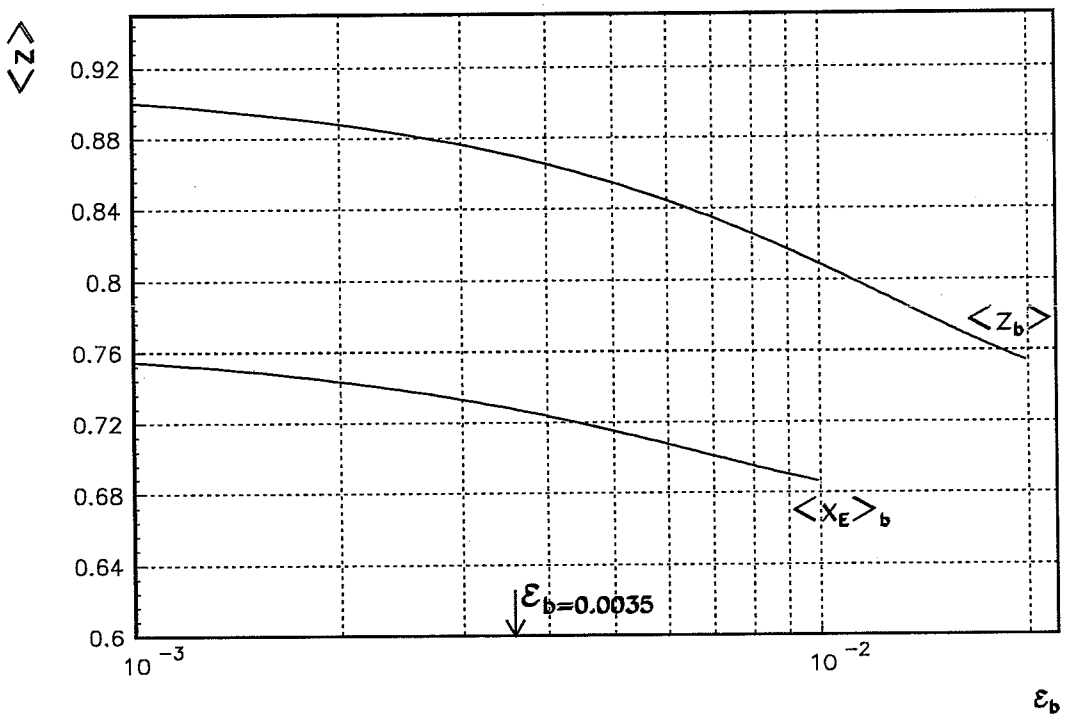

Figure 4.5: The variation of $\langle x_E \rangle$ and z for the first rank hadron produced in b quark fragmentation as a function of the Peterson-function parameter (ϵ_b). The value for ϵ_b chosen for use in the Monte Carlo is indicated. Adapted from [62].

that can fragment separately in the way described above. In the case of soft gluon emission, the gluon tends to be decelerated by the tension in the string and loses its energy before any breaks develop. The fragmentation of the system then proceeds as for a two jet event with the effect of the gluon being to introduce an acollinearity, and hence p_t, into the $q\bar{q}$ system.

Figure 4.7 illustrates the absence of a string directly connecting the quark and anti-quark in the case of a gluon also being present. A consequence of this is that the Lund model will generate a larger number of fragmentation products between quark-gluon or antiquark-gluon jets than between the quark-antiquark jets. This is commonly known as the 'string effect' and the predictions from JETSET are found to be in good agreement with measurements (e. g. from OPAL [67]). Note that an asymmetry of this kind between jets is also a consequence of soft gluon coherence mentioned in section 4.2.2.

A complication to the above picture of meson production from the string model is the production of baryons. In JETSET a baryon can be produced by one of two mechanisms with equal probability: The first works by simply replacing the production of a quark-antiquark pair at a string break with the production of an diquark-antidiquark pair i. e. $q_0 \rightarrow \bar{q}_1\bar{q}_2 + q_0q_1q_2$ (in the same numbering scheme as

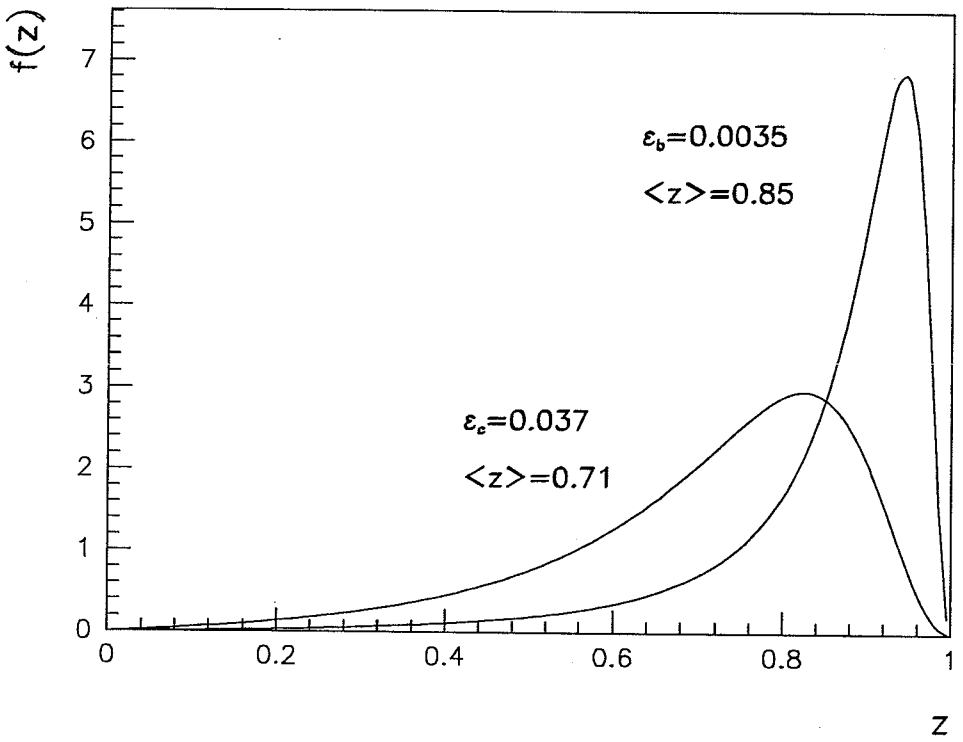

Figure 4.6: The form of the Peterson et al. fragmentation function for values of ϵ_c and ϵ_b chosen for the generation of JETSET events.

used in figure 4.3). Hence baryon-antibaryon pairs are produced in a directly analogous way to that of mesons seen earlier. Parameter values associated with diquark production are listed in table 4.3. The second mechanism [53] allows fluctuations in the colour field between the initial quark pair causing quark pairs to 'pop-out' one pair at a time from the field. If two such pairs appear both with colour charges different from one another and from the initial pair then a baryon-antibaryon pair can form.

4.2.4 Heavy Flavour Particle Content

Both the pseudoscalar and vector meson multiplets are contained in the Monte Carlo together with the 'octet' and 'decuplet' baryon multiplets.

In $Z^0 \rightarrow c\bar{c}$ events the production ratio of vector to pseudoscalar mesons present in JETSET is 3:1 (see Table 4.3). This results in charmed hadrons being present in the proportions D^0: D^+: D_s^+: Λ_c= 55 : 25 : 12 : 8, where Λ_c represents all charmed baryons. The excess in D^0 mesons is not due to any asymmetry in creating $u\bar{u}$ and $d\bar{d}$ pairs from the vacuum but rather an asymmetry in the decay of vector D mesons into charged and neutral pseudoscalar states. The charged vector meson decays into both neutral and charged states with equal probability. The decay of the D^{*0} meson into a $D^+\pi^-$ final state is however kinematically forbidden, leaving it

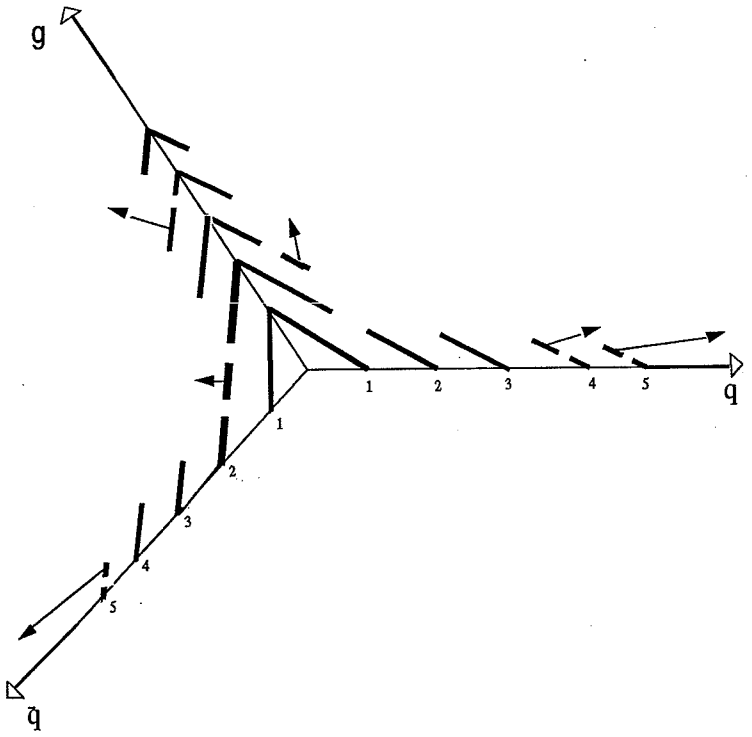

Figure 4.7: The development of a fragmenting quark-antiquark-gluon system in the Lund model. The numbers indicate increasing time slots in the evolution and the direction and magnitude of final state hadrons are indicated by the arrows.

to decay 100% of the time into a $D^0\pi^0/\gamma$. The relatively low rates of D_s^+ and baryon production are the result of the suppression (see Table 4.3) of strange quarks and diquarks from the vacuum.

For the B sector, JETSET again sets a vector to pseudoscalar ratio of 3:1 but there is no associated enhancement of B^0 production. Vector B mesons are assumed to decay electromagnetically since the vector-pseudoscalar mass difference is thought to be ~50 MeV. Hence the sign-changing process, $B^* \rightarrow B\pi^\pm$ is strictly forbidden. The subsequent proportions of bottom hadrons given by JETSET are B^0: B^+: B_s^0: Λ_b= 39.5 : 39.5 : 12.0 : 9.0, with Λ_b representing all b-flavoured baryons. The relatively low proportion of B_s^0 and Λ_b is again due to the suppression associated with pulling strange quarks and diquarks from the vacuum.

4.2.5 Heavy Flavour Decay - EURODEC

Before being forced to decay, B and D hadrons are tracked in the detector volume to distances dictated by their assigned mean lifetimes. Table 4.4 lists the lifetimes of all heavy flavour hadrons in the Monte Carlo that are assigned values different from zero.

The decay of all hadrons containing a c or b-quark was performed by interfac-

JETSET Name	Value	Parameter Definition
PARJ(2)	0.3	s:(u or d) quark-production ratio in the colour field
PARJ(1)	0.1	Diquark:quark production ratio in the colour field
PARJ(3)	0.4	Extra suppression of strange diquark production
PARJ(4)	0.05	Spin 1 diquark suppression factor
PARJ(11)	0.5	Probability that a light meson (containing u,d quarks only) formed in fragmentation, has spin 1
PARJ(12)	0.6	Probability that a strange meson has spin 1
PARJ(13)	0.75	Probability that a charm or heavier meson has spin 1

Table 4.3: Values of JETSET parameters specifically relating to fragmentation.

ing the JETSET algorithm to the EURODEC package [66] which contains a more comprehensive treatment than the default.

The philosophy behind the EURODEC approach to particle decays is to firstly calculate a maximum phase space weight based on the particle masses present for the decay mode in question. The momenta of the decay products are then distributed according to the phase space available. With the decay kinematics now fixed, and for the case of three-body modes only, the matrix element-squared is calculated based on a V-A weak decay matrix when dealing with pseudoscalar decays and a pure vector current element for use with vector particles. The matrix element-squared then introduces an additional contribution to the weight and all elements are normalized so as to ensure their maximum weight never exceeds one. Two-body heavy flavour decays are treated according to pure phase space with the decay branching fractions taken largely from experimental data.

For the case of charm decays, the maximum allowed number of particles in the final state is three and approximately 22% of the D^+ and 39% of the D^0 decays are two body modes. About 90% of the exclusive decay modes of the D^0 and D^+ are now known and that EURODEC reproduces well both the exclusive and inclusive decay rates measured from the data can be seen in [66]. Further, Figures 4.8(a) and (b) show that the charged particle multiplicity from D-meson decay is also adequately reproduced by the EURODEC prescription for decays.

Particular attention has been paid in EURODEC to ensure accurate modelling of the semi-leptonic momentum spectrum from B decays. The inclusive semi-leptonic branching fraction is set to 11.6% and the kinematics for the process $B \rightarrow D(D^*)\ell X$ are assigned according to the weak matrix element. Figure 4.9(a) compares the predicted electron spectrum from B decays at rest with CLEO data taken at the $\Upsilon(4S)$.

Particle	P. D. G. Lifetime (ps) [15]	Monte Carlo Input (ps)
D^0	0.42 ± 0.08	0.43
D^+	1.07 ± 0.02	1.07
D_s^+	0.45 ± 0.03	0.44
Λ_c^+	$0.19^{+0.2}_{-0.1}$	0.18
Ξ_c^+	$0.30^{+0.1}_{-0.06}$	0.43
Ξ_c^0	$0.08^{+0.06}_{-0.03}$	0.43
Ω_c^0	-	0.43
$\langle$B hadrons$\rangle$	1.29 ± 0.03	1.30

Table 4.4: The lifetimes of heavy flavour hadrons assigned in the Monte Carlo. All B sector hadrons are assigned the same lifetime reflecting the large uncertainties presently associated with attempts to measure specific B-hadron lifetimes (see Section 6.1.2). The mean D-hadron lifetime from these numbers, weighted by the relative abundance of D-hadron species present in JETSET, is 0.52 ps.

Approximately 62% of the B decay modes are modelled as two and three-body decay final states. The remaining 38% are decayed according to $B \rightarrow D(\text{or } D^*)\bar{u}d$, where the quarks are allowed to fragment so forcing the total multiplicity in the final state to be larger than three. The production ratio D^0:D^+ from B decays of 63.4:28.8 reproduces well the experimental data (see Table 4.5) and Figure 4.9(b) shows that the main features of the D^0 momentum spectrum from B decay are also well modelled. This is true also for D^+ mesons (not shown).

Inclusive decay mode	EURODEC Branching Ratio (%)	Experiment (%)
$B \rightarrow D^0 X$	63.35	63.0 ± 13.0
$D^+ X$	28.78	28.0 ± 10.0
$D_s^+ X$	9.97	11.0 ± 4.0
$\Lambda_c^+ X$	7.39	7.0 ± 3.0
$J/\psi X$	1.11	1.07 ± 0.003
$\psi' X$	0.0047	0.005 ± 0.003

Table 4.5: A comparison of B exclusive decay modes as given by the EURODEC package compared to experimental data collected at the $\Upsilon(4S)$ by the ARGUS and CLEO Collaborations. From [66].

The production of D_s^+ mesons via B-meson decay can occur via the two-body channels: $B \rightarrow DD_s$, D^*D_s, DD_s^*, $D^*D_s^*$ with 50% probability and the rest of the spectrum described by decays of the type: $B \rightarrow D_s X$ (X – multiplicity ≥ 2), $D_s DX'$

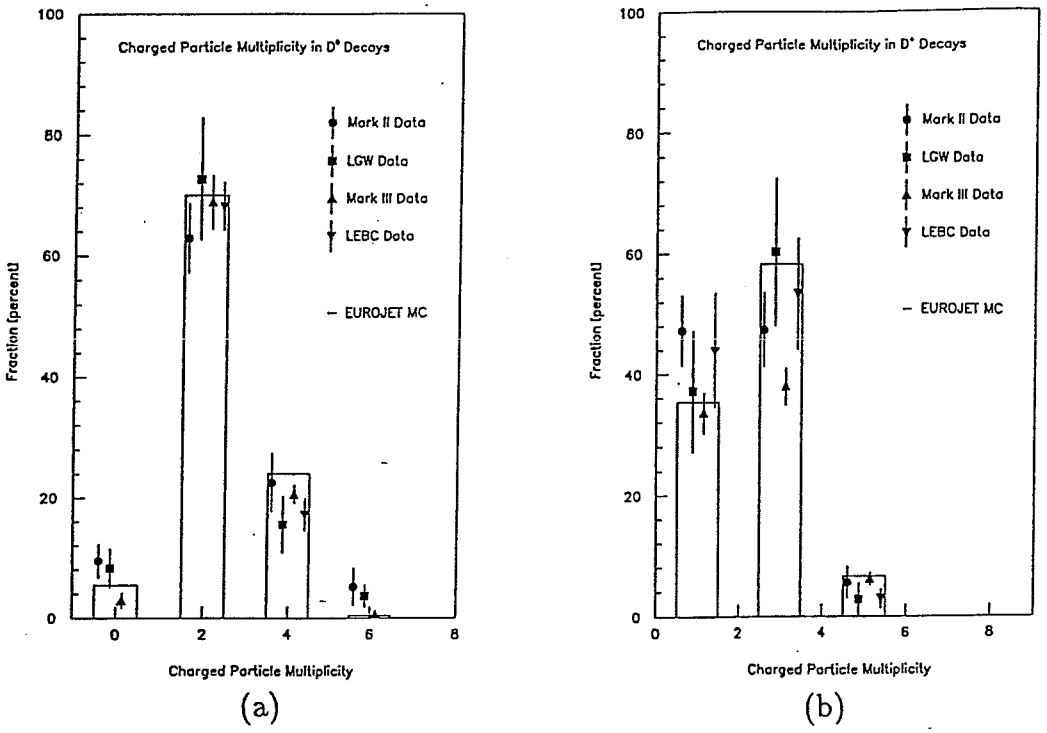

Figure 4.8: EURODEC D-decay multiplicity predictions compared to experiment for: (a) D^0 decay and (b) D^+ decay.

where the D_s and D may be either a pseudoscalar or vector meson. The phase space suppressed mode $B \rightarrow D_s D_s X$ can also contribute. Table 4.5 shows that the resulting inclusive rate to D_s from EURODEC is in good agreement with experiment representing a marked improvement on the JETSET approach (which agrees with experiment only within a factor two for this branching fraction). In addition, Figure 4.9(c) shows that within the errors, the predicted D_s^+ momentum spectrum is consistent with the measurements of ARGUS and CLEO.

B decays to charmed baryons are implemented with an overall rate of 9%. Table 4.5 shows that over 7% accounts for Λ_c production but decays via Σ_c^0 and Ξ_c^0 also contribute.

Figure 4.9(d) presents the charged particle multiplicity in $b\bar{b}$ events as measured by CLEO at the $\Upsilon(4S)$. The EURODEC prediction is shifted to higher values in this comparison (mainly because the data are uncorrected for detector efficiency) but the overall shape of the distribution is reasonably well modelled. The mean charged multiplicity from B decay seen in our Monte Carlo sample is 5.27. This number can be compared with care to measurements at the $\Upsilon(4S)$ ranging from, $5.5 \pm 0.03 \pm 0.15$ CLEO (1982) [63] to $5.75 \pm 0.10 \pm 0.10$ CLEO (1986) [63], which include contributions from Λ and K_s^0 decays.

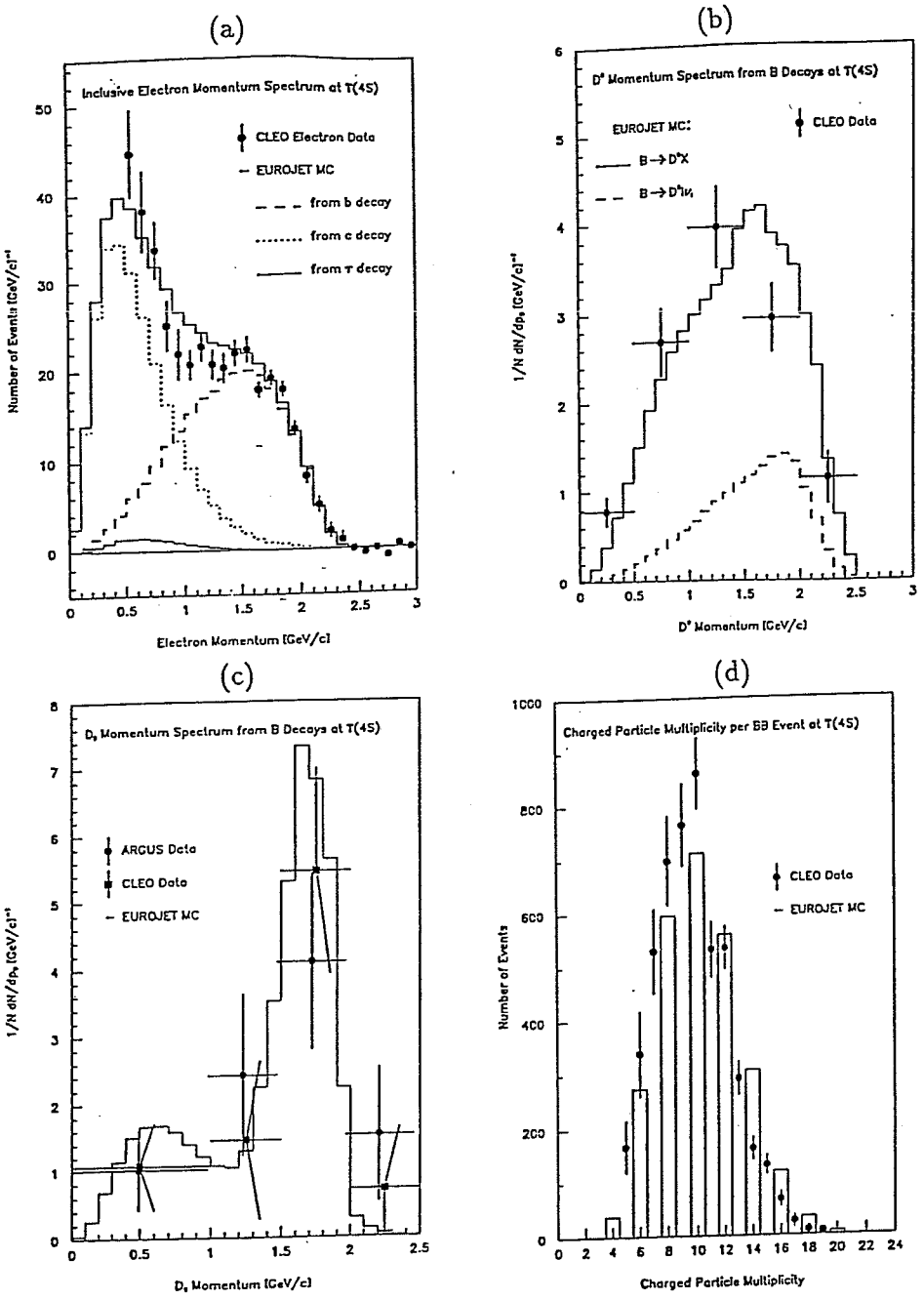

Figure 4.9: Some EURODEC B-decay predictions compared to CLEO and ARGUS measurements: (a) The inclusive electron momentum spectrum at the $\Upsilon(4S)$, (b) The inclusive D0 momentum spectrum from B decay, (c) The inclusive D_s^+ momentum spectrum from B decay, (d) The charged particle multiplicity distribution per $B\bar{B}$ event at the $\Upsilon(4S)$.

4.3 Simulating The OPAL Detector

4.3.1 GOPAL

The OPAL Monte Carlo program GOPAL [64] provides the framework inside which all aspects of data simulation are performed producing as output a copy of the OPAL raw data structure. For our purposes GOPAL provides the interface to the JETSET event generator and 'tracks' the resulting particles, using the GEANT3 package [65], through sensitive volumes representing the various components of OPAL with realistic descriptions of the many materials and tracking media present.

The tracking stage essentially comprises storing the position and momentum of particles as they traverse sensitive volumes and is very c.p.u.-intensive. The majority of the time is spent tracing the development of electromagnetic showers in the lead glass calorimetry. Because of this the Monte Carlo data produced specifically for the present analysis is based on the charged track information of the Central Detector only.

When the GEANT tracking is complete GOPAL enters the digitization phase where the track hits that go to form the raw data are produced based on a simulation of the detector response. The modelling of the Vertex Chamber response is dealt with in detail in the next section. The various aspects taken into account when modelling the Jet Chamber response include:

- Drift time resolution as a function of drift distance and track angle, which determines the spatial precision attainable in the $r - \phi$ plane.
- The charge resolution, which determines the precision of the z coordinate and of the $\mathrm{d}E/\mathrm{d}x$ measurement. The effects of saturation, cross-talk, attachment, anode wire stagger etc. are addressed.
- Noise in the chamber, either correlated with hits (e. g. pulse splitting) or uncorrelated (e. g. synchrotron radiation).
- Resolution degradation of multiple hits on wires.
- Resolution degradation due to the effects of δ-rays produced below the threshold for simulation.
- General detector inefficiencies.

The output of the digitization comprises values of drift time, z and charge which essentially mimic the output of the sub-detector online data acquisition system. The final step in the simulation process is then the reconstruction of the event by ROPE i. e. exactly the same reconstruction chain as that used for data and utilising the same calibration constants.

4.3.2 Modelling the Vertex Chamber Response

The accurate modelling of the response of a drift chamber to the passage of charged tracks, especially in a dense jet environment, is a complex task. This section describes an attempt to improve and extend all aspects of reproducing the Vertex Chamber raw data, deemed necessary before any physics analyses dependent on CV information could proceed.

Unless explicitly stated in the following, all reference to tracks implies track segments reconstructed internal to the Vertex Chamber using the CV processor (as described in Chapter 3). The version number from which the results of this investigation take effect is GOPAL126 and earlier version numbers represent previous iterations of detector simulation.

Wire Noise

We define wire noise in the chamber to be, for any wire, the mean number of hits per event that are unassigned to a track fit. The probability per wire per beam crossing is found from a data sample of random beam crossings [4]. To accurately model the variation of noise with radius through the chamber, separate noise levels for each radial wire plane in CV were implemented i. e. 18 separate noise levels. The agreement between data and Monte Carlo for the level of unassociated hits in events with 'physics' triggers is shown in Figure 4.10.

First Hit Properties

To find the chamber efficiency for first hits on wires, we used two different measures. The first, termed the 'counting' efficiency, takes tracks in CV formed entirely from first hits and asks which hits are missing from those expected, given the start and end point of the track. In this way an efficiency for each wire, except those at the inner and outer radius of each axial and stereo sector, can be formed. The second method, termed the 'swimming' efficiency, is based on tracing an identified track through the cell and determining if a given wire would reasonably be expected to register a hit on the track. An efficiency is then derived from the number of cases where the expectation is fulfilled.

As for the case of noise levels, the capability to set different first-hit efficiencies for each radial wire plane was introduced. This was necessary in particular to model the degradation in efficiency around the first wire in axial sectors. The efficiency one finds for muon-pair data from the counting or swimming method is higher by on average 1-2% than that seen in multi-hadronic tracks formed from first hits on wires.

[4] i. e. a data sample originating from random beam crossings for which the trigger decision was ignored.

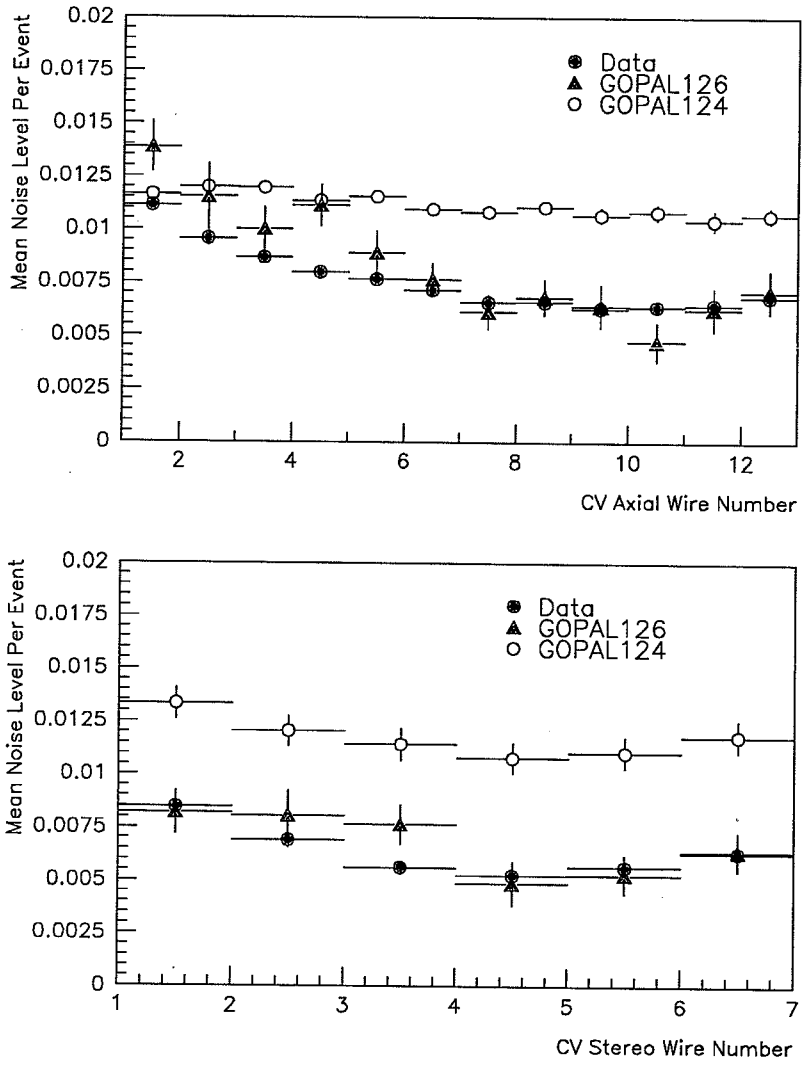

Figure 4.10: The noise level in CV as found from unassociated hits. The data are muon-pair events from 1990 and the Monte Carlo generator is KORALZ.

This discrepancy is believed to be due to increased coherent noise effects associated with the dense track environment of multi-hadronic events. It has not been possible to understand and model such effects in the time available and so a compromise first hit efficiency value of 96.7% was chosen for the axial sectors for all wires except the first, where a degraded efficiency of 96.5% is preferred. In stereo, all evidence suggests a slightly higher efficiency of 97.5%. Figure 4.11 plots both the swimming and counting efficiency as a function of CV wire number for multi-hadronic events.

In order to model the intrinsic resolution for hits, residuals to track fits made using only first hits on wires were studied. The resolution as a function of drift distance d is parameterised in terms of: the 'best' resolution, σ_{min}; the drift distance at which this resolution is achieved, d_{min}; the factor by which the resolution is degraded at the anode, f_{anode}; and the factor by which resolution is degraded at the

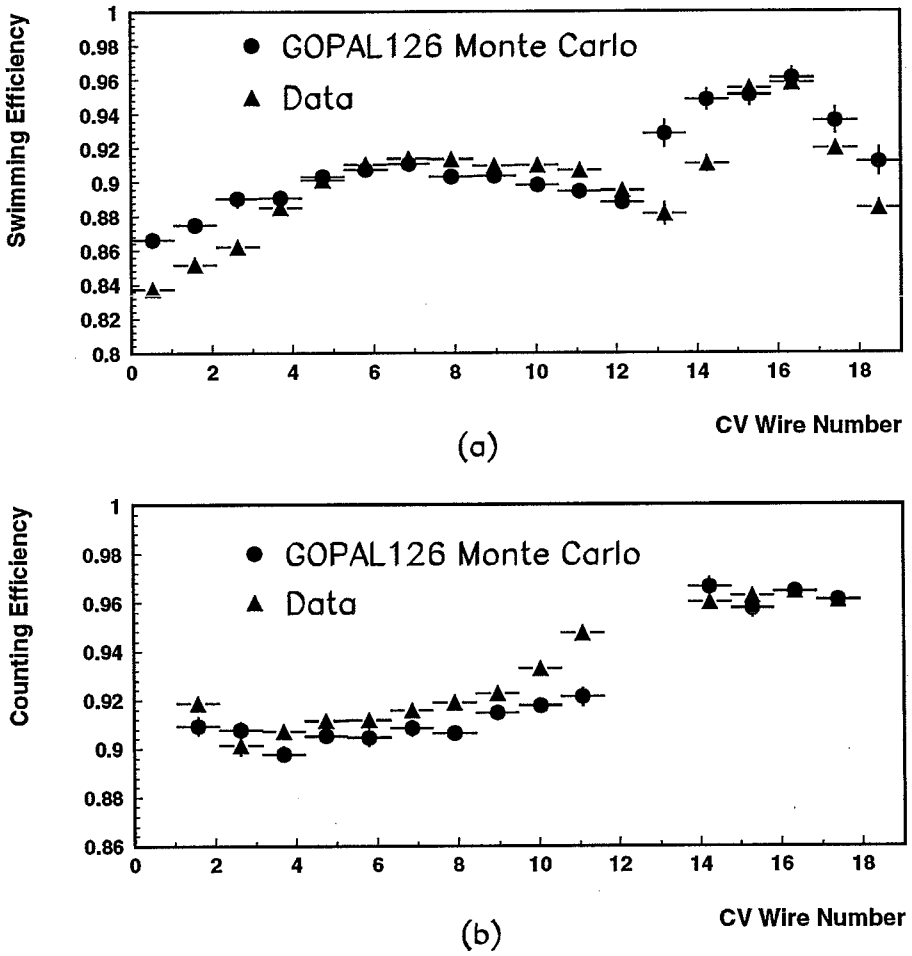

Figure 4.11: The variation of CV hit efficiency as a function of wire number based on (a) a swimming method and (b) a counting method for multi-hadronic events.

cathode, $f_{cathode}$. For drift distances less than d_{min} the resolution is then given by:-

$$\sigma = \sigma_{min}\left[1 + \left(\frac{d_{min} - d}{d + \frac{d_{min}}{(f_{anode}-1)^{0.4}}}\right)^{2.5}\right] \tag{4.5}$$

while for drift distances $d > d_{min}$,

$$\sigma = \sigma_{min}\left[1 + f_{cathode}\left(\frac{d - d_{min}}{d_{max} - d_{min}}\right)\right]. \tag{4.6}$$

In the above, d_{max} is the drift distance to the cathode, and is taken to be 1.5 cm. The form of this function is displayed in Figure 4.12. The first-hit residual resolution is shown in figure 4.13 (as a function of drift distance) for multi-hadronic data and compared to both the present simulation and a previous iteration of CV modelling.

All CV first-hit GOPAL parameters are collected together in Table 4.6.

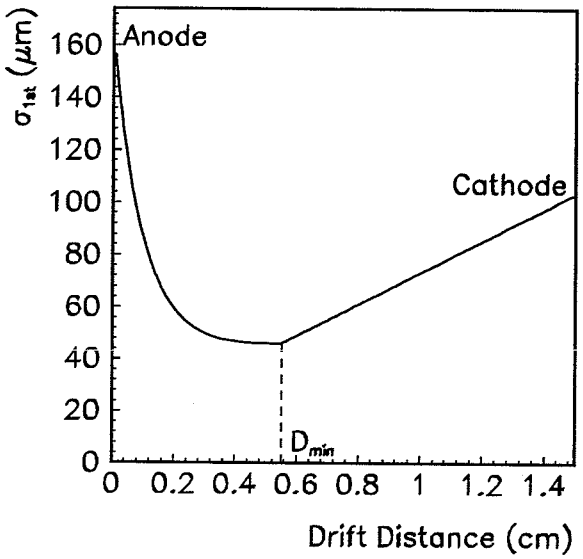

Figure 4.12: The resolution function for first hits on CV wires implemented in GOPAL. The function shown is based on parameter values valid for axial sectors.

	Axial Sectors	Stereo Sectors
Hit Efficiency (wire 1 only)	96.7 (96.5)%	97.5%
Minimum Timing Resolution	1.15 ns	1.40 ns
Position of Resolution Minimum, d_{min}	0.55 cm	0.55 cm
Anode Degrading Factor, f_{anode}	3.62	2.02
Cathode Degrading Factor, $f_{cathode}$	1.25	1.10

Table 4.6: CV first-hit parameter values for GOPAL.

Second Hit Properties

The efficiency and spatial resolution of the second of two hits drifting onto the same wire are determined from the data. The efficiency is given essentially by the measured distribution of separations in drift distance between first and second hits. Even given ideal two-hit resolution this distribution is not flat due to the collimation of tracks in jets and the geometrical properties of the cell. As described in Chapter 3, due to the intrinsic reset time of the electronics the detector is 'dead' with regard to second hits for a period of just over 40 ns leading to a 'blank-out' region. The effects of the tail of the first pulse means that the efficiency for detecting a second pulse rises over a finite distance but never returns to the full first-hit efficiency.

The shape of this 'turn-on' function is determined by dividing the hit-separation distribution seen in the data, by that expected for ideal two-hit resolution (obtain-

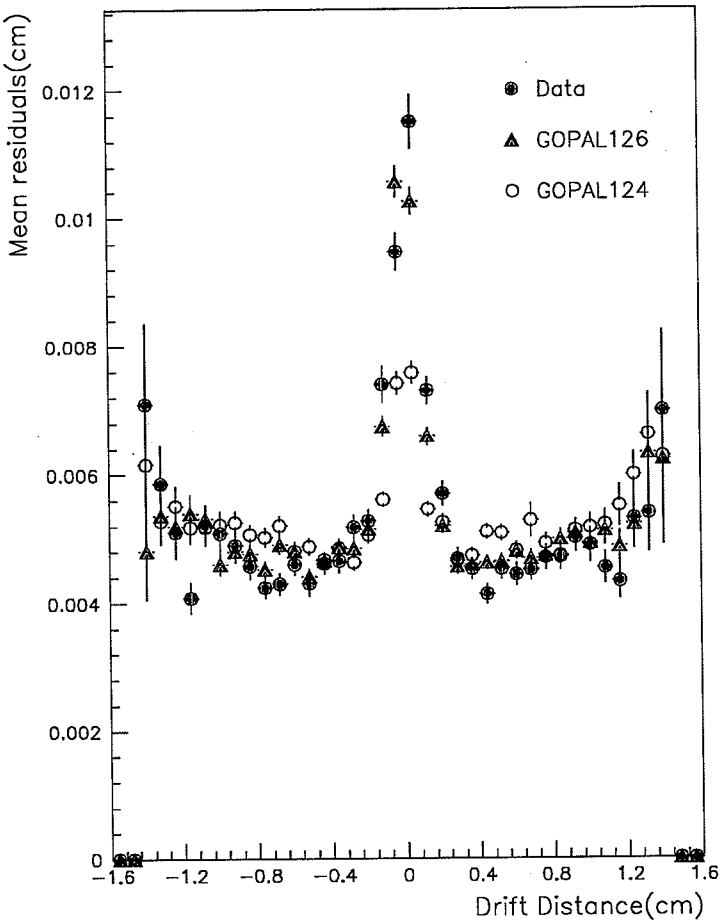

Figure 4.13: The mean residuals to CV axial fits for multi-hadronic tracks made of first hits on wires.

able from the Monte Carlo). The efficiency for registering second (or higher) hits on wires is then modelled by the implementation of the following function:

$$F_{2nd} = D_{2nd}\,(1 - exp(-(\delta - a_0)/a_1)) \tag{4.7}$$

where, a_0 and a_1 are the determined blank-out and turn-on distances respectively, D_{2nd} is the overall degradation factor in the efficiency for second hits and δ is the difference in drift distance between one hit and an earlier one. The form of this function is plotted in Figure 4.14. As a cross-check of the plateau level of the F_{2nd} function, the swimming efficiency method has been applied to tracks made exclusively of second hits. In general as the wire number increases so the hit separation also increases and the efficiencies obtained tend toward the plateau value. The asymptotic efficiencies obtained are seen to be in reasonable agreement with the values obtained directly from the 'shape' analysis described above.

A summary of all second-hit simulation parameters is given in Table 4.7.

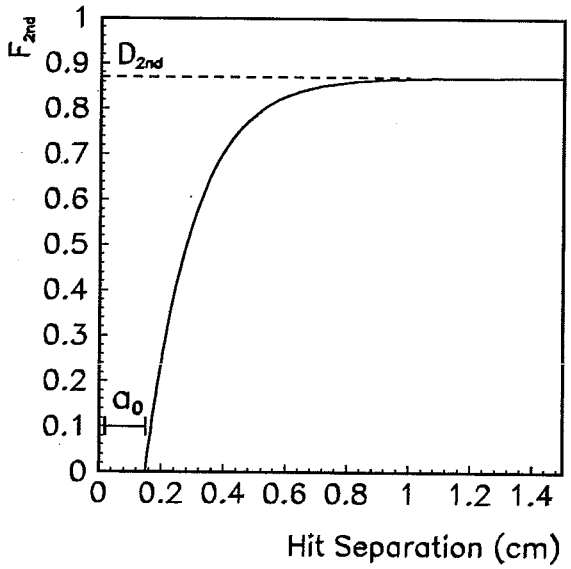

Figure 4.14: The second-hit efficiency function applied to multiple hits on CV wires in GOPAL. The function shown is based on parameter values valid for axial sectors.

	Axial Sectors	Stereo Sectors
Hit Efficiency Degrading Factor, D_{2nd}	0.87	1.00
Blank-out Distance, a_0	0.15 cm	0.17 cm
Turn-on Region, a_1	0.15 cm	0.08 cm
Resolution Degrading Factor	2.2	1.7

Table 4.7: CV second-hit parameter values for GOPAL.

The CV Contribution at the CT-Track Level

Figure 4.15 presents the distribution of CV hits on CT tracks that have been associated with CV track segments. The simulation is seen to be generally in good agreement with data largely as a consequence of modelling wire efficiencies realistically. If however we ask for the mean number of CT tracks per event that contain CV information we find,

$$N_{trk} = 10.48 \pm 0.05 \,(\text{in data})$$
$$N_{trk} = 12.81 \pm 0.05 \,(\text{in Monte Carlo}).$$

These numbers are based on multi-hadronic event samples each of 5000 events, and the tracks were required to contain six or more axial hits. Hence we see that there is an excess of more than two tracks per event in the simulation relative to the data.

A discrepancy of this kind could introduce serious differences between the sim-

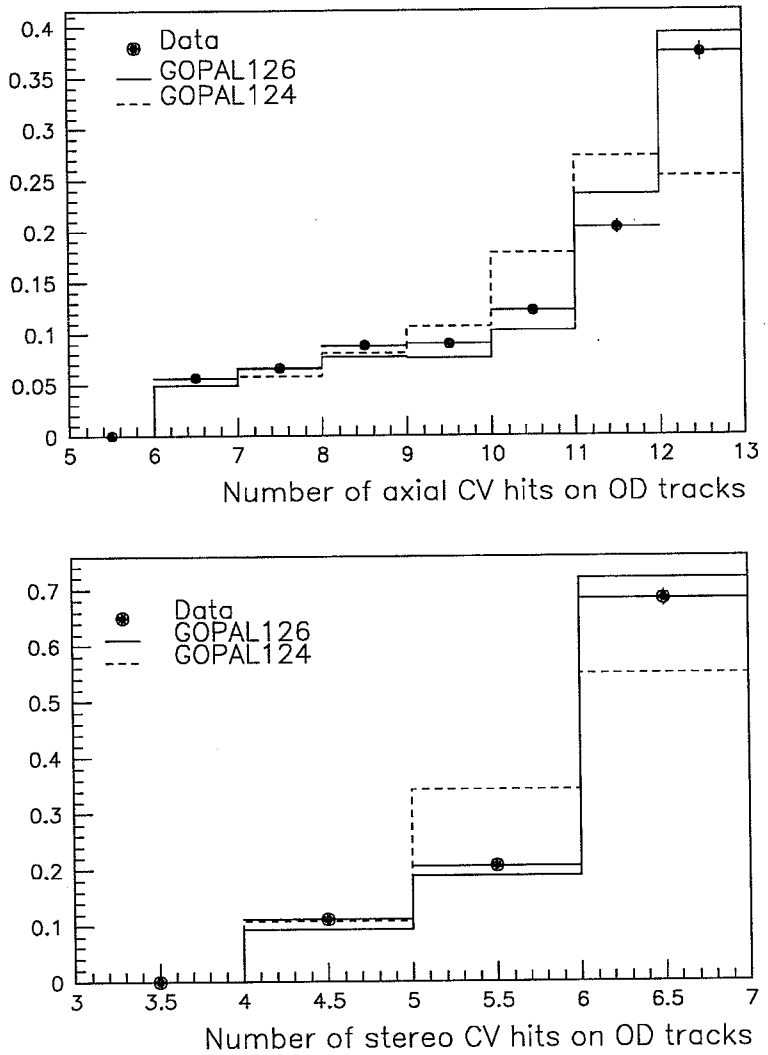

Figure 4.15: The number of CV hits from axial and stereo sectors associated with CT tracks from GPMH events. The distributions have been normalised to the same number of *tracks*. For comparison, the previous iteration of Vertex Chamber modelling (GOPAL version 124) is also shown.

ulation and data, particularly with regard to comparisons of spatial resolution. We have already seen in Figure 3.22 the significant improvement in d_0 resolution that CV information on CT tracks brings. This implies that the impact parameter resolution in the Monte Carlo might be expected, at some level, to be better than that found in the data due to there being a larger fraction of simulation tracks that contain CV information. An immediate way around this problem is to only consider tracks in both the data and Monte Carlo that contain some fixed number of CV hits. In fact, due to the improved resolution attainable we shall for the analysis presented in Chapters 5 and 6 only use CT tracks that contain six or more CV-axial hits.

A six-axial hit requirement will however result in there being, on average, about two extra tracks per simulation event relative to the data. This is again an undesir-

able situation since differences in the track multiplicity could introduce significant systematic effects between the simulation and data with regard to finding fitted vertex positions (see Chapter 6).

A study was therefore initiated to account for how the simulation was overestimating the multiplicity of CT tracks containing CV hits. Clearly this effect could be accounted for by a difference in the CV-CJ track segment matching efficiency during the CT-track making process. On the basis of the track multiplicities given on page 98, and assuming that the multiplicity of CV track segments going into the matching process are identical between data and Monte Carlo, the efficiencies would have to differ by $\sim 20\%$ to explain the effect. However as part of the study into the matching efficiency of CV information onto CT tracks (quoted in Section 3.3.2), it was found that there was at most a difference of 3% in the efficiency between data and Monte Carlo.

Further investigations revealed that the origin of the discrepancy was in the CV track multiplicity itself, where an excess of (on average) two tracks per event was measured in the simulation relative to the data. The bulk of the extra tracks were found to be due to those composed of second (or higher) hits on Vertex Detector wires. For these cases the cause was assumed to be residual second-hit effects, unaccounted for by the correction procedure described in Section 3.1.8, and which result in the CV segment no longer matching with the appropriate CJ segment. At a much lower level a similar excess was seen in tracks composed of first-hits on CV wires. In this case a likely cause are the effects of increased coherent noise in the chamber (not modelled in the simulation) associated with tracks present in a dense track environment. Possible evidence for the presence of such an effect was seen in Section 4.3.2 concerning the determination of the first-hit wire efficiencies.

As understanding and statistics improve, effects such as those mentioned above are being either corrected for in the data or at least modelled in the simulation. This however is an on-going process and for the purposes of this analysis, the CV track multiplicity excess was corrected for at the CT track level by simply stripping away tracks from the Monte Carlo to force agreement with the data. This was made possible since:

1. For subsequent analysis only CT tracks containing CV information were to be used. If this were not the case, stripping away complete CT tracks from the Monte Carlo only would result in a track multiplicity discrepancy at the CT level.

2. The 'extra' tracks were distributed uniformly across a Vertex Detector drift cell, allowing the track stripping to be performed in an unbiased way.

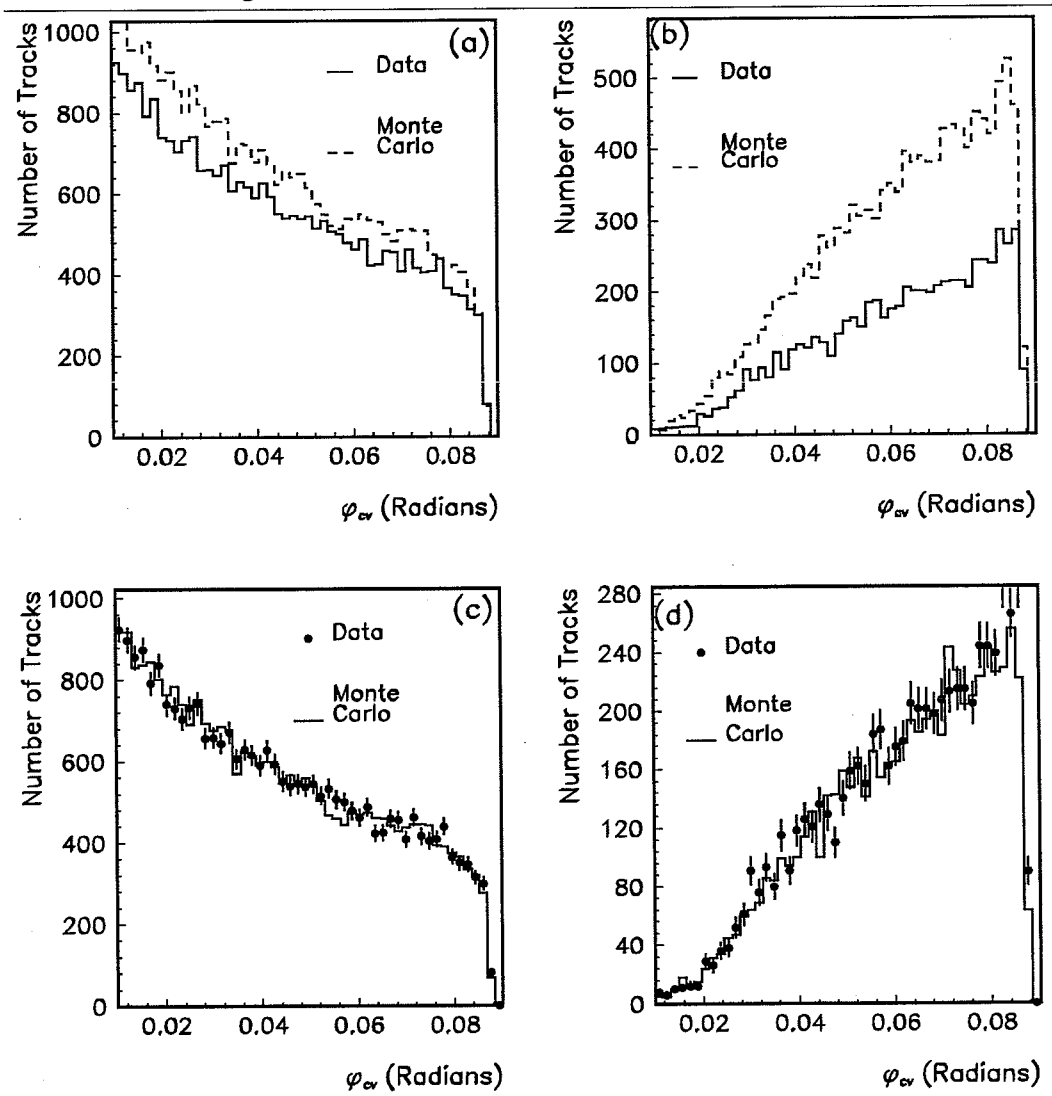

Figure 4.16: Track multiplicities as a function of the azimuthal angle to the CV anode plane for the two cases: (a) all associated CV hits are first hits on wires, (b) the CV information contains at least one multiple wire hit. Similar distributions are shown in (c) and (d) after the Monte Carlo track stripping process has been applied.

This second point is illustrated by Figure 4.16(a) and (b). Here we show distributions of CT-track multiplicities (normalised to the same number of *events*) with respect to the azimuthal angle that the track makes to the Vertex Detector anode plane [5]. The plots are made for CT tracks matched to 12 or more CV hits since at the CT level the excess was almost entirely contained in this class of track. Figure 4.16(a) is made for tracks matched to CV hits that are all first-hits on CV wires whereas the tracks that form Figure 4.16(b), contain at least one multiple CV-wire hit. Clearly the level of discrepancy is much larger for tracks containing CV multiple hits, making it necessary to perform the track stripping on the two track classes separately.

[5]This angle is defined in Section 3.1.7

A CT track was simply discarded if

$$R_{\#} < \epsilon_{1st}(\epsilon_{2nd}), \tag{4.8}$$

for $R_{\#}$ a uniform random number and where ϵ_{1st}, ϵ_{2nd}, take different values according to whether the track stripping is applied to tracks containing first-hit CV information or multiple hits. The result of this process can be seen in Figures 4.16(c) and (d), which correspond to 6.9% of all CT tracks (i.e. with *and* without CV hits) being discarded.

Following track stripping Figure 4.17 illustrates that the number of CV hits on CT tracks, when normalised to the same number of events, is in good agreement between the data and Monte Carlo. Consequently we find that the mean multiplicity

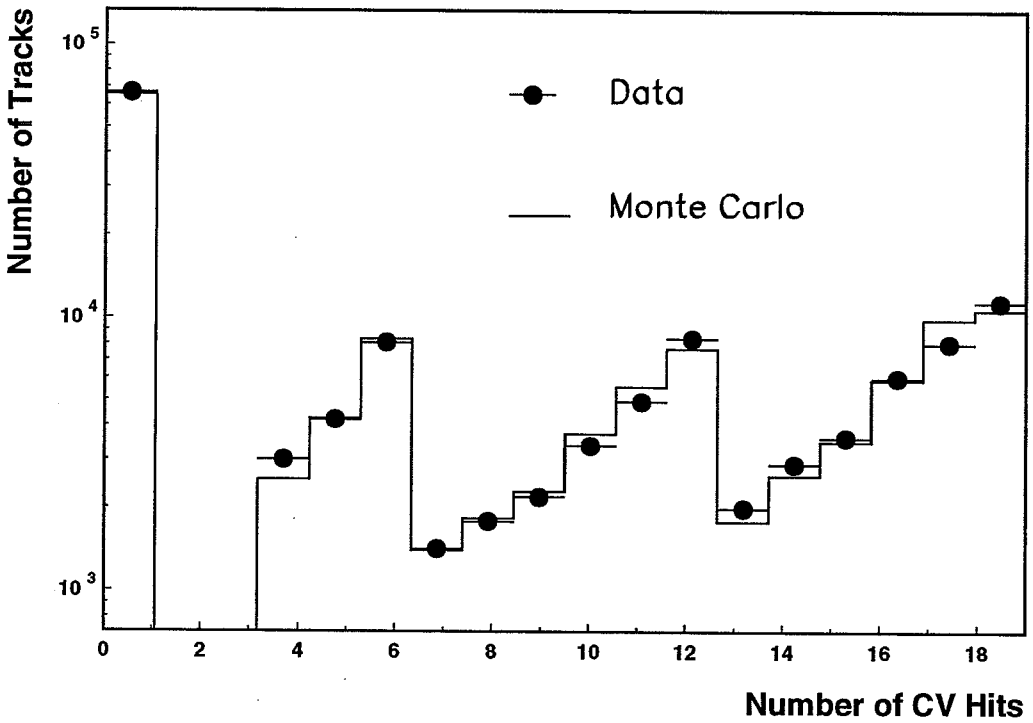

Figure 4.17: The number of CV hits associated with CT tracks. The distributions are formed from the same number of events in the data and Monte Carlo.

per event for tracks matched to six or more axial CV-hits becomes:

$$N_{trk} = 10.48 \pm 0.05 \text{ (in data)}$$
$$N_{trk} = 10.58 \pm 0.05 \text{ (in Monte Carlo)}.$$

4.4 Comparing Monte Carlo With Data

That the JETSET 7.2 event generator reproduces well the global features (as characterized by event shape variables) of Z^0 decays, is documented in [57]. We have

seen in the previous section that the multiplicity of tracks in the Vertex Detector was overestimated in the simulation due to the details of modelling detector response. A measure of the multiplicity much less sensitive to modelling inside dense track environments is given by considering the multiplicity of CT tracks (which coincides with that measured by the Jet Chamber alone). From Figure 4.18(a) we conclude that the simulation reproduces reasonably well the shape and mean of the data distribution.

Figure 4.18(b) shows the comparison plot for the variable $p_{xy} = \sqrt{p_x^2 + p_y^2}$ i. e. the momentum transverse to the z-axis. The agreement with data is seen to be good,

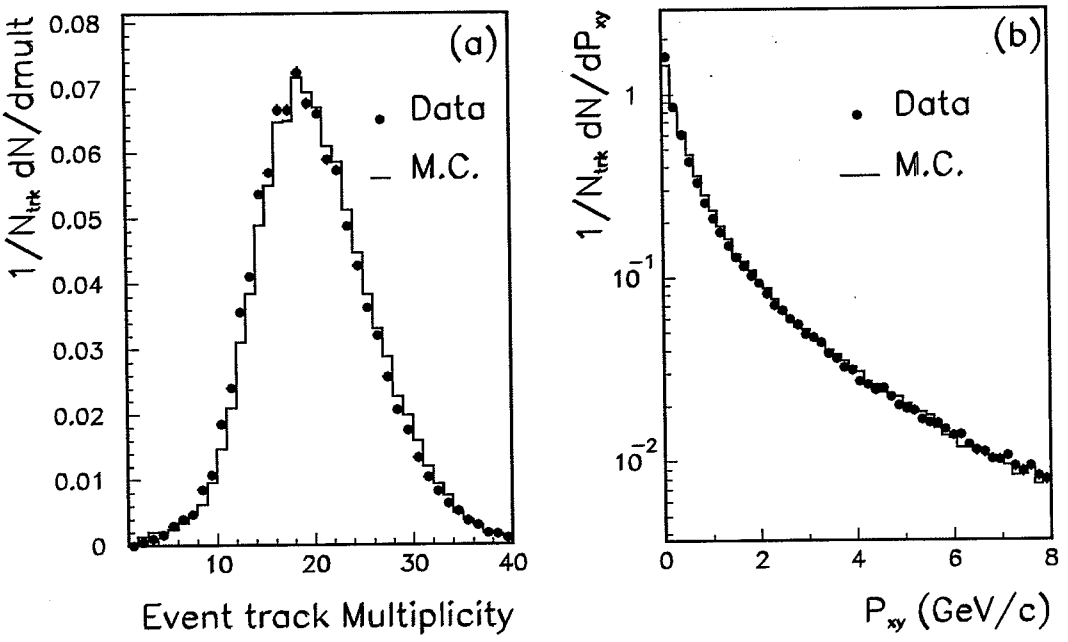

Figure 4.18: Comparing data with Monte Carlo: (a) The CT track multiplicity per event. All tracks pass a set of 'standard' quality cuts described in Section 5.2. (b) A distribution of track momentum transverse to the z-axis (p_{xy}). No track cuts are applied.

as is the transverse momentum distribution with respect to a jet axis estimate presented in Figure 5.12(b). Further, in Chapter 5 (see Figure 5.10) we find that given some definition of a jet, the Monte Carlo reproduces accurately the overall jet-rate observed in the data. Both the transverse momentum content and jet-rate of events depend directly on the details of gluon radiation. We conclude therefore that the parton shower approach of JETSET together with the tuned shower parameter values for Λ_{LLA} and Q_0, appear to adequately describe the data.

Turning now to a comparison at the track level, we have already seen from Figure 4.15 that the distribution of CV hits on tracks is quite well reproduced by the simulation. That this is also the case when considering the distribution of CJ hits associated to CT tracks can be seen in Figure 4.19.

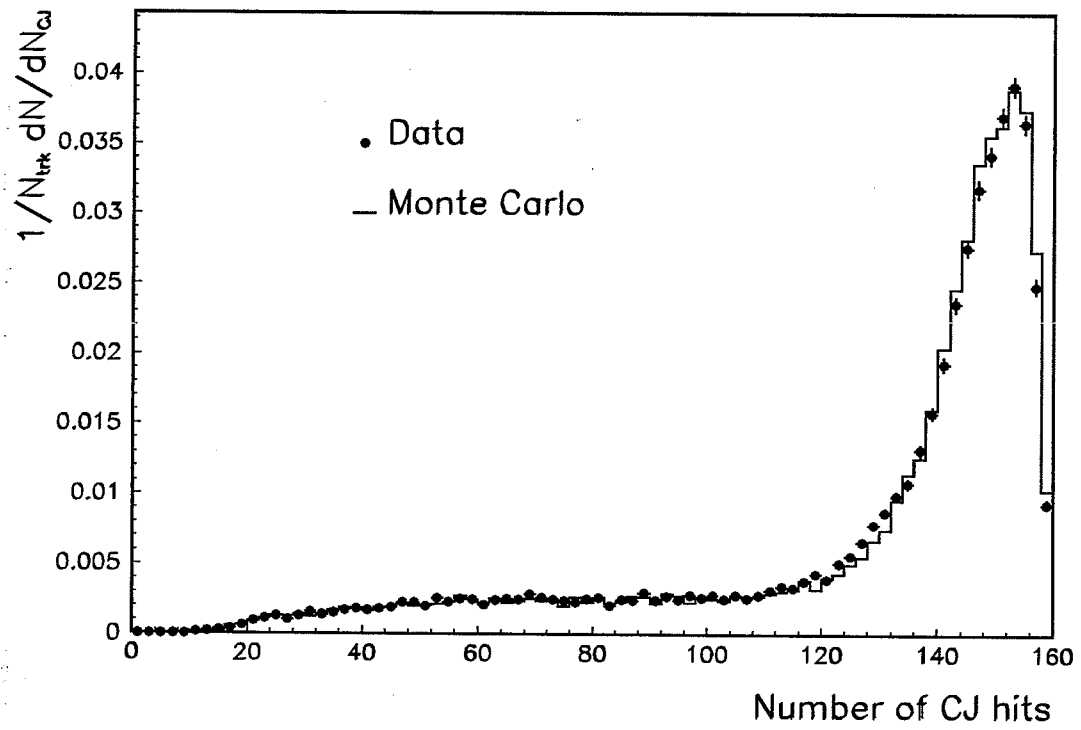

Figure 4.19: A comparison of the CJ hit distribution on CT tracks between data and Monte Carlo. All tracks contain at least 6 CV-axial hits and have $p_{xy} > 0.6\,\mathrm{GeV}/c$.

In Figure 4.20 we present the level of agreement in the three $r-\phi$ track parameters (κ, ϕ_0 and d_0) and in the track polar angle θ. The analysis presented in the following chapters, makes exclusive use of the particle tracking in the $r-\phi$ plane and so a reasonable level of agreement in these quantities is essential. The only suggestion of a systematic departure from the data distribution is in the d_0 distribution (note that a semi-log scale has been used).

The discrepancy seen between data and simulation in the d_0 distribution has important consequences for the subsequent analysis. The resolution of tracks extrapolated back to the interaction region is seen to be somewhat better in the Monte Carlo than that found in the data. A closer inspection also reveals that the fraction of tracks found in the distribution tails is underestimated in the simulation relative to the data. We find in Chapter 5 that this discrepancy filters through to affect the resolution attainable in a secondary vertex fit calculation (see Figure 5.15) and hence affects also the precision of any decay length calculation based on the vertex position (see Figure 5.17).

A good level of agreement with the simulation is clearly essential in order to extract reliable measurements of parameters, and so in Chapter 6 we make use of a 'folded' distribution to regain a good level of agreement with the data. This is made possible by the 'symmetric' nature of the discrepancy which is evident from

Figure 4.20(c).

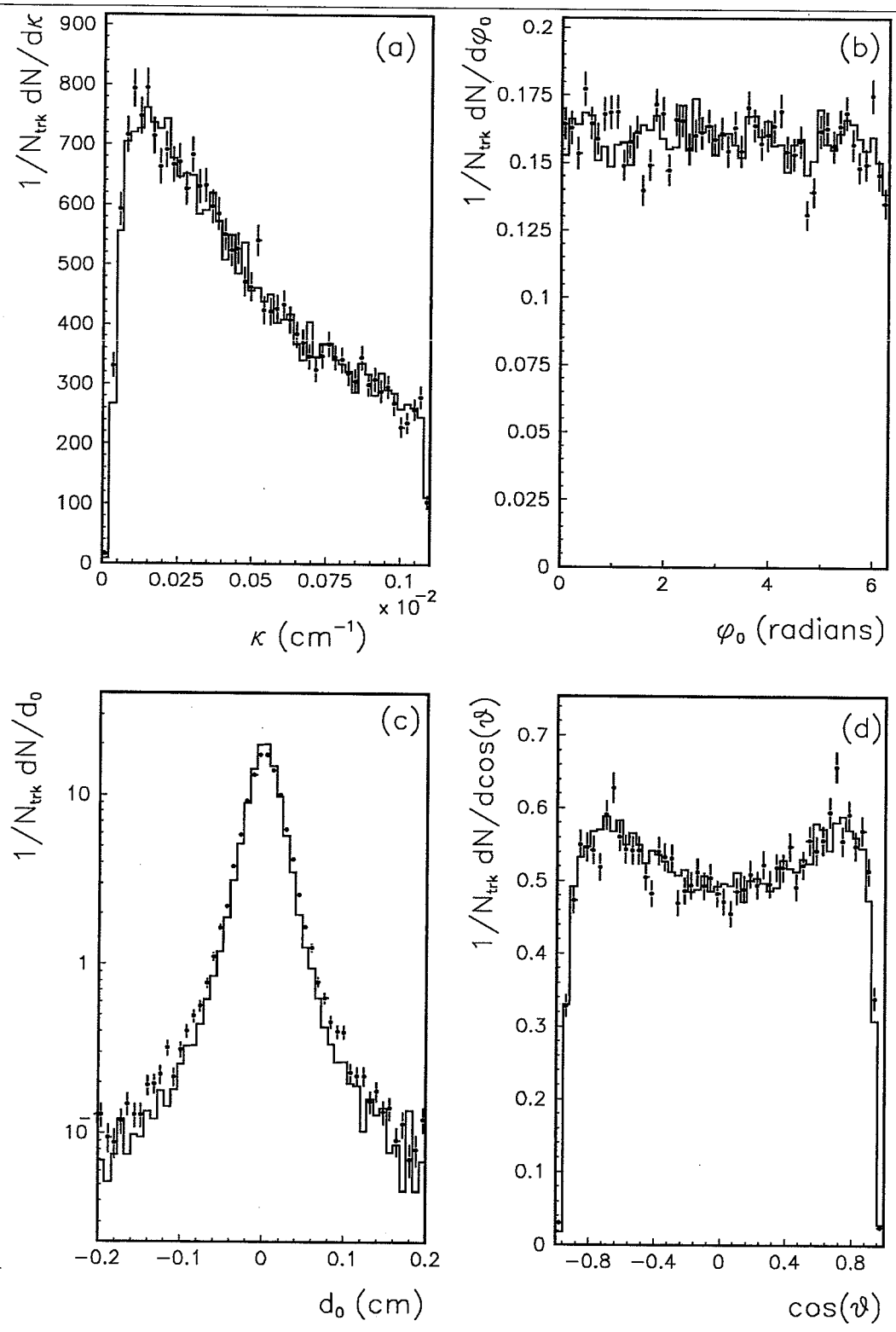

Figure 4.20: Comparing data with Monte Carlo at the track level: (a) κ the track curvature, (b) ϕ_0 the track azimuthal angle at the point of closest approach, (c) d_0 the track impact parameter corrected for the mean e^+e^- interaction position (see Section 5.3.3), (d) $\cos(\theta)$ for θ the track polar angle. In each case the data are represented by the points and the Monte Carlo data are the histogram. All tracks contain at least 6 CV-axial hits and have $p_{xy} > 0.6\,\mathrm{GeV}/c$.

Chapter 5

Tagging Bottom Events

5.1 Introduction

In order to study the physics of $Z^0 \rightarrow b\bar{b}$ decay, a way must first be found to discriminate or 'tag' these events from the background of charm and light-quark decays[1].

In this chapter we review and compare a number of tagging methods. Most of these techniques have been applied in the past at lower energy e^+e^- experiments and so emphasis is placed on the differences seen (if any) in the application of these techniques to the LEP environment. In particular, this study was initiated in order to determine a tagging method well suited to exploiting the spatial precision of the Vertex Chamber which could then be used to study details of the physics of the B-hadron.

All of the tagging techniques considered here can be split into two broad classes which we shall term: **kinematic** variables and **lifetime** variables.

Any method based on the use of kinematic variables to separate quark flavours relies on the parent quark mass being passed on in some way to the properties of the offspring jet. For the case of heavy flavours, such as jets from b-quarks, this should manifest itself as a relatively high jet invariant mass or as a large momentum component, transverse to the jet direction, carried by the hadrons or leptons of the jet.

Methods based on the use of lifetime variables rely on the relatively long lifetime of heavy quarks bound up in hadrons, to produce decay products typically at distances of order 1 mm per 10 GeV/c from the production point. The presence of a number of tracks in an event whose origin is offset from the rest, can then clearly be used as the basis for a heavy-flavour tag, given a detector with sufficient tracking resolution.

5.2 A Review of Tagging Techniques

The full Monte Carlo data sample of 60K multi-hadronic events as described in Chapter 4 was used for the comparison of tagging techniques. To guarantee con-

[1] Unless otherwise stated we will always refer to u,d and s quarks as being generically 'light'.

sistency, and so aid direct comparison, the same event and track selection criteria were applied in all cases. Only charged tracks that passed the following quality cuts were used:

- $p < 60.0$ GeV/c
- $p_{xy} > 0.15$ GeV/c
- $|d_0| \leq 5.0$ cm
- $|z_0| \leq 50.0$ cm
- Number of CJ space points > 40
- $\chi^2_{r\phi} < 999.0$

No information from neutral clusters in the event were used throughout this study.

Each event was split into two jets by the definition of hemispheres separated by the plane perpendicular to the principle thrust axis of the event (defined below). In addition, each event was required to be well contained in the detector volume by passing the following requirements:

- $|\cos(\theta_T)| < 0.8$, where θ_T is the event thrust axis polar angle.
- Each hemisphere must contain at least four tracks passing the quality cuts.

These quality cuts on events and tracks define what we refer to henceforth as the **standard** cuts, which reduces the Monte Carlo sample to 39,173 events.

5.2.1 High p_t Lepton Tagging

To begin this section we briefly describe a heavy flavour tagging method that deserves special mention but is not considered as part of the survey. Lepton tagging has traditionally been the most popular and successful means of tagging heavy flavour events.

Electrons and muons from the semi-leptonic decay of hadrons show a transverse [2] momentum (p_t) spectrum, that reflects the high mass of the parent ($\sim 5\,\mathrm{GeV}/c^2$). Figure 5.1 illustrates clearly that the hard end of the p_t spectrum for muons, is dominated by direct B decays and so makes a useful discriminating variable. Event samples that are 70-90% pure in $b\bar{b}$ events can be attained with a selection efficiency of $\lesssim 5\%$, by typically requiring momenta in the range, $p^\ell \gtrsim 3$ GeV/c and $p_t^\ell \gtrsim 1$ GeV/c.

[2] With respect to some measure of the flight path of the decaying particle.

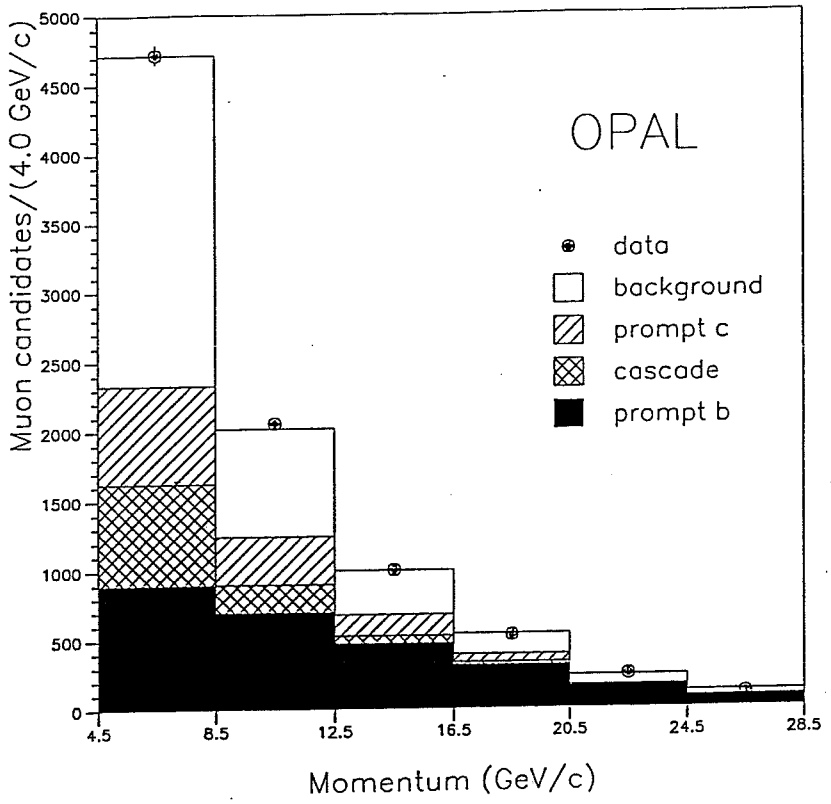

Figure 5.1: The measured p_t spectrum of muon candidates from various sources measured in OPAL data. From [68].

Experimentally lepton identification proves to be relatively simple. Electrons can be selected mainly through their specific ionisation in tracking chambers ($\mathrm{d}E/\mathrm{d}x$) and by comparing the energy deposited in calorimetry to the track momentum ($E/P \sim 1$), whereas muons traverse the calorimetry to leave track segments in the surrounding muon chambers which can then be matched to tracks found in the central tracking chambers.

There are however a few important disadvantages and caveats linked to this method in particular: Firstly, the semi-leptonic branching ratio is rather small (~ 10 %) which necessarily results in a low B-tagging efficiency. In addition, the branching ratio has presently a rather large error ($\sim$ 10 %) which directly filters through to an error on physics measurements such as the $\mathrm{Z}^0 \rightarrow \mathrm{b\bar{b}}$ branching ratio and mean B-lifetime. Further, lepton identification can suffer from rather high backgrounds which need to be well understood. Photon conversions, π and K decay all contribute background sources of leptons in addition to hadronic contamination of the muon sample from *sail-through* (hadrons that do not interact in the material) and from *punch-through* (hadrons whose interaction products penetrate the material).

These factors make it worthwhile investigating other ways of tagging heavy flavours based on methods that utilize all decay modes of B hadrons.

5.2.2 Event Shapes

The *shape* of an event is essentially a measure of how longitudinal and transverse momentum is shared among the various particles that make up the event. The details of how momenta are distributed in $e^+e^- \rightarrow q\bar{q}$ events is flavour dependent and hence potentially a tool to be used for flavour discrimination.

The prediction, which is born out from the results seen by (for example) experiments at PEP and PETRA, is for the mean p_t content of b-jets to be higher than for light-quark jets. As for the case of leptons this is just a reflection of the high B-hadron mass. In addition however, the relatively high decay multiplicity of the B leads to it's momentum being shared over many particles and results in the mean momentum of $b\bar{b}$ events being slightly lower than for u, d, s and c events. This combination of slightly higher mean p_t coupled with slightly lower mean momentum leads to b-jets being on average somewhat less collimated or more isotropic in nature than light-quark jets.

One way of quantifying this difference in shape is through the variables **Sphericity** and **Thrust**.

Sphericity is defined in terms of the eigenvalues of a sphericity tensor formed from all N-particles seen in the event,

$$M_{\alpha\beta} = \sum_{i=1}^{N} p_{i\alpha} p_{i\beta} \quad (\alpha, \beta = x, y, z). \tag{5.1}$$

This has normalized eigenvalues satisfying, $Q_1 + Q_2 + Q_3 = 1$ and ordered so that, $0 \leq Q_1 \leq Q_2 \leq Q_3$, in terms of which we can define the sphericity (S) and aplanarity (A) of the event,

$$S = \frac{3}{2}(Q_1 + Q_2) \tag{5.2}$$

$$A = \frac{3}{2}Q_1. \tag{5.3}$$

The sphericity axis is that direction along which the sum of the squares of the transverse momenta, $\sum_{i=1}^{N} p_t^{i2}$, is minimized and

$$S = \frac{3\sum_{i=1}^{N} p_t^{i2}}{2\sum_{i=1}^{N} p^{i2}} \quad (0 \leq S \leq 1). \tag{5.4}$$

For extreme two-jet events $S = 0$ and $S \rightarrow 1$ as the event becomes more isotropically distributed. Aplanarity ($0 \leq A \leq 0.5$) is a measure of how flat the event is, with extreme flat events having $A = 0$.

In practice, sphericity (and aplanarity) present a problem when attempting to compare data with theory due to their quadratic nature. This means that for a given initial four-momentum of a system of particles, the sphericity will alter its

value depending on the number of particles that the available four-momentum is shared between. This then makes sphericity very sensitive to the details of modelling fragmentation and to a lesser extent particle decay. The variable thrust (T) however, is a linear measure of two-jet properties and as such is much less dependent on fluctuations in the fragmentation.

$$T = \max \frac{\sum_{i=1}^{N} |p_l^i|}{\sum_{i=1}^{N} |p^i|} \quad \left(\frac{1}{2} \leq T \leq 1\right) \tag{5.5}$$

where, p_l is the component of particle momentum along an axis, the thrust axis, chosen so as to maximize T. An extreme two-jet event would therefore have $T = 1$.

Thus, S and T are variables sensitive to the distribution of p_t and p_l in an event and following the discussion at the beginning of this section, $Z^0 \rightarrow b\bar{b}$ events are more likely on average to be associated with larger values of sphericity and hence correspondingly smaller values of thrust, than the average c or light-quark event. Distributions of thrust and sphericity are shown in Figure 5.2(a) and (b) respectively comparing b-events to the lighter flavours.

Besides mass of the parent quark, there are two further sources of jet $p_t$not yet considered: The first is quark and gluon fragmentation which contributes on average 0.3 GeV/c per track of p_t(relative to the parent quark direction) independent of the initial energy. The contribution of fragmentation along the quark direction, as well as being dependent on the initial quark energy, is also flavour dependent suggesting kinematic variables based on transverse momenta maybe somewhat 'safer' than those looking in the longitudinal direction for flavour separation.

The second is gluon Bremsstrahlung from quarks. That a considerable fraction of multi-hadronic events contain gluon radiation can be seen from Figure 5.10, and it is the sensitivity of sphericity and thrust to such QCD effects that are largely responsible for the long tails seen in their distributions. It is now a well established fact, first proven in PETRA data, that $e^+e^- \rightarrow q\bar{q}g$ events are planar[3]. Hence by looking in the direction out of the $e^+e^- \rightarrow q\bar{q}g$ event plane it should be possible to drastically reduce the sensitivity to gluon radiation.

With these considerations in mind the variable **Transverse Jet Mass** (M_t) is considered where,

$$M_t = \frac{2E_{beam}}{E_{vis}} \sum_{i=1}^{N} \left|p_t^{out}\right|. \tag{5.6}$$

Here E_{beam} is the colliding beam energy and E_{vis} is the total visible event energy in charged tracks. The quantity p_t^{out} is the component of track-transverse momentum out of the event plane defined by the thrust vector and the orthogonal axis that

[3]Since the process is observed in a frame of reference that is also the centre-of-mass frame, the net momentum must vanish. Hence the gluon must appear in the same plane as the two quarks and the resulting system of jets will then largely retain this planar topology.

points along the direction that maximizes $\sum_{i=1}^{N} p_t$. A distribution of M_t is presented in Figure 5.2(c) comparing b-events to the lighter flavours.

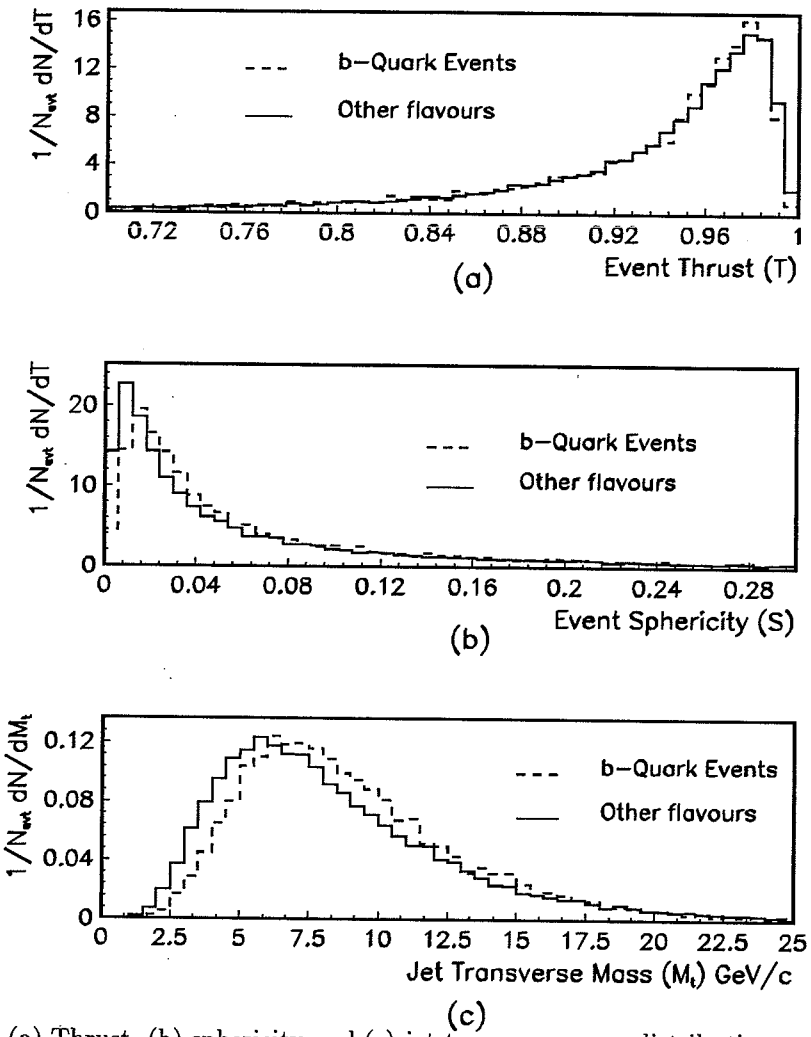

Figure 5.2: (a) Thrust, (b) sphericity and (c) jet transverse mass distributions comparing b-quark events to c and light-quark events.

Although the distributions of sphericity and thrust in Figure 5.2 show a systematically different shape between light and b-quarks, the difference is minimal and the main reasons for this are not difficult to find. As the ratio of the b-quark mass to the beam energy decreases so the distinction between the decay of a 'heavy' quark and a 'light' quark become masked i. e. the b-events become more 'jet-like' in nature. In addition, the presence of gluon radiation acts to smear out any contribution to the event p_t due to quark mass. At LEP energies of $W{\sim}90\,\mathrm{GeV}$ these problems become more acute than was the case at (say) PETRA energies of $W{\sim}30\,\mathrm{GeV}$ where already the basic application of these variables was showing no substantial separation of b-quark events [69].

As expected, we find the flavour-discriminating power of M_t to be superior to S or T albeit not at a level that could usefully be used for tagging b-events. M_t was

however successfully used as a discriminating variable at PETRA [69], the main difference now being the increased gluon p_t contribution at LEP energies. Although M_t is largely independent of QCD effects from $e^+e^- \rightarrow q\bar{q}g$ events, it is sensitive to gluon contributions in higher gluon multiplicity situations. These events will in general populate the tail of the M_t distribution (together with events where the thrust axis is poorly determined) and will act to blur the p_t^{out} contribution coming only from the quark mass. Relative figures of merit for flavour discrimination for theses event shape variables are presented in Table 5.1.

5.2.3 Scaled Invariant Jet Mass

A technique developed by Wyatt in [70] and applied to TASSO data, was based on the observation from the Monte Carlo modelling of jet fragmentation that often a large fraction of the jet energy was carried by a few high-momentum particles which together had a small invariant mass. The simulation of b jets suggests that the decay of massive B hadrons is less likely to produce such a high momentum, low-mass cluster. In order to isolate this cluster of tracks at the core of a jet, a procedure is used which acts to strip away tracks that contribute a large amount to the jet mass while only contributing a small amount to the jet energy. The candidate tagging variable is then the mass of those particles that survive the stripping procedure. In fact the variable we will consider here is the *scaled* invariant jet mass M_S where,

$$M_S = \frac{measured\ mass\ of\ the\ jet}{measured\ energy\ of\ the\ jet}. \tag{5.7}$$

M_S is a quantity that is less dependent on the jet constituents actually detected which can be an important consideration when, as is the case here, only charged tracks are considered and so any γ, ν_ℓ, n, K_L^0 ,etc. in the event are sources of missing energy.

The procedure used was the following:

1. The particles belonging to a jet (i. e. an event hemisphere) were ordered according to their rapidity along the event thrust axis.
2. The two particles highest in the rapidity order are then clustered together and their 4-momenta summed.
3. The addition of further particles to the cluster is then governed by the increase in scaled jet mass (ΔM_S) and scaled jet energy (ΔE_S) that the addition creates. More specifically, the third (and subsequent) particle(s) will be accepted into the cluster if,

$$R = \frac{\Delta M_S}{\Delta E_S} < R_{cut}.$$

The value of R_{cut} is chosen so as to optimize the flavour separation of the technique. The value $R_{cut} = 3.0$ was used.

4. If any track is rejected and then another track, lower in the rapidity order, is accepted into the cluster all rejected particles are again considered by repeating Step 3. This continues until a pass through all rejected tracks can be made without any being accepted. This step makes the technique essentially independent of the method used to order the tracks initially.

Figure 5.3(a) compares M_S distributions for b and light-quark events for clusters formed that contain at least three tracks. Only the lightest (i. e. the lowest M_S) cluster was considered per event unless only one of the two clusters satisfied the track multiplicity requirement, in which case it was used regardless. Hence there is one entry per event. Using mainly the lighter cluster reduces the effects of gluon Bremsstrahlung which contributes a larger tail to the M_S distribution for the heavier of the two clusters found. A systematic shift of the b-quark distribution to higher M_S values is evident and is quantified in Table 5.1.

Figure 5.3(b) shows how the efficiency and sample purity for tagging $Z^0 \rightarrow b\bar{b}$ events varies as one imposes cuts in the M_S variable. Here we define,

$$Efficiency = \frac{Number\ of\ b\ events\ passing\ the\ cut}{Number\ of\ b\ events\ generated} \tag{5.8}$$

$$Purity = \frac{Number\ of\ b\ events\ passing\ the\ cut}{Total\ number\ of\ events\ passing\ the\ cut} \tag{5.9}$$

From this method, a sample of events enhanced with ~30% $Z^0 \rightarrow b\bar{b}$ events can be attained with a selection efficiency of ~40%.

5.2.4 Boosted Sphericity Product

Boosted Sphericity Product (BSP) is a technique that aims to maximize the effect of the large p_t given to B-hadron decay products, by performing the sphericity calculation actually in the rest frame of the decaying parent particle. This calculation is performed separately for each jet and the product of the two values is used as the tagging variable for the event as a whole.

A (simplistic) explanation of how BSP can achieve discrimination between the quark flavour of jets, is based on the fact that the b-quark will travel away from the e^+e^- interaction point with a β that is somewhat less than that for light quarks. If one then Lorentz boosts the decay products of all quarks into the rest frame of the B hadron, the decay products of the b-quark will be isotropically distributed (i. e. high S) whereas the tracks constituting a light-quark jet will still be somewhat

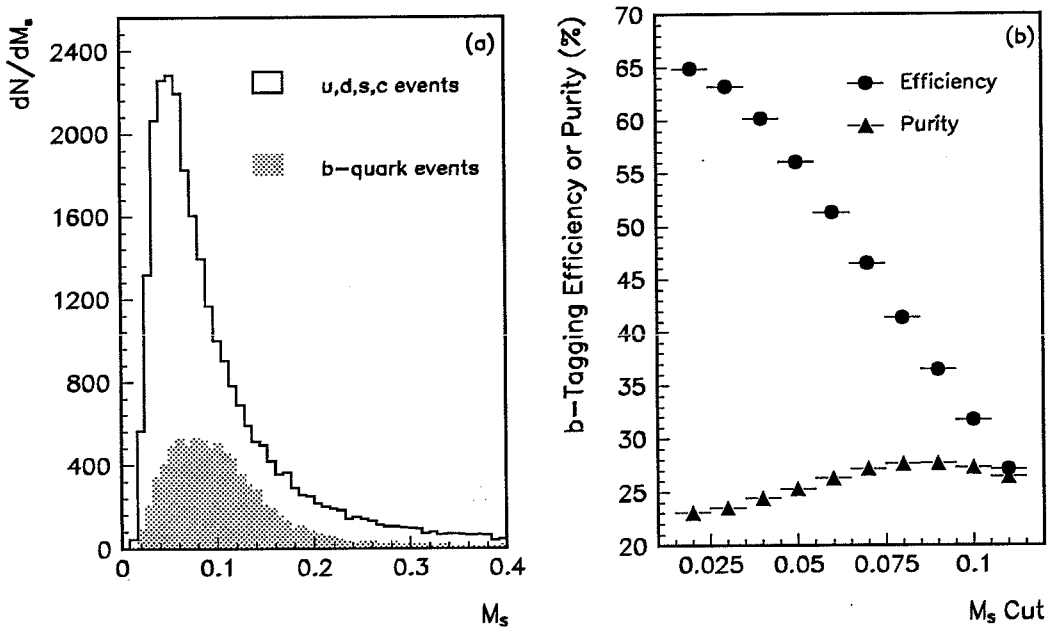

Figure 5.3: (a) Plots of M_S for b-events compared to light quark events. (b) The variation of b-tagging efficiency and purity as a function of the cut on M_s (The statistical errors are smaller than the symbol size).

collimated (i. e. of low S). Hence in this way, the BSP variable regains some of the quark-mass information that becomes increasingly masked by the jet-like structure of events at high energies and was a major flaw to the flavour tagging performance of the event shape variables studied earlier.

The distribution of BSP is shown in Figure 5.4(a) for the case of light and c-quark events compared to b-events. The tracks in each hemisphere of the event were Lorentz boosted by $\beta = 0.95$ along the thrust axis. The magnitude of the boost was chosen so as to maximize the flavour separation which is again quantified via a χ^2 comparison in Table 5.1. Figure 5.4(b) shows b-tagging efficiency and purity performance attainable by cutting on BSP and using the definitions of Equation 5.8 and Equation 5.9.

The separating power of this method appears to be the largest of any of the techniques studied up to this point. It is at first quite surprising that the 'optimum' value for β is so low since a b-quark at LEP has a γ factor of 9 which corresponds to a β of 0.99. This should be compared with the situation at TASSO [71], where the ideal β used to gain an enhanced sample of $b\bar{b}$ events via the BSP technique, was found to be consistent with that expected from events collected at W ~35 GeV. This situation illustrates a further important difference in the properties of b-quark jets at LEP energies compared to PETRA. As we shall find in section 5.3, b-jets at LEP can typically contain up to ~50 % of their tracks from the fragmentation process

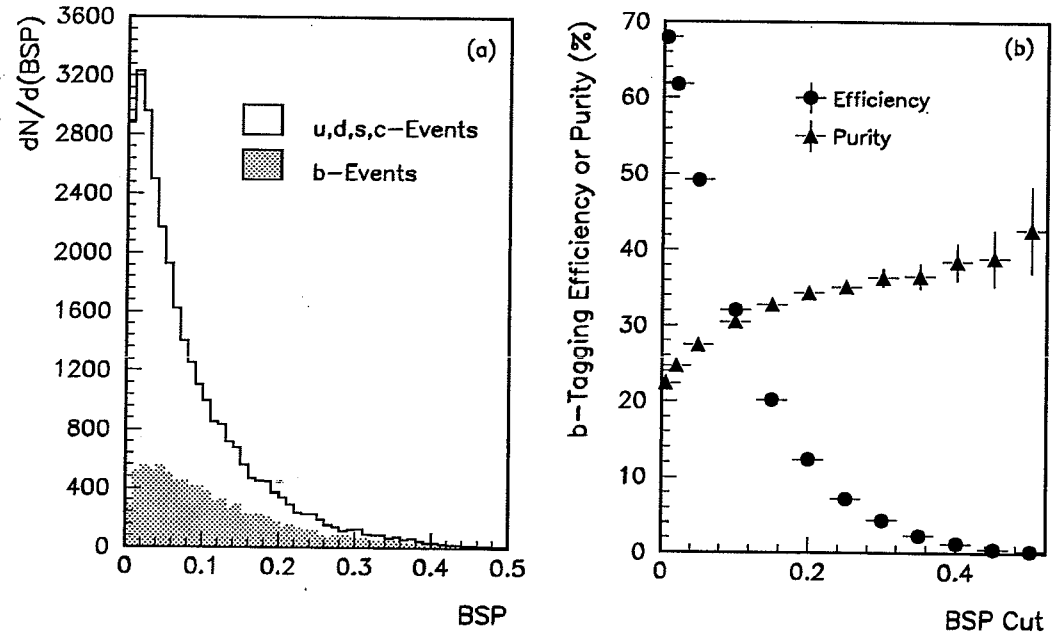

Figure 5.4: (a) Plots of *BSP* for b-events compared to light quark events. (b) The variation of b-tagging efficiency and purity as a function of the cut on *BSP*. The errors are statistical only.

which was not the case at PETRA. In the rest frame of the b-quark, these relatively soft fragmentation particles can have significant momenta back to the interaction point and so act to lower the jet sphericity measurement. We therefore find that the boost resulting in the best discrimination is not that which puts us into the rest frame of the b-quark, but rather that which takes us effectively into a rest frame for the whole *jet*.

Given that jet rest frames at LEP are largely flavour independent, i.e. the $\sum p_l$ distributions for b-jets are found to be only very slightly softer than for light quark-jets, it is instructive to consider from where the discriminating power of *BSP* derives. This can be partly understood from the definition of sphericity (Equation 5.4) and the fact that an average b-jet is characterized by the combination of slightly lower mean momentum and slightly higher mean p_t than the typical light-quark jet. Recent studies of OPAL data by Barlow et al. [72] suggest that the full separating power of the *BSP*, derives from a strong correlation that exists between p_t and p_l for b-jets which is only weakly present for light-quark jets. The sphericity variable, which depends essentially on the ratio of these quantities, make fortuitous use of this difference in correlation even though the reasons for it are unclear.

The conclusion from these results based on kinematical variables is that systematic differences between the quark flavours can be expected albeit at a reduced level from that attained at lower energy e^+e^- experiments.

Potentially a more effective property of $Z^0 \rightarrow b\bar{b}$ events to exploit for tagging,

mass when using kinematic variables, for this case of lifetime tagging the relatively large Lorentz boost given to B hadrons in jets should mean that LEP provides the best opportunity to date in which to lifetime-tag b-quark events. To test this claim within the Monte Carlo, we now investigate two techniques that are sensitive to tracks in jets that originate from points distant from the e^+e^- interaction point.

5.2.5 Impact Parameter Tagging

The daughter tracks of B hadrons, when extrapolated back to the e^+e^- interaction point (the B-production point), will clearly not in general pass through this point but will by virtue of the non-zero decay length, miss the production point by some distance - the impact parameter. When averaged over all decay lengths and decay kinematics the impact parameter is proportional to the lifetime of the B and thus can be used as a potential tagging variable.

Specifically we use here the projection of the impact parameter (δ) in the $r - \phi$ plane only, reflecting the superior spatial resolution attainable compared to the perpendicular plane (as seen in Chapter 3). Figure 5.5 defines δ for a single daughter track from a B-decay. Clearly to measure δ for a track, in addition to the track

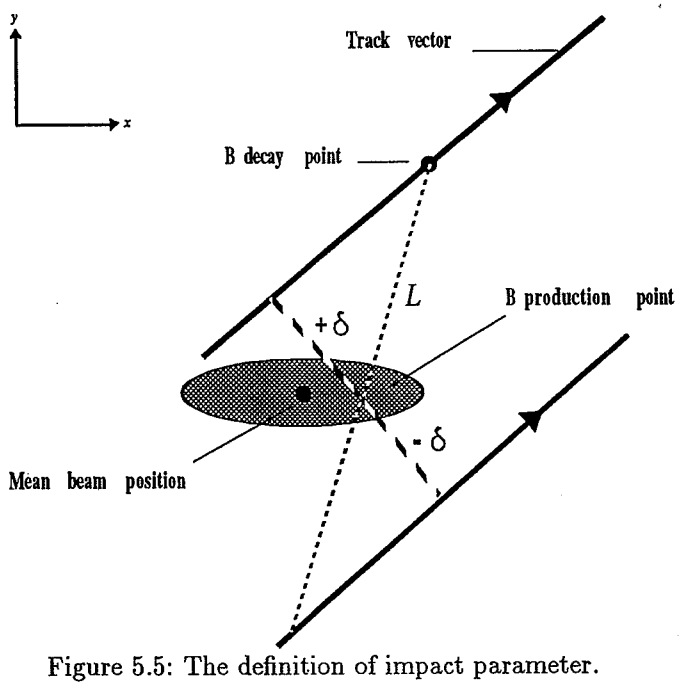

Figure 5.5: The definition of impact parameter.

trajectory, one needs some estimate of the B-production point and flight direction.

An estimate of the production point is provided here by a mean beam position averaged over many events within a machine fill. Further details of this beamspot are provided in Section 5.3. The direction of the primary B is estimated by the principle event thrust axis. Figure 5.5 shows too how δ is attributed a 'lifetime'-sign, reflecting that ideally it should be a positive-definite quantity in accordance

with the decay length. The figure shows that δ will pick up a negative sign if the track intercepts the B-axis 'behind' the production point. This situation can be caused by tracks not travelling in the same direction as the B because, for example, they originate from the fragmentation process, or due to errors made in estimating the B direction, track trajectory or production point. This convention for signing then ensures that δ measured for a typical B-decay product will on average be positive and a distribution over many $b\bar{b}$ events should show a marked positive tail compared to light-quark events.

A more reliable tagging variable than just simply δ, turns out to be the impact parameter scaled by its measurement error δ/σ_δ where,

$$(\sigma_\delta)^2 = \sigma_{d_0}^2 + (\sigma_{x_b} \sin\phi_0)^2 + (\sigma_{y_b} \cos\phi_0)^2 \tag{5.10}$$

The first term σ_{d_0} is the impact parameter resolution from the OPAL track fit and the remaining terms give the contribution from the primary vertex error ellipse projected along the impact parameter vector. In order to form a tagging variable for the event as a whole in line with the other techniques studied up to this point, we use the *mean* scaled impact parameter, $\langle\delta/\sigma_\delta\rangle$, taken over the event hemisphere containing the highest energy in charged tracks. To avoid this number being dominated by a single track of large d_0, the track quality cut is tightened to $|d_0| < 1$cm.

Figure 5.6 shows that a clear systematic shift exists between $b\bar{b}$ events and the light quark background which is quantified in terms of a χ^2 comparison in Table 5.1. It is clear that with only a very unsophisticated approach, the impact parameter has already matched the tagging performance of the kinematic variables and seems to confirm the suitability of lifetime based variables for tagging at LEP.

5.2.6 Decay Length

The decay length method aims to identify and fit the position of a *secondary* vertex, formed by a group of tracks originating at some point distant from the e^+e^- interaction point whose estimated position we term the *primary* vertex of the event. Vertices of this type exist particularly in $Z^0 \to b\bar{b}$ events, where a large proportion of the tracks originate from the decay chains of relatively long-lived B and D-decay vertices. Conversely, the vast majority of tracks in u,d,s events originate from the primary vertex itself. Hence a potential b-tagging variable is the 'decay length' i. e. the distance between an identified secondary and primary vertex. Because of the superior tracking resolution, as for the impact parameter study, we use only the $r-\phi$ projection of tracks and hence calculate strictly the decay length projected into the $r-\phi$ plane, L.

Figure 5.7(a) presents a schematic representation of an ideal $Z^0 \to b\bar{b}$ event as it would appear in a detector with perfect tracking resolution. Once the effects of

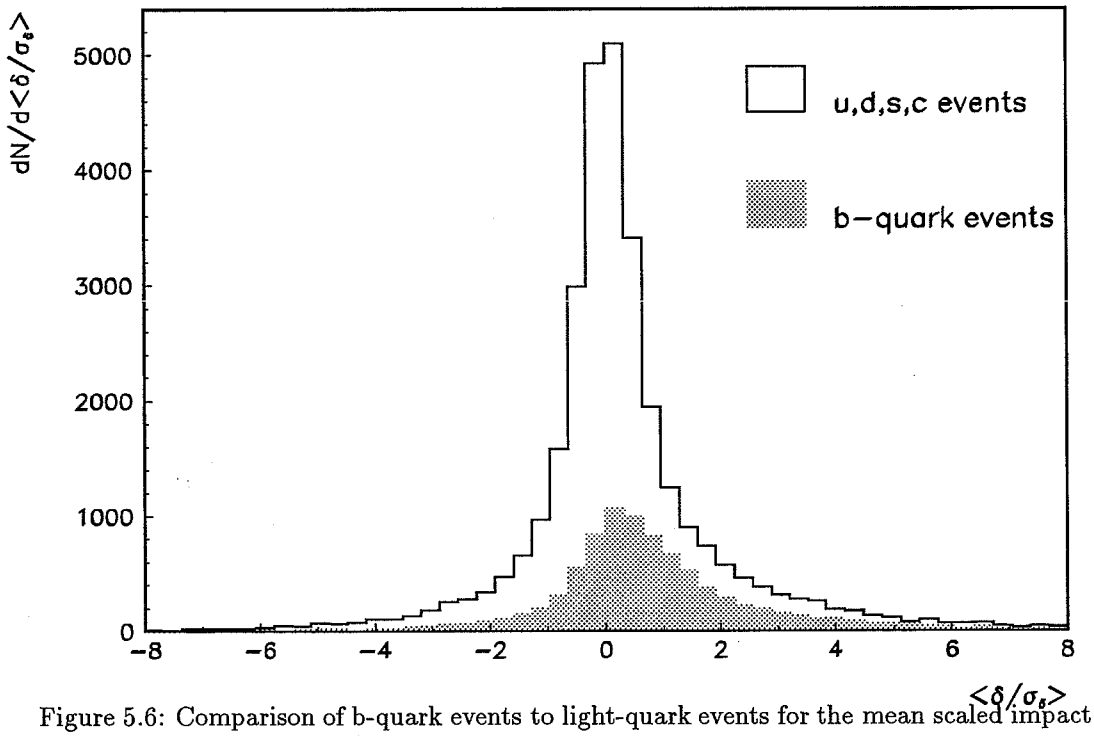

Figure 5.6: Comparison of b-quark events to light-quark events for the mean scaled impact parameter variable.

$r - \phi$ projection of tracks and hence calculate strictly the decay length projected into the $r - \phi$ plane, L.

Figure 5.7(a) presents a schematic representation of an ideal $Z^0 \rightarrow b\bar{b}$ event as it would appear in a detector with perfect tracking resolution. Once the effects of multiple scattering and finite detector resolution are included, tracks no longer extrapolate back exactly to their production vertices and any detector inefficiency and acceptance losses result in tracks being missed from the detected event altogether. These considerations mean that to reconstruct fully the decay vertices of B-mesons with any resonable efficiency is unlikely. However, the inclusion of as many tracks from a B-decay chain as possible into a secondary vertex fit will bias the vertex position to longer decay lengths when averaged over many events and to quantify the size of this effect the following procedure was adopted.

- An attempt is made to fit all standard tracks in an event hemisphere to a a common vertex position. Details of the fitting process are presented in Appendix C. As for the impact parameter study, the standard cut on track d_0 is tightened to $|d_0| < 1$cm.

- Any track that contributes a χ^2 of four [4] or more is then stripped away from the definition of the vertex and the fit repeated. This process continues until either all tracks in the fit contribute less than four to the χ^2 or the number

[4]This value was tuned to give the most uniform χ^2 probability distribution for the overall fit.

of tracks associated with the fit falls below three, in which case the fit is abandoned.

- The mean beam position used in the impact parameter study is again used as an estimate of the primary event vertex position.

- Given a secondary vertex position and an estimate of the primary event vertex together with their respective error ellipses, a further fit is performed (details of which are given in Appendix D) to determine the most likely distance between these two points given a directional constraint that is the event thrust axis. This quantity defines the projected decay length.

Figure 5.7(b) shows the result of applying the above procedure to the typical $Z^0 \rightarrow b\bar{b}$ event. In a similar way to the impact parameter definition, the projected decay length is 'lifetime' signed according to whether the secondary vertex is reconstructed 'in front' of or 'behind' the primary vertex position (see Figure 5.7(c)). Resolution effects therefore mean that the method applied to events where all tracks originate from the primary vertex (as is largely the case for u, d and s events), will result in a secondary vertex being reconstructed on average 50% of the time behind the primary position and 50% in front of it.

The only backgrounds as such to the situation described result from interactions in the detector volume plus Λ and K_s^0 decays. Since all of these sources are associated with decay lengths on the scale of (at least) cm's i. e. an order of magnitude larger than the region populated by heavy flavour decays, they provide no real confusion to any conclusions drawn. In addition, the two-prong charged decay vertices of Λ's and K_s^0's are heavily suppressed by the demand that the secondary vertex contain at least three charged tracks.

Hence the expectation is for the average b-quark event hemisphere to be reconstructed with a relatively large positive decay length in contrast to u,d,s events which should show a symmetric decay length distribution centered on zero, the width of which is set by the experimental resolution. $Z^0 \rightarrow c\bar{c}$ events in this respect should lie somewhere between these two extremes. The results from this method are shown in Figure 5.8.

5.2.7 Summary of Tagging Techniques

Two main conclusions can be drawn from the results of this survey of methods. Firstly past methods based on kinematic variables appear to be not as effective when applied to e^+e^- collisions at $\sqrt{s}$ =90 GeV, for reasons that in the main are understood. The second clear result is that the best discrimination of heavy flavours from the background is achieved by variables proportional to the lifetime of unstable

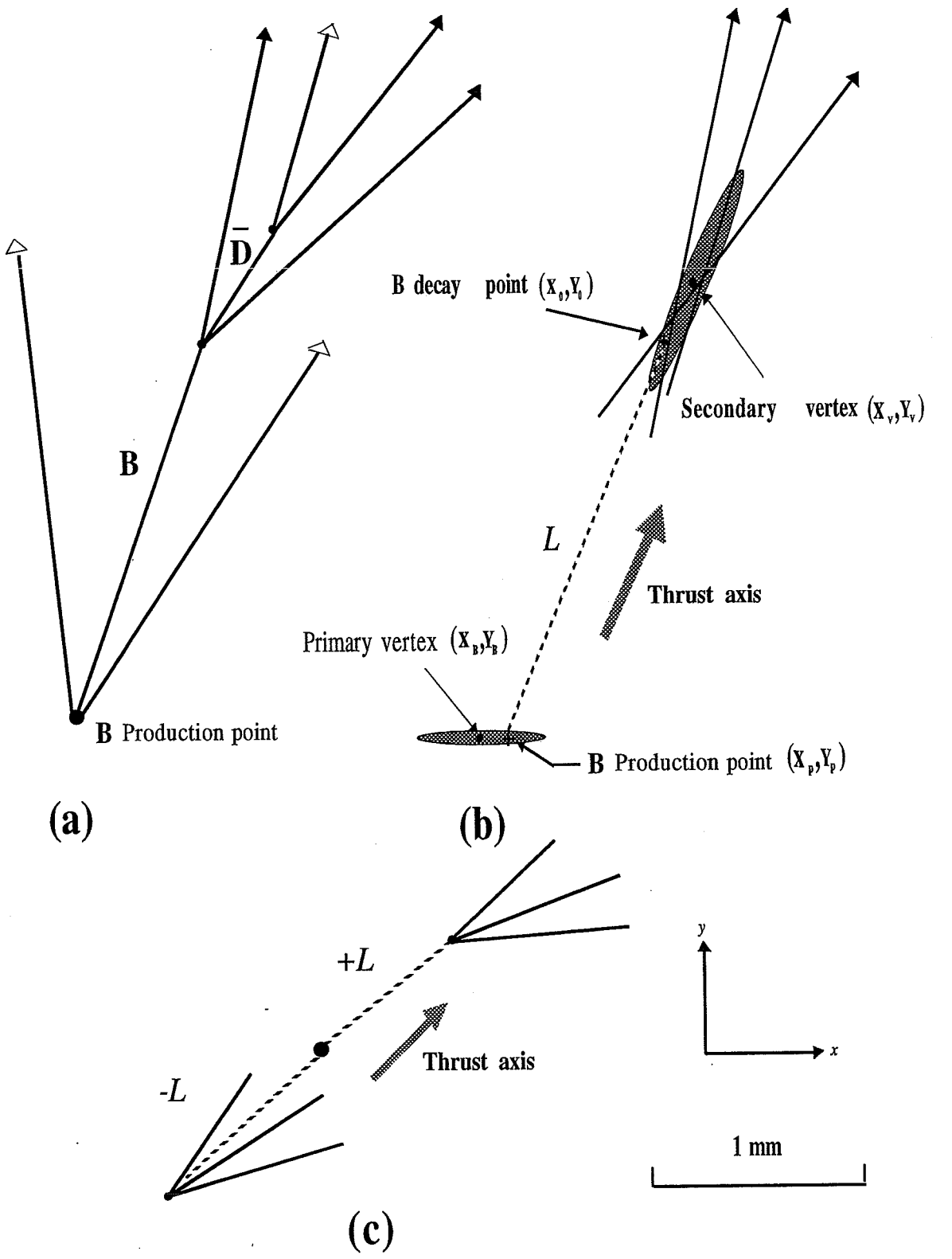

Figure 5.7: (a) Tracks from one hemisphere of an idealised $Z^0 \rightarrow b\bar{b}$ event. (b) The typical result of applying the decay length finding procedure to this event. Error ellipses are drawn roughly to scale and the secondary vertex consists of three tracks (drawn as they might appear in the detector), two of which come from the B-decay and one from the subsequent D-decay. (c) The lifetime signing convention for L.

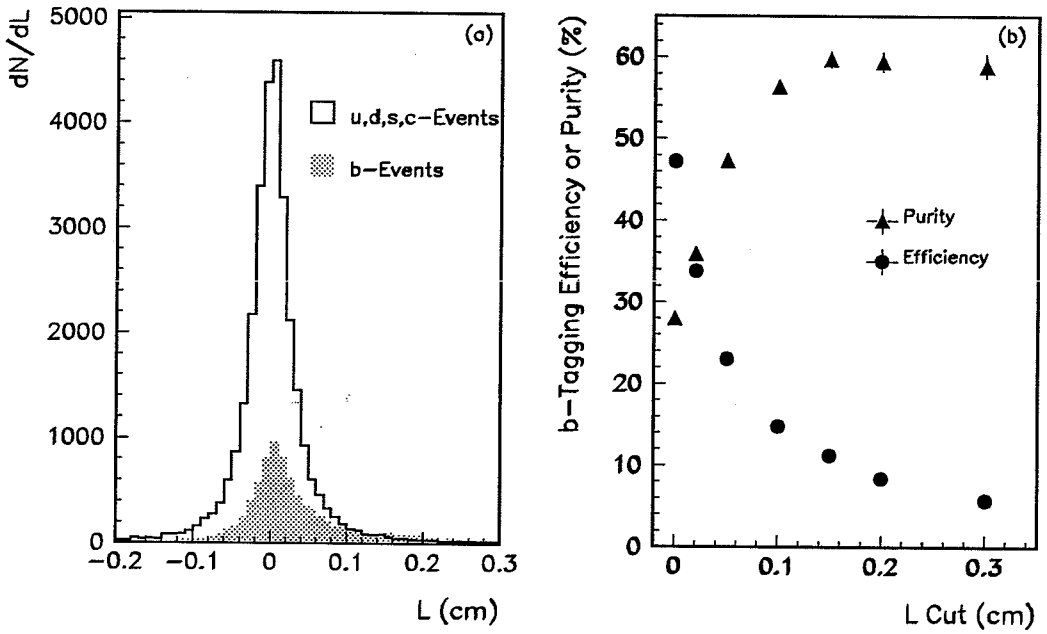

Figure 5.8: (a) Comparison of b-quark events to light-quark events for the projected decay length variable L. (b) The B-tagging efficiency and purity performance as a function of L. The errors are statistical only.

species in the event. These conclusions point towards a measurement of the mean B lifetime being particularly suited to the LEP environment.

Of all the variables considered, the projected decay length was seen to give potentially the best discrimination of $b\bar{b}$ events from other flavours. In addition, the design and performance of the OPAL Vertex Chamber is well suited to meet the high resolution demands of secondary vertex finding. For these reasons, in the following section we choose to further develop the decay length tagging technique, before using it in a new measurement of the mean B-lifetime (presented in Chapter 6).

5.3 Developing the Decay Length Method

This section is devoted to the optimization of the decay length method already introduced, in order to improve further the sensitivity of the variable to the B-lifetime and so give potentially the best possible statistical error from any subsequent lifetime measurement.

Sensitivity to the B-lifetime from this method obviously requires that as many of the B-decay daughters are included in the vertex fit as possible. Scanning Monte Carlo events with GROPE, reveals that the coordinates of a secondary vertex fit can be pulled or biased away from the true decay point by the inclusion of tracks in the fit whose origin is not from the decaying B-hadron e. g. especially tracks from

Variable	Relative χ^2
Thrust	1.0
Sphericity	4.3
Transverse mass	6.8
Scaled jet mass	12.3
Boosted sphericity product	16.0
Mean normalized impact parameter	15.0
Decay length	22.5

Table 5.1: A χ^2 comparison between the $b\bar{b}$ and light-quark distribution for the tagging variables considered in the survey. A binned χ^2 is formed in each case and normalized to that found for the thrust variable. (In all cases the χ^2 is summed over 50 bins with the range chosen so as to enclose the entire distribution).

the fragmentation process. Because of this observation the important quantity to optimize is not directly the number of tracks from the B-decay chain in the vertex fit, but rather the **proportion** of tracks from the B-chain as a fraction of the total number of tracks included in the fit.

Each step of the decay length finding method described in Subsection 5.2.6 is investigated in order to check if improvements to the lifetime sensitivity can be made.

5.3.1 Physics Cuts

The vertex finding process, which depends on track extrapolations to radii well within the beam pipe radius, relies on tracks that are well measured at the inner radii of OPAL. Badly measured tracks can add no information to the vertex fit and only act to degrade the overall resolution attainable.

It is thus essential to utilize fully the Vertex Chamber information available in events. The improvements to the impact parameter resolution that CV hits on tracks can make was seen in Chapter 3. To benefit from this, tracks will now be required to contain at least six hits from the axial layer of the Vertex Chamber corresponding to the minimum number of hits possible for the definition of a CV track segment.

The contribution of multiple scattering in the detector material becomes an important contribution to the overall tracking error at low momenta. A minimum momentum [5] requirement for tracks is thus important to reject the worse effects of

[5] In fact a cut on the projected momentum, $p_{xy}(= \sqrt{p_x^2 + p_y^2})$ is preferred, being a quantity defined entirely within the $r - \phi$ plane.

multiple scattering as can be seen from Figure 5.9(a). Further, Figure 5.9(b) shows that imposing a minimum momentum, favours the selection of tracks from B-decay over those originating from the fragmentation process. The cutoff point however, must clearly be chosen so as not to seriously reduce the efficiency for tracks from the B-decay chain and a compromise value of 0.6 GeV is selected.

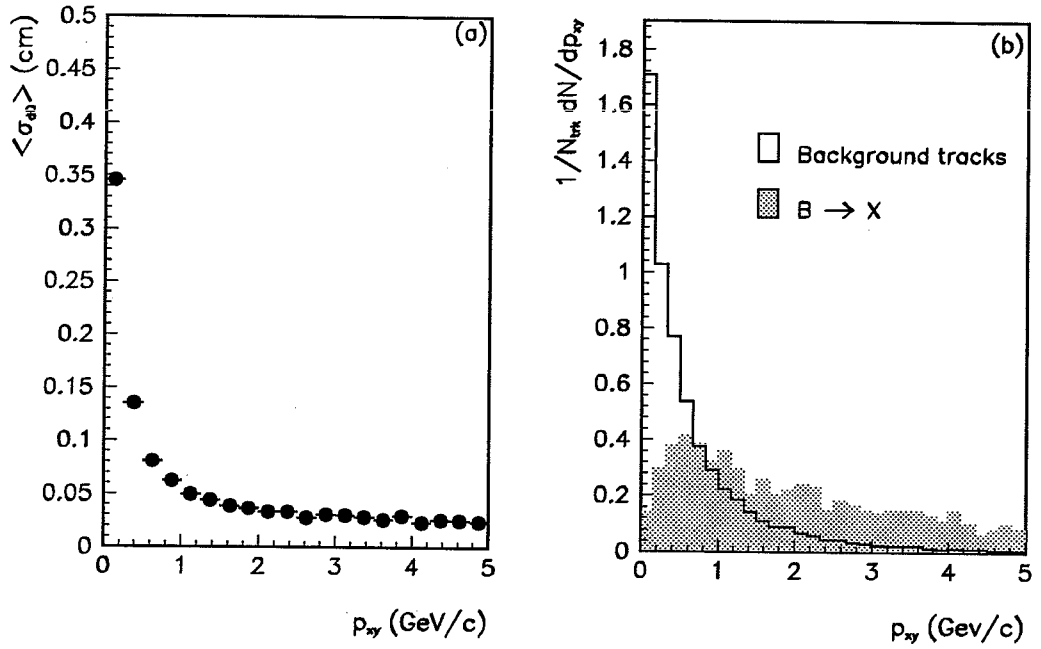

Figure 5.9: (a) Shows how the mean (taken over the range 0 to 1cm) of the error on d_0 from the track fit, σ_{d_0}, degrades as p_{xy} approaches zero. (b) The p_{xy} distribution for tracks from direct B decay compared to tracks whose origin was not the B decay chain.

A cut on the overall event track multiplicity is preferred to the previous standard containment cut based on the polar orientation of the thrust axis. Since at least three tracks are required to form a secondary vertex, a more natural containment requirement for the decay length method is at least three standard tracks in each of the event's 'quark' [6] jets.

In summary, the new minimum track and event requirements for the decay length finding process are listed below and replace the standard cuts of Section 5.2. A track must now satisfy,

- $p < 60.0$ GeV/c
- $p_{xy} > 0.60$ GeV/c
- $|d_0| \leq 1.0$ cm

[6] For cases where the definition of jets can lead to more than two jets per event, those two jets of highest energy are always assumed to be associated with quark fragmentation and are henceforth referred to as the quark jets.

- $|z_0| \leq 50.0$ cm
- Number of CV axial hits > 6
- Number of CJ hits > 40
- $\chi^2_{r\phi} < 999.0$

and each event must contain,

- At least three standard tracks in each of the two quark jets.

These cuts are henceforth referred to as the **physics** cuts. The application of the physics cuts results in the following average charged track multiplicity per event,

$$\begin{aligned} \text{Data} &= 6.50 \pm 0.01 \\ \text{Monte Carlo} &= 6.47 \pm 0.01 . \end{aligned}$$

5.3.2 Jet Clustering

The decay length method described in Subsection 5.2.6 searched for a secondary vertex candidate from all tracks in an event hemisphere. The inclusion of tracks from over such a wide angular region, can result in the B-hadron decay products forming only a small proportion of all tracks passed onto the vertex fitting stage.

To reduce the possibility of including tracks not from the B-decay chain in the definition of a secondary vertex, clearly it would be advantageous to keep such tracks to a minimum while at the same time ensuring that as many as possible of the genuine B-daughter tracks are considered. This problem is addressed by clustering the event into jets of collimated tracks in an attempt to locate a group of candidate B-hadron decay products. The vertex fitting procedure can then be applied to only these selected tracks.

We use the JADE scheme [73] to combine particles in jets, which uses the scaled mass, y_{ij},

$$y_{ij} = \frac{M_{ij}^2}{E_{vis}^2} = \frac{2E_iE_j(1-\cos\theta_{ij})}{E_{vis}^2} \tag{5.11}$$

as the jet resolution parameter. Here E_{vis} is the total event energy in charged tracks, M_{ij} is the invariant mass of a particle pair (i,j) assuming zero rest mass and θ_{ij} is the angle between the pair. The mass of each possible pair-combination in the event, is formed according to Equation 5.11. The pair with the lowest invariant mass,M_{ij}, are then combined to form a pseudoparticle (with 4-momentum $\mathbf{P_k} = \mathbf{P_i} + \mathbf{P_j}$) and if, $y_{ij} < y_{cut}$ the procedure is repeated until no pair of (pseudo)particles satisfy this requirement. The parameter y_{cut} thus controls the jet content, since a low value will result in a large number of very collimated jets whereas a large value results in a

situation approaching the definition of two event hemispheres used previously. The variation of jet multiplicity with y_{cut} is illustrated in Figure 5.10.

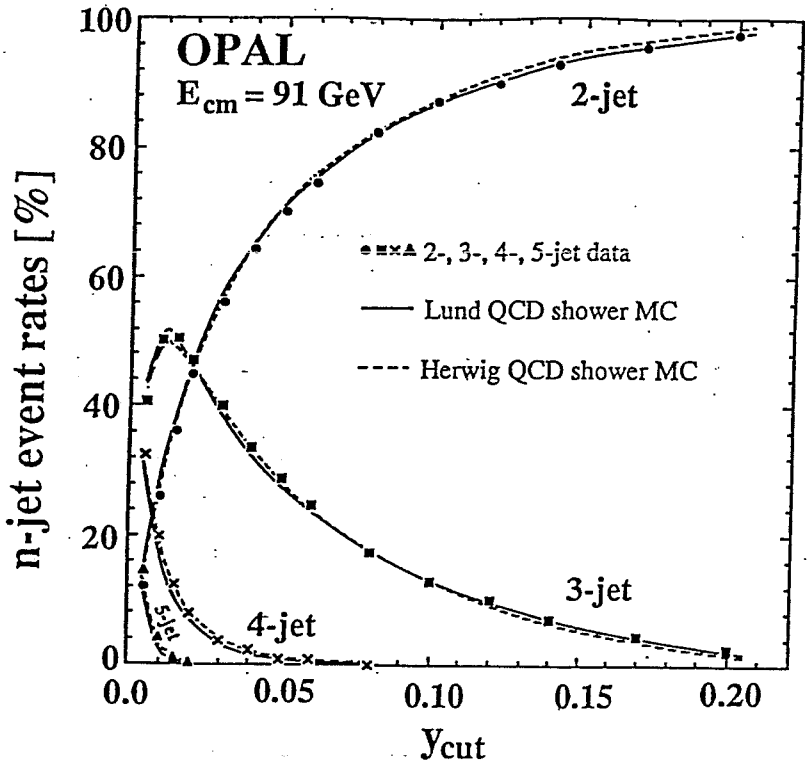

Figure 5.10: The two, three, four and five-jet event rates measured in the OPAL data as a function of y_{cut}. The data are also compared to two different QCD model calculations. The LUND model used in this analysis is seen to reproduce the data well. From [74].

The sample of Monte Carlo $b\bar{b}$ events was studied to investigate the dependence of the decay length method to the choice of y_{cut}. Events and tracks were again required to pass the standard quality cuts of Section 5.2. Only quark jets were considered and the source of tracks in jets was logged so that those originating from the B decay chain (the signal), were flagged separately from those originating elsewhere (the background) i. e. from the fragmentation, interactions in the detector volume or from gluon jets. Each jet was, in addition, required to contain at least three tracks.

To aid in optimizing the choice of y_{cut} we form, per jet, the quantities,

$$SIG = \frac{\#\, tracks\, from\, B\, decay\, chain}{\#\, number\, possible} \quad (5.12)$$

$$BKG = \frac{\#background\, tracks}{\#tracks\, in\, the\, jet} \quad (5.13)$$

Here the number of tracks possible refers to the number of reconstructed tracks, that also pass the standard cuts, from the decay chain of the B hadron. Normalizing to this number, for the B hadron associated [7] with the jet in question, makes SIG a

[7]The association of a primary B hadron from the Monte Carlo to a jet formed by the JADE

variable that is sensitive to B jets 'splitting' into two or more fragments. This will happen as the jet clustering resolution tightens and those tracks of highest p_t begin to get lost from the jet definition. Figure 5.11(a) shows that B jets begin to split in this way largely for values of $y_{cut} \lesssim 0.01$. This problem becomes less acute as the value of y_{cut} increases albeit at the expense of the inclusion of more background tracks into the jet definition as is seen in Figure 5.11(b).

In order to find the value of y_{cut} for which the definition of a jet contains the highest possible proportion of tracks from the B decay chain, we simply form the ratio; $R = SIG/BKG$. Figure 5.11(c) shows a plot of R as a function of y_{cut} and shows a clear maxima for a value of about 0.01. At this value of y_{cut} the Monte Carlo suggests that the average composition of a jet is,

- ~25% either direct from the B decay or from the subsequent cascade D-decay
- ~55% from anywhere along the B-decay chain and hence ~45% comes from background tracks.

As mentioned earlier, it is the improvement in the proportion of tracks from the decay chain of the B in the secondary vertex that is important. The track content of the vertex fit was found to follow closely the content of the parent jet with the result that the fraction of tracks from the B in an average vertex fit increased from below 1/2 with no jet clustering to somewhere approaching 2/3 for a y_{cut} value of 0.01.

An independent cross-check on this value for y_{cut} can be made by considering how well the jet axis reconstructs the direction of the B hadron. That this quantity is sensitive to the proportion of B-decay products in the jet can be seen from Figure 5.11(d). Here we plot the angular difference in the $r - \phi$ plane ($\Delta\phi$), between the jet axis and the generated momentum vector of the decaying primary B hadron associated with this jet. The accuracy with which the B direction can be reproduced is clearly improved as one requires the definition of the jet to contain exclusively tracks originating from the B-decay chain.

The B-direction is found to be best reproduced at $y_{cut} = 0.01$, confirming the result obtained from R. The accuracy of reconstruction at this point in both azimuthal and polar angles being,

$$\begin{aligned} \Delta\phi &= 0.054\,\text{radians} \\ \Delta\theta &= 0.050\,\text{radians} \end{aligned}$$

As an alternative to using a cutoff based on y_{cut} from Equation 5.11, the jet

algorithm, is made by selecting that primary whose flight direction most closely matches, in polar angle, the jet axis.

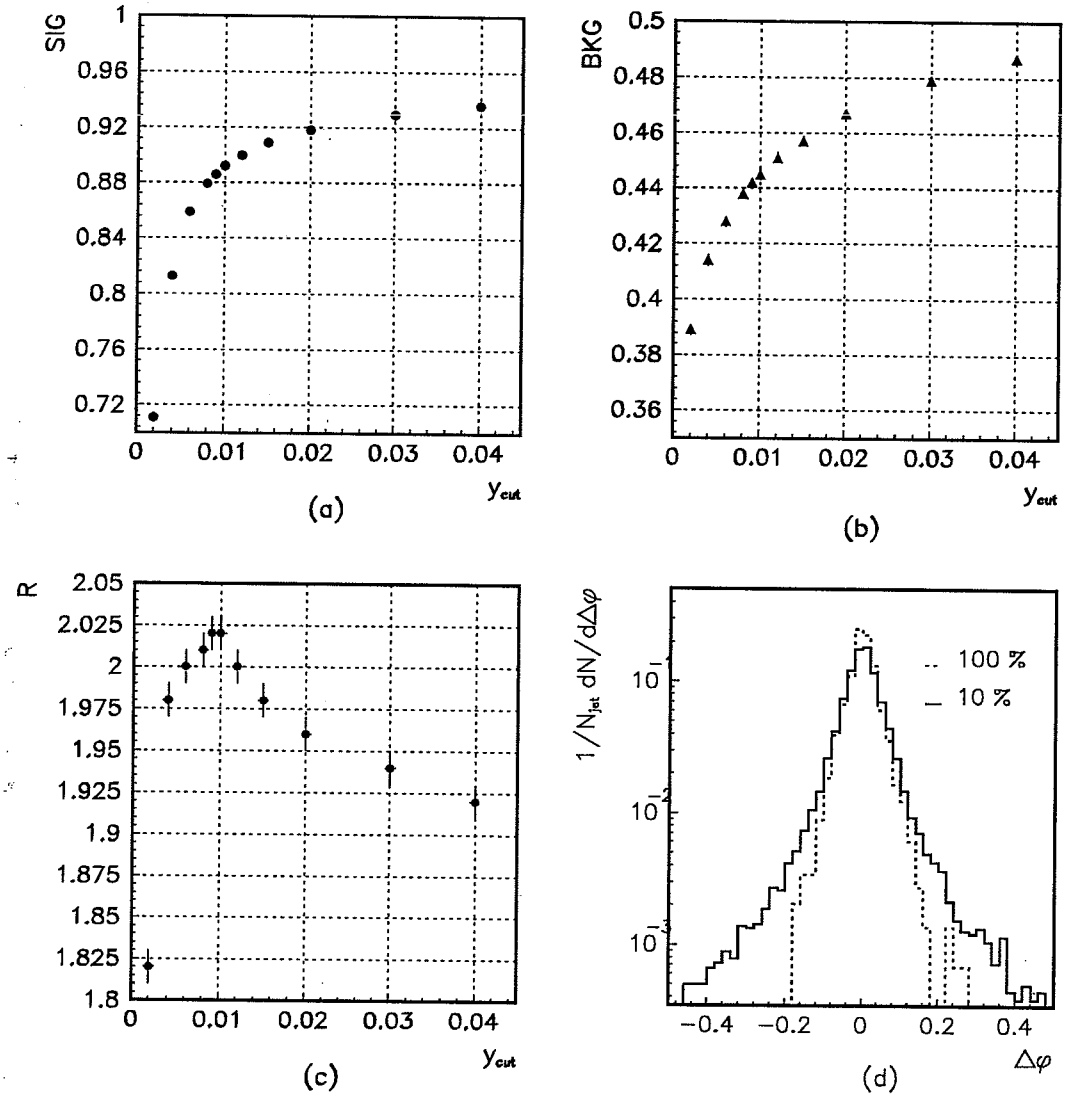

Figure 5.11: (a) The variation of SIG as a function of y_{cut}. (b) The variation of BKG as a function of y_{cut}. (c) The variation of the ratio $R = SIG/BKG$ as a function of y_{cut}. (d) The difference in azimuth between the generated and reconstructed B-direction, comparing the case where all tracks composing a jet originate from the B-decay chain to that where the jet contains only 10% of such tracks.

resolution parameter x_{min} may be used,

$$M_{ij}^2 < x_{min}. \tag{5.14}$$

In principle, using x_{min} instead of y_{cut} should give results less sensitive to fluctuations in the visible energy of the event and allow the cutoff to be set in terms of the jet mass itself, which is a reasonably well defined quantity for jets containing B hadrons. Again $\Delta\phi$ and $\Delta\theta$ are formed, this time for various values of x_{min} in order to find the point at which the B direction is best reproduced. This is found to be for an x_{min} value of $30.25\,\mathrm{GeV}^2$ although the overall accuracy attained is worse than that achieved using the y_{cut} scheme.

There is also some ambiguity involved in the details of how to combine particles which originates from the desire to make comparisons of measured jet rates with perturbative QCD predictions. This ambiguity arises because the $\mathcal{O}(\alpha_s)$ QCD calculations assume massless partons whereas a jet formed by adding the four-momenta of two partons is not massless. The JADE scheme of Equation 5.11 tackled the problem by neglecting explicit mass terms in forming M_{ij}^2. Three slightly different recombination schemes termed $E, p0$ and p (introduced in [75]) were compared for $y_{cut} = 0.01$. There were found to be only slight differences between the different schemes with the JADE scheme being marginally better than the rest.

We conclude from this study into the properties of y_{cut} that a value of 0.01 should be used based on the evidence of Monte Carlo. It is essential however to confirm as far as possible that this conclusion also holds for the data.

If the jet clustering was behaving differently between data and Monte Carlo one might expect the jet multiplicity to differ between the two samples. For y_{cut} of 0.01 the mean number of jets per event is measured to be,

$$\begin{aligned} 3.013 \pm 0.002 \quad & \text{in OPAL data} \\ 3.008 \pm 0.003 \quad & \text{in Monte Carlo.} \end{aligned}$$

In addition, the track multiplicity of jets was checked (see Figure 5.12(a)) and found to also be in excellent agreement. To have confidence that conclusions drawn about the accuracy with which the jet axis reconstructs the B-direction are at least consistent with the data, the distribution of p_t with respect to the jet axis was checked. The shape of this plot is clearly sensitive to the position of the jet axis and for a B jet, a high p_t tail will develop as the accuracy with which the axis reconstructs the B flight path degrades. Figure 5.12(b) shows that no significant discrepancy of shape exists between data and Monte Carlo for the chosen value of y_{cut}.

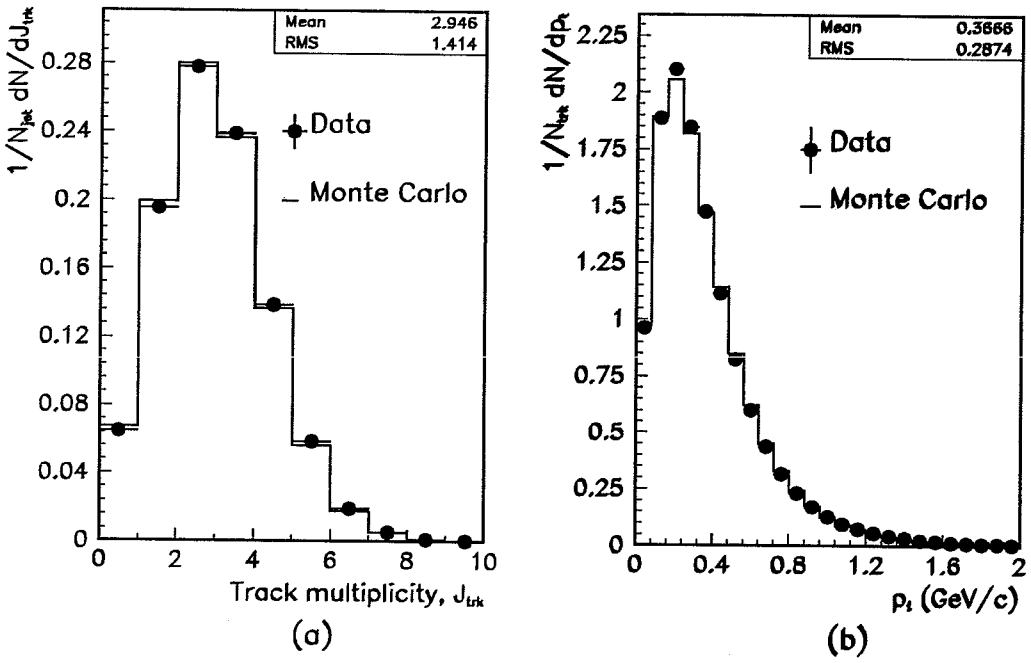

Figure 5.12: (a) The jet multiplicity of physics tracks at y_{cut}=0.01. (b) The p_t spectrum of quality tracks with respect to the jet axis for y_{cut} =0.01.

5.3.3 The Primary Vertex

In the study of Section 5.2.6, the primary event vertex was estimated by a determination of the mean beam position which is described in detail in [76]. In summary, the method used scans the events [8] in chronological order and a χ^2 fit is made to a vertex once there are 100 or more quality tracks (data aquisition run boundaries are respected). The track contributing the largest χ^2 (if > 10) is rejected and this process continues until all remaining tracks contribute $\chi^2 \leq 10$ to the vertex fit. The method then forms a weighted average of 30 such (contiguous) vertices. If there are less than 30 left at the end of a run the average runs over just those remaining, provided there are at least two. Finally, neighbouring vertex positions are joined together and the mean and error recalculated providing each new point is consistent with the running average up to that point.

Figure 5.13 shows how the primary vertex position calculated in this way varies across the full 1990 OPAL data set. Fluctuations in the beam position are observed of up to 200 μm in x and 100 μm in y and are largely correlated with LEP machine running periods. Some significant (few $\times$ 10 μm) jumps in position however, can be seen even within the same data run.

To gain the full error on the primary vertex position coordinates, one must add in quadrature the error on the mean resulting from the above method with the

[8] In principle all events are considered i. e. di-lepton, low multiplicity and multi-hadronic.

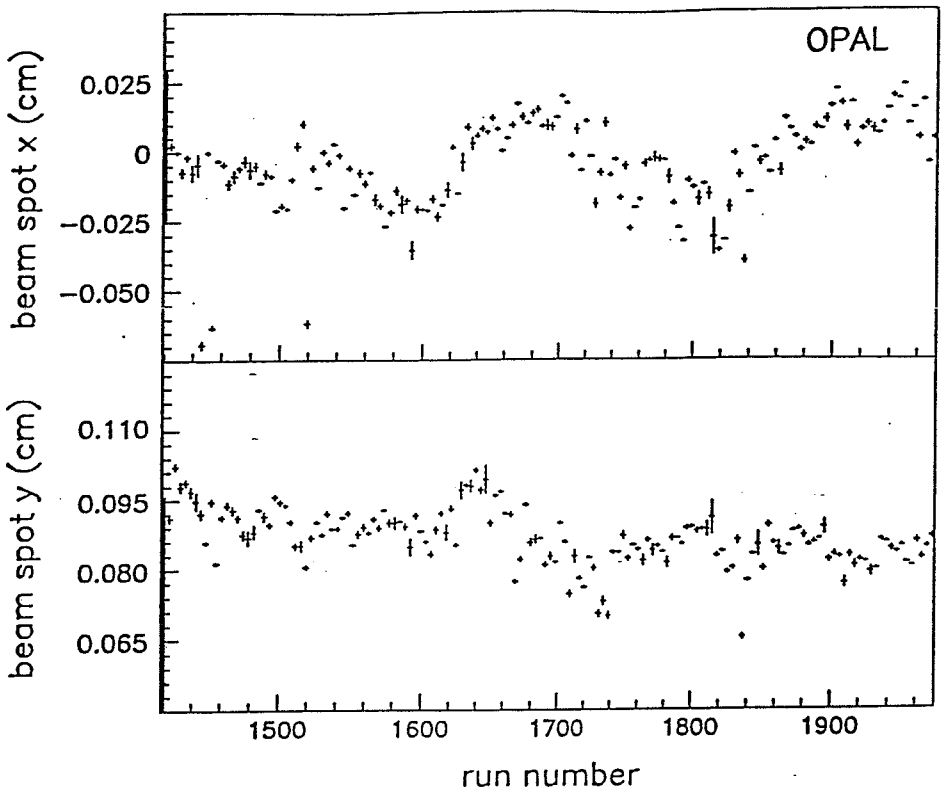

Figure 5.13: Distributions of the mean primary vertex coordinates as a function of OPAL run number in 1990. The error bars indicate the statistical precision on the means and are typically 6.7 μm for x and 4.5 μm for y. From [76].

intrinsic size of the LEP beam envelope in x and y. Assuming for now that the mean primary vertex position is known to arbitrary accuracy, then the impact parameter resolution for the class of tracks going vertically (horizontally) in the $r-\phi$ plane receives contributions only from the track fit, σ_{d_0}, and from the beam envelope, $\sigma_{x_b}(\sigma_{y_b})$. It turns out that σ_{d_0} is too large to be able to unfold the beam size in y by this method. From LEP machine parameters this width is known to lie somewhere between 6 and 11 μm. However, the width of the impact parameter distribution for a set of tracks along the horizontal or x axis does provide a estimate of σ_{d_0} (given that the beam error ellipse is small in comparison), which is used to gain a measure of the beam profile in the x direction. From [76], σ_{d_0} found in this way was 43 μmwhich when subtracted off in quadrature from the width of the d_0 distribution for vertical going tracks, results in a measurement of the beam envelope width in x of 157 $\pm$ 7 μm (averaged over all data periods in 1990). The magnitude of this width justifies treating the error on the mean as negligible initially.

The relatively large error contribution in x that the beam envelope gives to the mean primary vertex position, means that in principle fitting event-by-event for the primary vertex position may do better. A number of different methods were

investigated to this end, all of which suffered from the common problem that the primary vertex position was easily pulled towards secondary vertex positions if both fits contained some tracks in common. This bias could be removed if tracks used in secondary vertex fits were excluded from any primary vertex fit, but frequently this left too few tracks available for the primary fit to be either possible or result in an error competitive with using the mean position. Because of these considerations, the mean primary vertex position as described above was used in all subsequent analysis as being the estimate most likely to be free from bias with respect to reconstructing projected decay lengths.

5.3.4 The Secondary Vertex Fit

The error in extrapolating tracks back towards the interaction point from the Vertex Chamber radius, results in a 'smeared out' view (see for example Figure 5.20(b)) of the vertex topology and is a difficult environment for any secondary vertex finding algorithm to discriminate which tracks genuinely originate from a decay vertex and which are associated with the primary event vertex.

The method used to fit a secondary vertex in an event hemisphere was described in Section 5.2.6. This method essentially makes a vertex fit to all tracks in a jet and as such may be prone to including the odd track that, although not physically associated with the vertex, happens to fall within the χ^2 cut for the rejection of such tracks. To test this, a different technique is compared that in principle is more selective in the choice of tracks to be included in the fit.

The new technique attempts to find the best three-track vertex possible from the input tracks. In order to reject combinations likely not to have originated from a B decay, the sum of the measured charge was required to be ± 1. The remaining combinations are then fitted to a common vertex using the method detailed in Appendix C. Finally, the combination with the best χ^2[9] is taken to be the vertex candidate for the jet in question, providing the probability is greater than 1%.

The best three-track fitter is found to be slightly ($\sim$2%) more efficient at selecting tracks from the B decay chain over the background when compared directly to the old method of fitting. This is the case when forming vertices both at the hemisphere level and at the jet level with y_{cut} set at 0.01. This emphasizes that the dominant effect on the track content of the vertex fit is the sample of tracks input to the fitter itself, rather than the action of any fitting algorithm in being able to strip away tracks inconsistent with a secondary vertex. Specifically, when applied to physics tracks in jets ($y_{cut} = 0.01$), this method finds vertices in B jets with 66.2 % of the tracks originating from the B decay chain i. e. two out of the three tracks.

[9]For three tracks in the vertex fit, the χ^2 is always for one degree of freedom.

The B-tagging efficiency and purity from the projected decay length method based on the best-three track fitter, is found to be improved by a few percent over the whole range of cut values as one might expect from the slightly higher b-track content. In addition, this method is inherently less sensitive to the accuracy of simulating in Monte Carlo the track multiplicity of secondary vertices seen in the data. The accuracy of the fit coordinates is a strong function of how many tracks are included in the fit [10] and, of course, where they originate. In general, the level of agreement between data and Monte Carlo, with respect to the quality of vertices formed is superior for the best three-track method. Figure 5.14(a) compares the χ^2-probability for the vertex fit between data and Monte Carlo which shows reasonable agreement over most of the range but does indicate an excess of poorly measured vertices in the data. That this discrepancy does not lead to any systematic effect in the vertex position, can be seen in Figure 5.14(b). There is generally good agreement in both coordinates of the vertex point between data and Monte Carlo as a function of the fit χ^2. As expected, the mean vertex position is independent of the χ^2 for the fit. Figures 5.15(a) and (b) present the result of the fit in x and y with respect to the mean beam position. The plots indicate firstly that there is no obvious bias in either coordinate but secondly that the data is systematically broader in the tails of the distribution. This behaviour stems directly from the systematic discrepancy observed in the d_0 distribution of Figure 4.20(c) and filters through finally to also be present in the projected decay length variable. This effect is discussed further below and in Chapter 6, where possible causes are offered and a remedy relevant for the lifetime analysis is found.

Figures 5.15(c) and (d) show the distribution of errors obtained in x and y and the comparison with data whereas, (e) and (f) give the major and minor axes of the error ellipse defined by σ_x, σ_y and their correlations. In general the agreement can be seen to be reasonable.

For the reasons outlined above, the best three-track method is preferred over the original technique and is used in the subsequent lifetime analysis.

5.3.5 Results and Cross-checks

After combining all of the modifications described above into the original method, the flavour discrimination possible with the technique is presented in Figure 5.16(a). Those events containing lifetime information have clear projected decay length positive tails, including $c\bar{c}$ events which are clearly separated from the u,d,s and b samples. Figure 5.16(b) shows the B-tagging efficiency and purity performance

[10] To first order, for tracks with similar errors, the resolution on the vertex coordinates goes as $1/\sqrt{N_{trk}}$.

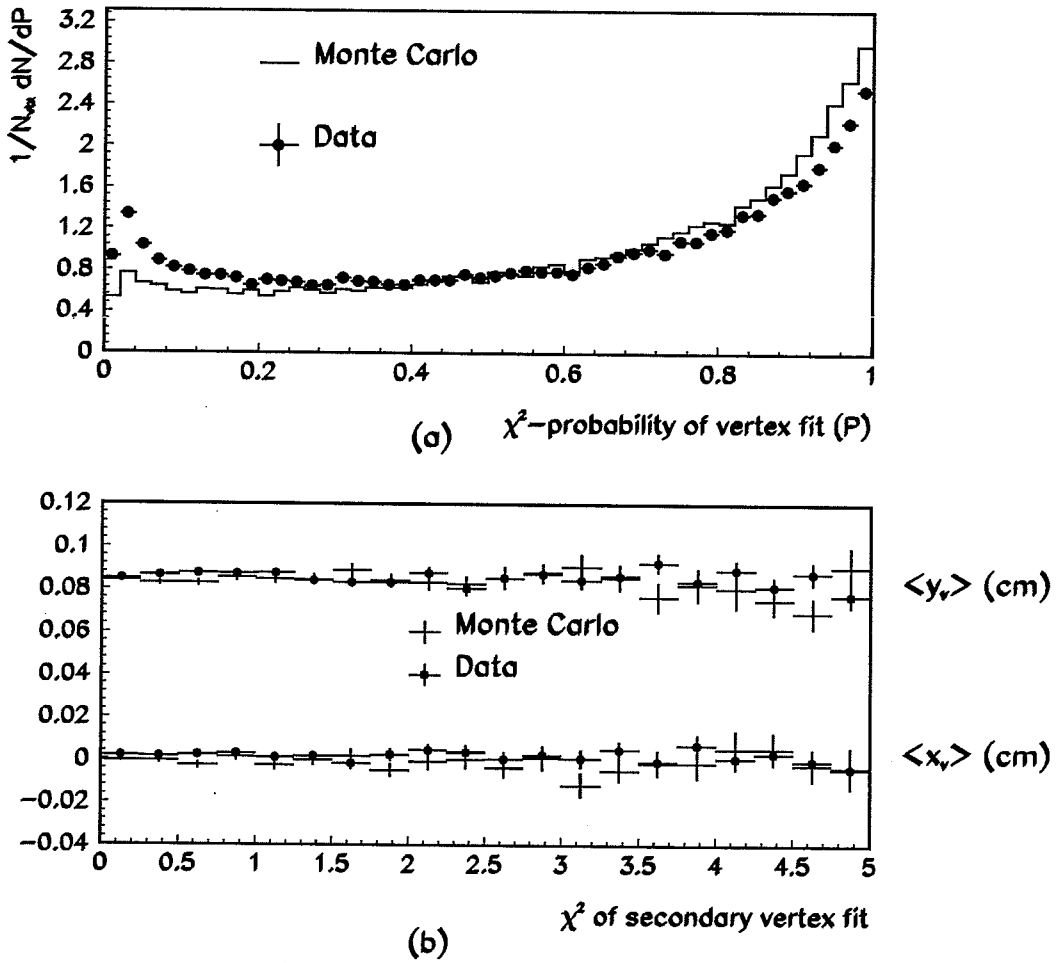

Figure 5.14: (a) Comparison of the χ^2-probability for a secondary vertex fit in a quark jet using the best three-track method. The forward peaked distribution is a result of the method selecting always that fit with the lowest χ^2. (b) The secondary vertex position as a function of the χ^2 for the fit. Note that the positions are uncorrected for the primary vertex position which is at approximately 800 μm in y.

from Monte Carlo, based on the projected decay length normalized by the measurement error. A selection efficiency of, for example, ~20 % is achieved for a purity in $b\bar{b}$ events of ~75 % and represents a performance very competitive with other techniques (e. g. see Section 5.2.1).

The degree to which the measured B-tagging performance can be relied upon to represent the situation in the data, depends ultimately on the level of agreement between data and Monte Carlo presented in Figure 5.17. The shapes of the projected decay length in data and Monte Carlo are seen to suffer from the same systematic broadening in the distribution tails, that was seen at both the individual track level (Figure 4.20(c)) and in the secondary vertex position (Figures 5.16(a) and (b)). This effect (addressed further in Chapter 6), implies that the shape of the efficiency/purity tagging curve expected for data will be somewhat offset to lower efficiencies than

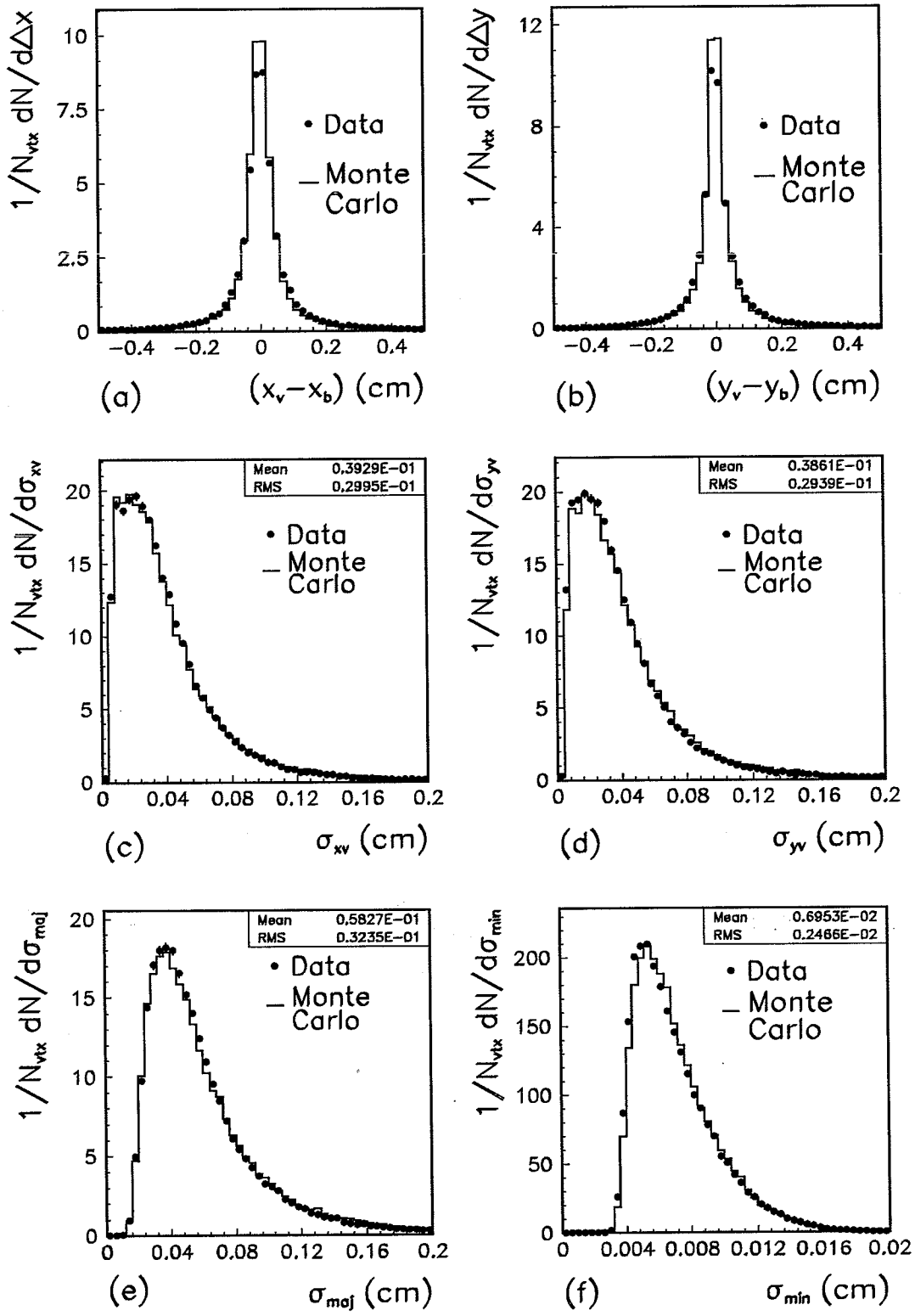

Figure 5.15: Comparing secondary vertex fit quantities between data and Monte Carlo: (a),(b) The interval between secondary and primary vertex positions in x and y. (c),(d) The error on the vertex fit coordinates. (e),(f) The major and minor axes of the secondary vertex fit error ellipse.

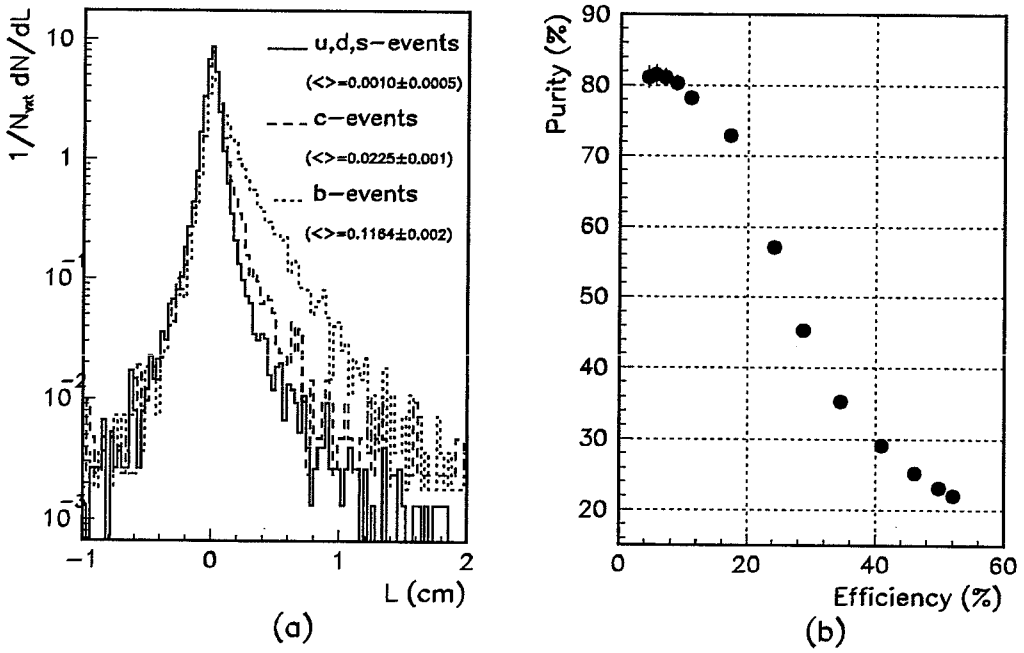

Figure 5.16: (a) The level of flavour separation given by the projected decay length (the two highest energy jets in the event are used). (b) The B-tagging efficiency/purity performance of the projected decay length (the errors are statistical only).

Figure 5.16(b) suggests and no attempt has been made to quantify this offset. There is however, no significant discrepancy between data and Monte Carlo in the tagging efficiency, due to the absolute number of events tagged in each case. We find that the proportion of all quark jets that are tagged by the full procedure[11] is,

$$34.8 \pm 0.1\% \quad \text{in OPAL data}$$
$$35.3 \pm 0.1\% \quad \text{in Monte Carlo.}$$

Further, within errors, the decay length finding procedure is found to give an equal tagging efficiency for all flavours.

That the method is truly sensitive to the B lifetime and not just some peculiarities of the kinematics or geometry of $b\bar{b}$ events, is shown firstly from the Monte Carlo, by increasing the mean B lifetime by a factor 1.5 from the nominal 1.3 ps. Figure 5.18(a) shows that a systematically larger tail develops in the sample with the longer lifetime and results in the distribution mean increasing from 0.129 ± 0.002 cm to 0.184 ± 0.002 cm. Figure 5.18(b) compares the projected decay length distribution measured in the data from the quark jets to that based on the third most energetic jet in the event (if existing). Because the least energetic jets are generally the result of gluon fragmentation, this sample is depleted in tracks carrying lifetime information. The measured distribution for the third jet is seen to give an almost

[11]That is, jets for which a decay length was successfully reconstructed.

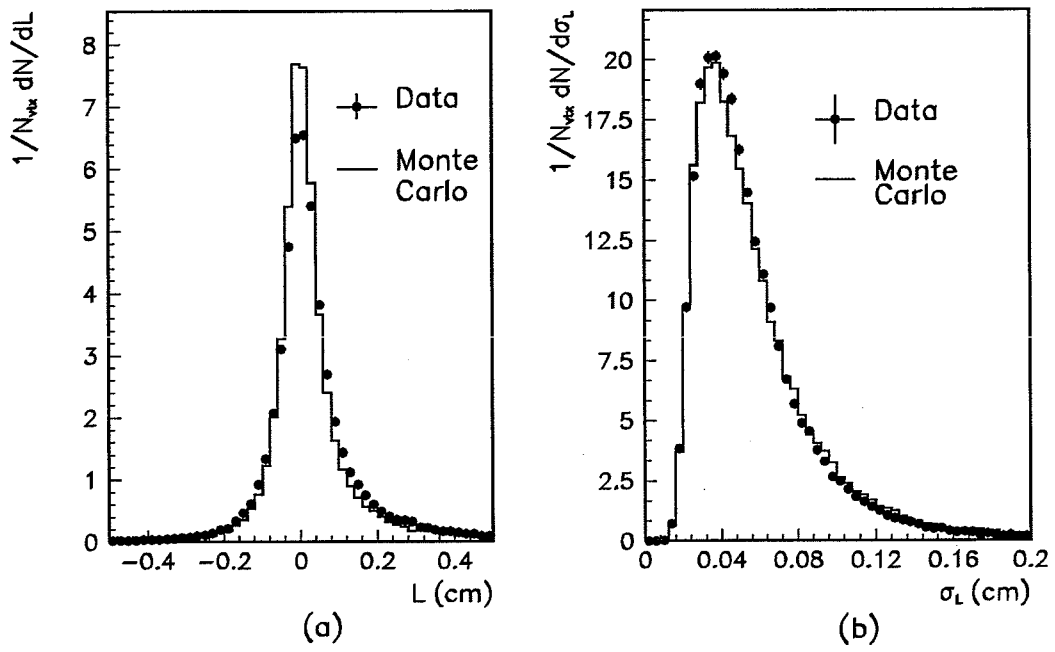

Figure 5.17: Level of agreement between data and Monte Carlo for, (a) the projected decay length, L and (b) the measured error σ_L.

symmetric distribution about $L = 0$ with a mean of $94\pm6\,\mu$m to be compared with a mean of $433\pm4\,\mu$m for the quark jet sample. A final check on the sensitivity of the method, is gained by considering events in the data containing muon candidates. The identification of muons in OPAL is described in detail in [68]. This study demands that a candidate muon be a good match between a track segment in the jet chamber and (at least) a track segment in the surrounding muon chambers. From Monte Carlo, events containing a muon defined in this way consists of, $40.4 \pm 1.5\%$ $b\bar{b}$ events i. e. an increase of a factor $\sim$2 over the generated $b\bar{b}$ fraction. The effect of this increase in b-purity is seen in Figure 5.18(c), where the distribution mean for events containing a muon in the data is $854 \pm 8\,\mu$m, representing almost a factor $\sim$2 increase over the value for all events. Finally, by imposing momentum cuts of $p^{\mu} > 3\,\mathrm{GeV}/c$ and $p_t^{\mu} > 1\,\mathrm{GeV}/c$ (with respect to the jet axis), the purity in b-events increases to $70.1\pm3.7\%$ and results in a mean projected decay length of $0.111\pm 0.002\,$cm.

A cross-check on whether the method is intrinsically sound, can be made by considering the subset of b jets in the Monte Carlo where the secondary vertex fit is made entirely from daughter tracks direct from the decay vertex of the B. For this case the B decay point should be reconstructed, within the measurement error, free from bias and this is studied by constructing the quantity,

$$PULL = \frac{L_{measued} - L_{generated}}{\sigma_L}. \tag{5.15}$$

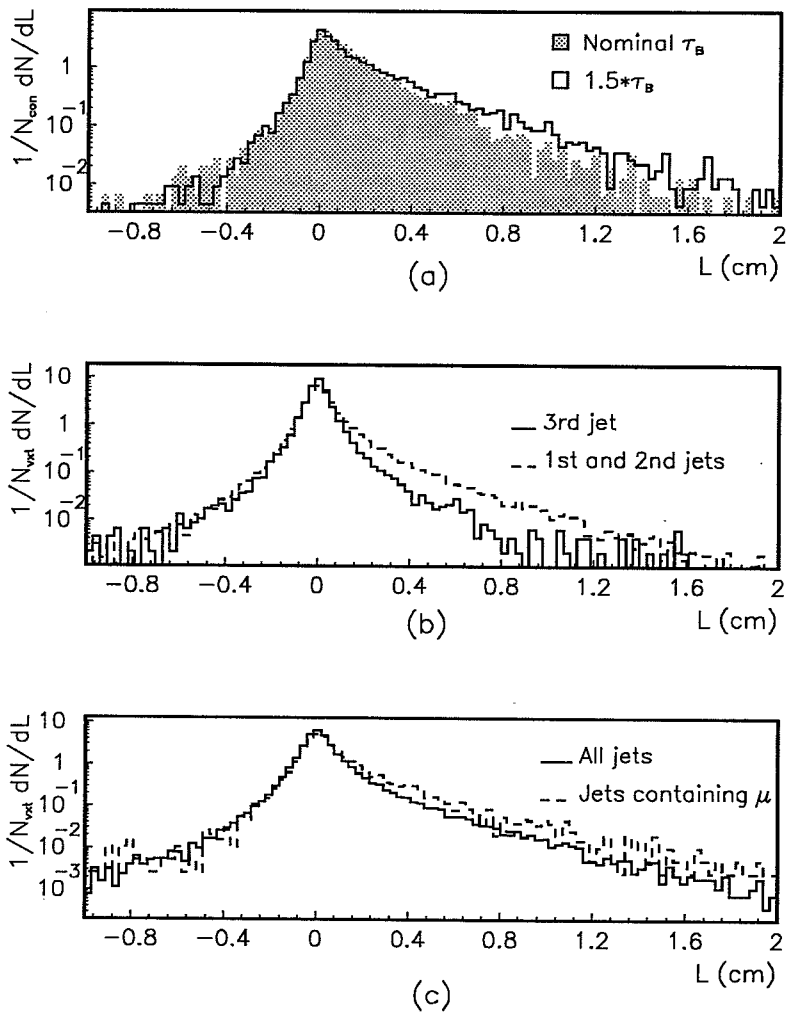

Figure 5.18: (a) Comparing the projected decay length distributions for the quark jets of $b\bar{b}$ events generated with the nominal B-hadron lifetime of 1.3 ps and with a lifetime of 1.5 × 1.3 ps. (b) Comparing the L-distribution measured in the third most energetic jet in the data, with that measured in the quark jets. (c) Comparing the L-distributions from quark jets for all events in the data, with that from only events containing a muon candidate.

Figure 5.19(a) shows that the *PULL* distribution for this class of vertex is indeed a Gaussian centered on zero, and with a width consistent with unity confirming that the measurement error σ_L is also free from bias. Figures 5.19(b)-(d) go on to show that there is a strong correlation between the generated and reconstructed decay lengths in two dimensions and that *PULL* remains free from bias as a function of the decay length and measurement error. That these conclusions are also true for the full three-dimensional decay length has also been checked.

Finally, in Figure 5.20 we present explicitly the vertex reconstruction performance of the method for the 'ideal' case where all three tracks in the vertex fit originate directly from the B decay. In this example a $\bar{B}^0$ was produced of energy

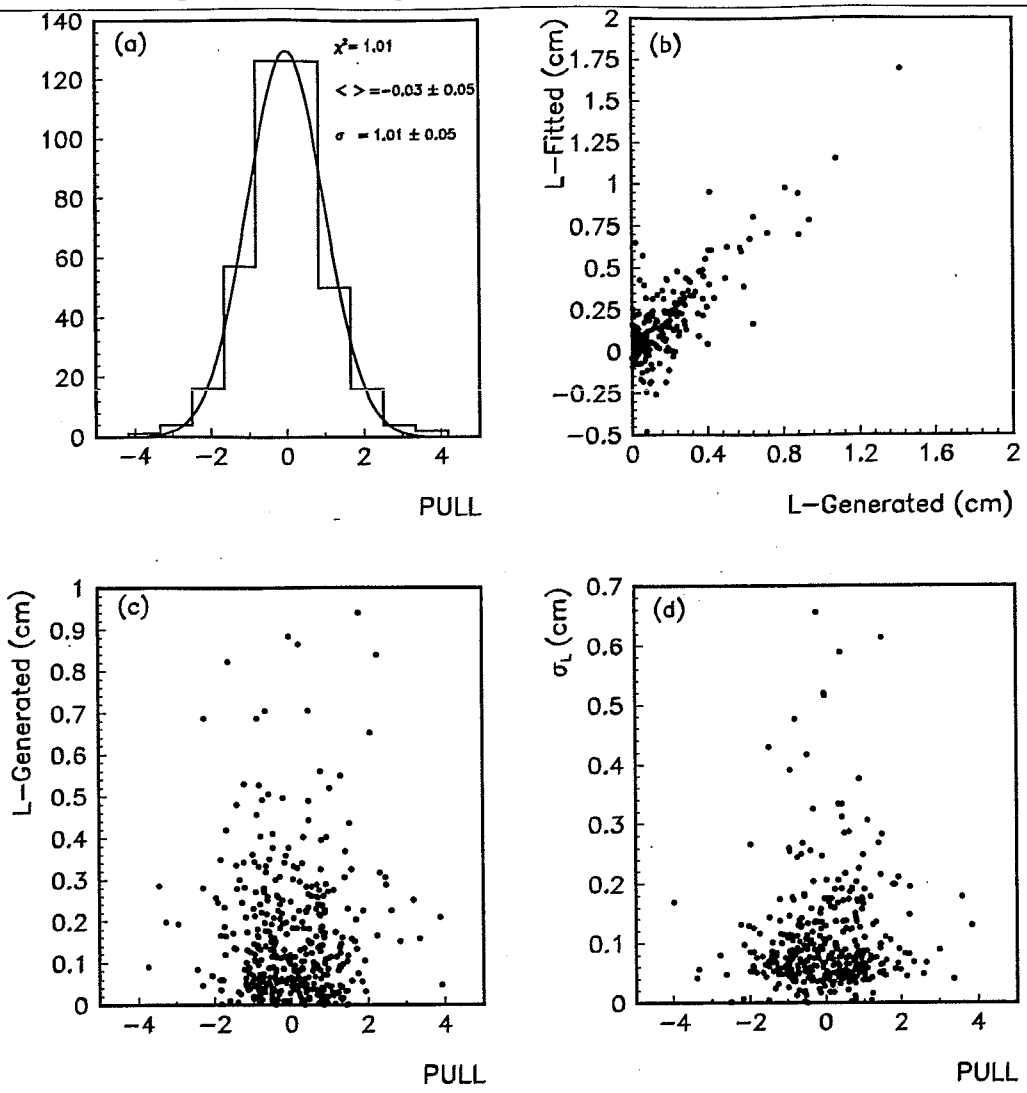

Figure 5.19: (a) The *PULL* distribution. (b) The correlation between the fitted and the generated projected decay length. (c) *PULL* as a function of the generated projected decay length. (d) *PULL* as a function of the measured error on the projected decay length.

42.9 GeV which subsequently decayed in the following way:

$$\bar{B}^0 \rightarrow D^{*+} K^- K^0 \pi^- \pi^+.$$

Figure 5.20(a) shows the decay topology based on the Monte Carlo 'cheat' information. The tracks labelled 1, 2 and 3 are those from the π^+, π^- and K^- respectively and are associated with the reconstructed CT tracks shown in Figure 5.20(b) that were selected and fitted to a secondary vertex position by our technique. The resulting vertex position was reconstructed at $(x, y) = (-1.59, 0.34)$ in comparison to the 'true' position of the decay vertex at (-1.61,0.36), where distances are in centimetres.

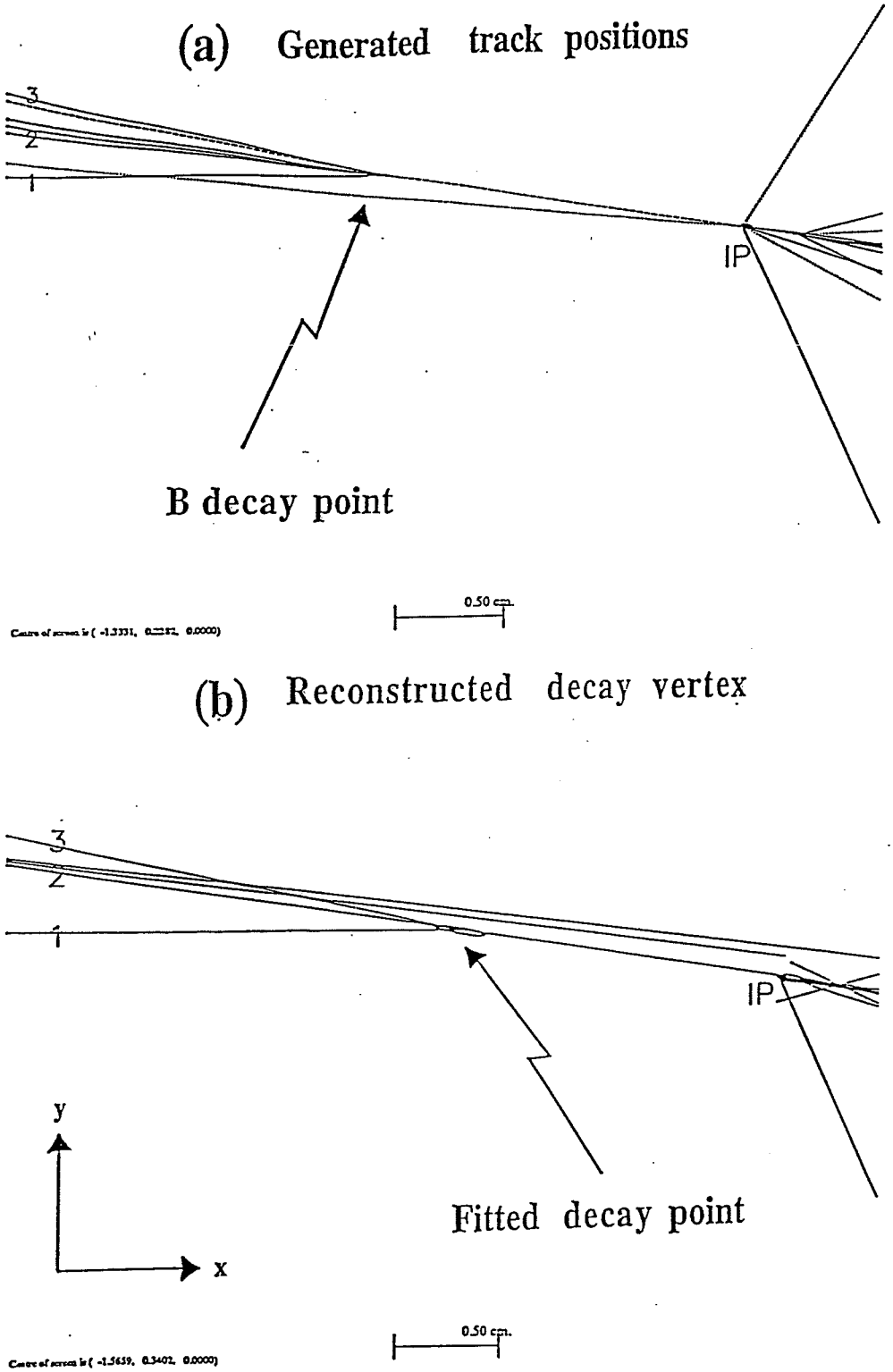

Figure 5.20: B decay vertex reconstruction: (a) The topology of a Monte Carlo generated $\bar{B}^0$ decay. The labelled tracks were successfully reconstructed and used to fit a secondary vertex position which is shown in (b) together with the associated error ellipse. 'IP' labels the meson production point in (a) and some estimate of the beamspot position in (b).

Chapter 6

A Measurement of the Mean B-Hadron Lifetime

6.1 A History and Survey of Measuring the B-Hadron Lifetime

In 1982 the JADE Collaboration at PETRA developed use of the impact parameter technique (described in Section 5.2.5) to set an upper limit on the mean B-hadron lifetime of; $\langle\tau_B\rangle < 1.4\,ps$. This measurement essentially laid the groundwork for what was to follow and represented an enormous improvement over the situation previous to 1982, where the failure to find long-lived, massive particles in hadronic and e^+e^- interactions implied that, $\tau_B < 5\times10^{-8}$ s and $\tau_B < 2\times10^{-9}$ s, respectively.

At this time, no experimental measure existed of the strength of mixing between the first and second fermion generations with the third. There was however evidence from the endpoint of the B-semi-leptonic decay spectrum, that the ratio $|V_{ub}|\,/\,|V_{cb}|$ was small i. e. that the b-quark couples predominantly to the c quark. Under the assumption that the strength of mixing between the second and third generations was the same as that existing between the first and second, it follows that the B lifetime should be of order 0.1 ps. Hence it came as a surprise when in 1983, the MAC and MARK II Collaborations at PEP, were able to infer that the lifetime was around 1 ps from the impact parameters of high momentum leptons in e^+e^- annihilations. Thus the new measurement provided for the first time a measure of $|V_{cb}|$ which in turn, after imposing unitarity constraints, led to the first complete picture of the magnitudes of all CKM elements.

The following year (1984) saw confirmation of the result by the DELCO experiment at PEP and soon after by TASSO and JADE at PETRA. All of these lifetime results, and including those to the present day, are from e^+e^- storage ring facilities able to produce B hadrons in a relatively clean environment and in sufficient numbers. At PEP and PETRA $b\bar{b}$ events accounted for 9 % of the hadronic cross section while at LEP they constitute 22 % of all hadronic decays of the Z^0. Although

the absolute cross section for B production from $p\bar{p}$ colliders is higher, it comprises only a small fraction of the total interaction rate and makes the identification of B-hadrons from the background difficult. [1]

6.1.1 Impact Parameter Measurements

Inclusive Leptons

As seen in Section 5.2.1, prompt lepton candidates can be isolated by imposing cuts on momentum and especially momentum transverse to a jet axis. These leptons, being tied to the decay vertex of the B, show on average discernibly positive impact parameter distributions when defined as in Figure 5.5. All of the recent lepton analyses extract a lifetime measurement from this distribution by using the method first introduced by the MARK II Collaboration [77] whereby the distribution is parameterised as the sum of five contributions,

$$P(\delta) = f_b P_b(\delta, \tau_b) + f_{bc} P_{bc}(\delta, \tau_b, \tau_c) + f_c P_c(\delta, \tau_c) + f_{pk} P_{pk}(\delta) + f_{mis} P_{mis}(\delta). \quad (6.1)$$

The contributions P_i, in order, correspond to: leptons directly from the decay of the B, leptons from cascade D-hadron decays in $b\bar{b}$ events, primary D-hadron leptons, leptons from pions and kaon decay and hadrons misidentified as leptons. The P_i are all normalized to unity and are weighted by factors f_i which are the fractions of the overall sample due to process i.

Analytic forms for the three contributions from heavy flavour lifetimes are usually obtained as the convolution of an underlying physics function, extracted from Monte Carlo at the generator level [2], with a resolution function measured from the data. These distributions are then simply scaled to be valid for any input lifetime. Of the remaining two contributions, the pion and kaon impact parameter distribution can be estimated from Monte Carlo whereas the misidentified hadron contribution can usually be estimated from the data. The B-lifetime is derived from a maximum likelihood fit of Equation 6.1 to the data, with $\langle \tau_B \rangle$ the only free parameter. The lepton impact parameter technique provided the the first credible B lifetime determination.

Even to the present day, the most accurate measurements still derive from this method largely due to it's relative insensitivity to the details of heavy-flavour hadron production and decay. Lepton spectra from B and D decay, as seen in Section 4.2.4, are both well known and relatively insensitive to the details of the primary heavy

[1] The situation here is however changing fast, with the CDF experiment at the Fermilab $p\bar{p}$ collider expected to produce lifetime measurements soon and the fixed target experiment E653, also at Fermilab, reporting measurements at present on specific B-hadron lifetimes (see Section 6.1.2).

[2] i. e. the impact parameters of particles taken before detector simulation but only for those whose reconstructed tracks pass all subsequent kinematic and lepton identification requirements.

quark fragmentation. All measurements of $\langle \tau_B \rangle$ to date via this method are collected in Figure 6.1.

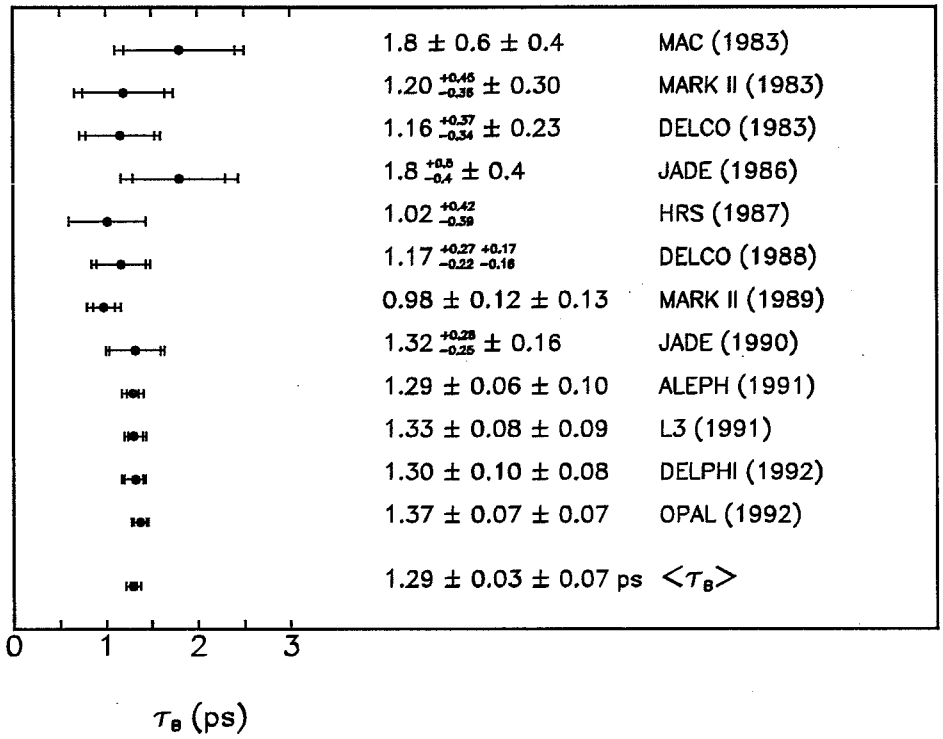

Figure 6.1: World measurements [78] of the mean B-hadron lifetime using the impact parameter distribution of inclusive lepton candidates The inner error bar gives the statistical error and the outer bar gives the total error i. e. the sum of the statistical and systematic errors added in quadrature. The mean value is calculated by weighting individual results by their total error. The statistical error on the mean is the resultant of all individual statistical errors and the overall systematic error is set to the smallest systematic error contributing. (The most recent measurement from this method, is a preliminary result from the ALEPH Collaboration, who measure $\tau_b = 1.45 \pm 0.03 \pm 0.06$ ps [79] representing the most accurate determination of $\langle \tau_B \rangle$ ever. It is interesting to note that this value is 2.4σ higher than the present world average).

Hadrons

There exist in addition, five measurements of $\langle \tau_B \rangle$ based on the impact parameters of all hadronic tracks. This method was seen to be sensitive to the B lifetime in Section 5.2.5 and in general has the advantage of smaller statistical errors. The price to pay however, is a greater dependence on the less well known details of B production and decay which lead ultimately to measurements with larger systematic errors than in the case of lepton-based measurements.

Past measurements using this method have generally used some form of $b\bar{b}$ enrichment of their data samples to benefit from the subsequent increase in sensitivity to the lifetime. TASSO for example made use of the boosted sphericity product

reviewed in Section 5.2.4. DELPHI on the other hand, employ no such enrichment scheme at all. The B lifetime is subsequently extracted by comparing the mean of the δ distribution from data, with Monte Carlo simulations for different B lifetimes. Figure 6.2 collects together all measurements to date.

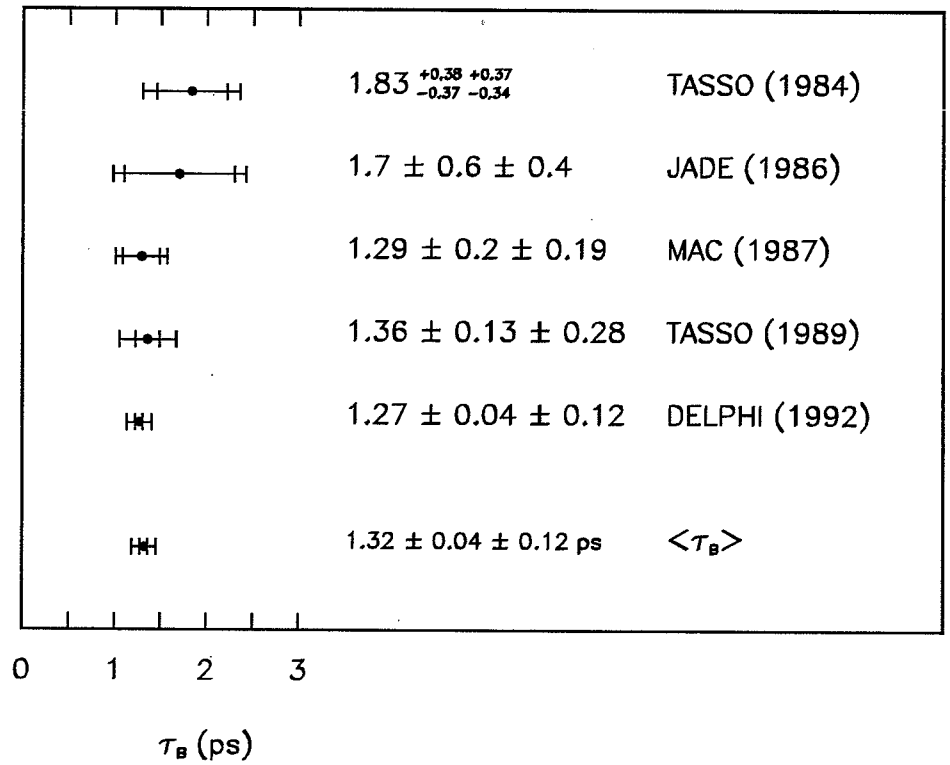

Figure 6.2: World measurements [80] of the mean B-hadron lifetime using the impact parameter distribution of hadronic tracks. The mean value is calculated in the same way as for Figure 6.1.

6.1.2 Non Impact Parameter Measurements

Mean B lifetime

Only four published measurements of $\langle\tau_B\rangle$ exsist that are not based on using track impact parameters but rely on the reconstruction of secondary vertices.

Of these, two form a decay length between the positions of a primary vertex estimate and a secondary vertex fitted inside a B jet. A measurement by the TASSO (1989) Collaboration was based on the projected decay length variable described in Section 5.2.6. The best three-track vertex is formed from quality tracks in event hemispheres and used to calculate the projected decay length using the event sphericity axis to approximate the B-hadron direction. The B lifetime is then derived by finding the best fit of the Monte Carlo to the data as $\langle\tau_B\rangle$ varies in the simulation. The second measurement, from OPAL, attempts to tag the presence of a B meson by reconstructing the di-lepton decay vertex of a J/ψ. A signal consisting of 45 events

is found from the 1990 multi-hadronic data set. The full three-dimensional decay length (see Equation 6.4) distribution is formed and $\langle\tau_B\rangle$ extracted via a maximum likelihood fit.

The remaining two measurements derive from use of the 'dipole' length which exploits the fact that to some approximation, B hadrons are produced back-to-back, in $b\bar{b}$ events. This method forms secondary vertices in both jets of two jet events and uses the distance between them as an estimate of the distance between the B and $\bar{B}$-hadron decay vertices. If for whatever reason, one vertex position is reconstructed 'behind' the other, the dipole length acquires a negative sign.

The first of these measurements from TASSO (1989), defines an event axis in the $r-\phi$ plane by translating the position of the projected event sphericity axis until the variance of the crossing points of all tracks in the event with this axis is minimized. The event is then divided into two jets by the plane perpendicular to the event axis and the average crossing point of all tracks in the jet used to define a vertex position. The second dipole measurement, from the JADE (1990) Collaboration, again splits the event into two jets using the sphericity axis. The tracks from each jet are then fit to a secondary vertex in the $r-\phi$ plane, the position of which is constrained to lie on the projected sphericity axis.

Presentation of the results of these four measurements is deferred until the end of this chapter, where in Figure 6.13 they are presented along with the result of this analysis.

Specific B-Hadron Lifetimes

Secondary vertex finding is necessarily used in direct attempts to measure the lifetimes of individual hadron species, since to make separation possible most of the decay chain must be reconstructed. Figure 6.3 presents all measurements on this subject to date.

The MARK II and ALEPH Collaborations both use the channel $D^{*-} \rightarrow \ell^- \nu$ to tag B^0 mesons. In addition, ALEPH tag B^+ mesons via the channel $B^+ \rightarrow \bar{D}^0 \ell^+ \nu$ in a determination of τ_{B^+} from which they quote a value for τ_{B^+}/τ_{B^0} of $0.96^{+0.69}_{-0.49}$. Within the rather large errors the results are in agreement between the two experiments and also with previous (indirect) measurements of τ_{B^+}/τ_{B^0} by ARGUS and CLEO [82]. Finally, there are some recent results from the fixed target experiment E653 at Fermilab. An incident 600 GeV/c pion beam, is used to produce $b\bar{b}$ events identified by the presence of muons with large momenta transverse to the beam line. To date, about ten reconstructed charged and neutral B-hadron vertices have been identified and the results are shown in Figure 6.3.

To conclude this brief review, it is interesting to note in passing that if $\tau_{B^+}/\tau_{B^0} \neq 1$, one could reasonably expect a difference to exist in $\langle\tau_B\rangle$ between semi-leptonic

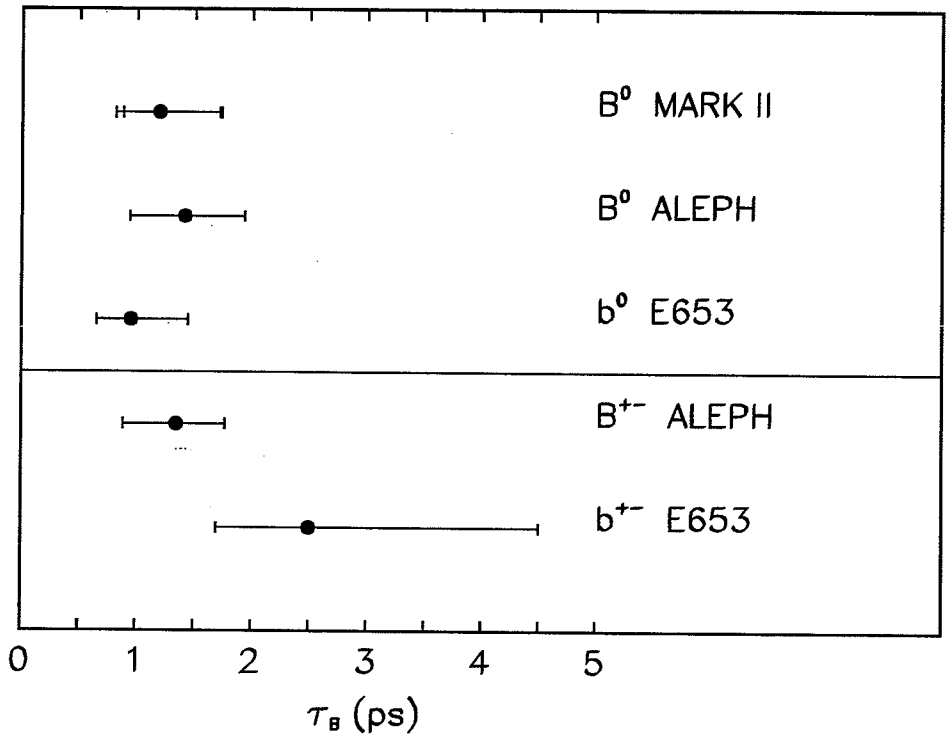

Figure 6.3: World measurements [81] of specific B-hadron lifetimes. Note that the E653 result does not separate B mesons from baryons hence use of the lowercase 'b'. The ALEPH Collaboration have recently used the identification of identified $\Lambda\ell$ combinations in B jets, to make the first (preliminary) measurement of the b-baryon lifetime, $\tau_b(\Lambda_b) = 1.12^{+0.29}_{-0.26} \pm 0.18$ ps [79].

and hadronic-based analyses. This is a consequence of the two approaches not measuring exactly the same physical quantity. The semi-leptonic analyses reviewed in Section 6.1.1, determine the B lifetime averaged over all B-hadron species, weighted by the product of their respective semi-leptonic branching ratios and production cross sections. Whereas analyses based on all hadronic decays of the B, are measuring the B lifetime averaged over all B-hadron species weighted only by their production cross sections.

Based on the assumption that the semi-leptonic widths for B^0 and B^+ decay are equal, Jaros [83] points out that for $\tau_{B^+}/\tau_{B^0} \neq 1$, it follows that $\tau_{lepton} > \tau_{hadron}$. The effect is very small with only a 10% variation in the lifetimes expected for a τ_{B^+}/τ_{B^0} range of 0.5 to 2.0. Hence the conclusion must be that the accuracy of existing and probably future measurements by any of the current methods, are insufficient to test this prediction.

6.2 Measuring the Mean B-Hadron Lifetime

This section deals with details of extracting a B lifetime measurement from the projected decay length distribution. In general, this can only be achieved by comparing the data with a distribution whose B-hadron content has a known lifetime. Practically, this invariably means use of Monte Carlo techniques. In order for the resulting measurement to be at all meaningful, a high level of agreement must exist between the simulation and the data, or at the very least any discrepancies understood to the point where they can be accounted for via corrections and systematic error assignments.

The question of overall agreement is dealt with now to be followed by an account of all the choices made leading to the eventual result.

6.2.1 The Folded Distribution

The level of agreement between data and Monte Carlo for the projected decay length variable (L) was seen in Figure 5.17. It is important to understand the nature of this discrepancy, particularly with respect to any lifetime content of the distribution.

Figure 5.17(a) illustrates that the negative or 'resolution' tail of the distribution is systematically underestimated in the simulation. It is also evident that the simulation in general underestimates the fraction of tracks found in the distribution tails. That this discrepancy is largely independent of lifetime information has already been shown in part, from the results of Section 5.3.5. Here we saw that the disagreement was present at the same level in the distribution for the third highest energy jet in an event, which is known to be somewhat depleted in lifetime content.

Chapter 4 presented the quite detailed level of Monte Carlo modelling undertaken to reproduce data in the Vertex Chamber. Although the major effects are now accounted for, this subject is an on-going process and as always residual problems may still remain. It transpires however that in order to account for the size of discrepancy seen at the track (Figure 4.20) and vertex level (Figures 5.15(a), (b) and 5.17(a)), one has to consider the modelling of tracks extrapolated into the Vertex Chamber from the surrounding Jet Chamber.

Following an observation [84] made using a fast simulation (SMEAR mode [85]) of the OPAL detector, an investigation was undertaken to determine at what level CT tracks contain the 'wrong' CV information. SMEAR mode indicated that impact parameter distributions of tracks containing CV hits in the data were better modelled, especially in the distribution tails, if the Monte Carlo track sample contained a proportion of tracks containing no CV information. A possible scenario where CV information on tracks would be effectively 'ignored' in this way, is if the CV hits were not physically associated with the matched CJ track extrapolation.

Thus a check was made to find if the impact parameter distribution for tracks containing no CV hits is consistent with that obtained when the wrong CV track segment is associated with a CT track. This effect is a potential 'explanation' for the overall discrepancy. Using 'cheat' information which allows a correspondence to be made between a generated particle and a reconstructed track, it is possible to determine when a CJ track segment has been matched to a CV segment which does not share the same origin. Figure 6.4(b) shows the result of this study, based on 1500 events, where clearly the distribution for tracks matched to the wrong CV information is consistent with that where no CV hits are present in the track fit.

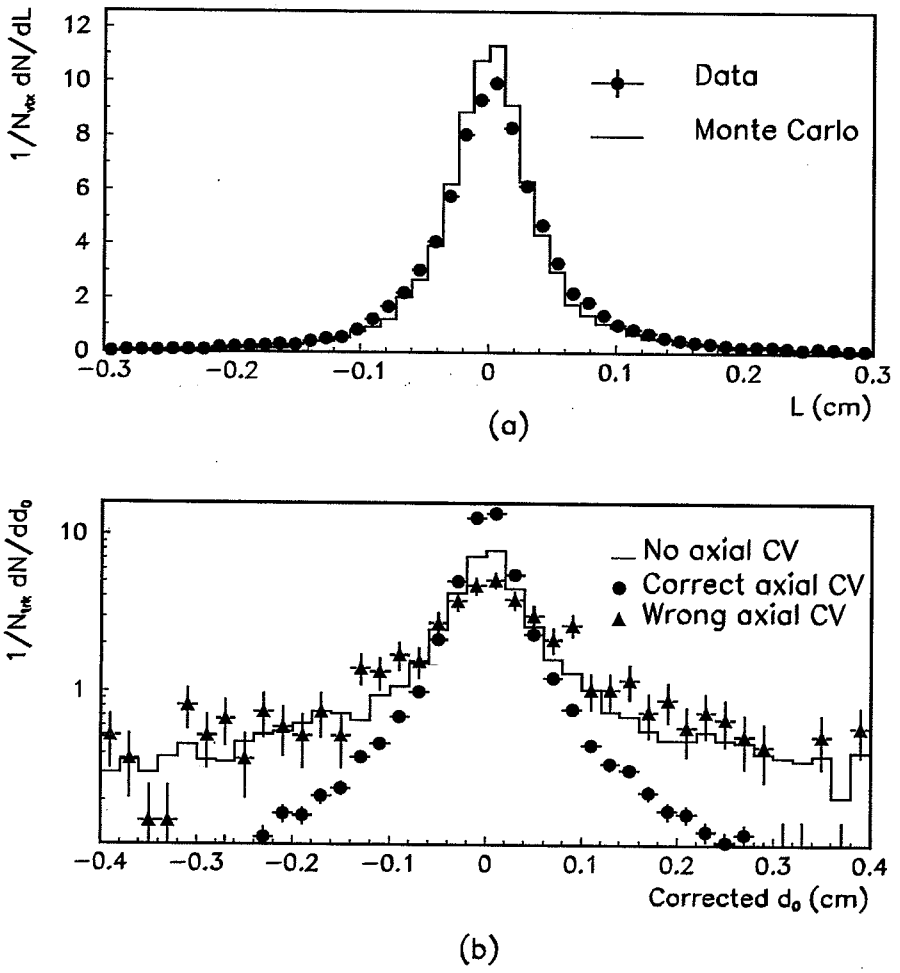

Figure 6.4: (a) Comparing decay length distributions for the third highest energy jet in an event, between data and Monte Carlo. (b) The impact parameter distribution for CT tracks containing no CV information compared to cases where tracks are matched to the wrong CV tracks segment. For comparison, the distribution for tracks matched to the correct CV hits is also shown.

The wrong match was seen to occur in Monte Carlo on $4.4 \pm 0.1\%$ of all tracks containing CV hits. For this effect to account entirely for the discrepancy seen in the impact parameter and similar variables, we estimate that the problem would need to occur at the 10% level. The expectation is for this effect to be more frequent in

the data due to systematic shifts in the positions of CJ track segments not modelled by the Monte Carlo. That this could be the case is confirmed by the marked degradation in data/Monte Carlo agreement in the impact parameter distribution, when considering tracks containing CJ hits only.

One solution, to regaining agreement in the L distribution, is to essentially degrade the resolution in the Monte Carlo distribution by a 'smearing' technique. This is described further in Section 6.3 where it is used as a cross-check on the final method. The preferred solution however, is use of a **folded** distribution. This technique involves subtracting the resolution tail of the L distribution from the lifetime tail to leave a single, positive decay length tail to the distribution. Thus contributions to the L distribution that are symmetric with respect to the lifetime signing i. e. resolution type effects are, to first order, cancelled leaving in principle just the lifetime information from the initial distribution [3]. In fact, besides intrinsic physics reasons, there are very few systematic effects that could influence the lifetime tail of the L distribution in a different way to the resolution tail (or vice versa). That this is a possibility however is addressed in the assigning of systematic errors to the measurement in Section 6.4.

Because the L distribution is almost symmetric close to the $L = 0$ region, statistical fluctuations in bin contents can result particularly in the first few bins of the folded histogram, having negative contents. This region, for L measurements up to about the magnitude of the resolution (σ_L), can contribute no significant lifetime information and is therefore unimportant. Hence in all subsequent applications of the folded distribution, the region $|L| \leq 0.08\,\mathrm{cm}$ is discarded before the folded distribution is formed.

The flavour composition of the folded distribution is presented in Figure 6.5. The distribution is seen to be dominated by the contribution from $\mathrm{b\bar{b}}$ events in contrast to the situation for the full L distribution (Figure 5.8) where, of course, the contribution is at about the level of $\mathrm{BR}(\mathrm{Z^0} \rightarrow \mathrm{b\bar{b}})$. This represents an important advantage to use of the folded plot, since any dependence on the details of modelling light flavours has been significantly reduced and at least for the case of u, d, s events all but eliminated.

6.2.2 The Method

The measurement is made by varying the mean B-hadron lifetime in the simulation distribution to find the best fit to the data. The following χ^2 is formed between the

[3] This conclusion is only approximately true since the measured L-distribution takes the analytical form of a Gaussian (containing all symmetric contributions) convoluted with an exponential (containing all the event decay length information).

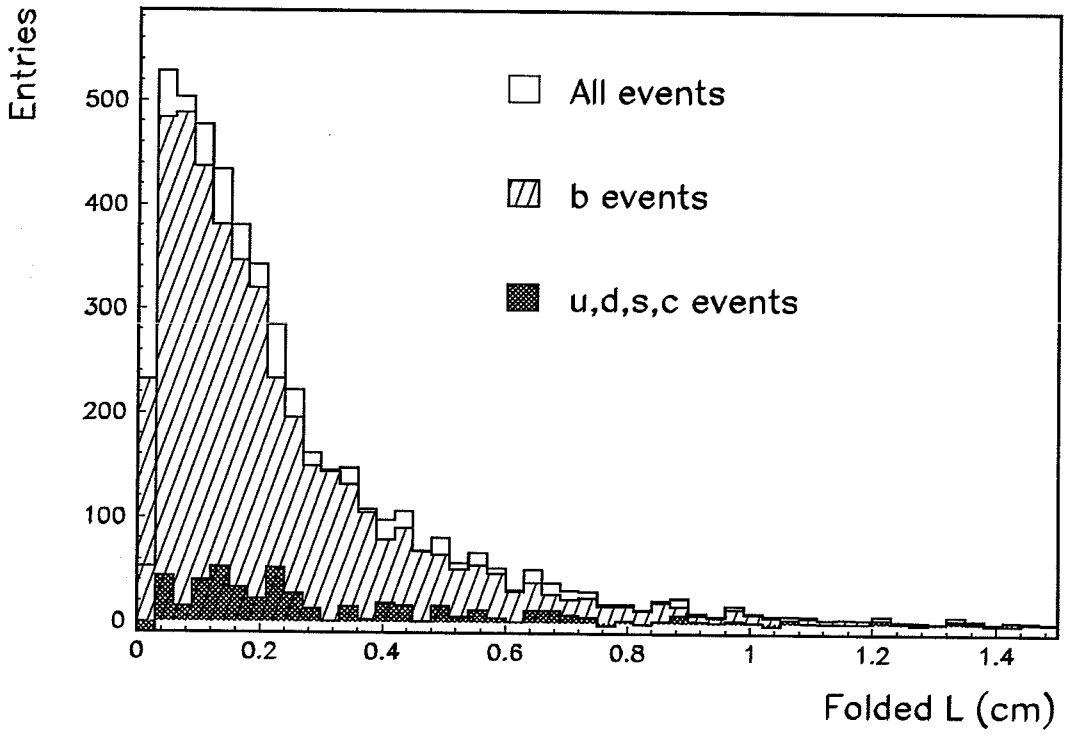

Figure 6.5: The event flavour composition of the folded L distribution. Both quark jets are used.

two normalized distributions,

$$\chi^2(\langle\tau_B\rangle) = \sum_i \frac{[N_i^{data} - N_i^{sim}]^2}{[(E_i^{data})^2 + (E_i^{sim})^2]} \tag{6.2}$$

where N_i is the sum of weights of entries in bin i and E_i is the error on that sum. The normalization is based on the number of events passing all selection and analysis cuts. This χ^2 is minimized with respect to the B lifetime present in the Monte Carlo. The variation of N_i^{sim} with $\langle\tau_B\rangle$ was evaluated by a weighting technique [4] to transform the Monte Carlo distribution generated with a mean lifetime τ_B^{old} to one of τ_B^{new}. This weight is just the ratio of exponential decay probability distributions,

$$W_{life}(t, \tau_B^{old}, \tau_B^{new}) = \left(\frac{\tau_B^{old}}{\tau_B^{new}}\right) \exp\left(-t.\frac{\tau_B^{old} - \tau_B^{new}}{\tau_B^{old}\tau_B^{new}}\right). \tag{6.3}$$

The overall weight for the event, W, is then the product of all weights for each B hadron. Additional weights are used extensively in the evaluation of systematic errors discussed in Section 6.4.

6.2.3 The OPAL 1990 Data

The data sample used was collected by the OPAL detector during the 1990 running period of LEP, at centre-of-mass energies ranging from 88.2 GeV to 94.2 GeV.

[4] This avoids the need to generate many separate Monte Carlo samples of different $\langle\tau_B\rangle$.

Multi-hadronic Z^0 decays were selected on the basis of energy clusters in the electromagnetic calorimetry and charged track multiplicity. Clusters were required to have,

- an energy of at least 100 MeV in the barrel region
- at least 200 MeV in the endcaps. In addition, clusters in the endcaps must contain at least two adjacent blocks.

Tracks were required to have,

- at least 20 measured space points
- $|d_0| < 2\,\text{cm}$ and $|z_0| < 40\,\text{cm}$
- $p_{xy} > 50\,\text{GeV}/c$.

A multi-hadronic candidate must then pass the following four requirements:

- at least 7 clusters
- at least 5 tracks
- $\frac{\sum E_{clus}}{\sqrt{s}} \geq 0.1$, where E_{clus} is the energy of a single cluster
- $\frac{\sum (E_{clus} \cdot \cos\theta)}{\sum E_{clus}} \leq 0.65$, where θ is the polar angle of the cluster.

The data is divided into periods which correspond to continuous LEP physics runs between shutdowns or machine development periods. Physics runs last typically from a few days to a couple of weeks and for 1990 produced yields of multi-hadronic events listed in Table 6.1. Period 9 is affected by an uncorrected hardware fault in the Jet Chamber which results in the tracking close to wire planes being degraded for some runs. For this reason, Period 9 data is removed from the analysis. In addition, the Vertex Chamber and Jet Chamber are required to be fully functional and working optimally for the data to be accepted which, results in the loss of 3,593 multi-hadronic events. These considerations reduce the 1990 data set to 125,645 multi-hadronic events. From [30] this selection is estimated to be 98.4% efficient with a background contamination of 0.2% from Z^0 leptonic decays and two-photon scattering events. This background level is reduced still further by the containment requirement of the physics cuts (Section 5.3.1), which requires there to be at least three standard tracks in each of the two quark jets.

The Monte Carlo sample described in Chapter 4, for practical reasons simulates only charged track information in the Central Detector. The absence of neutral clusters implies that the Monte Carlo cannot be passed through the same multi-hadronic selection applied to the data. To ensure there is no resulting bias from the

Period	Selected multi-hadrons
8	4,983
9	16,134
10	15,148
11	5,324
12	8,786
13	6,519
14	6,127
15	11,458
16	13,082
17	8,167
18	17,989
19	31,655
Total	145,372

Table 6.1: The OPAL 1990 multi-hadronic data set. The periods span the time range 23/03/90 to 29/08/90.

event selection a sample of 10800 full detector simulation events (JETSET72) were passed through the multi-hadronic cuts. The result was that 148 events failed the cuts. However, only 17 of these 148 events passed the track multiplicity requirement of the physics cuts listed in Section 5.3.1. We conclude therefore that $17/10800 = 0.16 \pm 0.04\%$ of the Monte Carlo events, that were actually used in the decay length finding analysis, would be expected to fail the multi-hadronic selection applied to the data (if it could be applied) and is thus a negligible effect.

We find that after passing through the full decay length finding process, an L-measurement exists in 44,602 (22,322) of the highest energy quark jets in the data (simulation).

6.2.4 The Measurement

For the lifetime measurement, it is preferred to use only the highest energy quark jet. Since the lowest energy quark jet is more liable on average to be the result of gluon emission, this requirement reduces to a minimum any dependence on modelling QCD effects. Monte Carlo suggests that the highest energy jet in an event is associated with quark fragmentation ~92% of the time. Since our result is ultimately not constrained by lack of statistics, the loss of data associated with tagging events by

just one jet is unimportant to our conclusions.

To ensure the reliability of the lifetime fit, two further analysis cuts are applied. The first requires that the χ^2 probability for the decay length fit (see Appendix D) be better than 1%. This rejects cases where the primary and secondary vertex positions are clearly not compatible with each other within the directional constraint. The probability distribution is presented in Figure 6.6. The second cut is to require

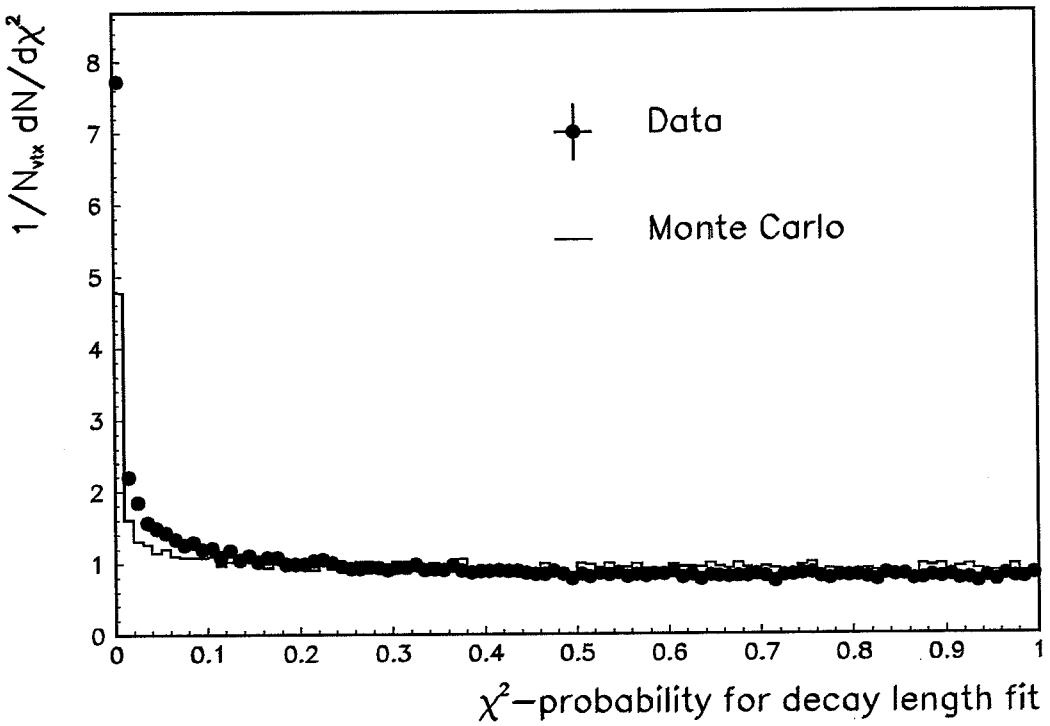

Figure 6.6: The χ^2-probability for the projected decay length fit. Both quark jets are considered.

that the measured error on the projected decay length be less than 0.18 cm. This represents about three times the mean error on L and sits well into the tail of the distribution (see Figure 5.17).

The result of the fit [5] is shown in Figure 6.7 based on an L distribution containing 80 bins before forming the folded distribution and covering the range $|L| \leq 1.5$ cm. The fit corresponds to the following mean B-hadron lifetime,

$$\langle \tau_b \rangle = 1.359 \pm 0.055\,\text{ps} \quad \left(\chi^2/d.o.f. = 38.1/37.0\right)$$

where the error is statistical only.

[5] The minimization of the χ^2 was performed using the MINUIT package [86].

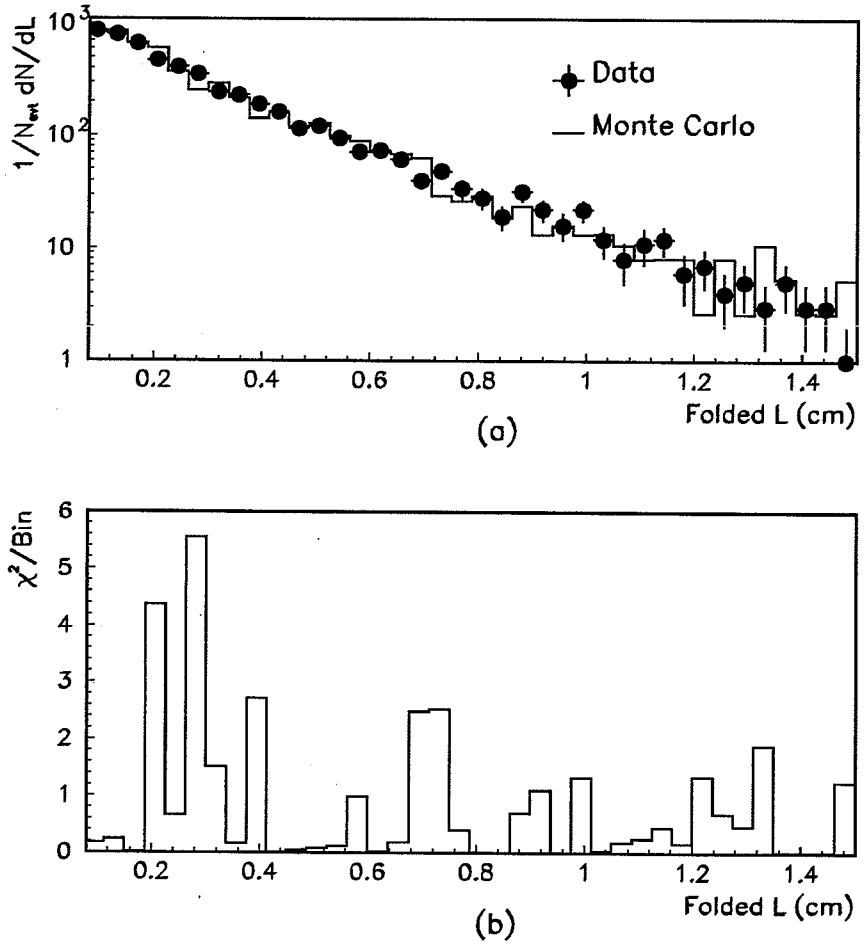

Figure 6.7: (a) The result of fitting the Monte Carlo L distribution to the data. (b) The binned χ^2 formed between the data and Monte Carlo plots.

6.3 Crosschecks of Technique

6.3.1 Consistency Checks

As a test of the lifetime weighting procedure, the $b\bar{b}$ events in the Monte Carlo were replaced by a sample generated at a lifetime of 1.5×1.3 ps. Clearly the initial result should be recovered within errors, for Monte Carlo samples based on any $\langle \tau_B \rangle$ within reasonable bounds. The fit was repeated with the result, $\langle \tau_B \rangle = 1.343 \pm 0.069$ ps.

Although the decision was made to base the result on only the highest energy jet in an event, by way of a consistency check the fit was repeated based only on the second quark jet. The result was, $\langle \tau_B \rangle = 1.292 \pm 0.072$ ps.

The full, three-dimensional decay length follows from the $r-\phi$ projected quantity via

$$L_{3D} = \frac{L}{\sin\theta} \tag{6.4}$$

where, θ is the polar angle of the decaying particle approximated in this analysis

by θ_{jet}. Basing a fit for $\langle\tau_B\rangle$ on the L_{3D} distribution under identical conditions to those used for the two dimensional variable, results in $\langle\tau_B\rangle = 1.363 \pm 0.056$ ps. That the result from both variables is in good agreement confirms that there can be no significant difference between data and Monte Carlo from use of the jet axis as an estimate of particle direction.

6.3.2 Selection Parameters

The choice of all variables concerning the selection of the data sets used for the measurement have been studied to check for possible systematic biases.

Figures 6.8(a) and (b) show that there is no systematic variation in the result as both the distribution binning and fit range are altered. A range of $|L| \lesssim 1$ cm or

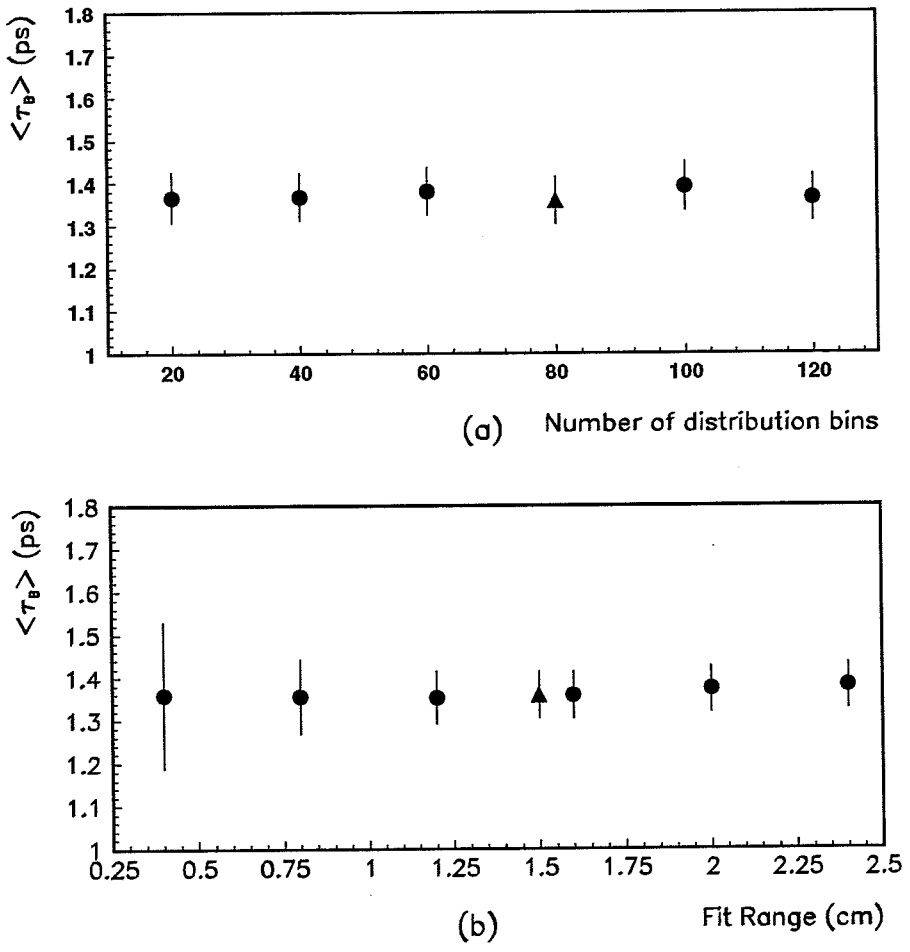

Figure 6.8: The variation of the lifetime fit result as a function of (a) distribution binning and (b) fit range. In both cases the odd point corresponds to our central result.

larger was found to be necessary to ensure that the majority of the lifetime tail was enclosed. That this is important in gaining the best possible statistical error is evident from Figure 6.8(b).

In addition, the positions of the cuts made on σ_L and L were checked for any systematic effect on the lifetime result. The variations observed are presented in Figures 6.9. No obvious systematic trend is seen.

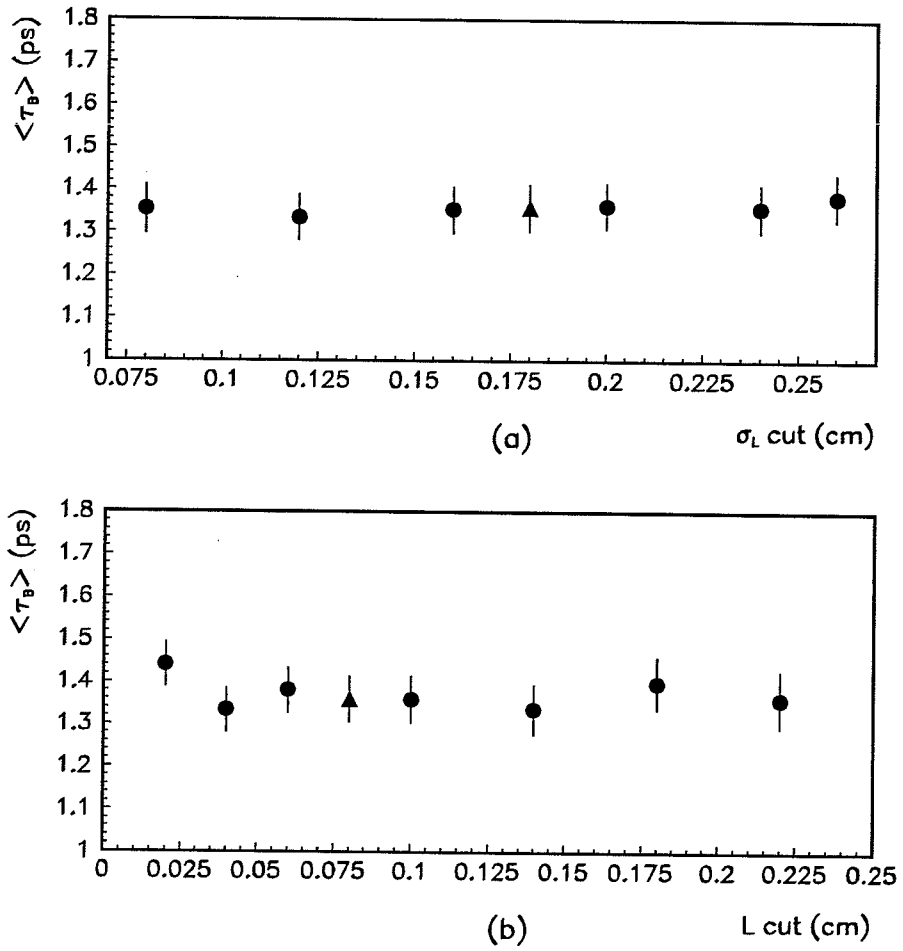

Figure 6.9: The variation in the lifetime fit result as a function of (a) the cut on σ_L and (b) the cut on L before the formation of the folded distribution. In both cases the odd point corresponds to our central result.

6.3.3 Data Sub-Sets

A number of checks have been performed to determine whether data sub-sets are statistically compatible. Table 6.2 shows lifetime fit results based on data sub-sets formed with respect to: (i) the quality of the secondary vertex fit, (ii) the quality of the projected decay length fit, (iii) the azimuthal angle of the jet axis and (iv) the polar angle of the jet axis. No significant systematic variations are observed.

χ^2Probability of secondary vertex fit	$\langle\tau_B\rangle$ (ps)
0 - 0.01	1.185 ± 0.190
0.01 - 0.50	1.388 ± 0.110
0.50 - 1.0	1.346 ± 0.072
χ^2-Probability of decay length fit	$\langle\tau_B\rangle$ (ps)
0 - 0.01	1.304 ± 0.153
0.01 - 0.50	1.342 ± 0.066
0.50 - 1.0	1.364 ± 0.089
ϕ(jet axis)	$\langle\tau_B\rangle$ (ps)
Quadrant 1	1.326 ± 0.092
Quadrant 2	1.416 ± 0.105
Quadrant 3	1.290 ± 0.111
Quadrant 4	1.419 ± 0.103
$\cos\theta$(jet axis)	$\langle\tau_B\rangle$ (ps)
$-1.0 \leq \cos\theta < -0.5$	1.576 ± 0.115
$-0.5 \leq \cos\theta < 0.0$	1.255 ± 0.091
$0.0 \leq \cos\theta < 0.5$	1.362 ± 0.088
$0.5 \leq \cos\theta \leq 1.0$	1.292 ± 0.105

Table 6.2: The dependence of the $\langle\tau_B\rangle$ measurement on secondary vertex-fit quality, projected decay length-fit quality, the azimuthal and polar angle of the jet axis.

6.3.4 The Gradient Method

An independent method of measuring $\langle \tau_B \rangle$ and hence a useful consistency check on the result, is based on the sensitivity of the lifetime tail for the full decay length distribution to the lifetime of the B.

The decay length in three dimensions was calculated as in Equation 6.4. The expected exponential form of the lifetime tail results in the folded decay length log-distribution being, to first order, linear. By fitting for the gradient of the tail, Monte Carlo samples weighted for various assumed mean B lifetimes can be compared to the situation in the data.

Figure 6.10 shows the dependence from Monte Carlo of the tail-gradient for different input mean lifetimes of the B. To be consistent with the previous measurement, only data from the highest energy jet was considered and all quality and analysis cuts were in common to the two methods. The point at which the gradient measured in the data agrees with that from the Monte Carlo, is for $\langle \tau_B \rangle = 1.39 \pm 0.06$ ps, in excellent agreement with our previous result.

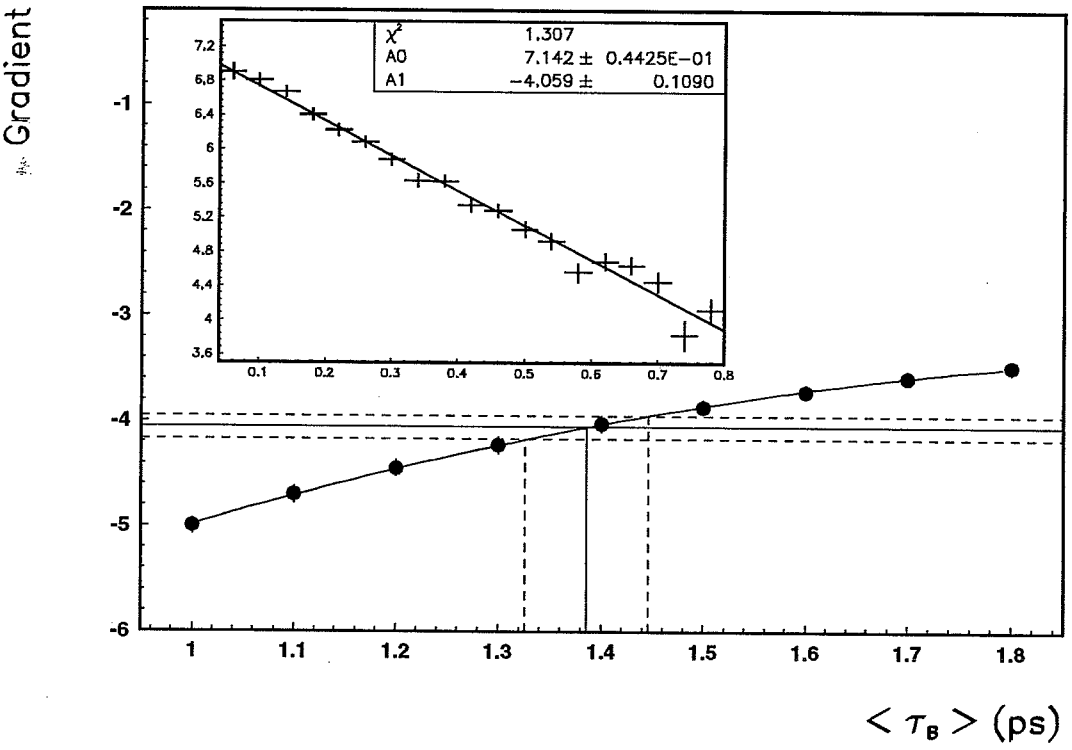

Figure 6.10: The variation of the lifetime-tail gradient as a function of $\langle \tau_B \rangle$ in the Monte Carlo. The insert displays the fit to the data distribution, the result of which is represented by the horizontal line along with the one standard deviation error.

6.3.5 The Proportion of $Z^0 \rightarrow b\bar{b}$ Events

The fitting method as described above leaves only the mean B lifetime as a free parameter. Hence the fraction of $Z^0 \rightarrow b\bar{b}$ events is fixed at whatever level is present in the data. The Monte Carlo generates a $b\bar{b}$ content at the Standard Model prediction which, after events have passed through the decay length finding process, increases slightly to 22.5%. The B lifetime measurement should however in principle be independent of the initial proportion of $Z^0 \rightarrow b\bar{b}$ decays present in the data set.

This was tested by enhancing the data and Monte Carlo event samples in $Z^0 \rightarrow b\bar{b}$ events, by requiring decay lengths to pass some cut value analogous to the procedure used in Section 5.2.6. So as not to bias the sample to long decay lengths however, this cut was applied to projected decay lengths found only in the lowest energy quark jet, leaving the higher energy jet to be used for the lifetime fit as before.

Figure 6.11 shows how the lifetime fit result varies as the sample purity in $Z^0 \rightarrow b\bar{b}$ events increases. There is no evident systematic dependence of the result for $b\bar{b}$-purities over the full range up to the maximum attainable of $\sim$ 60 % (according to the Monte Carlo), corresponding to a cut on L for the second jet at $\gtrsim$ 2.0 mm.

A systematic bias to smaller $\langle \tau_B \rangle$ values is seen to develop however, if this cut is extended further to around 4 mm or so. This effect was found to be caused by two effects that both act to bias the decay length sample to smaller values: The first was where the decay length in the second jet was large due mainly to the primary vertex being a poor estimate of the true interaction point. This often leads to the decay length in the opposite jet i. e. the highest energy jet, being correspondingly short simply because the two quark jets are nearly always approximately back-to-back. The second cause was found mainly in u,d,s events, where a poorly reconstructed secondary vertex position in the lower energy jet could pass the cut imposed on L and so mimic a B decay. When this occurs, the decay length from the opposite jet used for the lifetime fit is generally relatively small due to the low lifetime content of u, d, s events.

6.4 Systematic Effects

6.4.1 b and c-Quark Fragmentation

Section 4.2.3 described how the Peterson et al. function (Equation 4.4), was chosen to model the fraction of initial quark energy carried by the first rank B or D hadrons. For the case of b-quarks, the parameter ϵ_q was chosen to agree with the OPAL measurement of $\langle x_E \rangle_b$ from $b \rightarrow \mu$ events of, $0.726 \pm 0.007 \pm 0.022$. The systematic error from b-quark fragmentation uncertainties is thus estimated based on vary-

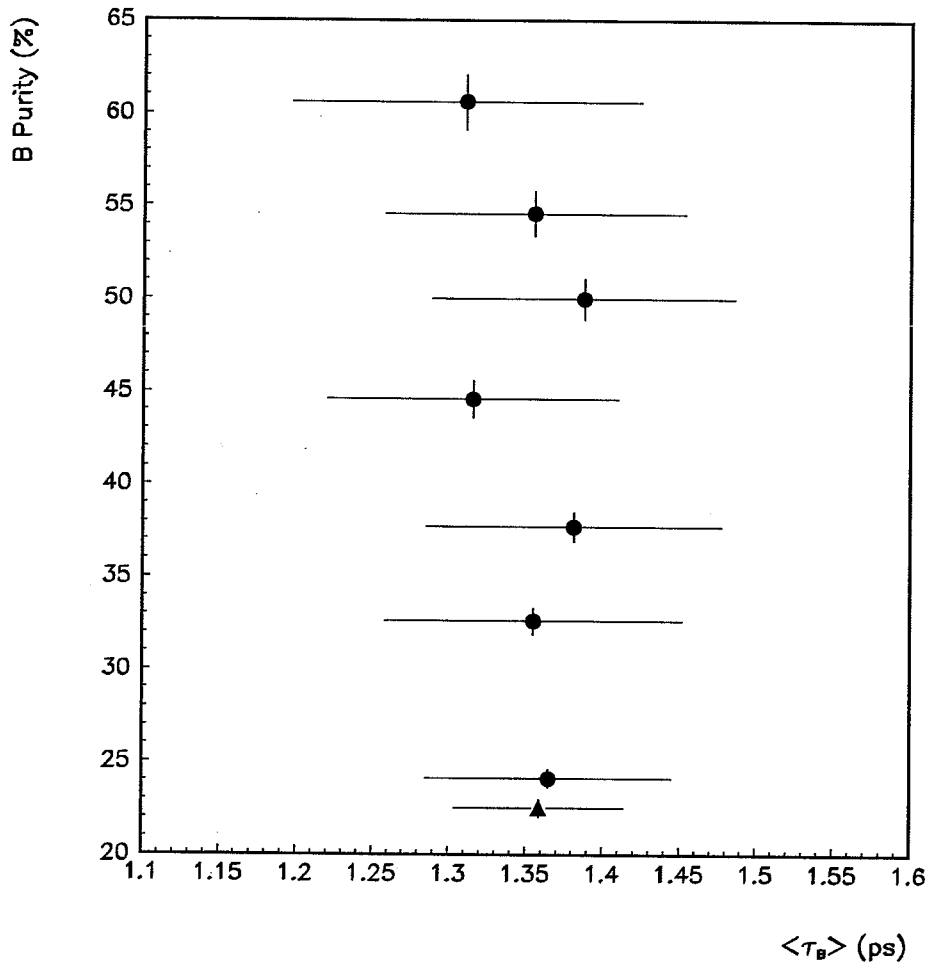

Figure 6.11: $\langle \tau_B \rangle$ as a function of the data set purity in $Z^0 \to b\bar{b}$ events. The cuts imposed on the L distribution for the next highest jet range from -0.2 to 0.15 cm. The odd point corresponds to our central result.

ing the fragmentation within the error on the OPAL number. This was achieved by re-weighting the existing Monte Carlo b-events for a Peterson function where ϵ_b was allowed to vary between 0.008 and 0.001. This corresponds to a variation in $\langle x_E \rangle_b$ from 0.70 to 0.75 (see Figure 4.5).

For the case of charm fragmentation, $\epsilon_c = 0.037$ was chosen to agree with the OPAL measurement of $\langle x_E \rangle_{c \to D^*} = 0.52 \pm 0.03 \pm 0.01$. The systematic error contribution was evaluated in the same way as for the b-sector where ϵ_c was allowed to vary between 0.016 and 0.070. This corresponds to a variation in $\langle x_E \rangle_c$ from 0.49 to 0.55 (see Figure 4.4).

The resulting systematic errors from these two sources are shown in Table 6.4.

6.4.2 Centre of Mass Energy

The 1990 data, as shown in Section 6.2.3, was collected over a range of centre-of-mass energies spanning 6 GeV. The corresponding standard deviation on $\sqrt{s}$ taken over all multi-hadronic events was measured to be 0.922 ± 0.003 GeV. This variation, given that the Monte Carlo events were all generated at a centre-of-mass energy of $m_Z = 91.5$ GeV, is a potential source of systematic error to the lifetime determination.

That the effect is negligible to this analysis however, can be seen by translating the one standard deviation shift in $\sqrt{s}$ into an extra contribution to the error on $\langle x_E \rangle_b$ considered in the previous section. Based on a mean B-hadron energy of 30 GeV and a b-quark production energy of 45 GeV, the corresponding variation in $\langle x_E \rangle_b$ is seen to be ± 0.007. Adding this error in quadrature to the existing (total) error on $\langle x_E \rangle_b$ of 0.023, results in an increase of 0.001. A change of this order is small enough so as to already be included in the range over which $\langle x_E \rangle_b$ is varied for the evaluation of the b-fragmentation systematic error and no additional contribution is made to account for the centre-of-mass energy.

6.4.3 Heavy Flavour Fractions

$\Gamma_{b\bar{b}}/\Gamma_{had}$

The systematic dependence of the lifetime measurement on $\Gamma_{b\bar{b}}/\Gamma_{had}$ was evaluated by re-weighting the Monte Carlo sample to different b fractions over a range consistent with the uncertainty from OPAL measurements. OPAL has two published values for $\Gamma_{b\bar{b}}/\Gamma_{had}$, one from $b \rightarrow \mu$ studies (0.193 ± 0.025 [68]) and the other from a study of of $b \rightarrow e$ events (0.226 ± 0.020 [87]). The fraction was varied by ± 0.025 about the central value in the Monte Carlo and the resulting change used to calculate the systematic contribution listed in Table 6.4.

$\Gamma_{c\bar{c}}/\Gamma_{had}$

The systematic errors due to uncertainty in $\Gamma_{c\bar{c}}/\Gamma_{had}$ was evaluated by varying the fraction over a range given by the error on the OPAL measurement, $\Gamma_{c\bar{c}}/\Gamma_{had}$= 0.186 ± 0.040 [60]. The variation in the lifetime result was used to calculate the systematic contribution listed in Table 6.4.

6.4.4 B Decay Multiplicity

By influencing the secondary vertex finding efficiency in b jets, the B decay multiplicity has an analogous systematic effect on the lifetime measurement as that from $\Gamma_{b\bar{b}}/\Gamma_{had}$.

The measured decay multiplicity distribution for B hadrons from the Monte Carlo was taken and the bin contents re-distributed in a consistent way so as to give a new distribution valid for a different mean B multiplicity. This technique was used to form a weighting factor for the $b\bar{b}$ events in the simulation, to study the sensitivity of the lifetime measurement to changes in the multiplicity.

Current measurements of the charged multiplicity in $b\bar{b}$ events and the uncertainties associated with them were discussed in Section 4.2.4. To account fully for the present errors on this number a broad range of ± 0.3 tracks per event was imposed and the corresponding variation in the lifetime measurement used to calculate the resulting systematic contribution presented in Table 6.4.

6.4.5 D Hadron Lifetimes

The mean lifetimes assigned to D hadrons in the Monte Carlo were reviewed in Section 4.2.4. The current precisions with which these lifetimes are known are listed in Table 6.3.

D hadron	Fractional error on $\langle \tau_D \rangle$ (%)
D^0	1.90
D^+	2.16
D_s^+	6.22
Λ_c^+	7.07
Ξ_c^+	26.67
Ξ_c^0	54.27

Table 6.3: Current measurement errors on the lifetimes of D hadron species that appear in the Monte Carlo sample. From the Particle Data Group [15] (The assumed abundance of the Ω_c^0 is negligibly small and is not considered as part of this systematic study).

The systematic errors on $\langle \tau_B \rangle$ from this source were evaluated by allowing a $\pm 2\sigma$ variation in the D-hadron lifetimes based on the uncertainties in Table 6.3. Table 6.4 lists the assigned error.

6.4.6 D^0/D^+ Ratio

As reviewed in Section 4.2.4, the lifetimes of D^+ and D^0 mesons differ by more than a factor two making the relative abundance of neutral-to-charged charm mesons a potential source of systematic error to the lifetime measurement.

Because of the asymmetric decay of vector mesons into charged and neutral pseudoscalars, the D^0/ D^+ yield is dependent on the probability P_V of producing a charmed vector meson rather than a pseudoscalar:

$$P_V = V/(V + P). \tag{6.5}$$

Table 4.1 shows that the assumed value for P_V in the LUND Monte Carlo is 0.75, which results in approximately 2.2 times more D^0 mesons than D^+ mesons in $c\bar{c}$ events.

ALEPH [88] have recently made measurements of P_V which range from 0.65 ± 0.13 for an event sample with a 76% c-purity to 0.58 ± 0.13 for a 65% b-purity. From an almost pure $c\bar{c}$ sample CLEO [89] using the same method measure $P_V = 0.80 \pm 0.13$. Hence in $c\bar{c}$ events, the relative proportions of D^0/D^+ mesons were varied to cover the range suggested by the ALEPH and CLEO results.

CLEO [90] and ARGUS [91] have also measured the pseudoscalar to vector ratio from B decays to be approximately 0.3 ± 0.1. This result was thus taken with the ALEPH measurement to form a range over which to vary the D^0/D^+ ratio in $b\bar{b}$ events.

Again, by using a weighting technique the D^0/D^+ ratios were varied over the suggested ranges for $c\bar{c}$ and $b\bar{b}$ events separately to find the resulting variation in $\langle \tau_B \rangle$. The combined systematic from this source is assigned by adding in quadrature these two contributions and results in only a 0.6% correction overall.

6.4.7 Primary Vertex

The procedure described in Section 5.3.3 used to estimate the e^+e^- interaction point, is designed to trace all significant shifts in the beamspot position to within a fraction of a running period. To evaluate the effect on the measurement of offsets in the beamspot not traced in the data, the x and y coordinates of the vertex were shifted simultaneously by their calculated errors of 6.7 μm and 4.5 μm respectively. This resulted in a 0.3% shift in $\langle \tau_B \rangle$.

The effect of stretching the assumed size of the beam envelope (σ_{xb}, σ_{yb}) was also studied. The widths in both directions were scaled by $\pm$20% in the Monte Carlo representing a change in σ_x of $\pm$ 31 μm. This resulted in $\langle \tau_B \rangle$ varying by 1.6%. The total error assigned to primary vertex systematic shifts is listed in Table 6.4.

By way of a consistency check on this result, the measurement was repeated using an event-by-event calculated primary vertex position. In each multi-hadronic event, all tracks passing the standard quality cuts were fitted to a common vertex position using the method described in Section 5.2.6. In cases where the primary vertex fit failed for whatever reason, the mean position was used as normal. Use of a fitted vertex per event, can potentially give an improved determination of the

interaction point since it is not subject to the size of the beam envelope (which in the x coordinate at least is the dominant factor). The fit result was $\langle\tau_B\rangle = 1.339 \pm 0.060$ ps corresponding to a 1.5% shift from the standard result. This gives independent confirmation of the sensitivity to the primary vertex but is also nicely consistent, within the statistics, with our initial result.

6.4.8 Jet axis

On page 127 we saw the accuracy with which the jet axis at $y_{cut} = 0.01$ reproduces the flight path of the decaying B-hadron. This degree of uncertainty, based on a lever arm of 2 mm, translates into a spatial shift of $\sim 100\,\mu$mwhich when projected along the decay length vector corresponds to a shift of order $100 \times \sin(0.05) = 5\,\mu$m. This size of change is well within the measurement error on the projected decay length and confirms that the jet axis reproduces the B flight path well enough for any directional uncertainty to be absent from the χ^2 formalism of Appendix D. Further, use of the folded distribution increases the insensitivity to directional uncertainties of the jet axis by virtue of their symmetric effect on the L distribution. This is shown by Figure 6.12, where we compare the folded L distribution based on a directional constraint given by the jet axis with that using the generated direction of the B hadron. The difference is seen to be minimal.

Although expected to be small therefore, any systematic differences in the accuracy of the axis reconstruction between the data and simulation provides a source of error in the lifetime measurement. In order to evaluate the size of any such effect, the average angle between the jet axis and the flight direction of the B hadron associated with the jet, was varied by $\pm 20\%$. The resulting change in $\langle\tau_B\rangle$ was 0.004 ps corresponding to a fractional error of just 0.3%.

6.4.9 Detector Effects

Resolution Smearing

The implementation of a folded distribution was deemed necessary in Section 6.2.1, to cancel resolution type effects in the L distribution that act symmetrically over both the resolution and lifetime tails. That this is the case, was checked by 'smearing' the Monte Carlo distribution to model more closely the resolution found in the data and repeating the lifetime fit to check for consistency.

The smearing was performed by simply transforming each $L \rightarrow L + \Delta L$, for ΔL a Gaussian random number based on a distribution of width,

$$\sigma^2 = \beta\sigma_L^2 - \sigma_L^2. \tag{6.6}$$

The scaling parameter β can then be varied to set the degree of smearing required.

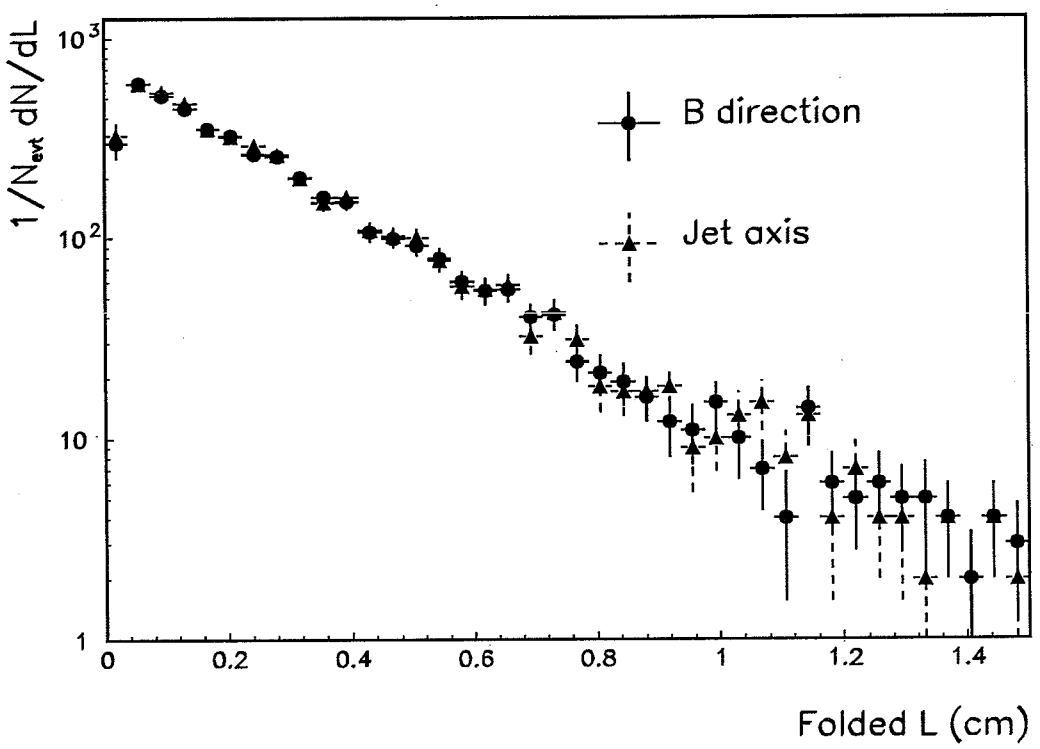

Figure 6.12: The folded L distribution for the case where the generated B-hadron direction forms the directional constraint, compared to the experimental situation where the jet axis direction is used.

The level of smearing found to give the best agreement with the data distribution, based on a χ^2 comparison, was found to be for $\beta = 1.17$. For this level of smearing the resulting lifetime measurement was essentially unchanged at $\langle\tau_B\rangle = 1.358 \pm 0.056$ ps. Smearing of this type was unable to simultaneously reproduce all aspects of the L distribution in data and to properly account for the lifetime tail required an additional smearing of around 10%, corresponding to a β of 1.28. At this point the χ^2 was approximately double that at the minimum point and the lifetime fit was repeated to give, $\langle\tau_B\rangle = 1.342 \pm 0.064$ ps.

We conclude from these results that the folded distribution is to first order insensitive to smearing of this type, which simulates resolution-type differences between data and Monte Carlo. In order to be conservative, we assign a systematic error of ± 0.017 ps, corresponding to the difference in the measurement seen over the smearing range investigated.

Given the nature of the discrepancy between data and Monte Carlo discussed in Section 6.2.1, a simple Gaussian degradation of the decay length resolution is clearly inappropriate to accurately model the data. Given that the fraction of tracks in the tails of decay-length based variables is in discrepancy in addition to the resolution, a more sophisticated smearing prescription at the track level would be needed to

describe the data via this approach.

Multiple CV Hits

Correcting the data for effects associated with multiple hits on the same wire in the Vertex Chamber, was discussed in Section 3.1.8. Unless properly accounted for, the positions of multiple hits can be pulled closer to the anode plane and hence ultimately shift the trajectories of reconstructed tracks. This effect in principle can influence the decay length since, for example, tracks that straddle an anode plane will have their nominal crossing point shifted to larger radii.

In order to quantify any such effect on the measured lifetime, the fit was repeated using tracks whose only CV content was from hits that were first hits on wires. The result of the fit was, $\langle\tau_B\rangle = 1.327 \pm 0.105$ ps i. e. a change in the measured lifetime of 0.032 ps.

The effect of varying the number of CV axial hits imposed on tracks by the physics cuts was also studied. The resulting variation in $\langle\tau_B\rangle$ was found to be negligible.

CV Anode Plane Azimuthal Cut

In Section 3.1.8 we described the presence in the data of an overestimate of the CV drift velocity at small drift distances. This necessarily led to the rejection of tracks within 0.01 mrad of the anode plane. It is important to verify that this effect has no residual influence on the lifetime measurement. In principle the crossing point of two tracks straddling an anode plane will be forced to shorter decay lengths, if either (or both) of the tracks have their positions shifted to longer drift distances.

The anode cut was doubled to 0.02 mrad and the fit repeated with the result that $\langle\tau_B\rangle = 1.339 \pm 0.066$ ps i. e. a change in the measured lifetime of 0.020 ps.

6.5 Results

Combining all error contributions from Table 6.4 in quadrature, the total systematic error is estimated to be 0.111 ps. Hence the mean B-hadron lifetime is determined to be,

$$\boxed{\langle\tau_B\rangle = 1.359 \pm 0.055\,(\text{stat.}) \pm 0.111\,(\text{syst.})\,\text{ps.}}$$

To put the result in context, Figure 6.13 presents a comparison with all previous measurements from decay length-related methods which were reviewed in Section 6.1.2.

Source	Error on $\langle\tau_B\rangle$ (ps)
b fragmentation	0.085
c fragmentation	0.009
$\Gamma_{b\bar{b}}/\Gamma_{had}$	0.043
$\Gamma_{c\bar{c}}/\Gamma_{had}$	0.020
B decay multiplicity	0.020
D hadron lifetime	0.012
D^0/ D^+ ratio	0.008
Primary vertex	0.022
Jet axis	0.002
Resolution	0.017
CV multiple hits	0.032
CV anode cut	0.020
Total	0.111

Table 6.4: Systematic errors on $\langle\tau_B\rangle$.

Finally, this measurement of the B-hadron lifetime, combined with a previous measurement from OPAL of the semi-leptonic branching ratio, $Br(B \to \ell\nu X) = 0.104 \pm 0.007$[6], can be used to determine the magnitude of the CKM matrix element $|V_{cb}|$. By rearranging Equation 1.32 we have that

$$|V_{cb}|^2 = \frac{Br_{sl}}{40.67\,(2.08R+1)}\frac{1}{\langle\tau_B\rangle}, \tag{6.7}$$

where $R = \frac{|V_{ub}|^2}{|V_{cb}|^2}$. Measurements [93] of the endpoint of the lepton momentum spectrum from B-meson semi-leptonic decays give model dependent values for ratio $|V_{ub}|\,/\,|V_{cb}|$, in the range 0.1 to 0.2. We choose a value of 0.15 ± 0.10. The values chosen for quark masses and $\alpha_s(m_b)$ in order to form Equation 6.7 were detailed in Section 1.4.3. In addition, to include fully theoretical model uncertainties, we choose to increase the quoted error (from Equation 1.23) on m_b to $\pm 0.3\,\mathrm{GeV}/c^2$ and take $m_u = 0.2 \pm 0.2\,\mathrm{GeV}/c^2$.

Hence based on our measurement of $\langle\tau_B\rangle$ we find,

$$\boxed{|V_{cb}| = 0.042 \pm 0.002 \pm 0.003}$$

where the first error is due to the combined statistical and systematic error on $\langle\tau_B\rangle$ and the second is due to uncertainties in the theory, including the errors on

[6]This number derives from the OPAL measurement [68] of $\Gamma_{b\bar{b}}/\Gamma_{had} \times Br(B \to \ell\nu X) = 0.0226 \pm 0.0015$ and assuming the Standard Model prediction for $\Gamma_{b\bar{b}}/\Gamma_{had}$ of 0.218.

$|V_{ub}|/|V_{cb}|$, the quark masses and α_s.

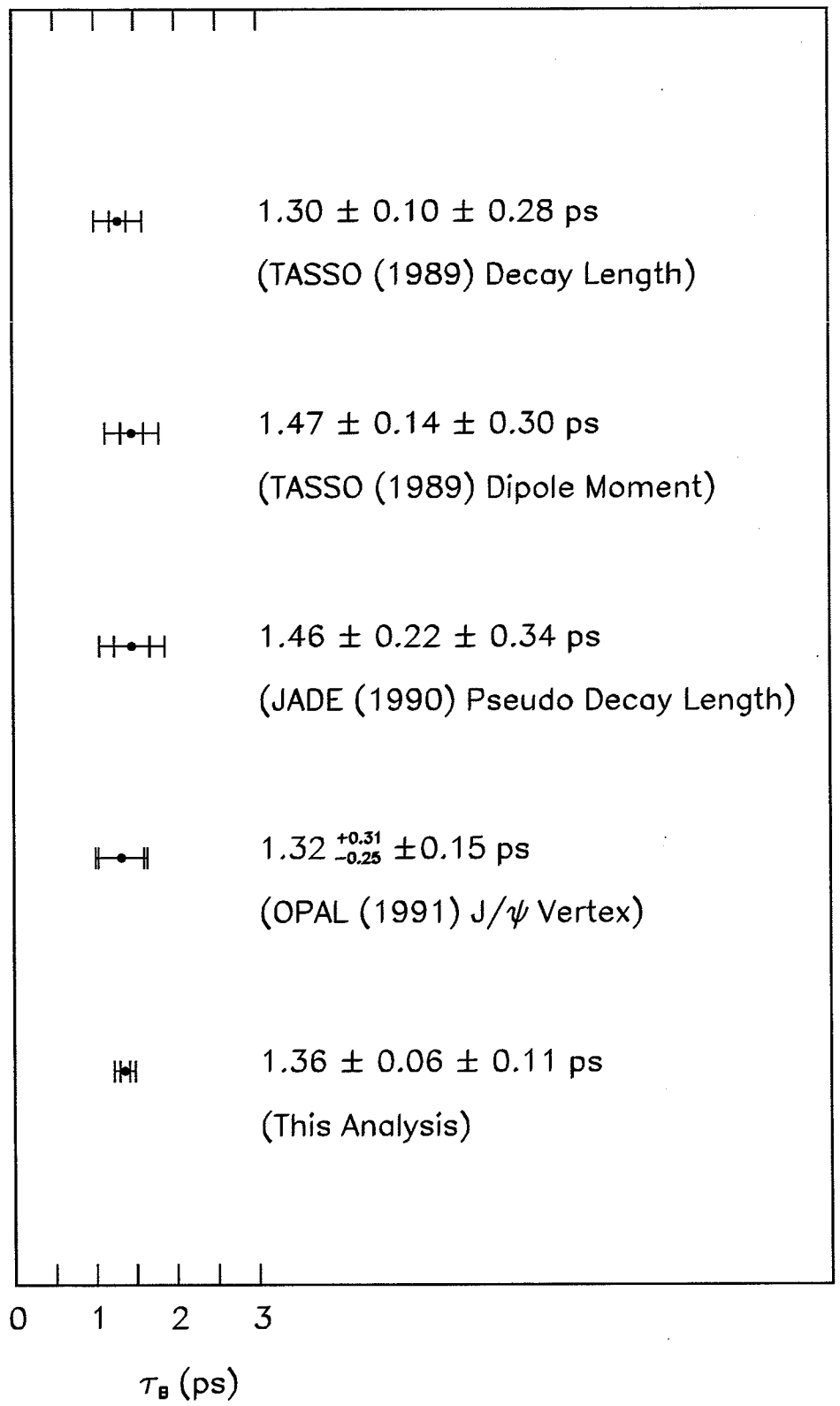

Figure 6.13: World measurements [92] of the mean B-hadron lifetime using decay length-related variables. The measurement from this analysis is included for comparison. The ALEPH Collaboration have recently presented a preliminary result based on the J/ψ vertex from their 1990 and 1991 data sets (450K multi-hadrons). They measure, $\tau_b = 1.40^{+0.20}_{-0.18} \pm 0.07$ ps [79].

Appendix A

Coordinate Systems

A.1 The OPAL Master Reference System

The OPAL **M**aster **R**eference **S**ystem (MRS), shown in figure A.1, is a 3D right-handed Cartesian coordinate system whose origin is at the nominal e^+e^- interaction point. The z-axis points along the electron direction and is inclined by 1.39% with respect to the horizontal. It follows that the y-axis is inclined by the same amount to the vertical. A track vector projected into the plane tranverse to the z-axis (in

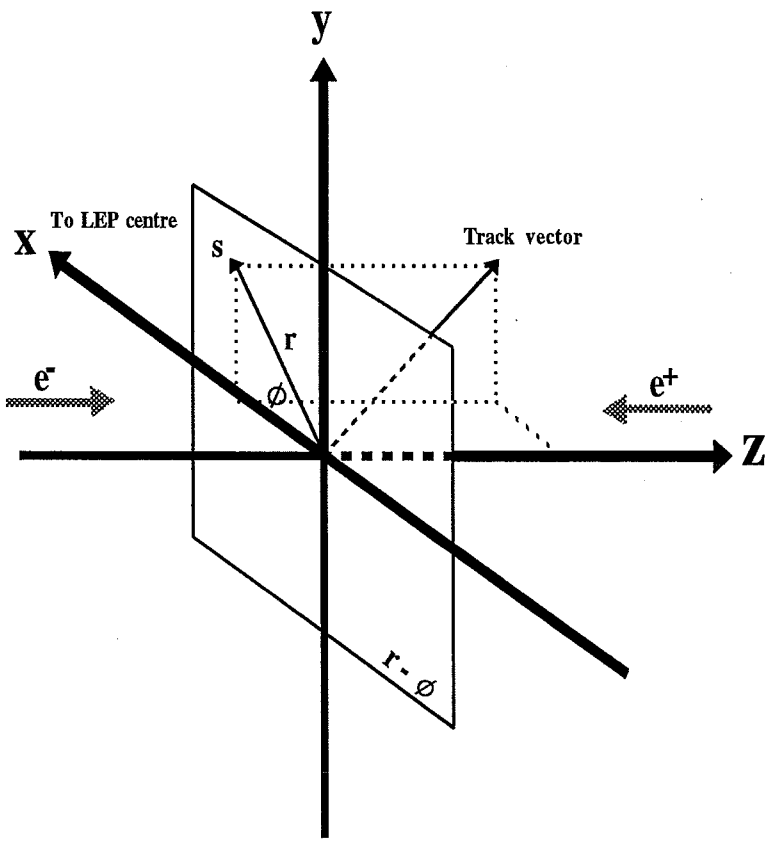

Figure A.1: The OPAL MRS

polar coordinates, the $r-\phi$ plane), is a vector whose angle to the positive x-axis is the *azimuthal* angle, ϕ, and the vector s points along the trajectory in this plane. The *polar* angle, θ, is then defined to be the angle between the positive z-axis and the track vector in the $s-z$ plane.

A.2 The Vertex Chamber Coordinate System

The coordinate system of the Jet Chamber coincides with the OPAL MRS as defined above. In addition a **chamber construction** coordinate system, (x_c, y_c, z_c), is defined internally to the Vertex Chamber. Here the x_c axis lies along a CV cathode plane that nominally lines up with x_{MRS}, and z_c lies along the chamber cylindrical axis in the same directional sense as z_{MRS}. The y_c axis is then constrained by the condition that the axes should be right-handed and orthonormal.

In principle the construction and MRS systems should be the same, however in practice there will be a small displacement of the CV from the nominal position together with a small rotation. The transformation of coordinates from the construction frame to the MRS is thus specified by three orthogonal translations $(\Delta x, \Delta y, \Delta z)_{MRS}$ and three rotations $(\alpha, \beta, \gamma)_{MRS}$ about the z, y and x axes respectively.

Appendix B

OPAL Track Parameter Definitions

Tracks reconstructed in the Central Detector define a helix in three dimensions with five free parameters; (κ, ϕ_0, d_0, $\tan\lambda$, z_0), defined as below and illustrated in Figure B.1:

- κ is the curvature where,

$$|\kappa| = \frac{1}{2\rho} \tag{B.1}$$

  for ρ the radius of curvature of the track. The curvature is signed such that $\kappa > 0$ implies ϕ increases in moving along the track from the point of closest approach (p.c.a.) to the origin in the $r-\phi$ plane. Given that the OPAL magnetic field (B_z) points axially along the positive z-axis, then $\kappa > 0$ corresponds to a particle with negative physical charge.

- ϕ_0 is the azimuthal angle made by the track tangent at the p.c.a.

- d_0 is the impact parameter i. e. $|d_0|$ is the distance from the origin to the p.c.a. Defining $\underline{d}$ to be the vector from the origin to the p.c.a., $\underline{\hat{\phi}}$ the unit track vector at the p.c.a. and $\underline{\hat{z}}$ the unit vector along the z axis, then the relative sign carried by d_0 is given by the formal definition:

$$d_0 = \underline{\hat{\phi}} \times \underline{d} \cdot \underline{\hat{z}} \tag{B.2}$$

- $\tan\lambda = \cot\theta$, where θ is the track polar angle.

- z_0 is the z-coordinate of the track at the p.c.a. The projection of the helix in the $s-z$ plane is then simply:

$$z = z_0 + s\tan\lambda \tag{B.3}$$

  where s is the arc length of the track in the $r-\phi$ plane from the p.c.a.

These parameters are related to the physics track variables by:

$$p_{\mathrm{xy}} = a|\frac{B_z}{\kappa}| \tag{B.4}$$

where if $p_{xy}(= \sqrt{p_x^2 + p_y^2})$ is measured in GeV/c, B_z in kG and κ in cm^{-1}, then $a = \frac{c}{2} \times 10^{-14} \simeq 1.5 \times 10^{-4}$ and where,

$$p_x = p_{\mathrm{xy}} \cos\phi_0 \tag{B.5}$$

$$p_y = p_{\mathrm{xy}} \sin\phi_0 \tag{B.6}$$

$$p_z = p_{\mathrm{xy}} \tan\lambda \tag{B.7}$$

$$p = p_{\mathrm{xy}}\sqrt{1 + \tan^2\lambda} \tag{B.8}$$

$$q = (\text{particle charge}) = -(\text{sign of } (\frac{B_z}{\kappa})). \tag{B.9}$$

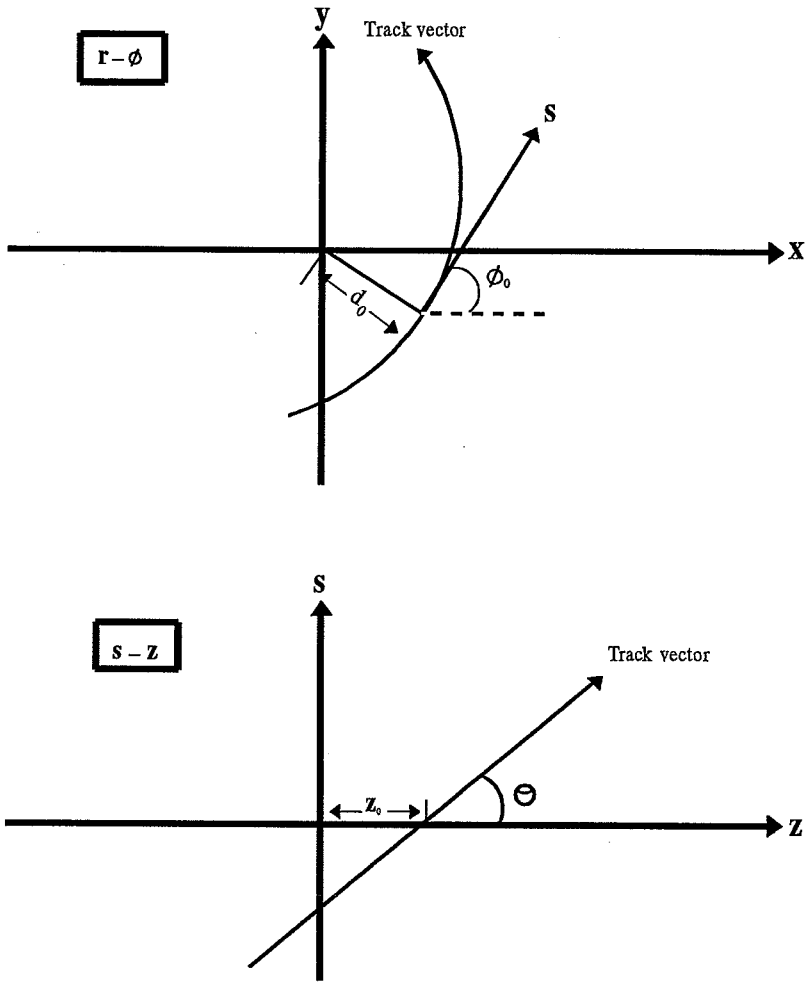

Figure B.1: The definition of OPAL track parameters.

Appendix C

Formalism For Vertex Fitting in 2-Dimensions

In the $r-\phi$ plane track trajectories describe circles,

$$(x-A)^2+(y-B)^2=R^2 \tag{C.1}$$

where A, B are the coordinates of the circle centre (see Figure C.1). In terms of OPAL track parameters we have,

$$A \equiv -(d_0+\frac{1}{2\kappa})\sin\phi_0, \quad B \equiv (d_0+\frac{1}{2\kappa})\cos\phi_0, \quad R \equiv \frac{1}{2\mid\kappa\mid} \tag{C.2}$$

In general, the normal distance of a point (x_v, y_v) from the circle is

$$\pm D = R - \sqrt{(x_v-A)^2+(y_v-B)^2} \tag{C.3}$$

The problem of interest is the determination of the most probable common point, (x_v, y_v), through which a set of tracks, $(1, ..., N)$, may pass. This essentially requires the minimisation of the following χ^2,

$$\chi^2 = \sum_{i=1}^{N} \frac{D_i^2}{\sigma_{D_i}^2} \tag{C.4}$$

For computational efficiency and accuracy it turns out that a more suitable form of Equation C.3 is the following approximation due to Karimaki [94] (valid for large R),

$$D = \frac{R}{2} - \frac{1}{2R}[(x_v-A)^2+(y_v-B)^2] + \ldots \tag{C.5}$$

which in terms of OPAL parameters becomes,

$$D = y_v\cos\phi_0 - d_0 - x_v\sin\phi_0 - \kappa[(x_v+d_0\sin\phi_0)^2+(y_v-d\cos\phi_0)^2] \tag{C.6}$$

Using the covariance matrix of the $r-\phi$ track parameters from the track fit and Equation C.6, the variance on D can now be calculated as,

$$\begin{aligned}\sigma_D^2 \;=\; & \sigma_{d_0}^2(\frac{\partial D}{\partial d_0})^2 + \sigma_{\phi_0}^2(\frac{\partial D}{\partial \phi_0})^2 + \sigma_\kappa^2(\frac{\partial D}{\partial \kappa})^2 \\ & +2\sigma_{d_0,\phi_0}\frac{\partial D}{\partial \phi_0}\frac{\partial D}{\partial d_0} + 2\sigma_{\kappa,\phi_0}\frac{\partial D}{\partial \phi_0}\frac{\partial D}{\partial \kappa} + 2\sigma_{d_0,\kappa}\frac{\partial D}{\partial \kappa}\frac{\partial D}{\partial d_0}\end{aligned} \tag{C.7}$$

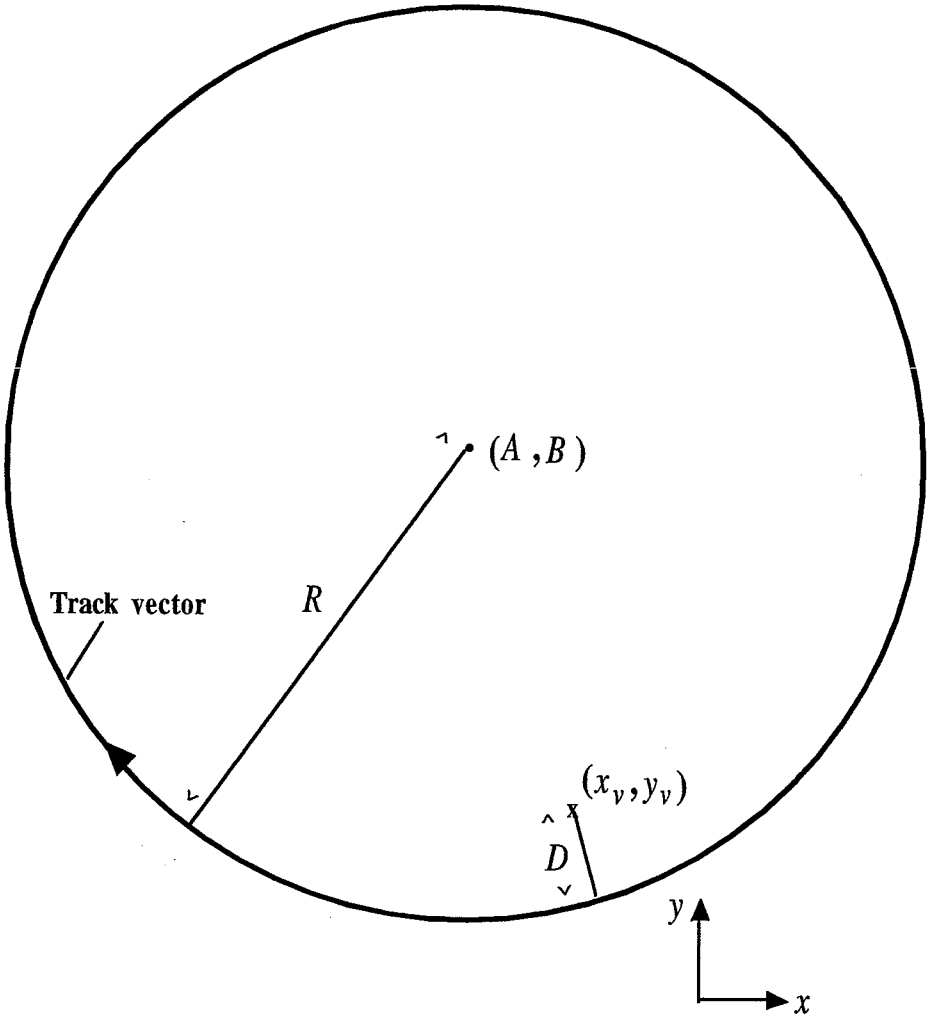

Figure C.1: Vertex fit definitions.

Since from Equation C.3 the problem is clearly non-linear in x_v and y_v, we must minimise Equation C.4 by an iterative process. We define,

$$\Delta x \equiv x_v - x_o \tag{C.8}$$

$$\Delta y \equiv y_v - y_o \tag{C.9}$$

$$g_x \equiv \sum_{k=1}^{N} \frac{D_k(\partial D_k/\partial x_v)}{\sigma_{D_k}^2} \sim \frac{\partial \chi^2}{\partial x_v} \tag{C.10}$$

$$g_y \equiv \sum_{k=1}^{N} \frac{D_k(\partial D_k/\partial y_v)}{\sigma_{D_k}^2} \sim \frac{\partial \chi^2}{\partial y_v} \tag{C.11}$$

$$g_{xx} \equiv \sum_{k=1}^{N} \frac{(\partial D_k/\partial x_v)^2}{\sigma_{D_k}^2} \sim \frac{\partial^2 \chi^2}{\partial x_v^2} \tag{C.12}$$

$$g_{yy} \equiv \sum_{k=1}^{N} \frac{(\partial D_k/\partial y_v)^2}{\sigma_{D_k}^2} \sim \frac{\partial^2 \chi^2}{\partial y_v^2} \tag{C.13}$$

$$g_{xy} \equiv \sum_{k=1}^{N} \frac{(\partial D_k/\partial x_v)(\partial D_k/\partial y_v)}{\sigma_{D_k}^2} \sim \frac{\partial^2 \chi^2}{\partial x_v \partial y_v} \tag{C.14}$$

By making Taylor expansions (keeping zeroth and first-order terms only) of, $\frac{\partial \chi^2}{\partial x_v}$ and $\frac{\partial \chi^2}{\partial y_v}$ about the point (x_0, y_0), representing an initial estimate of (x_v, y_v), the problem reduces to solving the two simultaneous equations,

$$g_x(x_o, y_o) + g_{xx}(x_o, y_o)\Delta x + g_{xy}(x_o, y_o)\Delta y = 0 \quad \text{(C.15)}$$

$$g_y(x_o, y_o) + g_{yx}(x_o, y_o)\Delta x + g_{yy}(x_o, y_o)\Delta y = 0 \quad \text{(C.16)}$$

The solution then for each iterative step is,

$$\begin{pmatrix} \Delta x_v \\ \Delta y_v \end{pmatrix} = \begin{pmatrix} g_{xx} & g_{xy} \\ g_{xy} & g_{yy} \end{pmatrix}^{-1} \begin{pmatrix} -g_x \\ -g_y \end{pmatrix} = \frac{1}{g_{xx}g_{yy} - g_{xy}^2} \begin{pmatrix} g_{yy} & -g_{xy} \\ -g_{xy} & g_{xx} \end{pmatrix} \begin{pmatrix} -g_x \\ -g_y \end{pmatrix} \quad \text{(C.17)}$$

where again the derivatives are taken at $x_v = x_o$ and $y_v = y_o$.

Appendix D

Formalism For 2-Dimensional Decay Length Fitting

The problem to be solved is the determination of the most likely decay length of a particle in the $r-\phi$ plane given estimates of the decay point (x_0, y_0) and production point (x_p, y_p) together with the direction of the decay length vector, which is assumed to be known exactly.

Following the nomenclature of Figure 5.7, the essential input numbers are:

- Some estimate of the production point i. e. the mean primary vertex position, (x_b, y_b), with associated covariance matrix,

$$C_b = \begin{pmatrix} C_b^{xx} & 0 \\ 0 & C_b^{yy} \end{pmatrix} \tag{D.1}$$

- Some estimate of the decay point, i. e. the measured secondary vertex position, (x_v, y_v), with associated covariance matrix,

$$C_v = \begin{pmatrix} C_v^{xx} & C_v^{xy} \\ C_v^{xy} & C_v^{yy} \end{pmatrix} \tag{D.2}$$

- Some estimate of the decaying particles flight direction, (T_x, T_y). This is provided, for example, by the event thrust axis or by a jet axis where; $t_x^2 + t_y^2 = 1$.

Following [95], a least-squares minimisation procedure is applied to,

$$\chi^2 = (x_b - x_p, y_b - y_p) {C_b}^{-1} \begin{pmatrix} x_b - x_p \\ y_b - y_p \end{pmatrix} + (x_v - x_0, y_v - y_0) {C_v}^{-1} \begin{pmatrix} x_v - x_0 \\ y_v - y_0 \end{pmatrix} \tag{D.3}$$

By imposing the flight direction constraint,

$$x_0 = x_p + L.T_x \tag{D.4}$$

$$y_0 = y_p + L.T_y \tag{D.5}$$

the problem reduces to minimising the χ^2 with respect to the three unknowns (x_p, y_p, L). This essentially means simultaneously solving, $\frac{\partial\chi^2}{\partial x_p} = \frac{\partial\chi^2}{\partial y_p} = \frac{\partial\chi^2}{\partial L} = 0$, which has exact linear solutions.

Using the following identities,

$$x \equiv x_v - x_b \tag{D.6}$$

$$y \equiv y_v - y_b \tag{D.7}$$

$$C \equiv C_b + C_v \tag{D.8}$$

$$D \equiv T_y^2 C_{xx} + T_x^2 C_{yy} - 2T_x T_y C_{xy}, \tag{D.9}$$

the result for the decay length is,

$$L = \frac{xT_x C_{yy} + yT_y C_{xx} - (xT_y + yT_x)C_{xy}}{D} \tag{D.10}$$

$$\sigma_L = \sqrt{\frac{C_{xx}C_{yy} - C_{xy}^2}{D}} \tag{D.11}$$

$$\chi^2_{min} = \frac{(xT_y - yT_x)^2}{D} \tag{D.12}$$

Bibliography

[1] G. 't Hooft, Nuc. Phys. **B35** (1971) 167.

[2] J. R. Carter, *Precision Tests of the Standard Model at LEP*, a plenary session talk presented at the Lepton-Photon Symposium and Europhysics Conference on High Energy Physics, Geneva, 1991.

[3] K. Sliwa, in *Proceedings of the XXVth Recontres de Moriond p.459 (Editions Frontières, 1990).*

[4] S. Glashow, Nuc. Phys. **B22** (1961) 579.

[5] S. Weinberg, Phys. Rev. Lett. **19** (1967) 1264;
A. Salam, *Elementary Particle Theory*, from *Weak and Electromagnetic Interactions*, edited by N. Svartholm, Almqvist and Wiksell, Stockholm, 1968.

[6] M. Davier, *Searches For New Particles At LEP*, a plenary session talk presented at the Lepton-Photon Symposium and Europhysics Conference on High Energy Physics, Geneva, 1991.

[7] UA1 Collab., G. Arnison et al., Phys. Letters **B122** (1983) 103;
UA2 Collab., M. Banner et al., Phys. Letters **B122** (1983) 476.

[8] UA1 Collab., G. Arnison et al., Phys. Letters **B126** (1983) 398;
UA2 Collab., M. Bagnaia et al., Phys. Letters **B129** (1983) 130.

[9] L. E. Ibañez, CERN-TH.5237/88, November 1988.

[10] S. W. Herb et al., CFS Collab., Phys. Rev. Lett. **39** (1977) 252.

[11] S. Okubu, Phys. Letters **B5** (1963) 165;
G. Zweig, CERN-TH-401, TH-402 (1964);
J. Iizuka, Prog. Theor. Phys. Supp. **37-38** (1966) 21.

[12] A. Ali, from *B Decays* edited by S. Stone, World Scientific 1992.

[13] D. Andrews et al., CLEO Collab., Phys. Rev. Lett. **44** (1980) 1108;
T. Böhringer et al., CUSB Collab., Phys. Rev. Lett. **44** (1980) 1111.

[14] L. Rolandi, *Precision Tests of the Electroweak Interaction*, a talk presented at the International Conference on High Energy Physics, Dallas, USA (1992).

[15] Particle Data Group, K. Hikasa et al., Phys. Rep. **45** (1992) 11.

[16] J. H. Kühn, P. M. Zerwas, from *Z Physics at LEP 1*, volume 1, CERN 89-08 (1989).

[17] P. Roudeau, *Heavy Flavour Physics at LEP*, plenary session talk presented at the Lepton-Photon Symposium and Europhysics Conference on High Energy Physics, Geneva, 1991.

[18] P. S. Wells, *Partial Widths of the Z^0 to $b\bar{b}$ and $c\bar{c}$ at LEP*, a talk presented at the 4^{th} International Symposium on Heavy Flavour Physics, Orsay, France (1991).

[19] N. Cabibbo, Phys. Rev. Lett. **10** (1963) 531;
M. Kobayashi, T. Maskawa, Prog. Theor. Phys. **49** (1973) 652.

[20] G. Altarelli, N. Cabibbo, G. Corbo, L. Maiani and G. Martinelli, Nuc. Phys. **B208** (1982) 365.

[21] ARGUS Collab., H. Albrecht et al., Phys. Letters **B249** (1990) 360;
E. H. Thorndike, *Proc. 1985 Int. Sym. on Lepton and Photon Interactions at High Energies*, edited by M. Konumu and K. Takahashi, Kyoto 1986, p406.

[22] C. S. Kim, A. D. Martin, Phys. Letters **B225** (1989) 186.

[23] S. Stone, *Semileptonic B Decays - Experimental*, from *B Decays* edited by S. Stone, World Scientific 1992.

[24] M. V. Danilov, *Heavy Flavour Physics*, plenary session talk presented at the Lepton-Photon Symposium and Europhysics Conference on High Energy Physics, Geneva, 1991.

[25] A. Ali, E. Picturinen, Nuc. Phys. **B154** (1979) 519.

[26] S. Bethke, private communication.

[27] OPAL Collab., P. D. Acton et al., Z. Phys. **C55** (1992) 1.

[28] *The LEP Main Ring Accelerating Structure*, CERN 89-09.

[29] Nucl. Instr. and Meth. **A305** (1991) 275-319.

[30] OPAL Collab., M. Z. Akrawy et al., Z. Phys. **C52** (1991) 175-207.

[31] A. A. Carter et al., Nucl. Instr. and Meth. **A250** (1986) 503-513.

[32] M. Arignon et al., CERN-PPE/91-32.

[33] P. Bock and G. Tysarczyk-Niemeyer. *Online Pattern Recognition for the QPAL Jet Chamber*, OPAL internal note.

[34] OPAL collab. On-line Group, *The OPAL Data Aquisition System*, OPAL internal note.

[35] *ZEBRA Data Structure Management System*, CERN Computer Centre Library.

[36] S. Weisz, D. Lellouch and C. Hawkes, *Rope Primer - Latest revision for ROPE400.*

[37] A. Buijs. *The OPAL DST (OD) Processor in ROPE (version 311)*, OPAL internal note.

[38] R. Cranfield, B. Holl, R. W. L. Jones, *OPCAL User Guide*, OPAL internal note.

[39] D. Ward, *A GRope Primer*, OPAL internal note.

[40] H. Drumm et al., Nucl. Instr. and Meth. **A176** (1980) 333-334.

[41] J. M. Roney, *The OPAL Vertex Detector*, Ph. D. Thesis, Carleton Institute for Physics, Ottawa, Canada;
J. M. Roney et al., Nucl. Instr. and Meth. **A279** (1989) 236.

[42] M. M. B. Lasota, *The Development of High Precision Drift-Chambers and the OPAL Vertex Detector*, Ph.D. Thesis, Queen Mary College, University of London;
J. R. Carter et al., Nucl. Instr. and Meth. **A278** (1989) 725

[43] J. Mildenberger, *CV Calibrations for the 1990 reROPE*, OPAL internal note (1991).

[44] L. Janissen, B. Carnegie, *Correction of CV Second Hit Drift Distance*, OPAL internal note (1990).

[45] R. D. Heuer, A. Wagner, Nucl. Instr. and Meth. **A265** (1988) 11-19.

[46] H. M. Fischer et al., Nucl. Instr. and Meth. **A283** (1989) 492-501

[47] P. Bock, J. Heintze, T. Kunst, B. Schmidt, L. Smolik, Nucl. Instr. and Meth. **A242** (1986) 237-246.

[48] D. Schaile, O. Schaile, J. Schwarz, Nucl. Instr. and Meth. **A242** (1986) 247-253.

[49] *The CJ Processor for ROPE*, OPAL internal note.

[50] O. Biebel, et al., CERN PPE/91-019.

[51] R. Van Kooten, *Performance of the OPAL Jet Chamber*, talk presented at the 1992 Vienna Wire Chamber Conference, CERN-PPE/92-55.

[52] P. Billoir, Nucl. Instr. and Meth. **A225** (1984) 352-366.

[53] T. Sjöstrand, *A Manual to the Lund Monte Carlo for Jet Fragmentation and* e^+e^- *Physics*, 1989;
T. Sjöstrand, in *Z Physics at LEP 1*, Volume 3, CERN 89-08 (1989).

[54] B. Anderson, G. Gustafson, G. Ingelman, T. Sjöstrand, Phys. Rep. **97** (1983) 31.

[55] F.A. Berends, R. Kleiss, S. Jadach, Nuc. Phys. **B202** (1982) 63.

[56] G. Altarelli, G. Parisi, Nuc. Phys. **B126** (1977) 298.

[57] OPAL Collab., M. Z. Akrawy et al., Z. Phys. **C47** (1990) 505-521.

[58] OPAL Collab., M. Z. Akrawy et al., Phys. Letters **B247** (1990) 617-628.

[59] C. Peterson et al., Phys. Rev. **D27** (1983) 105.

[60] OPAL Collab., G. Alexander et al.,Phys. Letters **B262** (1991) 341-350.

[61] OPAL Collab., M. Z. Akrawy et al., Phys. Letters **B262** (1991) 311-324.

[62] Jan Chrin, OPAL Technical Note TN030, (1991).

[63] CLEO Collab., M. S. Alam et al., Phys. Rev. Lett. **49** (1982) 357;
CLEO Collab., M. S. Alam et al., Bull. Am. Phys. Soc. **31**, 4 (1986) 790.

[64] D. R. Ward, *The OPAL Monte Carlo Program - GOPAL*, OPAL-CR024, Invited talk given at the MC91 Workshop, Amsterdam, April 8-12 1991.

[65] J. Allison et al., Comp. Phys. Comm. **47** (1987) 55.

[66] K. Bos, B. Van Eijk, *(Heavy Flavour) Decays in Eurodec*, DELPHI 89-50 PHYS 44, 1989.

[67] OPAL Collab., M. Z. Akrawy et al., Phys. Letters **B261** (1991) 334-346.

[68] OPAL Collab., M. Z. Akrawy et al., Phys. Letters **B263** (1991) 311-324.

[69] R. Marshall, Z. Phys. **C26** (1984) 291-299.

[70] T. Wyatt, *A Study of the Production of b-Quarks in* e^+e^- *Annihilation at High Energies*, Ph. D. Thesis, University of Oxford.

[71] TASSO Collab., W. Baunschweig et al., Z. Phys. **C44** (1989) 1-13.

[72] R. Barlow, S. Pawley and N. Wood, *b Physics using Event Shapes at OPAL*, OPAL Technical Note TN075.

[73] JADE Collab., S. Bethke et al., Phys. Letters **B213** (1988) 235.

[74] OPAL Collab., M. Z. Akrawy et al., Phys. Letters **B235** (1990) 389-398.

[75] OPAL Collab., M. Z. Akrawy et al., Z. Phys. **C49** (1991) 375.

[76] S. de Jong, *Determination of the LEP Beam Spot Location in OPAL with PASS3 Data*, OPAL Technical Note TN041, (1991).

[77] René Ong, *Measurement of the B Hadron Lifetime*, Ph. D. Thesis, SLAC report 320 (1987).

[78] MAC Collab., E. fernandez et al., Phys. Rev. Lett. **51** (1983) 1022;
MARK II Collab., N. S. Lockyer et al., Phys. Rev. Lett. **51** (1983) 1316;
DELCO Collab., D. E. Klem et al., Phys. Rev. Lett. **53** (1984) 1873;
JADE Collab., W. Bartel et al., Z. Phys. **C31** (1986) 349;
HRS Collab., J.-M. Brom et al., Phys. Letters **B195** (1987) 301;
DELCO Collab., D. E. Klem et al., Phys. Rev. **D37** (1988) 41;
MARK II Collab., R. A. Ong et al., Phys. Rev. Lett. **62** (1989) 1236;
JADE Collab., J. Hagemann et al., Z. Phys. **C48** (1990) 401;
ALEPH Collab., D. Decamp et al., Phys. Letters **B257** (1991) 492;
DELPHI Collab., P. Abreu et al., Z. Phys. **C53** (1992) 567-580;
L3 Collab., B. Adeva et al., Phys. Letters **B270** (1991) 111-122;
OPAL Collab., P. D. Acton et al., Phys. Letters **B274** (1992) 513-525.

[79] J. Kroll, Talk presented at the XXVII Recontres de Moriond, 15-22 March 1992.

[80] TASSO Collab., M. Althoff et al.,Phys. Letters **B149** (1984) 524;
JADE Collab., W. Bartel et al., Z. Phys. **C31** (1986) 349;
MAC Collab., W. W. Ash et al., Phys. Rev. Lett. **58** (1987) 640;
TASSO Collab., W. Braunschweig et al., Z. Phys. **C44** (1989) 1;
DELPHI Collab., P. Abreu et al., Z. Phys. **C53** (1992) 567-580.

[81] MARK II Collab., S. R. Wagner et al., Phys. Rev. Lett. **64** (1990) 1095;
ALEPH Collab., preliminary results presented at the Int. Symp. on Lepton and Photon Interactions at High Energy, Geneva, August 1991;
E653 Collab., *Beauty Pairs and Charm Semileptonic Decays from Fermilab E653*, presented by N. R. Stanton at the 3rd Topical Seminar on Heavy Flavours, San Miniato, June 1991.

[82] CLEO Collab., R. Fulton et al., Phys. Rep. **43** (1991) 651;
ARGUS Collab., H. Albrecht et al., Phys. Letters **B232** (1989) 554.

[83] J. Jaros, in *Proc. Physics in Collision 4*, Santa Cruz, 1984.

[84] S. Lloyd, private communication.

[85] J. Allison et al., CERN PPE/91-234.

[86] F. James, M. Roos, *MINUIT Function normalization and Error Analysis*, CERN D506 (1988).

[87] OPAL Collab., P. D. Acton et al., Z. Phys. **C55** (1992) 191.

[88] ALEPH Collab., D. Decamp et al., Phys. Letters **B266** (1991) 218.

[89] CLEO Collab., D. Bortoletto et al., Phys. Rep. **37** (198) 1719; Phys. Rep. **39** (1989) 1471.

[90] CLEO Collab., R. Fulton et al., Phys. Rep. **43** (1991) 651.

[91] ARGUS Collab., H. Albrecht et al., DESY-92-029, February 1992.

[92] TASSO Collab., W. Braunschweig et al., Z. Phys. **C44** (1989) 1;
JADE Collab., J. Hagemann et al., Z. Phys. **C48** (1990) 401;
OPAL Collab., G. Alexander et al., Phys. Letters **B266** (1991) 485.

[93] CLEO Collab., R. Fulton et al., Phys. Rev. Lett. **64** (1990) 16;
ARGUS Collab., H. Albrecht et al., Phys. Letters **B255** (1991) 297.

[94] V. Karimaki, CERN UA1/TN-82-24.

[95] René Ong, Keith Riles, *The Decay Length Method*, MARK II/SLAC note # 166, (1986).